Development of CCD and EM-CCD Technology for High Resolution X-Ray Spectrometry

Thesis

UNRESTRICTED

Development of CCD and EM-CCD technology for high resolution X-ray spectrometry

Thesis submitted for the degree of

Doctor of Philosophy

at The Open University

by

James Henry Tutt

e2v Centre for electronic imaging

Discipline of Planetary and Space Science

Department of Physical Science

06 November 2012

Date of Submission: 26 June 2012

Date of Award: 6 November 2012.

ProQuest LLC.
789 East Eisenhower Parkway
P.O. Box 1346
Ann Arbor, MI 48106 – 1346

Development of CCD and EM-CCD technology for high resolution X-ray spectrometry

James Henry Tutt

Abstract

This thesis discusses the development of Charge-Couple Device (CCD) and Electron Multiplying CCD (EM-CCD) technology for high resolution X-ray spectroscopy. Of particular interest is the spectral resolution performance of the devices alongside the optimisation of the quantum efficiency through the use of back-illuminated CCDs, thin filter technology and improved passivation techniques. The early chapters (1 through 5) focus on the background and theory that is required to understand the purpose of the work in this thesis and how semiconductors can be used as the detector of high resolution X-ray spectrometers. Chapter 6 focuses on the soft X-ray performance of three different types of conventional CCD using the PTB beamline at BESSY II. The results show that there is degradation in spectral resolution in all three devices below 500 eV due to incomplete charge collection and X-ray peak asymmetry. The Hamamatsu device is shown to degrade faster than the CCD30-11 variants and this is attributed to the thickness of the active silicon (>50 μm) in the device and also its thicker dead-layer (~75 nm) which is found by evaluating the device's soft X-ray QE). The charge loss at the back-surface generation/recombination centres is also investigated and is found to be higher in the Hamamatsu device, again due to its thicker dead-layer. Chapter 7 is an investigation of the Modified Fano Factor which aims to describe the spectral resolution degradation that is expected when an EM-CCD is used to directly detect soft X-rays. The factor is predicted analytically, modelled and then verified experimentally allowing EM-CCD performance over the soft X-ray range to be predicted with high levels of confidence. Chapter 8 is a detailed look into work completed for the phase 0 study of the off plane X-ray grating spectrometer on the International X-ray Observatory. The work includes a detailed contamination study, effective area analysis, the pointing knowledge requirement and the use of filters to minimise optical background

Declaration

I hereby declare that no part of this thesis has been previously submitted to this or any other university as part of the requirement for a higher degree. The work described herein was conducted solely by the undersigned except for those colleagues and other workers acknowledged in the text.

James Henry Tutt

06 November 2012

Dedication

To my mother and my father

Acknowledgements

I would like to acknowledge quite a lot of people for their help and encouragement over the duration of my thesis.

Thanks to my supervisors Andrew Holland, Neil Murray, David Hall and James Endicott for their guidance and technical support.

Thanks to David Burt, David Lumb and Mark Robbins for imparting fractions of their vast knowledge and experiences on me.

Thanks to the current and former members of the CEI, Ben Dryer, Anthony Evagora, Richard Harriss, Phillipa Smith, Mathew Soman, Andrew Clarke, Edgar Allanwood, Jason Gow, Ross Burgon, Calum MacCormick, Tom Greig, Simeon Barber, George Seabroke and Salah Karout, who provided friendship, entertainment and insight over my time with the group.

Thanks to Greg Bale who, during my time working for e2v scientific instruments, encouraged me to develop my understanding of semiconductor devices. Without Greg, I would never have started my PhD.

Thank you to my friends and colleagues at the Open University who have all helped make the past three years an enjoyable and memorable experience. There are far too many of you to include here, but here are some names that come to mind. Ben Rozitis, Andreas Morlok, Andrew Needham, Manish Patel, Brijen Hathi, Kathryn McDermott, Adam Stevens, Feargus Abertheny, Ian Wright, Monica Grady, Jon Zarnecki, Andrew Carter, Bethany Alden, Naomi Murdoch, Jon Mason, Andy Morris.

I would like to thank Helen Greatrex for her support during this study. I like to come across as a relaxed person who deals with periods of stress well. If I have been successful in portraying this demeanour all credit must go to Helen and I am sorry for putting all of my concerns and stresses on you.

I would like to gratefully acknowledge the financial support received from the Science and Technologies Facilities Council and e2v technologies during my research studentship.

Finally I would like to thank the collaborators that I have had over the course of my studies for their help, support and expertise. They include the team at the PTB beamline in BESSY II, Randall McEntaffer from the University of Iowa, Webster Cash from the University of Colorado and Hiroshi Tsunami from Osaka University.

List of Acronyms

AC	Alternating Current
ACIS	Advanced CCD Imaging Spectrometer
ACIS-I	Advanced CCD Imaging Spectrometer - Imager
ACIS-S	Advanced CCD Imaging Spectrometer - Spectrometer
ADC	Analogue-to-Digital Converter
AGN	Active Galactic Nuclei
AR	Anti-Reflection
ASCA	Advanced Satellite for Cosmology and Astrophysics
ATHENA	Advanced Telescope for High Energy Astrophysics
BI	Back-Illuminated
CASE	Cooperative Award in Science and Engineering
CAT-GS	Critical Angle Transmission Grating Spectrometer
CCD	Charge-Coupled Device
CDS	Correlated Double Sampling
CIC	Clock-Induced-Charge
CMBR	Cosmic Microwave Background Radiation
CTI	Charge-Transfer Inefficiency
DC	Direct Current
DEPFET	Depleted p-channel Field-Effect Transistors
DN	Digital Number
EEV	English Electric Valve
EM-CCD	Electron-Multiplying Charge-Coupled Device
ENF	Excess Noise Factor
EOS	Equation Of State
EPIC	European Photon Imaging Camera
ESA	European Space Agency
EUV	Extreme Ultra Violet
E-WFI	Extended Wide-Field Imager
FDM	Frequency Domain Multiplexing
FI	Front-illuminated
FIP	Fixed Instrument Platform
FOV	Field Of View
FPGA	Field Programmable Gate Array
FWHM	Full-Width Half-Maximum
GEC	General Electric Company
GEM	Gas Electron Multiplier
GILD	Gas Immersion Laser Doping
GIS	Gas Scintillation Imaging proportional counter
HEG	High Energy Gratings
HEO	Highly Elliptical Orbit
HETG	High Energy Transmission Grating
HEW	Half-Energy Width
HPD	Half-Power Diameter
HRC	High Resolution Camera
HRMA	High Resolution Mirror Assembly
HTRS	High Time Resolution Spectrometer
HV	High Voltage

HXD	Hard X-ray Detector
HXI	Hard X-ray Imager
HXT	Hard X-ray Telescope
ISO	International Organisation for Standardization
IXO	International X-ray Observatory
JAXA	Japanese Aerospace eXploration Agency
L2	Lagrange point 2
L3	Low-Light-Level
LEO	Low Earth Orbit
LETG	Low Energy Transmission Grating
MBE	Molecular Beam Epitaxy
MCP	Micro-Channel Plate
MEG	Medium Energy Gratings
MIP	Moveable Instrument Platform
MOS	Metal-Oxide Semiconductor
MOSFET	Metal-Oxide Semiconductor Field-Effect Transistor
MSSL	Mullard Space Science Laboratory
NASA	National Aeronautics and Space Administration
NFI	Narrow-Field Imager
NIR	Near InfraRed
OM	Optical Monitor
OP-XGS	Off-Plane X-ray Grating Spectrometer
PC	Personal Computer
PCC	Poly-Cold Compact
PDA	Photo-Diode array
PFO	Particle Fallout
PMT	Photo-Multiplier Tube
PSF	Point Spread Function
PTB	Physikalisch-Technische Bundesanstalt
QCD	Quantum Chromo-Dynamics
QE	Quantum Efficiency
QED	Quantum Electro-Dynamics
r.m.s.	Root Mean Squared
RGS	Reflection Grating Spectrometer
ROI	Region Of Interest
ROSAT	Röntgensatellit
SCM	Standard Cosmological Model
SIMS	Secondary Ion Mass Spectrometry
SIS	Solid-state Imaging Spectrometer
S/N	Signal-to-noise Ratio
SNR	Supernova Remnant
SPO	Silicon Pore Optics
SRON	Stichting Ruimte Onderzoek Nederland
STFC	Science and Technology Facilities Council
STJ	Superconducting Tunnel Junction
SXT	Soft X-ray Telescope
TDI	Time Delay Integration
TDM	Time Domain Multiplexing
TEC	Thermo-Electric Cooler

TES	Transition Edge Sensor
TRL	Technology Readiness Level
UK	United Kingdom
USA	United States of America
USB	Universal Serial Bus
UV	Ultra Violet
WFI	Wide-Field Imager
WHIM	warm-Hot Intergalactic Medium
WHIMEx	Warm-Hot Intergalactic Medium Explorer
XEUS	X-ray Evolving Universe Spectroscopy
XGS	X-ray Grating Spectrometer
XIS	X-ray Imaging Spectrometer
XMM-Newton	X-ray Multi-mirror Mission - Newton
XMS	X-ray Micro-Calorimeter
XMS	X-ray Microcalorimeter
X-POL	X-ray Polarimeter
XRS	X-ray Spectrometer

Contents

Chapter 1: Introduction

1.1 X-ray astronomy

X-rays are a form of radiation that occupies the shorter, ionising, wavelengths (10^{-8} m to 10^{-11} m) of the electro-magnetic spectrum. They are produced by the most energetic cosmological events and travel across the Universe with low attenuation from the inter-galactic medium. X-ray astronomy refers to the observation and study of X-rays to determine the properties of the region of the Universe they were emitted from. However, as the Earth's atmosphere is opaque to X-rays, X-ray observations have to be made above the Earth's atmosphere.

X-rays are generated through 3 main mechanisms. Thermal, where the temperature of an object causes X-ray emission, Synchrotron/Bremsstrahlung, where X-rays are emitted due to a change in the velocity of charged particles and ionisation, where the removal of an electron from an atom allows an electron at a higher energy to fill the vacancy emitting an X-ray photon.

Stars, like the sun, produce X-rays due to their high temperature (coronal temperature of ~10^6 K) and through the detection of these X-ray photons, properties of the star can be inferred. Strong gravity regions also emit X-ray photons through synchrotron emission, as the matter trapped inside the strong gravitational region is accelerated[Gorenstein, 1990].

Astrophysicists are interested in large scale structure formation and feedback mechanisms. The key to understanding these processes lies in understanding the properties of regions of high temperature or strong gravity and in forming a clear picture of the make-up of the intergalactic medium. In particular, the intergalactic medium is thought to be the location of much of the missing baryonic content of the Universe [Nicastro, 2010]. Through the identification of this content, feedback mechanisms in the galaxy can be better understood and the Standard Cosmological Model can be better constrained [Barcons, 2010].

Charge-Coupled Devices (CCDs) have been regarded as excellent detectors for X-ray detection since they were first flown on the Japanese mission ASCA (Advanced Satellite for Cosmology and

Astrophysics) [Tanaka 1994]. With its good spatial and spectral resolution, low dark current when cooled, large format image area, low readout noise and space heritage, the CCD is a reliable and effective detector for X-ray instruments [Lumb, 1990].

1.2 Research goals

The research goal of this thesis is the optimisation of CCDs for soft X-ray detection on future space missions. To optimise the CCDs, an evaluation of the performance of different detector types was necessary to identify characteristics that improve soft X-ray detection.

The research goal was achieved through the evaluation of traditional CCDs at soft X-ray energies to investigate how developments in back-surface passivation techniques have affected performance in both e2v and Hamamatsu detectors. The work was designed to feedback information into the WHIMEx (Warm-Hot Intergalactic Medium Explorer) proposal to NASA (National Aeronautics and Space Administration) for an explorer mission. WHIMEx was a high resolution X-ray spectrometer designed to cover the 0.25 keV to 2.5 keV energy range making high spectral resolution at low X-ray energies a vital specification on the detectors for the mission.

A second study evaluated the performance of Electron-Multiplying CCDs (EM-CCDs) at soft X-ray energies, specifically the noise effect that the use of multiplication gain had on the spectral resolution. It is well understood that multiplication gain can be used to reduce the effective readout noise of a device to sub-electron levels and in optical applications where readout noise is dominant; this makes low-light-level imaging possible. At X-ray energies the shot noise on the signal becomes dominant and as there are a large number of electrons in the charge cloud, multiplication noise also has a more significant effect on the total noise. The work in this study was designed to develop and test a hypothesis that would allow the noise generated by the multiplication gain process to be predicted, allowing the spectral resolution performance of the device to be calculated for different energies and levels of gain. The suppression of the readout noise that an EM-CCD makes possible allows lower energy X-ray events to be detected. On a spectrometer, where position determines energy, the detection of part of a low energy soft X-ray

interaction is enough to re-construct that interaction and, with internal gain, an EM-CCD enables these events to be seen. The degradation in spectral resolution can interfere with order separation, so this study will enable the instrument to be designed to allow for this effect.

A third study investigated the dead-layer thickness of CCDs passivated using ion implantation at e2v technologies. Using a Secondary Ion Mass Spectrometer (SIMS) it was possible to map the boron concentration as a function of depth into the device and this information could be used to produce more accurate models for the quantum efficiency performance of the device.

The work carried out for this thesis was funded by a Co-operative Award in Science and Engineering (CASE) studentship from STFC in collaboration with e2v technologies of Chelmsford, Essex, UK.

1.3 Thesis organisation

This thesis is organised into 9 chapters including this introduction with the early chapters developing the techniques and understanding needed for the later experimental chapters where the research goals of the thesis are investigated.

Chapter 2 reviews X-ray detection, focussing on achieving high resolution through the use of reflection spectrometers. The technology developed for X-ray detection is discussed and each technique is shown to provide a way of optimising a particular aspect of X-ray detection. Past, current and future X-ray space missions are described, paying attention to the detectors that are used and how future missions will lead to an improvement in scientific capability.

Chapter 3 explains the operation of a Charge-Coupled Device (CCD), from the doping of silicon allowing the manipulation of the photon detection performance to device architecture and readout modes. The buried channel CCD and its development from the combination of a MOS capacitor and p-n junction led to advances in noise performance and charge transfer operations that are discussed. CCDs have become a major component in X-ray instruments due to their high quantum efficiency. The readout noise of CCDs has been minimised with the advent of EM-CCDs

that use internal gain to effectively reduce this noise; therefore, the advantages and disadvantages of this new technology are evaluated.

Chapter 4 focuses on back-illumination technology, as the work in this thesis is based on soft X-ray detection where back-illumination provides the highest Quantum Efficiency (QE). The back-thinning of CCDs and the resulting oxide growth causes an accumulation region to develop close to the $Si\text{-}SiO_2$ interface that can result in lost charge. To mitigate this effect several back-surface passivation processes have been developed and they are described and evaluated.

Chapter 5 is a summary of the devices used in this thesis, the laboratory equipment that made the characterisation and testing of the devices possible and the data analysis techniques used. Specialist equipment to allow the cooling of the CCDs under a vacuum environment was necessary to test the devices in similar conditions to those that would be expected on a space mission. The equipment also needed to be adaptable enough to be used with different device types and at different locations. The data analysis tools enabled raw data to be turned into a meaningful result and they are used throughout this thesis.

Chapter 6 describes a series of experiments using the PTB (Physikalisch-Technische Bundesanstalt) beamlines at the BESSY II synchrotron in Berlin. The CCDs (CCD30-11 and Hamamatsu S7171-0909) were tested at soft X-ray energies and their performance compared. The measurements that were of specific interest were the energy resolution across the 150 eV to 1900 eV energy range, the partial event fraction (especially at the lower energies) and the QE of the Hamamatsu device. The PTB beamline and its operation is discussed in some detail, as the broadband high accuracy energy provision and tuneable flux of the beamline is very important to the success of the experiment, before focussing on the experiment and results from the CCDs.

Chapter 7 introduces the Modified Fano Factor as an extension of the Excess Noise Factor. The Modified Fano Factor, which is a measure of the degradation in spectral resolution expected when detecting X-rays in an EM-CCD with multiplication gain, is predicted analytically, modelled with a Monte Carlo simulation and then verified experimentally with ^{55}Fe X-rays (5898 eV). The

result of this factor is then used to evaluate the performance of EM-CCDs on future X-ray space missions. The investigation into the Modified Fano Factor continues, but at 1000 eV and with two different devices. The first experiment was unable to verify the Modified Fano Factor due to event splitting and the causes of this are explored. The second experiment is designed to minimise event splitting allowing the Modified Fano Factor to be verified for 1000 eV photons. Finally, the Modified Fano Factor is investigated using the K-shell fluorescence of aluminium (1487 eV).

Chapter 8 discusses the proposed International X-ray Observatory (IXO). The work in this thesis is tuned towards the improvement of CCD detector technology for soft X-ray spectrometers such as the Off-Plane X-ray Grating Spectrometer (OP-XGS) on IXO. The OP-XGS was planned to be the highest resolution spectrometer of its type and the planning and development that was required to present a possible instrument is documented, focusing on the work completed for this study by the author. The major contributions that the author made to this study were on QE prediction, effective area, stray light requirements and filter development, pointing knowledge, camera array layout and contamination. The work covered in this chapter is also applicable to the WHIMEx mission proposal.

Chapter 9, the final chapter, recounts the main conclusions arising from the work of this thesis and assesses the possible directions for further work that could be undertaken.

1.4 Publications

1.4.1 Peer Reviewed

Tutt, James H.; Holland, Andrew D.; Murray, Neil J.; Hall, David J.; Harriss, Richard D.; Clarke, Andrew; Evagora, Anthony M., "The Noise Performance of Electron-Multiplying Charge-Coupled Devices at soft X-ray Energies", IEEE Transactions on Electron Devices, Vol. 59, Issue 9 (2012), p.p. 2192-2198.

Tutt, James H.; Holland, Andrew D.; Murray, Neil J.; Harriss, Richard D.; Hall, David J.; Soman, Mathew, "Electron-Multiplying CCDs for future soft X-ray spectrometers", Journal of Instrumentation, Vol. 7, Issue 2, (2012), p.p. C02031.

Tutt, James H.; Holland, Andrew D.; Hall, David J.; Harriss, Richard D.; Murray, Neil J.; "The Noise Performance of Electron-Multiplying Charge-Coupled Devices at X-ray Energies", IEEE Transactions on Electron Devices, Vol. 59, Issue 1, (2012), p.p. 167-175.

Hall, David J.; Soman, Matthew R.; **Tutt, James H.**; Murray, Neil J.; Holland, Andrew D.; Schmitt, T.; Raabe, J.; Strocov, V. N.; Schmitt, B., "Improving the resolution in soft X-ray emission spectrometers through photon-counting using an Electron Multiplying CCD", Journal of Instrumentation, Vol. 7, (2012), p.p. C01063.

Soman, Matthew R.; Hall, David J.; **Tutt, James H.**; Murray, Neil J.; Holland, Andrew D.; Schmitt, T.; Raabe, J.; Schmitt, B., "Improving the spatial resolution of a soft X-ray Charge Coupled Device used for Resonant Inelastic X-ray Scattering", Journal of Instrumentation, Vol. 6, Issue 11, (2011), p.p. C11021.

1.4.2 Conference proceedings

Tutt, James H.; Holland, Andrew D.; Murray, Neil J.; Harriss, Richard D.; Hall, David J.; Soman, Mathew; McEntaffer, Randall L.; Endicott, James, "The use of EM-CCDs on high resolution soft X-ray spectrometers", Proc. SPIE, Vol. 8145, (2011), p.p. 81450L-81450L-12

Harriss, Richard D.; Holland, Andrew D.; Barber, Simeon J.; Karout, Salah; Burgon, Ross; Dryer, Ben J.; Murray, Neil J.; Hall, David J.; Smith, Phillipa H.; Grieg, Tom; **Tutt, James H.**; Endicott, James; Jerram, Paul; Morris, David; Robbins, Mark; Prevost, V.; Holland, Karen, "Compact CMOS Camera Demonstrator (C3D) for Ukube-1", Proc. SPIE, Vol. 8146, (2011), p.p. 81460U-81460U-13

Tutt, James H.; Holland, Andrew D.; Murray, Neil J.; Hall, David J.; McEntaffer, Randall L.; Endicott, James; Robbins, Mark, "A study of Electron-Multiplying CCDs for use on the International X-ray Observatory Off-Plane X-ray Grating Spectrometer", Proc. SPIE, Vol. 7742, (2010), p.p. 774205-774205-12

Murray, Neil J.; Holland, Andrew D.; Harriss, Richard D.; **Tutt, James H.**, Barber, Simeon J.; Pool, Peter; Burt, David; Walton, Dave; Page, Matt; McEntaffer, Randall L.; Schultz, Ted; Cash, Webster; Lillie, Chuck; Casement, Suzanne, "Off-Plane X-ray grating spectrometer camera for IXO", Proc. SPIE, Vol. 7742, (2010), p.p. 77420X-77420X-10

McEntaffer, Randall L.; Murray, Neil J.; Holland, Andrew D.; **Tutt, James H.**; Barber, Simeon J.; Harriss, Richard D.; Schultz, Ted; Casement, Suzanne; Lillie, Chuck; Dailey, D.; Johnson, T.; Danner, R.; Cash, Webster; Zeiger, B; Shipley, A.; Page, Matt; Walton, Dave; Pool, Peter; Endicott, James; Willingale, Dick, "Developments of the Off-Plane X-ray Grating Spectrometer", Proc. SPIE, Vol. 7732, (2010), p.p. 77321K-77321K-13

Holland, Andrew D.; Murray, Neil J.; **Tutt, James H.**; McEntaffer, Randall L.; Pool, Peter; Endicott, James, "CCD readout for the IXO off-plane grating spectrometer", Proc. SPIE, Vol. 7435, (2009), p.p. 74350Y-74350Y-9

Chapter 2: X-ray spectrometers

2.1 Introduction

Spectroscopy originated as the study of visible light dispersed according to its wavelength through a prism, but has since expanded to cover the majority of the electro-magnetic spectrum. Spectroscopy is now the study of the interaction of matter and electro-magnetic radiation through the discrimination of different wavelengths of photons either by a detector or through the use of a dispersive element. By having an understanding of atoms, spectroscopy can be used to determine the constituent parts that exist in fluoresced materials [Bearden, 1967].

According to quantum mechanics, the energy levels within an atom are limited to certain discrete values determined by the energy levels of their electron shells. When an atomic or molecular system absorbs or emits electro-magnetic radiation, the system goes from one energy level to another. The Bohr Frequency Condition states that the difference in energy level must equal the energy of the Electro-Magnetic radiation absorbed or emitted, Equation 2.1 [Bohr, 1913], where E_1 and E_2 are the separate energy levels that the transition occurs between (J), ν is the frequency of the electro-magnetic radiation related to this transition (s^{-1}) and h is Planck's constant (6.626×10^{-34} J s^{-1}).

$$\Delta E = E_2 - E_1 = h\nu \tag{2.1}$$

Spectrometry is more restrictive than spectroscopy as it refers to the measurement of the intensity of absorption or emission at specific energies, rather than a range. A spectrometer is an instrument used to probe a property of electro-magnetic radiation at a specific frequency. In the case of X-ray spectrometers the radiation is at X-ray energies. Through the analysis of detected X-rays, features about the material that the X-rays have passed through or been generated by can be found from their absorption and emission spectra.

2.2 Absorption and emission spectra

The process of absorption occurs when an atom absorbs a photon and goes to a higher energy state, usually due to an electron exciting into a higher energy electron shell. When the atom or molecule subsequently relaxes, the electron falls into a lower, unoccupied shell and a photon corresponding to the transition energy is radiated. The photon can be emitted in any direction causing an absorption line in the spectrum indicating which atom absorbed the photon as each atom has a unique set of spectroscopic energies.

The emitted photon from the atom is seen as a peak in the detected spectrum, also giving information about the nature of the substance if it can be resolved, which requires the use of an X-ray spectrometer [Young, 2000].

2.3 An Introduction to X-ray Spectrometers

X-ray spectrometers are able to determine the energy of incident electro-magnetic radiation, either through the inherent spectral resolution of the detector used or through the use of a dispersive element such as a grating.

2.3.1 Electro-Magnetic Radiation

A wave has three distinct properties: wavelength, frequency and amplitude. The wavelength, λ (m), of a wave is the distance between two corresponding positions on a wave as shown in Figure 2.1.

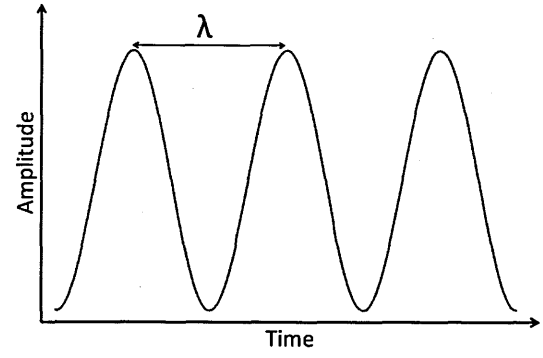

Figure 2.1: A typical wave shown with respect to time and wave amplitude. The wavelength, λ, is marked.

The frequency, ν (s^{-1}), is a measure of the number of waves that pass a given point in 1 second and the product of the wavelength, λ (m), and the frequency is the velocity, V (m/s) which, for electro-magnetic radiation in a vacuum is equal to the speed of light, c (~3 x 10^8 m s^{-1}).

$$c = \lambda\nu \tag{2.2}$$

In 1905, Albert Einstein used the photo-electric effect to explain the behaviour of light using a particle model [Einstein, 1905]. Einstein suggested that each particle of light had a specific amount of energy, E, that depends on its frequency, Equation 2.3:

$$E = h\nu \tag{2.3}$$

The photo-electric effect shows that light energy is quantised and each quantum is called a photon; light can be thought of as a particle [Young, 2000].

2.3.2 Spectral resolution

The spectral resolution of a detector is often described by the Full-Width-Half-Maximum (FWHM) of the detected photon peak, Figure 2.2.

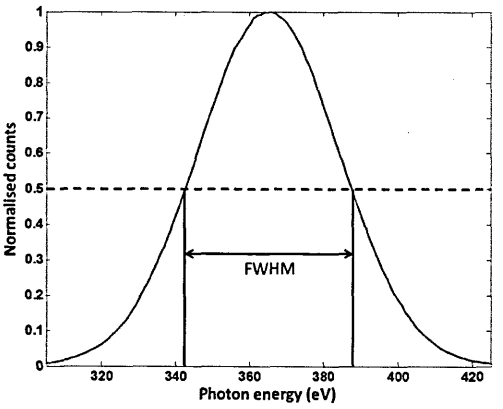

Figure 2.2: The figure shows a typical Gaussian X-ray peak for 365 eV X-ray photons. The FWHM of the peak is a measure of the width of the peak at half of the maximum amplitude and can be used to describe a detector's spectral resolution.

The limit on how narrow an X-ray peak FWHM can be is determined by the intrinsic statistical fluctuations and other noise sources in the system. The smaller the FWHM, the higher the spectral resolution of the detector and so the closer two spectral lines can be together and still be resolved. In order to develop an instrument with a total resolution that is not limited by the

performance of the detector, a dispersive element such as a grating is required (Section 2.3.7).

2.3.3 Spatial Resolution

Spatial resolution is a measurement of how accurately the position of photon interaction can be determined. In the case of a dispersive spectrometer, the position that the photon interaction occurred determines the photon's energy and so a high spatial resolution will allow the spectrometer to have a high total energy resolution. The effect of having more pixels in a detector on the spatial resolution is shown in Figure 2.3.

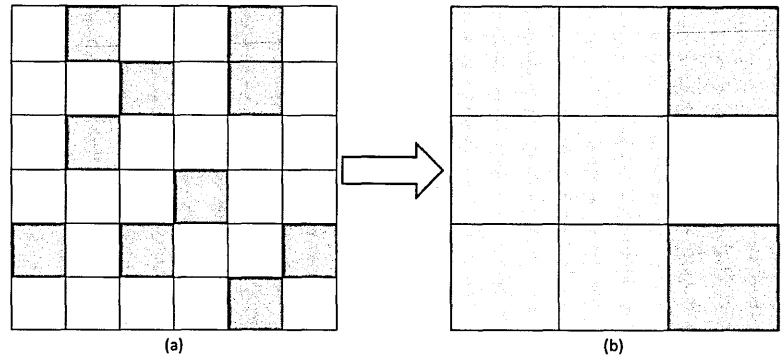

Figure 2.3: The loss of spatial resolution by going from a 6x6 pixel array (a) to a 3x3 array (b) is shown. The arrays are the same size, but the higher pixel density in array (a) gives more spatial information.

2.3.4 Angular Resolution

Angular resolution is a measure of the focusing ability of an optic. The angular resolution is usually given as the Point Spread Function (PSF), the Half Energy Width (HEW) or the Half Power Diameter (HPD). The PSF describes the response of an imaging system to a point source or object, the HEW and the HPD are a measure of the angle within which half the photons coming from a point source are focused by the optics with the HEW being European and the HPD being American [Tanaka 1994].

2.3.5 Instrument resolution

Total instrument resolution is a measure of the angular resolution of the optic, the spatial resolution of the dispersive element and the spectral resolution of the detector combined. The resolution gives an indication of how close two different spectral signals can be to each other and still be identified as different signals. For a reflection based grating spectrometer, the resolution

that is achieved is a function of the groove density on the grating and the distance between the grating and the target where the dispersed spectrum will be collected (known as the throw). For a perfect grating the resolving power of a spectrometer is defined by Equation 2.4, where V is the equivalent velocity Doppler width [Ball, 2006].

$$R = \frac{\lambda}{\Delta\lambda} = \frac{E}{\Delta E} = \frac{c}{V} \tag{2.4}$$

Factors that also need to be taken into consideration when calculating the resolving power of the grating include: alignment, surface roughness and contamination. For example, the spectrometer on XMM-Newton has a resolution of 300 which equates to being able to resolve photon signals at 598 eV from those at 602 eV [Brinkman, 1996]. In practice the gratings will never disperse perfectly as the dispersion will be degraded by scattering due to the inherent roughness of the surface and contamination. In addition, imperfections in the alignment of the grating to the incident radiation will cause changes in the grazing incidence onto the grating, affecting its reflectivity. Imperfections in the grating may cause the same energy and order of radiation to be dispersed to different parts of the focal plane causing a more diffuse reflection than normal. To cater for these imperfections an instrument is designed to have better resolution than required (a safety margin). To distinguish two X-ray energies from each other the instrument must be able to correctly identify the two separate photon peaks or to be able to deconvolve the spectra to regain the initial photon information. One method to determine if the discrimination is possible is called the "baseline criterion" which requires that the first photon peak has fallen to the background noise value before the second photon peak begins to rise. A second method is the "Rayleigh criterion" which requires that the maximum in one peak occurs at the point that the other peak has fallen to the background level [Rayleigh, 1879]; however, if the response is Gaussian it will never reach the baseline level and so the point that the peak reaches half maximum is used. These criteria are illustrated by Figure 2.4.

The greater the dispersion from the grating, the larger the separation between the peak maximums and this leads to a higher resolution. The dispersion is dependent on the grating

instrument design (groove density and throw) which is discussed in more detail later in the chapter. The width on the peak is caused by imperfections in the grating (or detector) as discussed previously.

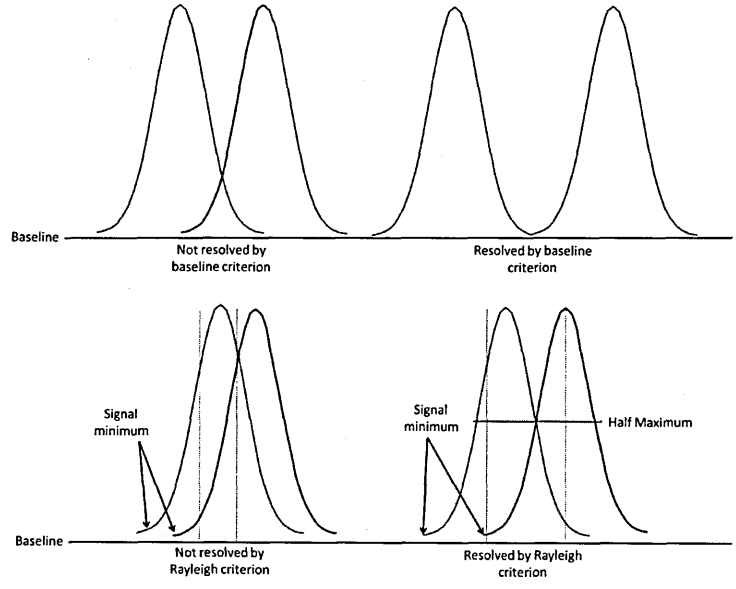

Figure 2.4: The wavelength separation required to achieve baseline criterion resolution (top) and Rayleigh criterion resolution (bottom) is shown.

2.3.6 X-ray optics

X-ray optics use total external reflection to focus the X-rays.

2.3.6.1 Total external reflection

Total external reflection is the method used to disperse X-rays from a surface, which requires the X-rays to be reflected at an angle less than the critical angle for the incident photon (grazing incidence). Total external reflection occurs when a photon is completely reflected by a surface when travelling in a different medium, hence external to the surface. The photon travels in a vacuum and is reflected off the grating surface. If the angle is larger than the critical angle the photon will transmit through or be absorbed by the surface. The critical angle for total external reflection, θ_c, is given by Equation 2.5, where λ is the wavelength of the X-rays, r_0 is the classical electron radius and N_e is the electron density of the reflector material, Figure 2.5 [Kahn, 2005].

$$\theta_c = \sqrt{4\pi(\lambda^2 r_0 N_e)} \tag{2.5}$$

Equation 2.5 shows that the critical angle is proportional to the wavelength or inversely proportional to the energy of the X-ray. The higher the energy of the X-rays, the shallower the angle needs to be for total external reflection and this requirement led to the development of graze angle X-ray optics.

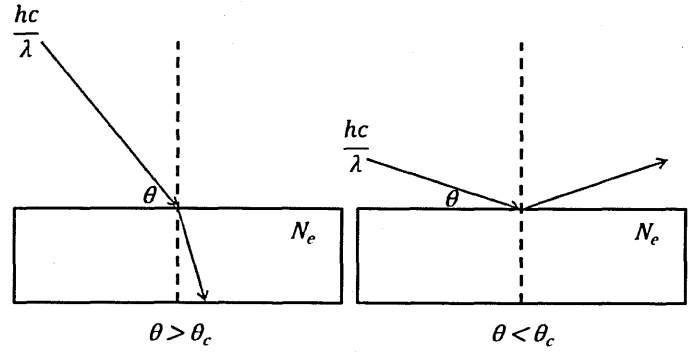

Figure 2.5: The image shows the critical angle for total external reflection of a material. Equation 2.5 calculates the angle at which incident radiation will reflect off a surface and is vital to X-ray optics.

2.3.6.2 X-ray optic design

Giacconi and Rossi proposed a telescope design in 1960 that used a parabolic mirror to focus on-axis X-rays; however, off-axis images suffered from a coma effect causing the X-rays to be magnified by different amounts, hence causing oval distortions [Gaicconi, 1960], Figure 2.6.

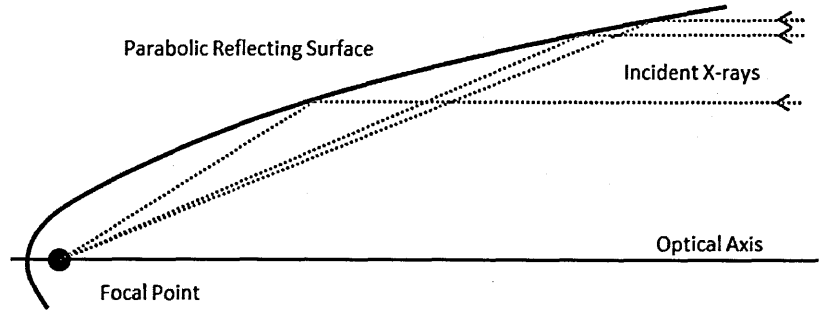

Figure 2.6: An image of the Giacconi & Rossi parabolic optic.

In order to fix the coma effect and produce highly focused off-axis images with X-ray optics, a second stage hyperboloid (Wolter I and II optics) or ellipsoid (Walter III optic) reflecting mirror was incorporated into the design, Figure 2.7.

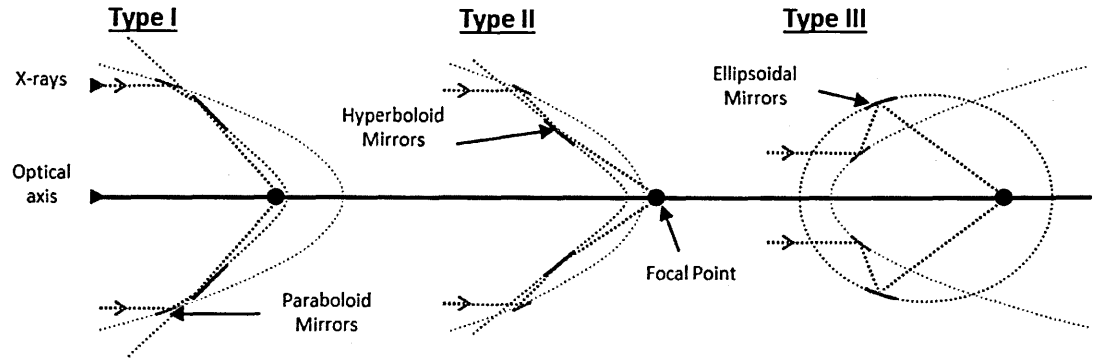

Figure 2.7: Images showing the Wolter type I, II and III optics.

The Wolter type I and II optics can be built in a very compact style and so make them very useful for space missions. The optic mirrors can be nested in shells around the focal point to increase the effective area of the optics, Figure 2.8.

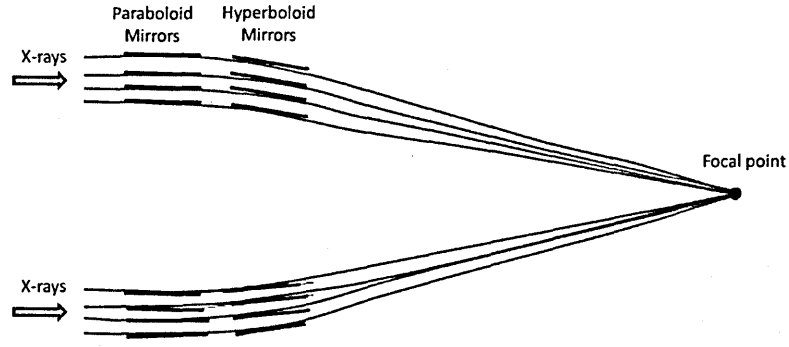

Figure 2.8: An example of the nested shells of X-ray optics mirrors. Successive shells of paraboloid and hyperboloid mirrors enable an optic to be developed with high throughput and large effective area [Barcons, 2010]

Each shell needs to be aligned at a slightly different angle to cause the X-rays to be focused at the same point on the focal plane. The mirrors have to be flat (have a small figure error) to ensure that the graze angle is always below θ_c and have to be smooth so that there is very little scattering from the surface to maintain the X-ray focus, and thereby ensure a high level of throughput and angular resolution.

2.3.7 Gratings

A grating spectrometer uses the principle of X-ray diffraction to disperse the incident radiation and is based on the principle first explained by Thomas Young in 1803 using the double slit experiment. The experiment showed that light passing through two slits creates a pattern of interference fringes on a screen which can be explained by the diffraction of the light as it passes

through the slits. The size of this dispersion is defined by the slit spacing, the distance that the dispersion occurs over (throw) and the wavelength of the incident radiation.

When photons are reflected, a smooth surface will reflect all of the waves in the same direction (specular reflection) and an uneven surface will cause the radiation to be reflected in a variety of directions (diffuse reflection) [van de Hulst, 1981].

If there is a requirement on the spectrometer to provide a certain level of resolution, the gratings must have a high enough groove density and the throw must be long enough to achieve this requirement. The groove density is the number of lines that are etched onto the grating substrate per mm (analogous to split spacing) and the throw is the distance between the gratings and the instruments focal plane. The relationship between dispersion angle, groove density and wavelength, λ (m), can be seen from Equation 2.6, where m is the order of diffraction, P is the grating period (the distance between adjacent grooves (mm)), α is the angle of incidence of the radiation and $\beta(\lambda)m$ is the angle of diffraction for order m [Heilmann, 2011].

$$m\lambda = P(sin\alpha - sin\beta(\lambda)_m) \tag{2.6}$$

Assuming that the order, the incident angle and the wavelength of the radiation are constant then Equation 2.6 becomes:

$$P\sin\beta \propto constant \tag{2.7}$$

Therefore, if P increases, β (the angle of dispersion) decreases and, as P is the distance between grooves, to achieve a larger dispersion the grooves have to be closer together giving a higher groove density. With a larger throw, the different energy photons will become more dispersed before they reach the focal plane increasing resolution.

There are two types of dispersive grating; the transmission grating and the reflection grating.

2.3.7.1 Transmission gratings

A transmission grating is made up of a series of slits that the incident radiation passes through, Figure 2.9.

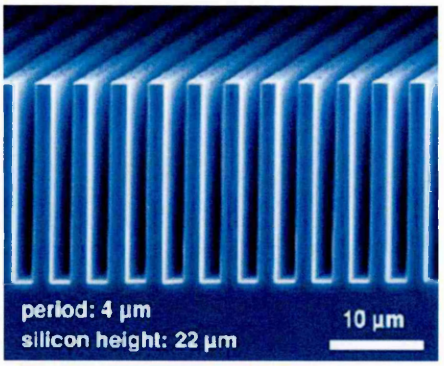

Figure 2.9: A transmission grating used that could be used for X-ray grating spectrometers that is made out of silicon [Weitkamp, 2005].

The width between the slits in the grating determines the amount of dispersion that occurs and is described by the grating equation (Equation 2.6). The dispersion created by a transmission grating is shown in Figure 2.10.

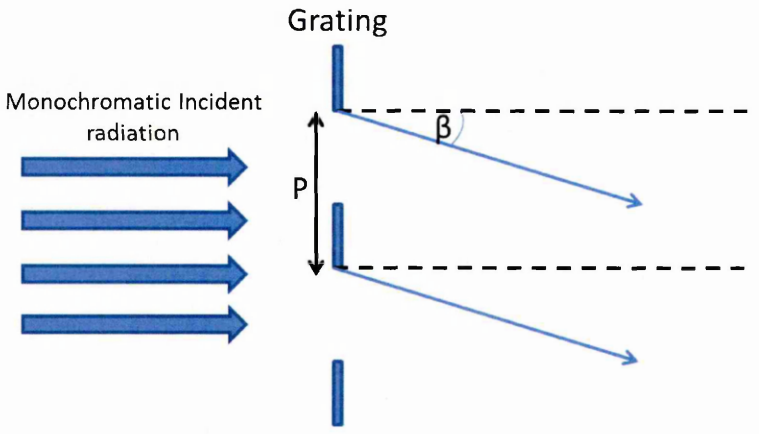

Figure 2.10: The figure shows incident radiation falling onto a grating normal to the grating surface ($\alpha = 0$). The radiation is dispersed by an angle β that is dependent on the grating period, P, the dispersed order, m, and the wavelength, λ.

Electro-magnetic radiation at different wavelengths will be dispersed by the transmission grating at different angles causing each wavelength to be detected at a different position on a detector array. A transmission grating disperses its radiation to both sides of the zero-order position, the position that the un-dispersed waves would be detected (specular reflection); therefore, in order to detect all of the dispersed radiation either two detector arrays have to be used on either side of zero order or the grating can be blazed, Figure 2.11.

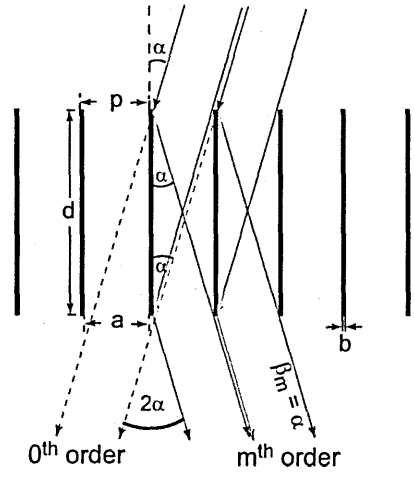

Figure 2.11: For the blazed transmission grating shown, the grating slits are held at an angle to the incident radiation, α, causing a reflection off the grating surface, preferentially dispersing the radiation to one side of the zero order position. The creation of a reflection in the transmission grating by altering α is the equivalent of blaze in a reflection grating [Heilmann, 2011].

The introduction of blaze into the system forms a Critical Angle Transmission Grating. The reflection of the grating wall has to be shallower than the critical angle so that the X-rays totally externally reflect which puts a limit on the maximum blaze that the grating can have and, as the angle is so shallow, can lead to alignment problems. The blaze angle on a transmission grating is equal to the incident angle, α. The blaze causes a reflection of the photons off one side of the grating, and the X-rays are dispersed to one side of the zero order. To ensure the grating has a high efficiency the angle of incidence, α, needs to be such that the photons have a high reflectivity off the surface. At X-ray energies this requires an angle of grazing incidence < 3° (Figure 2.17). The depth of the grating, d, needs to be short enough that the incident radiation only reflects off one side of the grating and the thickness of the grating, b, needs to be thin to maximise the mechanical throughput of the system. If radiation is incident on the edge of the grating slits it will not be transmitted, reducing the efficiency of the grating. The grating needs to be designed to be thin, but also strong, as it may be required to withstand the forces associated with a launch into space. The major challenge with transmission gratings is making them strong enough for space applications while having good efficiency and high throughput.

2.3.7.2 Reflection gratings

Reflection gratings use the reflection of the incident radiation from the surface to disperse the radiation according to its wavelength. The grating has a surface that has been ruled with closely

spaced grooves, tuned to the wavelength, λ, of the incoming radiation and the level of dispersion required. When incident electro-magnetic radiation is reflected from the grating surface, each groove acts like an independent transmission slit dispersing the radiation depending on its wavelength, λ, as given by the grating equation [Cash, 1991], [McEntaffer, 2004], where d is the distance between consecutive grooves (groove density is therefore $1/d$), α is the angle of the incoming light, β is the direction of preferential diffraction, γ is the graze angle of the radiation to the gratings and m is the order of the diffraction (Equation 2.8). Figure 2.12 shows an off-plane grating as the dispersion of the X-rays is across the plane of the groove direction.

$$dsin\gamma(sin\alpha + sin\beta) = m\lambda \tag{2.8}$$

When m = 0 the incident radiation is not dispersed and travels to the zero-order position (specular reflection). Increasing integers of m (1, 2, 3...) are called the 1st, 2nd, 3rd... orders respectively and fall at different positions on the focal plane.

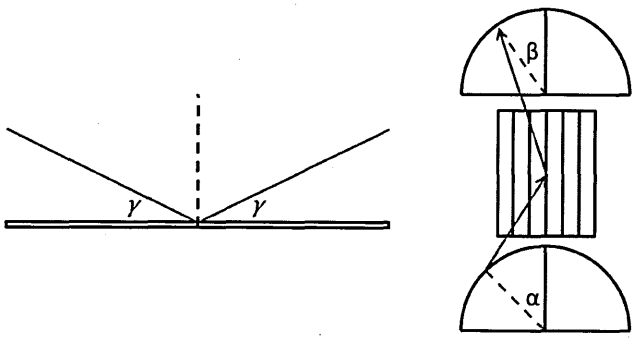

Figure 2.12: The basic design of a reflective off-plane grating is shown. The orientation of the incoming X-rays to a grating is shown from the side (a) indicating the graze angle, γ, and from above (b) indicating the angle of the incoming light, α, and the dispersion direction, β.

The dispersed orders can be both positive and negative and fall on both sides of the zero-order position, Figure 2.13. The dispersion into positive and negative orders, as with the transmission grating, means that to collect all of the dispersed radiation two detector arrays or blazed gratings are required.

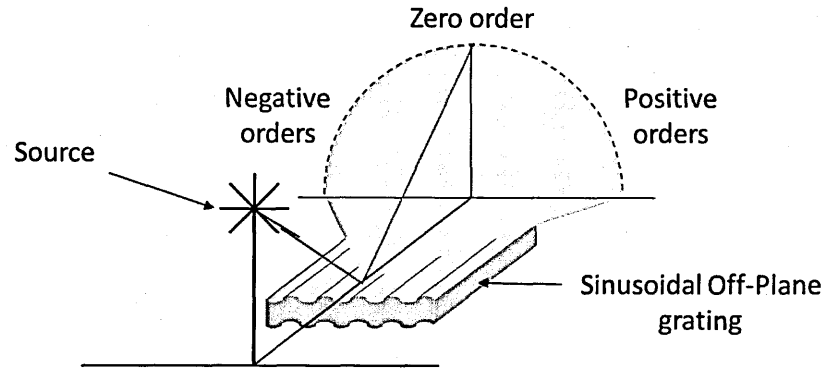

Figure 2.13: The figure shows dispersed radiation falling to either side of the zero-order in positive and negative orders when dispersed from an off-plane sinusoidal grating.

To make a reflection grating blazed the grating profile goes from a sinusoid, Figure 2.13, to a saw tooth, Figure 2.14. The saw tooth profile preferentially disperses the incident X-rays to one side of the zero-order position, allowing twice the throughput of dispersed X-rays to be collected by a single detector array.

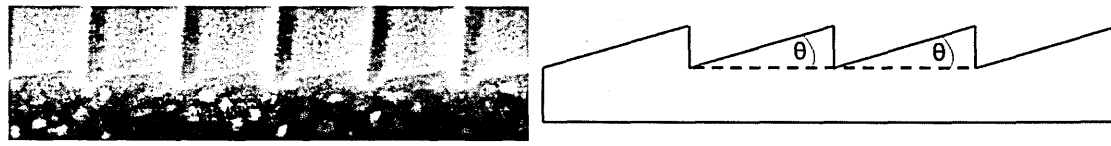

(a) (b)

Figure 2.14: SEM image of a blazed reflection grating (a) [Chang, 2004], with a schematic of the blazing shown in (b).

In a blazed grating, the grating will have its highest efficiency when $\alpha = \beta = \theta$ (where θ is the blaze angle shown in Figure 2.14(b)). By solving Equation 2.8 for this condition the gratings can be optimised to maximise the diffraction efficiency at a particular wavelength.

$$2dsin\gamma sin\theta = m\lambda \tag{2.9}$$

The maximum will occur at different wavelengths in different orders and so multiple orders can be used across the bandpass to maximise the throughput of the grating across the desired energy band, Figure 2.15. The blaze angle can be manufactured to be preferential in either positive or negative orders.

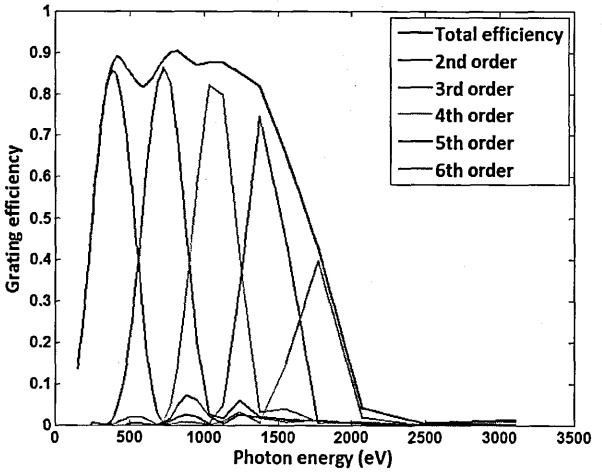

Figure 2.15: The grating efficiency of different orders of dispersed radiation with the grating blazed to maximise efficiency at 400 eV in the second order. To achieve a high total efficiency, several dispersed orders are required.

The reflection grating described above is known as an off-plane grating as the dispersion is not in the plane of the incident radiation (the dispersion is also known as conical diffraction). Another form of reflection grating is the "on-plane" grating (used on the RGS on XMM-Newton, Section 2.4.1). The RGS grating has the grooves rotated by 90° making them perpendicular to the incident radiation (Figure 2.16). The dispersion is then in the same plane as the incident radiation [Brinkman, 1996].

The on-plane grating method of diffraction is the same as in the off-plane case allowing the grooves of the gratings to be preferentially blazed; however, on-plane gratings can have problems with full-illumination, grating array stacking and high surface flatness requirements. These issues are discussed in more detail in Chapter 8.

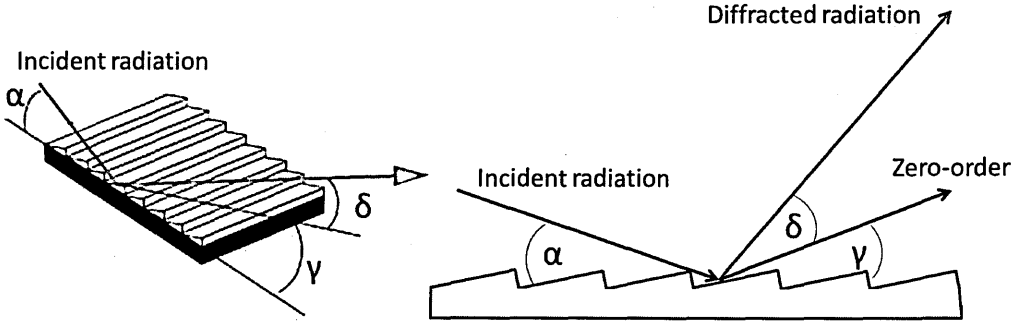

Figure 2.16: Diagrams to show the dispersion from an on-plane grating. The image shows the graze angle, γ, which is equal to the incident angle, α, and the angle that the radiation is diffracted by is also shown, δ [den Herder 2001].

While dispersive grating elements produce high resolution spectra, the detection efficiency of the instrument is low (<20% of the incident photons) due to obscuration and reflection and transmission losses [de Korte, 2000]. High resolution spectra can be produced through the use of cryo-cooled detectors and so the choice of detector for an instrument is vital to the instrument design.

2.3.8 Detecting the spectrum

There are many types of detector that are capable of detecting the spectra dispersed from a grating, but they are all required to have certain features:

- They must be able to respond to changes in the incident photon intensity, requiring good responsivity, sensitivity and dynamic range.
- They must have a good Signal-to-Noise (S/N) ratio.

The detectors are normally split into "scanned systems", where a single-element sensor is used to detect different energies through scanning it across the focal plane, or "static systems", where position-sensitive arrays detect the position at which the photon interaction occurs. As most of the detectors are made from silicon, they have the same quantum efficiency for a given energy.

2.3.9 Scanned systems

2.3.9.1 Phototube

A phototube uses the photo-electric effect to generate a current from absorbed photons. A metal surface with a low work function absorbs the photons and electrons are emitted. They are attracted to the positively biased anode and the current measured is proportional to the number of photons absorbed. Phototubes were formally used for the reading of optical soundtracks for projected films but have been superseded by photodiodes.

2.3.9.2 Photomultiplier tubes

A Photomultiplier Tube (PMT), like the phototube, uses the photo-electric effect to generate electrons that are attracted by an anode; however, a PMT has several electrodes (called dynodes) that are at sequentially higher voltages. The electrons are attracted to each dynode and strike its'

surface releasing more electrons creating an electron cascade. The multiplication of the signal makes the PMT ideal for photon starved applications, but higher flux applications can cause detector saturation. PMTs are used in medical applications such as blood analysis and in research to measure the intensity and spectrum of light-emitting materials [Young, 2000].

2.3.9.3 Proportional/gas counter

A proportional counter detects X-rays through the photo-ionisation of an inert gas, such as Argon or Helium. The number of ion pairs collected by the anode directly relates to the operating voltage allowing the energy of the incoming photon to be found. Using an array of proportional counters allows the spatial position of the photon interaction to also be found. Proportional counters were used on Einstein, Ginga and ROSAT [Giacconi, 1979], [Turner, 1989], [Truemper, 1982].

2.3.9.4 Micro-Channel Plate

A Micro-Channel Plate (MCP) is made from millions of thin capillaries (micro-channels) that have been fused together and sliced into a plate. When a photon is incident onto the MCP it enters one of the micro-channels and frees an electron from the channel wall through photoelectric emission. The channel is held at a high potential difference along its length and the electric field accelerates the photo-generated electron through the micro-channel. The impact with the wall of the channel then causes several electrons to be freed by via secondary emission. The emitted electrons in turn impact on the micro-channel wall generating more electrons. The secondary emission multiplication process repeats itself through the length of the micro-channel until several thousand electrons emerge from the rear plate. MCPs are compact, lightweight, have good temporal resolution and have a high gain that allows them to detect very small signals; however, as the multiplication gain is noisy the detector has poor spectral resolution. MCPs are used in analogue oscilloscopes to produce more intense on screen images and are often found in mass spectrometers [Wiza, 1979].

2.3.9.5 Bolometer/calorimeter

Calorimeters use absorber crystals that are heated through detection of an incident X-ray photon. The photon excites an electron from the absorber material which can then move through the crystal dispersing its energy which is detected as heat. The increase in temperature, measured with a thermometer, is directly proportional to the energy of the incident photon. The absorbers' temperature is reset through a thermal connection to a heat sink. A calorimeter needs to be kept at very low temperatures as the change in temperature caused by an incident photon is small. An array of small calorimeters (microcalorimeters) can be used to spatially resolve incident photons [de Korte, 2000]; however, their use in space applications has so far been unsuccessful, most recently with the cryogenic failure of Suzaku [Takahashi, 1998], [Mitsuda, 2007].

2.3.9.6 Transition Edge Sensors

A Transition Edge Sensor (TES) is a highly sensitive thermometer used to measure the temperature change in a bolometer or calorimeter. The sensor uses the strongly temperature dependent resistance of the superconducting phase transition. By cooling a TES to just below its superconducting critical temperature and electrically biasing it, the TES has a small resistance. The detected photon in the material above the transition edge sensor raises its temperature, driving the TES into a non-conducting state and increasing its resistance. The change in resistance relates to an increase in temperature and therefore, the amount the energy of the incident photon can be calculated [de Korte, 2000], [Moseley, 1984].

2.3.9.7 Superconducting Tunnel Junction

A Superconducting Tunnel Junction (STJ) consists of two superconductors separated by a thin insulating layer. Current is able to pass between the superconductors through quantum tunnelling providing high sensitivity detection with good temporal resolution. Incident photons excite electrons into the conduction band of the top superconductor and these electrons are detected as they tunnel across the junction. By placing a bias across the junction an absorbed photon generates a tunnelling current proportional to the photon energy in the direction of the

bias. STJs are used in photon detectors across energy ranges from X-ray (1 nm) to infrared (1 μm) [de Korte, 2000].

2.3.9.8 Depleted p-channel Field-Effect Transistors

DEPFETs consist of a p-channel field effect transistor that is integrated on the surface of a high resistivity n-type silicon bulk. This bulk can be fully depleted using sideways depletion and any charge generation from photon interactions is collected beneath the channel of the FET in the internal gate where it is stored. The external gate electrode can then be used to move the charge on the internal gate out of the DEPFET. The size of the charge cloud is related to the number of electrons created by the photon interaction allowing the energy of the photon to be calculated. The clear gate can also be used to "dump" any unwanted charge out of the device. DEPFETs are used in space applications, often in arrays, to provide high sensitivity X-ray detection over a wide field-of-view [Richter, 2003].

2.3.10 Static systems

2.3.10.1 Photodiode array (PDA)

Small p-type semiconductor reverse-biased diodes are embedded in an n-type Si substrate. Incoming photons cause holes to build-up in the semiconductor, which are filled by electrons from the substrate. The number of electrons required to neutralise the charge is proportional to the number of incident photons. PDAs are used in electronic products such as compact disc players, smoke detectors and remote control devices, but can also be used in scientific applications where energy and spatial resolution are required [Young, 2000].

2.3.10.2 Charge-Coupled devices (CCDs)

Photon interaction causes the photo-generation of electrons in silicon, the number of which is related to the incident photon energy. These electrons are then collected in potential wells formed in the device by applying biases to gate electrodes where they can be stored and read out. CCDs have been used on the XMM-Newton Reflection Grating Spectrometer [den Herder 2001] and the Chandra High-Energy Transmission Grating [Weisskopf 2002]. CCDs are extremely

sensitive and can detect very low energy photons, especially if cooled to minimise dark current. For a CCD to be used as an X-ray spectrometer, no more than one photon can be incident per pixel and the signal generated by that photon must be collected within that pixel. Any spreading of charge between the pixels will lead to incomplete charge collection and a reduction in the apparent energy measured [Lumb 1990].

2.3.10.3 Detector device comparison

Table 2.1: The advantages and disadvantages of different detector types.

Detector	System type	Advantages	Disadvantages
PMT	Scanned	High sensitivity High Temporal resolution (~1 ns) Low noise Internal gain Compact and light weight	High voltage (~1000 V) High flux over-excitation can reduce gain Sensitive to magnetic field High duty cycle Low stability to low signal levels
Proportional Counter	Scanned	Low operating voltage Avalanche ionisation leads to high S/N High sensitivity Altering operating voltage changes detection mode	No spatial resolution Requires the use of an inert gas Poor spectral resolution
MCP	Scanned	High sensitivity High temporal resolution (~10 ns) Internal gain Compact and light weight Low dark current at room temperature	Requires a high voltage High noise on gain Requires a strong electric field
Calorimeter	Scanned	High sensitivity High detection efficiency High spectral resolution (~7 eV @ 5.9 keV)	Limited by quality of thermometer readout Requires very low temperatures
STJ	Scanned	High sensitivity High spectral resolution (e~10 eV @ 5.9 keV)	Requires very low temperatures Poor performance in high flux applications Thin and so poor high energy performance
DEPFET	Scanned	In pixel amplification Low noise Random access readout (as an array) Full depletion Low power	Poor spatial resolution unless in an array Low Technology Readiness Level
PDA	Static	Low noise Low cost No high voltage required Compact and light weight Linear response	High dark current at room temperature No internal gain (unless avalanche photodiode) Low sensitivity Low temporal resolution
CCD	Static	Linear response Large dynamic range High QE High sensitivity Good spatial resolution	Low spectral resolution (~120 eV @ 5.9 keV) High dark current at room temperature Poor time resolution Poor detection efficiency above 10 keV No internal gain (unless EM-CCD)

2.3.11 Soft X-ray spectrometer

In the case of "soft" X-ray spectrometers, the energy range of operating is typically between 20 eV (Extreme Ultra-Violet) and 2500 eV. Examples of UV and soft X-ray spectrometers include the inverse photoemission spectrometer in Grenoble that has the energy range 20 eV to 100 eV [Chauvet, 1981] and the Reflection Grating Spectrometer on XMM-Newton that has the energy range 350 eV to 2500 eV [Brinkman, 1996]. A 2000 eV forbidden region is caused by poor X-ray

reflection at this energy for iridium coated optics, Figure 2.17. Any high Z material can be used for the coating on the optics as long as it is stable and easy to work with (gold was used on XMM). The practical limits on the energies that an X-ray spectrometer can resolve are defined by the graze angle of the X-rays onto the grating, the groove density and the optic material. The upper limit set on the dispersion of the incident X-rays, in terms of energy, is due to the practical limits in groove density that can be manufactured (the current limit is of the order 5500 grooves mm^{-1}) and the reflectance of X-rays from the grating surface. Taking a grating that is iridium coated for high soft X-ray reflectivity and graze angles of 1°, 2° and 3°, a plot of reflectivity against energy as a function of graze angle can be produced, Figure 2.17.

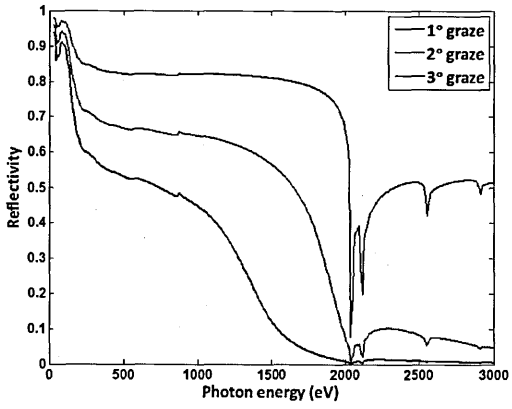

Figure 2.17: Reflectivity of an iridium grating at different energies as a function of graze angle is shown. This shows a clear forbidden region at 2000 eV regardless of angle [Henke, 1993].

For the optics and gratings in an instrument smaller graze angles improve reflectivity; give high throughput and a larger effective area for the instrument. The larger the graze angle the higher the probability of the incident X-rays being absorbed in the iridium. There is a physical cut-off or major reduction in reflectivity at 2000 eV regardless of graze angle caused by the M-shell absorption line of iridium that is the cause of the upper limit of the instruments' energy range [Henke, 1993]. Smaller angles would allow higher reflectivity up to higher energies, but this would lead to increasing problems with alignment, flatness tolerances and contamination. The energy range of such an instrument allows measurements to be made of features in the "hot" Universe (~10^6 K).

X-rays from space are generated by matter under extreme conditions in the "hot" Universe which include: accreting black holes and shock fronts in supernovae remnants (SNR) and high z-Active Galactic Nuclei (AGN) that are at a long distance from Earth (highly Doppler shifted) [Vikhlinin, 2010], [Fabian, 2010], [Miller, 2010a] , [Miller, 2010b]. There are many cases where key diagnostic tools for the objects in the "hot" Universe occur at soft X-ray energies. One such example of the science that a soft X-ray spectrometer could achieve would be in the hunt for the missing baryonic content of the Universe that is thought to reside in the vast empty stretches between galaxies. The baryonic content of the Universe is predicted by the Standard Cosmological Model (SCM) and the Cosmic Microwave Background Radiation (CMBR) and visible matter only accounts for half of the baryons. The presence of the other 50% is inferred from absorption lines in AGN outflows and this vast web of baryonic matter is known as the Warm-Hot Intergalactic Medium (WHIM) [Nicastro, 2010], [Lillie, 2011]. To fully characterise absorption lines from the WHIM, thermally broadened single lines need to be resolved so that they can be differentiated by their Doppler shift from lines from distant galaxies. The thermal broadening from an oxygen line at 10^6 K gives a velocity width of ~60 km s^{-1} and simulations have shown that spectral features are typically separated by ~75 km s^{-1}, requiring the use of a high resolution spectrometer [Cash, 2011], [Lillie, 2011]. Using Equation 2.4 it can be calculated that a resolution of at least 4000 is required for spectral lines of this velocity width. The lines generated at these high temperatures will be broadened by Doppler shifting of the atoms in the plasma and many of them emit at soft X-ray energies such as the He-like and H-like resonance lines of carbon (C V, C VI), nitrogen (N VI, N VII) and oxygen (O VII, O VIII) [Bregman, 2010]. These lines are from highly ionised atoms of carbon, nitrogen and oxygen. The low energy nature of soft X-rays causes problems in being able to detect the photons effectively and hence detectors have been manufactured to optimise soft X-ray performance.

2.4 Current X-ray Spectroscopy Missions

X-ray spectroscopy is an important diagnostic tool for astrophysicists looking at the hot Universe and led to the launch of several major observatories over the last 30 years. With every next

generation space mission, the peak resolution of the instruments increases by an order of magnitude compared to the previous generation, Figure 2.18; however, as a CCD's resolution is Fano-limited (Section 3.6), the introduction of novel detectors is needed to allow a higher resolution performance. Alternatively, a dispersive spectrometer with CCDs can be used, but this will cause the instrument to lose its imaging capability [Tsunemi, 2005].

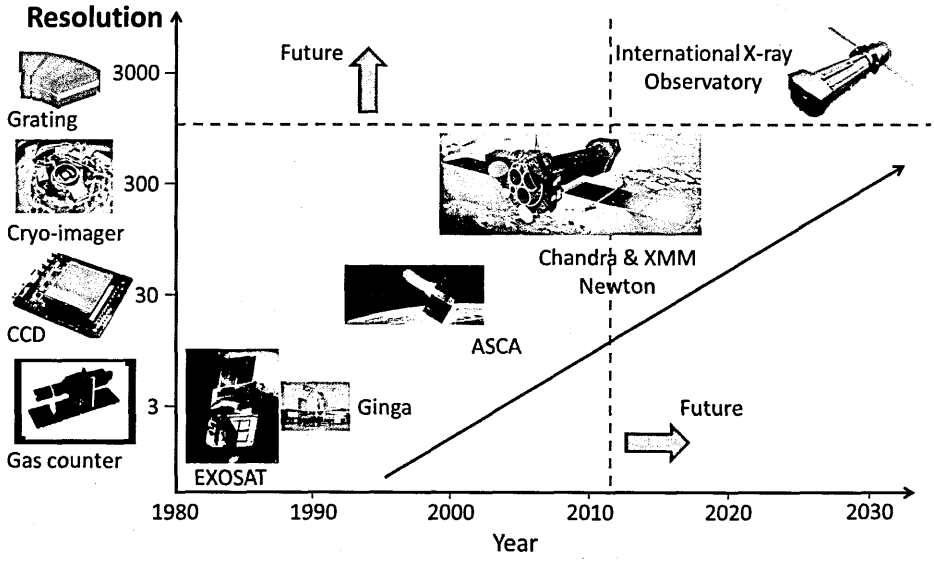

Figure 2.18: The progression of the upper resolution limit of X-ray missions over time. With each next generation X-ray missions, new technology leads to an increased resolution of the instruments from the use of gas counters in the 1980s to the densely ruled dispersive gratings proposed for future missions.

2.4.1 XMM-Newton

XMM-Newton is an ESA X-ray observatory launched in 1999 to a Highly Eccentric Orbit (HEO 114000 km apogee, 7000 km perigee) [Weisskopf, 2002]. HEO was chosen in order to keep the instruments out of the high radiation environments found in the Van Allen belts and South Atlantic Anomaly and to allow long exposure times by avoiding eclipsing the telescope with the Earth (10^5 seconds compared with 10^3 for Low Earth Orbit (LEO)). It carries 2 main instruments: EPIC (European Photon Imaging Camera) and the RGS (Reflection Grating Spectrometer). The satellite is made up of 3 co-aligned telescopes, two of which contain RGS instruments. The X-rays are directed to the focal point of the telescope onto the EPIC array using a Wolter I type optic. Approximately 40% of this converging beam is then incident onto the gratings. The two RGS instruments disperse the X-rays incident on their grating surfaces onto associated CCD camera arrays. EPIC is at the focus of the telescope's optic [Turner, 2000] and it offers the opportunity to

perform extremely sensitive imaging observations over the telescope's field of view. Across the energy range 0.15 keV to 15 keV the instrument has a spectral resolution of $\frac{E}{\Delta E}$ = 20-50 and an angular resolution of 6 arcsec FWHM (PSF). One of the two EPIC MOS cameras is shown in Figure 2.19 which uses the e2v CCD22 [Struder, 2001], [Turner, 2000].

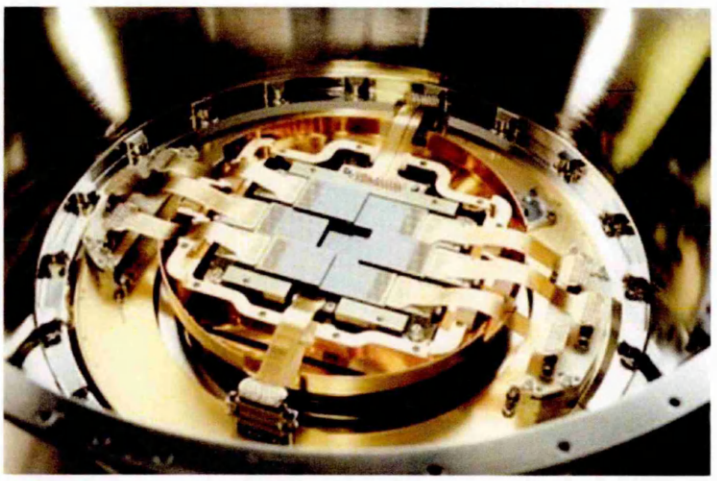

Figure 2.19: One of the EPIC MOS camera arrays, made up of 7 front-illuminated CCDs [Turner, 2000].

The RGS consists of a set of on-plane grating arrays with a variable line density between 626 and 6565 lines/mm (Figure 2.20). Photons focused onto these gratings are dispersed onto two identical CCD camera arrays that are offset from the main focus of the telescope. The three telescopes are co-aligned allowing them to observe simultaneously. The RGS places an array of reflection gratings (182 separate gratings) into the converging beam produced by the telescope's optic (Figure 2.21(a)). Each CCD array is made up of 9 CCDs each of which are 726 pixel x 1024 pixel arrays initially cooled to -80 °C (Figure 2.21(b)). The CCDs were later cooled to -120 °C to help mitigate radiation damage issues. The position at which an X-ray photon is incident on the CCD array gives a high resolution measurement of the photon energy. The inherent spectral resolution of the CCD is used to separate X-ray events at different energies in different dispersive orders as they will be detected at the same spatial point in the array (Chapter 8). The spectral resolution is also used to reduce background signal and to separate the in-flight calibration sources from the genuine X-ray data.

The RGS gratings measure 10 cm x 20 cm (cross-dispersion and dispersion direction respectively) and are mounted at grazing incidence to the incident beam in order to maximise the instrument's

throughput. The RGS gratings intercept 40% of the telescope beam with the other 60% going to the EPIC detectors at the focus of the telescopes. The grating substrates are manufactured from SiC, which gives the required strength to survive launch loads whilst also being thin enough to minimise obscuration. The gratings had to have a figure error over their length better than 1 λ in the long direction and better than 10 λ in the short direction (at 634.8 nm) relating to an r.m.s. deviation in the surface of the grating, relative to a perfectly flat surface, of no more than 634.8 nm in the long direction and no more than 6348 nm in the short direction. On the scale of a few mm the gratings are required to be atomically flat. Figure 2.21(a) shows the RGS grating array assembled and ready to be mounted behind the XMM-Newton mirror and Figure 2.21(b) shows one of the RGS camera arrays made up of back-illuminated CCDs.

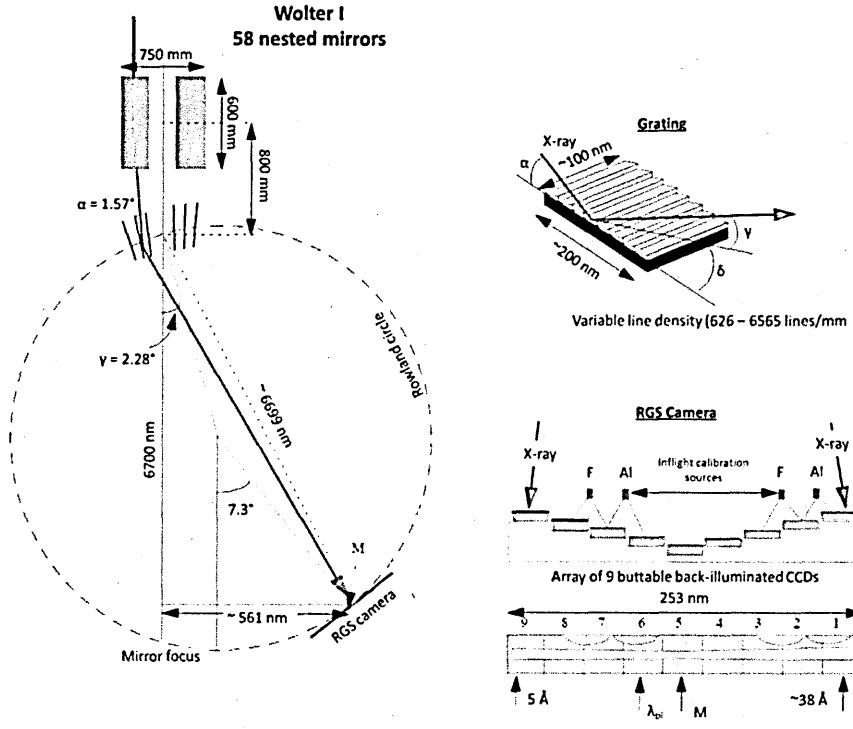

Figure 2.20: The reflection gratings disperse the converging X-rays from a Wolter I type mirror onto a CCD camera array offset from the main focus of the telescope. The orientation of the grating grooves, their blaze and the design of the RGS camera are shown [Brinkman, 1996].

The nine CCDs are back-illuminated GEC/EEV CCD15 frame transfer devices with 384 pixels x 1024 pixels each 27 µm x 27 µm [Bootsma, 2000], [van den Berg, 1996]. Their frame-transfer design allows the data to be collected in the image section and then quickly moved to the store

section prior to readout minimising any smearing of the signal thereby helping background rejection and improving the Signal-to-Noise Ratio (S/N).

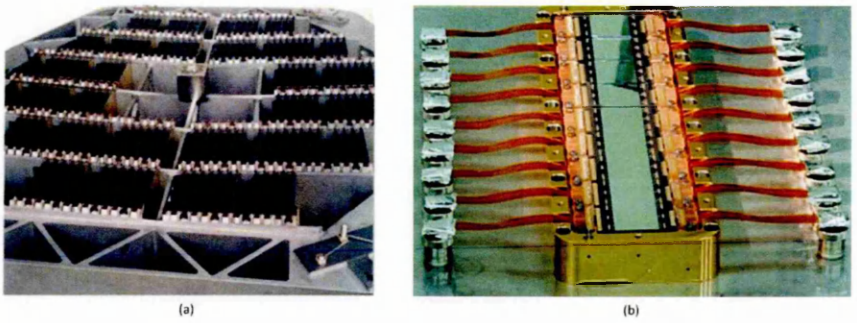

Figure 2.21: The RGS grating arrays ready for mounting behind XMM-Newton's optic (a) and one of the two CCD camera arrays for the RGS (b) [Optocorp a, 2008].

To maximise the chance of the detected radiation being collected in a single pixel the RGS CCD pixels are binned (3x3 binning). Binning is the process by which charge packets in adjacent pixels are combined before the signal is read out [Brinkman, 1996] forming a larger "pixel" area (81 µm x 81 µm), Figure 2.22.

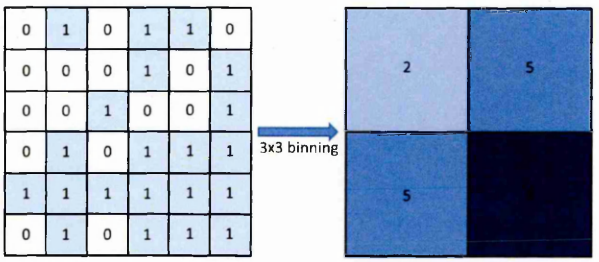

Figure 2.22: 3x3 binning of a 9x9 array of the 27 µm x 27 µm pixels gives a 2x2 array of pixels with 81 µm x81 µm pixels. All of the charge in the original array is now summed into these larger pixels.

CCDs are very effective detectors of optical photons and as the telescope will also project a large amount of "stray light", filters have to be incorporated into the instrument design comprising of a thin layer of Al on top of an insulating barrier layer to stop the optical photons from being detected. The CCDs that detect the higher energy X-rays are able to have thicker filters than the lower energy devices, leading to a staggered approach to filter thickness. All of the aluminium filters sit upon a 26 nm layer of MgF_2 to insulate the Al from the SiO_2 on the detector surface, which stops the conductive Al layer shorting to the underlying silicon. The thinnest Al filter is 45 nm, the middle thickness is 68 nm and the thickest filter is 75 nm [Brinkman, 1996]. Thinner filters are desirable as low energy X-rays will also be attenuated by the Al, but the optical

straylight needs to be reduced as much as possible. The thinner filters are used over the CCDs that will detect the lowest energy X-rays to maximise the CCDs' quantum efficiency performance at a cost to an increased background due to straylight. Where higher energy X-rays are detected, the filters can be thicker without a cost to quantum efficiency improving straylight rejection.

The RGS has a resolving power of 400 for photon energies in the region of 500 eV and utilises 3 spectral orders (1^{st}, 2^{nd} and 3^{rd}). The use of different spectral orders allows the instrument to maximise its efficiency across the energy range. The effective area across the RGS energy range is 100 cm^2.

2.4.2 Chandra

Launched at the same time as XMM-Newton, Chandra is also an X-ray observatory launched by NASA into an HEO orbit (140000 km apogee and 10000 km perigee [Weisskopf, 2002]). The orbit was chosen for the same reasons as the XMM-Newton. XMM-Newton was designed to provide high resolution X-ray spectroscopy whereas Chandra, with its state of the art mirror and high angular resolution, was designed to provide sub-arcsec imaging over the energy range of 0.08 eV to 10 keV. Chandra also had a high resolution spectroscopy capability based on transmission gratings, but the gratings were not fixed in the telescope beam. Chandra consists of a High-Resolution Mirror Assemble (HRMA) and an Optical Bench Assembly (OBA). The instrumentation on the OBA is on a translation stage in order to make it possible to move instruments in and out of the focal plane.

The HRMA is made of four-mirror pair grazing-incidence X-ray optics that are coated with iridium (high X-ray reflectivity and chemical stability). Behind the HRMA are mounted the two objective transmission gratings. The Low-Energy Transmission Grating (LETG) and High-Energy Transmission Grating (HETG) are mechanically moved into the beam in order to provide different diffraction performance. The LETG consists of 540 grating facets and uses a transmission grating with a grating period of 991 nm, providing high resolution spectroscopy over the 0.08 keV to 2 keV energy range [Weisskopf, 2002]. The HETG employs two types of grating facets. The

Medium Energy Gratings (MEGs) disperse X-rays in the 0.4 keV to 4 keV energy range and are mounted behind the HRMA's two outermost shells and the High Energy Gratings (HEGs) disperse X-rays in the 0.8 keV to 8 keV energy range and are mounted behind the HRMA's two inner most shells.

The focal array of Chandra consists of two focal plane science instruments: The High Resolution Camera (HRC) and the Advanced CCD Imaging Spectrometer (ACIS) (Figure 2.23). The HRC is a 10 cm^2 microchannel plate (Section 2.3.9.4) that has a 31 arcmin field of view. The HRC is the primary readout for the LETG. The ACIS-I is made up of a 2 x 2 array of large format front-illuminated CCDs (2.5 cm^2) providing high resolution spectrometric imaging over a 17 arcmin square field of view [Weisskopf, 2002]. There is also a 6 x 1 array of four front-illuminated and 2 back-illuminated CCDs mounted along the dispersion direction (ACIS-S). ACIS-S is used as the primary detector of the HETG and the back-illuminated detectors can be moved to the focal point of the optics to provide high-resolution spectroscopic imaging with high Quantum Efficiency. The detectors are Lincoln Lab framestore CCDs and have image areas with 1024 pixels x 1024 pixels each measuring 24 μm x 24 μm [Townsley, 2002].

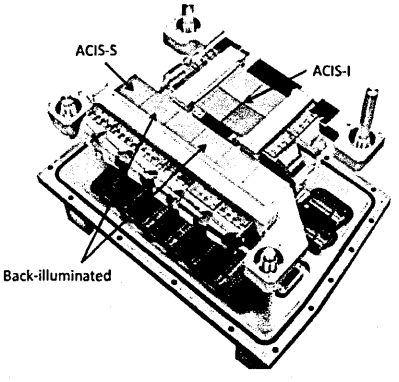

Figure 2.23: The ACIS with the imaging (I) and spectroscopy (S) sections and the two back-illuminated CCDs shown [Optocorp b, 2008].

Chandra is designed to have an effective area of ~800 cm^2 at energies below 2 keV and ~400 cm^2 between 2 keV and 5 keV and has become a key tool in the observation of the X-ray Universe.

During the time that XMM-Newton and Chandra have been large scale X-ray facilities available to astronomers, the Japanese have launched a series of small, specialist missions that have often

been technology drivers for future X-ray missions and have provided increased resolution and effective area across the X-ray energy range for relatively short periods of time.

2.4.3 Japanese Missions

JAXA, the Japan Aerospace Exploration Industry has produced several small, highly specialised X-ray satellite missions.

2.4.3.1 The Advanced Satellite for Cosmology and Astrophysics (ASCA) – Astro-D

ASCA was launched in 1993, was operational for 8 years and had an energy range of 0.4 keV to 12 keV. It was the first satellite to carry CCDs for X-ray astronomy and so was able to provide an imaging capability along with good spectral resolution (Figure 2.24) [Burke, 1994], [Tanaka 1994]. The two CCDs made up the Solid-state Imaging Spectrometer (SIS) and ASCA also carried two gas scintillation imaging proportional counters (GIS) (Section 2.3.9.3). ASCA's mission was terminated in 2001.

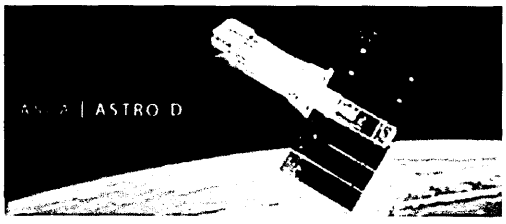

Figure 2.24: The Advanced Satellite for Cosmology and Astrophysics (ASCA) – Astro-D [JAXA, 2008].

2.4.3.2 Suzaku – Astro-E2

Suzaku was launched in 2005 and was the first satellite to carry an X-ray micro-calorimeter on the X-ray Spectrometer instrument (XRS), which provides an unprecedented spectral resolution compared with its non-dispersive counterparts. The satellite also holds an X-ray Imaging Spectrometer (XIS) that uses 3 front-illuminated CCDs and one back-illuminated CCD and a hard X-ray detector (HXD) that uses GSO crystal scintillators and silicon PIN diodes giving Suzaku an energy range of 0.2 keV to 600 keV (Figure 2.25 [Mitsuda, 2007]). However, due to a leak of coolant, the micro-calorimeter (Section 2.3.9.5) on the XRS instrument failed.

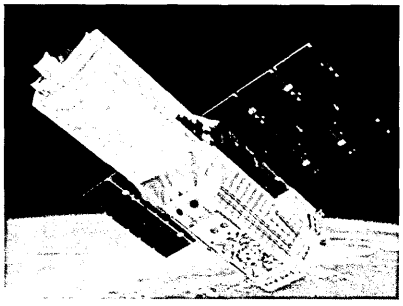

Figure 2.25: Suzaku – Astro-E2 [NASA, 2011].

2.5 Possible future X-ray Spectroscopy Missions

To maintain and improve our understanding of the X-ray Universe, future missions have been proposed that offer a higher resolution and effective area than previous missions, enabling the instruments to probe deeper into X-ray science.

2.5.1 The X-ray Evolving Universe Spectroscopy (XEUS) mission

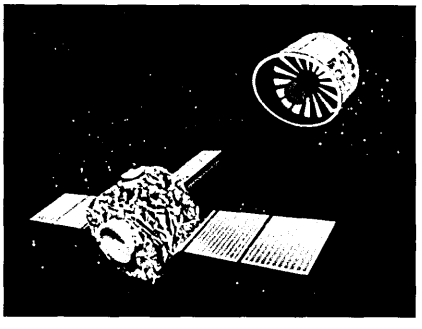

Figure 2.26: An artist impression of the formation flying XEUS spacecraft [Laboratorie AIM].

The X-ray Evolving Universe Spectroscopy (XEUS) mission was an ESA mission designed to follow XMM-Newton with a proposed launch in 2030. Through the separation of the focusing optics from the focal bench, XEUS would be able to have a focal length in excess of 35 m (Figure 2.26) allowing far greater sensitivity than XMM-Newton or Chandra [Gondoin, 2008]. XEUS was to be sent to orbit the second Lagrange point (L2) in order to be able to make uninterrupted observations of the X-ray Universe and was considered the next step forward in X-ray detection [Barret, 2003].

XEUS would contain three main instruments at the primary focus of the optic. An active pixel DEPFET (Section 2.3.9.8) Wide-Field Imager (WFI) providing a 7 arcmin field of view and resolution of 50 eV FWHM at the carbon k-shell (277 eV) and 125 eV FWHM at the manganese k_α shell (5898

eV) [de Korte, 2008]. The Narrow-Field Imagers (NFIs) would use Superconductor Tunnel Junction (STJ) (Section 2.3.9.7) and Transition Edge Sensor (TES) (Section 2.3.9.6) technology to resolve the fine structure of X-ray emission. The NFI's would have a resolution of 1 eV to 10 eV over the 0.1 keV to 30 keV energy range [Bavdaz, 1999].

The focal plane would not be entirely covered by the WFI and NFI technology and so it was further proposed to use MOS CCDs around the WFI in order to serendipitously find events of cosmological interest that would otherwise have been missed by the focal plane instrumentation, leading to the idea of an Extended Wide-Field Imager (E-WFI) [Holland, 2005].

However, due to creation of the International X-ray Observatory mission concept, XEUS was not selected for launch.

2.5.2 Constellation-X

Constellation-X was designed to follow on from NASA's Chandra mission and was being designed parallel to the XEUS concept. The telescope was to have an effective area 50 – 100 times greater than the current missions in space, a resolution $\left(\frac{E}{\Delta E}\right)$ of 300 – 1500 across X-ray energies and a focal length of 10 metres. The satellite design was to incorporate four identical satellites flying in formation in order to increase the effective area whilst keeping the weight of the satellite at a minimum due to lightweight optics (Figure 2.27).

The payload was to be split into two, with each section targeting different energies. The optic was split into a configuration of a Soft X-ray Telescope (SXT) mirror assembly and 3 Hard X-ray Telescope (HXT) mirror assemblies. The HXT would focus the hard X-rays (6 keV to 40 keV) onto the focal plane of the telescope where one of three Hard X-ray Imaging (HXI) cameras would detect the focused photons.

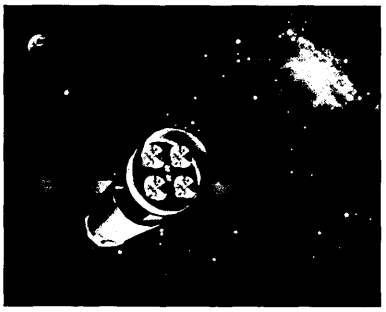

Figure 2.27: An artist impression of one of the four satellites of Constellation-X [Hornschemeier, 2007].

The SXT would also focus the soft X-rays (0.3 keV to 10 keV) onto a separate X-ray micro-calorimeter (XMS) (Section 2.3.9.5), but an X-ray grating spectrometer would disperse a proportion of these soft X-rays onto a CCD camera based spectrometer providing a ~1250 resolution across the 0.3 keV to 1 keV energy range. All instruments on the focal plane would be able to operate simultaneously. The layout of this payload is shown in Figure 2.28. Constellation-X was not selected due to its amalgamation with XEUS to form the International X-ray Observatory [Tananbaum, 1999].

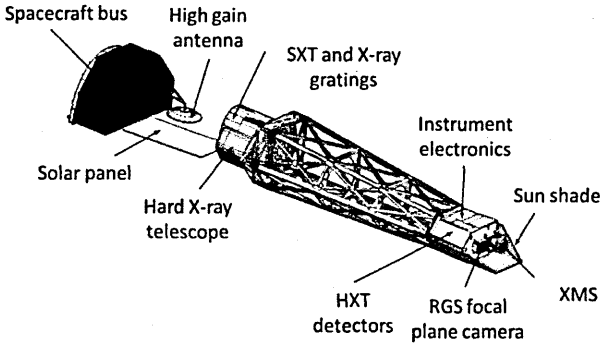

Figure 2.28: The separate HXT and SXT are shown with the separate focal points and energy specific instruments on the focal plane [Tananbaum, 1999].

2.5.3 Mission summary table

Table 2.2: The performance characteristics of current and planned NASA, ESA and JAXA space missions

	Mission	Instruments	Optic	Sensitivity (erg $cm^{-2}s^{-1}$)	Angular resolution	Effective area	Energy range	Focal length (m)	Orbit	Year
	ASCA – ASTRO-D	SIS and GIS	4 optics - 1.2 m diameter telescopes	$4x10^{-14}$	1' PSF	1400 cm^2 @ 1.5 keV 800 cm^2 @ 5 keV	0.2 keV to 600 keV	3.5	LEO	1993
	XMM-Newton	2 RGS, 3 EPIC and OM	3 optics – 1550 cm^2 effective area @ 1.5 keV each	EPIC ~ $1x10^{-14}$ RGS ~ $8x10^{-5}$	6" PSF 15" PSF	4650 cm^2 @ 1.5 keV	RGS – 0.35 keV to 2.5 keV EPIC – 0.2 keV to 10 keV	7.5	LEO	1999
	Chandra	LETG, HETG, HRC and ACIS	1.2 m diameter	$4x10^{-14}$	0.22" PSF <0.5" HPD PSF	700 cm^2 @ 1.5 keV	LETG – 0.08 keV to 2 keV HETG – 0.8 keV to 8 keV	10	LEO	1999
	Suzaku Astro E-2	XIS, XRT and XRS	3 X-ray telescopes	$3x10^{-11}$	1.8' to 2.3' HPD	400 cm^2 @ 1.5 keV 250 cm^2 @ 8 keV	0.4 keV to 12 keV	4.75	LEO	2005
	Constellation-X*	X-ray calorimeter and 3 CdZnTe	1.6 m diameter (1xSXT) and 40 cm diameter (3xHXT)	$8x10^{-14}$	15" HPD from 0.25 keV to 10 keV 1' HPD above 10 keV	15000 cm^2 @ 1 keV 6000 cm^2 @ 6.4 keV 1500 cm^2 @ 40 keV	0.25 keV to 40 keV	10	L2	n/a
	XEUS**	WFI and 2 NFI	10 m diameter	$<1x10^{-18}$	2" HEW	30 m^2 @ 1 keV 3 m^2 @ 8 kev	0.05 keV to 30 keV	50	L2	n/a
Studied during thesis	**IXO**	WFI, HXI, SMX, HTRS, X-POL, XGS	3 m diameter	$3x10^{-17}$	5" HEW	2.8 m^2 @ 1.5 keV	0.1 keV to 40 keV	20	L2	n/a
	WHIMEx	XGS	2 rectangular modules (0.8 x 0.125 m)	$4x10^{-15}$	15" HEW	>250 cm^2 @ 0.2 keV to 0.8 keV	0.2 keV to 2.5 keV	7	LEO	n/a
	ATHENA***	XMS and WFI	1.8 m x 1 m petal	$4x10^{-17}$	5" HEW	1 m^2 @ 1 keV 0.5 m^2 @ 6 keV	XMS – 0.3 keV to 12 keV WFI – 0.1 keV to 15 keV	12	L2	2025

*Constellation-X was designed to be made of 4 identical telescopes all with the same pointing (formation flying)
**This is for XEUS with the fully grown mirror module (MSC2) attached. The original mirror (MSC1) will have a 4.5 metre diameter
***ATHENA's optic is made up of two ellipsoidal petal shapes and uses silicon pore optics

2.6 Summary

X-ray spectrometers rely on high resolution performance in order to be able to identify spectral lines in emission and absorption spectra. The principles of X-ray spectroscopy have been used for decades and new instruments aim to use X-ray dispersion to provide instruments of high resolution.

To design a high resolution X-ray spectrometer, a complementary detector technology is required to take advantage of the resolution provided by the telescope. The detector that should be used is heavily dependent on the type of instrument that is used in the telescope.

Future X-ray spectroscopy missions will require a high resolution that can only be generated with dispersive grating elements. To complement these dispersive gratings high spatial and spectral resolution detectors and high angular resolution optics are also required. Satellites with these characteristics have been proposed and will enable high level diagnostics of the X-ray Universe.

Several detectors exist to complement high resolution spectrometers and can be used in scanned and static systems. All solutions have advantages and disadvantages that include spatial, spectral and temporal resolution, size and pixel format. The choice of detector can have a large impact on the overall performance of the instrument.

The choice between having a dispersive and non-dispersive is an important trade off to make when designing an instrument. A detector like a micro-calorimeter is capable of producing relatively high resolution spectra without the need of a dispersive element such as a grating. As a result all photons can be detected by the instrument (no loss due to mechanical structure), 2D imaging is possible and higher energy X-rays can be detected (gratings are limited by what energies they can reflect with high efficiency). However, the highest possible resolutions can only be achieved using a grating, making this style of instrument desirable for the work in this thesis.

Chapter 3: The Charge-Coupled Device

Chapter 3 discusses the history of the Charge-Coupled Device (CCD) and some necessary semiconductor theory. Application specific detector technology is then described, focussing on how the CCD can be manufactured and operated to optimise performance at soft X-ray energies.

3.1 The history of CCDs

The CCD was invented in 1969 at AT&T Bell Labs by Willard Boyle and George E. Smith [Boyle, 1970]. Through a construction of the magnetic-bubble memory from their earlier work they conceived a way that an equivalent "charge-bubble" could be transferred through linear and area registers in a semiconductor by the manipulation of gate potentials in the device. The "charge-bubble" transfer was later extended to handle photon-generated charge signals to form practical solid-state imaging sensors.

By 1974, Fairchild had produced commercially a 500 element linear device, a 100 x 100 2D pixel array and a CCD for the KH-11 KENNAN reconnaissance satellite for use in optical imaging [Brunn, 2004]. In 1993, the ASCA (Advanced Satellite for Cosmology and Astronomy or ASTRO-D) became the first satellite to use CCDs to perform X-ray astronomy in orbit [Tsusaka, 1995]. CCDs have not only driven changes in the field of photography, but have provided high resolution imagers in medicine and are used on several space missions. Examples of this include CCDs for X-ray detection in teeth [Davis, 1996] and on space missions such as XMM-Newton [Brinkman, 1996] and Chandra [Weisskopf, 2002].

In 2006 Boyle and Smith were awarded the National Academy of Engineering Charles Stark Draper Prize and in 2009 they were awarded the Nobel Prize for Physics for their work on Charge-Coupled Devices.

3.2 Semiconductor theory

Silicon is an extrinsic semiconductor with a crystalline structure and its conduction properties can be altered by doping the silicon with acceptor or donor atoms. In a semiconductor the doping can

be considered to be n-type or p-type through the addition of phosphorus or boron atoms respectively into the silicon lattice. n-type doping produces an additional free electron in the silicon lattice (negative) and p-type produces an additional hole which is the absence of an electron in the lattice (positive). Electrons are the charge carriers in the conduction band and holes are the charge carriers in the valence band [Amelio, 1971], [Lutz, 1999]. Silicon has 4 electrons bound in the outer electron shell, allowing covalent bonding with 4 other silicon atoms to enter a stable state with 8 electrons in the outer shell. Through the addition of phosphorus (Figure 3.1), which contains 5 electrons in the outer electron shell, the silicon lattice structure has one additional electron, termed a free electron, which is known as the majority charge carrier. Conversely, p-type doping adds an atom to the lattice (typically boron) that only has three electrons in the outer electron shell, leading to an imbalance in the number of electrons and the formation of a hole (absence of electron) in the lattice. In the case of p-type doping, this hole is the majority carrier with the electron now being the minority carrier [Sze, 1981], [Kittel, 2005].

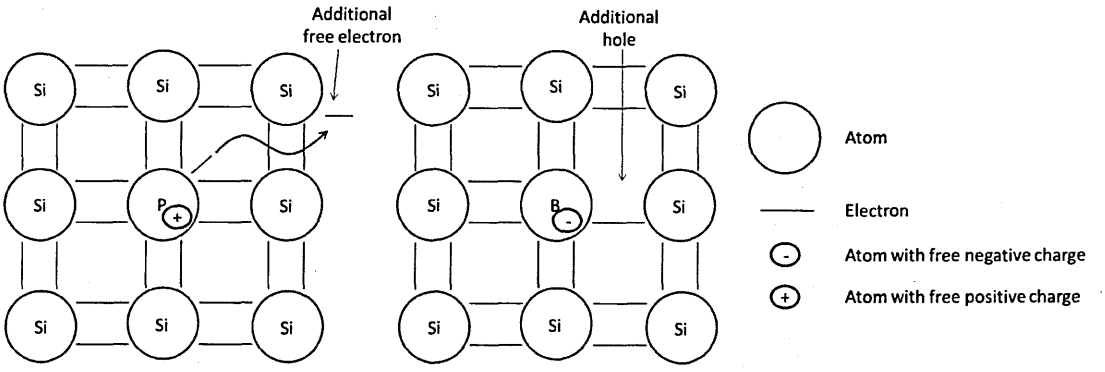

Figure 3.1: A figure to show n-type doping with phosphorus as a donor atom generating an additional electron in the silicon lattice and p-type doping with a boron atom as an acceptor atom generating a hole (absence of electron) in the lattice. The additional electron in the case of phosphorus leaves the nucleus with an apparently positive charge and the additional hole with boron doping leaves the nucleus with an apparent negative charge

3.2.1 The p-n junction

The doping of p-type and n-type silicon generates holes and free electrons respectively (Figure 3.2). These additional charges are countered by the inherent charge of the doped atoms (negative for phosphorus and positive for boron) [Lutz, 1999] and so the two pieces of independent silicon are electrically neutral and in equilibrium.

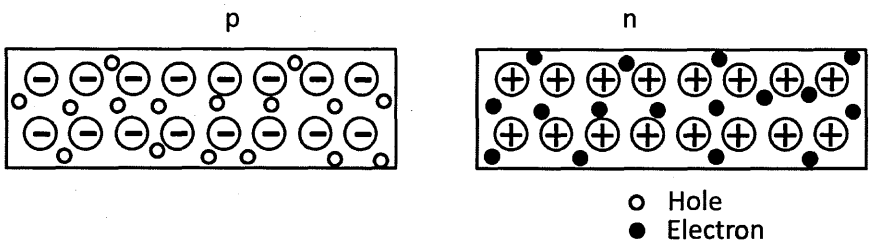

Figure 3.2: Isolated p-type and n-type insulators showing an even distribution of electrons and holes.

If the two pieces of silicon in Figure 3.2 are brought into contact without a potential being applied across the junction, electrons will flow from the n-type material into the p-type material, combining with the holes in the silicon, Figure 3.3. The negatively charged atoms in the p-type are now no longer balanced by the holes and negative charge will build up. Likewise, the positively charged atoms in the n-type material are no longer balanced by electrons causing positive charge to build up. The resulting electric field from these charges counteracts the diffusion of electrons from the n-type to the p-type silicon and the p-n junction reaches a new equilibrium state, Figure 3.3.

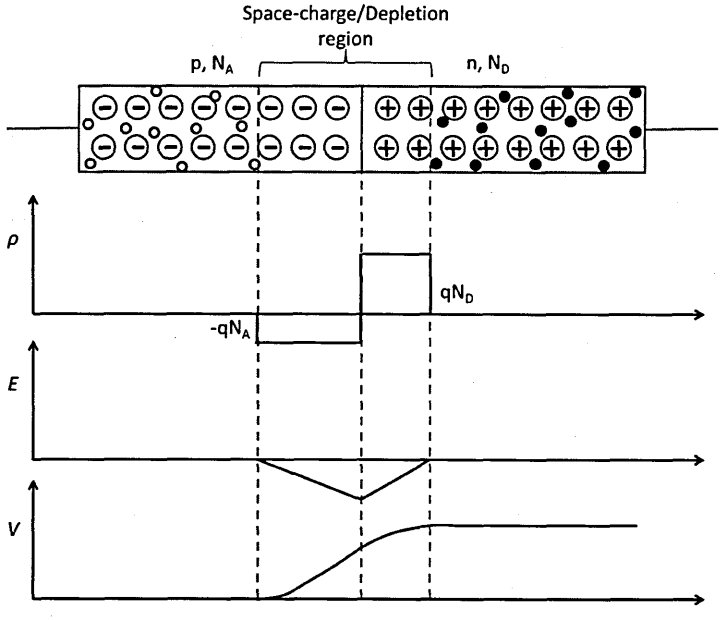

Figure 3.3: A p-n junction with distribution of carriers in the p-type and n-type material. The charge density (ρ), electric field (E) and potential in the junction (V) against position across the p-n junction is indicated.

The magnitude of the charge density, ρ, electric field, E, and potential step, V, across the junction can be controlled by altering the doping levels of the p-type and n-type silicon. The region that contains no free-electrons or holes either side of the p-n junction is called the "depleted region".

If the device is used to detect photons, the electron-hole (e-h) pairs generated in this region are separated, with the electrons swept into the n-type silicon and the holes swept into the p-type silicon [Lutz, 1999].

The Fermi level of the p-type doped silicon (Ef_p) is lower than that of the n-type doped silicon (Ef_n). When the n-type and p-type silicon are brought together in order to be in equilibrium their Fermi levels must align, changing the potential profile of the conduction band (E_c) and valence band (E_v) of the silicon as shown in Figure 3.4. The potential change creates a barrier potential (ϕ_B) that restricts the movement of electrons and holes in the silicon.

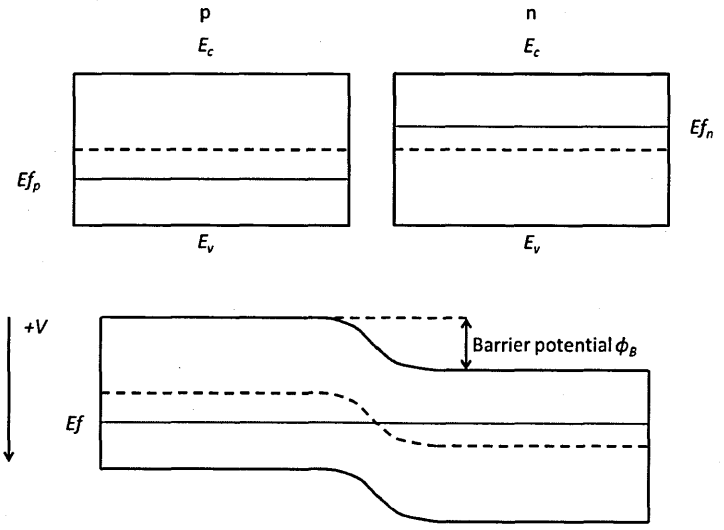

Figure 3.4: The change in the valence band and conduction band in n-type and p-type doped silicon when they are brought into contact and are in equilibrium. The Fermi level must be constant across the junction creating a barrier potential, ϕ_B.

3.2.2 Metal-Oxide-Semiconductor (MOS) capacitor

A Metal-Oxide-Semiconductor (MOS) capacitor uses a potential on the front surface of the capacitor (the gate electrode) to alter the properties of the semiconductor beneath the insulated oxide (Figure 3.5).

When no potential is applied to the gate electrode, the semiconductor is in equilibrium and is electrically neutral (Condition 1 in Figure 3.5). Applying a negative bias to the gate electrode in a p-type MOS capacitor attracts excess free holes to the oxide-semiconductor interface forming an accumulation layer (Condition 2 in Figure 3.5), but the remainder of the semiconductor is still in equilibrium. Applying a positive potential to the gate electrode repels holes from the

oxide-semiconductor interface and a depletion layer is formed in the underlying silicon (Condition 3 in Figure 3.5).

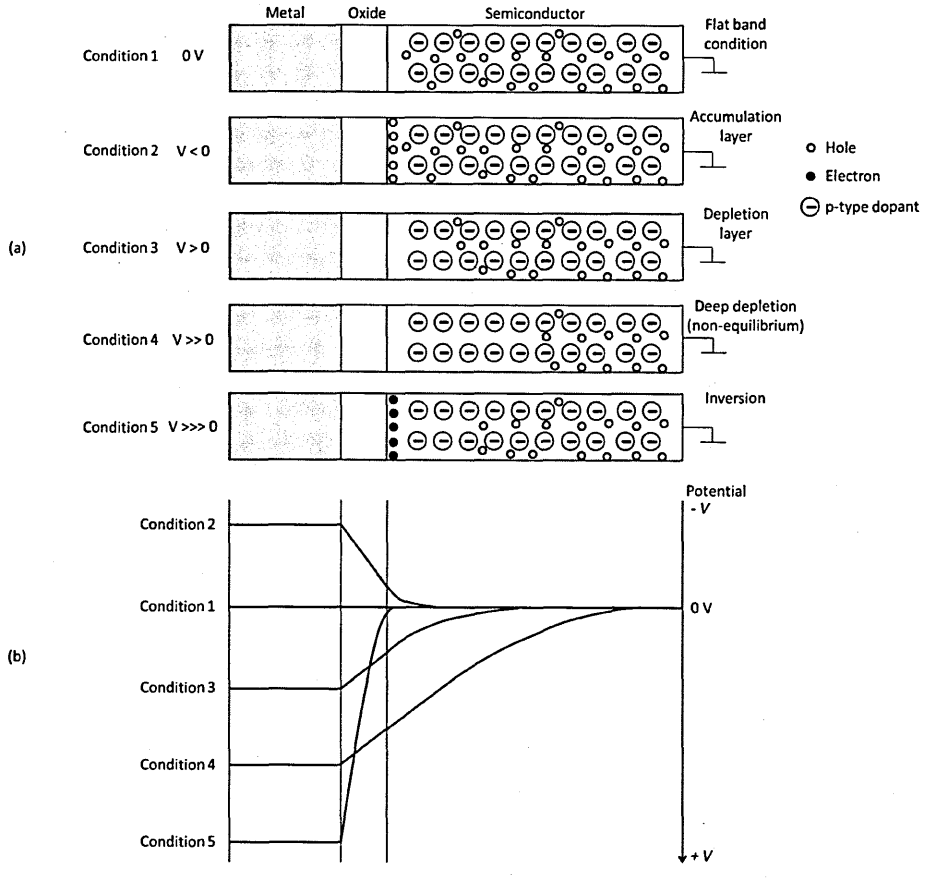

Figure 3.5: A p-type Metal-Oxide-semiconductor capacitor is shown with different levels of bias applied to the gate (a) and potential profiles through the MOS capacitor are shown on the same potential profile (b). The potential here is shown in reverse as is the convention with semiconductors.

If the positive potential is increased, more holes are repelled and this generates a much larger depth of depletion (Condition 4 in Figure 3.5). Under these conditions, thermally generated e-h pairs are separated and the electrons are swept towards the front surface of the device where they form an "inversion layer" at the oxide-semiconductor interface (build-up of electrons at the oxide-semiconductor interface). The negatively charged electrons counteract the negative lattice charge in the depletion region and the depth of depletion therefore reduces. Operating a MOS capacitor with the potential profile shown for condition 5 in Figure 3.5 is avoided as it generates a large potential swing.

3.2.3 MOS Field-Effect Transistor (MOSFET)

A MOS transistor can be used to amplify or switch electronic signals. A potential on the gate electrode can be used to induce a conducting channel between two other connections known as the source and drain (Figure 3.6). With a 0 V potential applied to the gate, there is no conduction path between the heavily n-type doped source and drain regions. Increasing the potential on the gate causes an inversion layer to form in the p-type silicon under the gate and, with a positive bias on the drain, a current can flow between the source and drain [Horowitz, 1989].

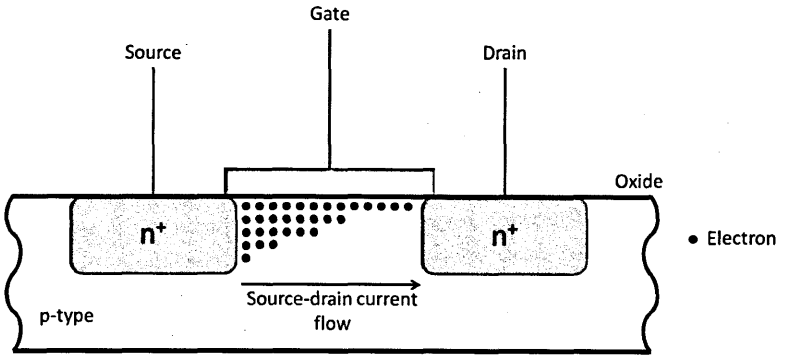

Figure 3.6: A MOS transistor, showing the gate, source and drain with electron flow due to a bias on the Gate creating a conducting channel between the Source and Drain.

The amount of current that flows between the source and drain, I_d, is dependent on the potential applied to the gate, V_G, according to Equation 3.1, where the factor β (the DC current gain) depends on the length, L, width, W, and capacitance, C_0, of the transistor ($\beta = \frac{\mu C_0 W}{2L}$) and V_T is a threshold voltage dependent on the positive charge in the oxide [Horowitz, 1989].

$$I_d = \frac{1}{2}\beta(V_G - V_T)^2 \tag{3.1}$$

In "switching" mode, if the gate potential is zero then no current flows between the source and drain and the switch is effectively "off". If a positive gate potential is then applied, current can flow between the source and drain and the switch is effectively "on". Alternatively, in an analogue mode, the gate potential can be set to an intermediate value with a small current flowing. Any small change of gate potential can give rise to a change of current flow and this can be turned into an output potential using a load resistor.

3.3 Photo-generation of electron-hole pairs

Semiconductors (in this case silicon) have conductive properties; if an electron is excited from the valence band to the conduction band it can be considered as a "free" electron and can therefore contribute to the electrical conductivity. The hole that remains due to the absence of this electron will also contribute to electrical conductivity. This electron-hole combination is known as an electron-hole pair [Kane, 1962].

3.3.1 Photoelectric effect and avalanche ionisation

The number of free electrons and holes in the silicon is highly dependent on the doping that is added into the lattice (Section 3.2). The doping creates acceptor and donor states that can more easily provide free electrons or holes. Thermal excitations in the silicon lattice are not of a sufficient energy to ionise electrons across the band gap, ω, from the conduction band to the valence band. For non-negligible thermal generation to occur intermediate traps in the silicon are required to allow the thermal generation to occur in two stages. These are defects in the silicon that can store and release electrons. If the silicon does not contain traps the dark current produced will be small which would be ideal for the use of these detectors for photon generation. With an increase in temperature, if mid-band traps are present, thermal signal created across this two stage ionisation will increase (Figure 3.7) [Kittel, 2005].

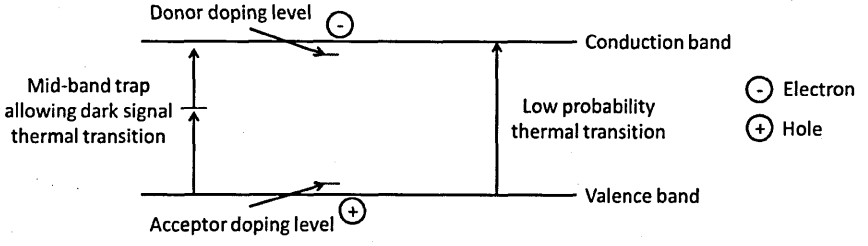

Figure 3.7: An image representing the band-gap between the conduction and valence band in silicon. To directly cross the band-gap an energy of at least 1.11 eV is required. In order for thermal generation to occur a mid-band trap is required.

Through the absorption of photons, electrons can also acquire sufficient energy to cross the band gap. When a photon is incident onto a material it can impart its energy into that material through the photo-electric effect [Einstein, 1905]. The photon energy can be given to an electron in the lattice and, in the case of a semiconductor, if the energy is greater than or equal to the band gap

the electron will enter the conduction band in a process known as "direct photon absorption", with any additional energy in the photon passed to the electron and conserved as kinetic energy (Figure 3.8 [Kittel, 2005]).

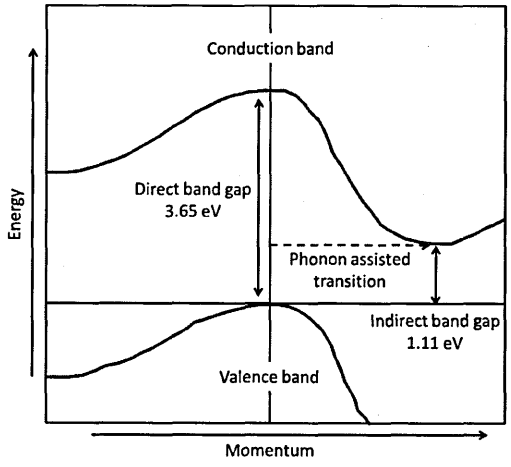

Figure 3.8: The direct and indirect band gap in silicon. If the photon has enough energy the electron jumps to the conduction band without a change of momentum, but if the energy is not sufficient a phonon interaction is required to change the electron's momentum allowing it to cross the indirect band gap [Sze, 1981].

If the kinetic energy of the released electron is sufficient it can collide with other electrons in the lattice, imparting enough energy to cross the band gap and enter the conduction band. The process will continue until the electrons in the conduction band have less energy than is required to excite further electrons into a conductive state (Figure 3.9). The process of generating further e-h pairs through collisions in the lattice is a form of impact ionisation known as avalanche ionisation [Geist, 1983] and the mean number of electrons that are excited into the conduction band, for a photon of energy $E > 3.65\ eV$, is $\frac{E}{3.65}$ [Geist, 1979]. Photon energies as low as 1.11 eV can also generate free electrons with the addition of the thermal energy from the lattice (phonon assisted); these interactions are termed "indirect transitions" (Figure 3.8). No further additional electrons will be generated through avalanche ionisation.

The corresponding hole in the e-h pair is not a physical particle, but an absence of an electron; however, holes can be transferred through the device by moving electrons in the lattice allowing the collection of holes to be used to determine the energy of the incident electron [Kane, 1962].

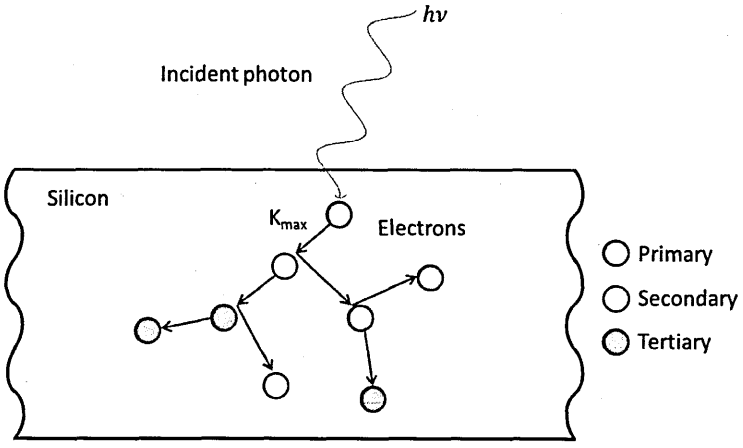

Figure 3.9: The incident photon of energy $h\nu$ ionises an electron with more energy than the direct band gap of the silicon. This electron (red) has energy K_{max} and impacts onto a second electron (yellow). These two electrons then move through the lattice causing further ionisation.

3.4 CCD basic principles

3.4.1 Introduction to basic CCDs

A requirement of CCDs is to separate the photo-generated electron and hole before they can recombine. Thus, in the case of a reverse biased p-n junction the potential step formed through the different doping across the junction separates the electron and hole. Alternatively, the MOS capacitor in deep depletion can achieve a similar effect (Figure 3.10).

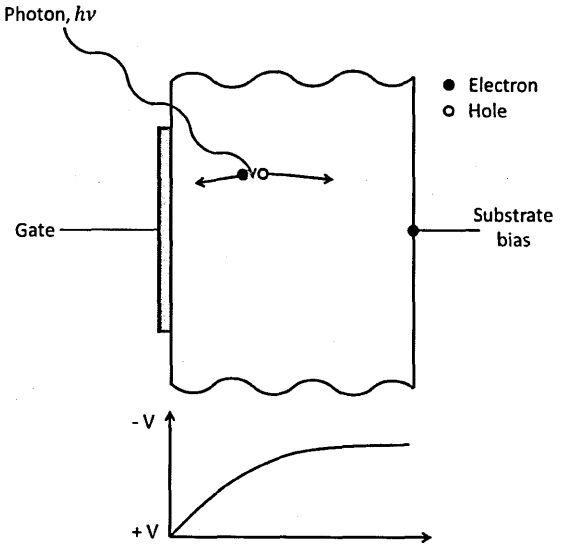

Figure 3.10: A MOS capacitor being used as a photo-sensitive device.

The electrons move to the surface of the silicon where they are stored and the holes move into the substrate and are lost through the bias connection. Therefore, the electrons can be collected at the surface, in the pixel structure, and read out. The charge-collection and readout process is often described using the "buckets on a conveyer belt" analogy (Figure 3.11).

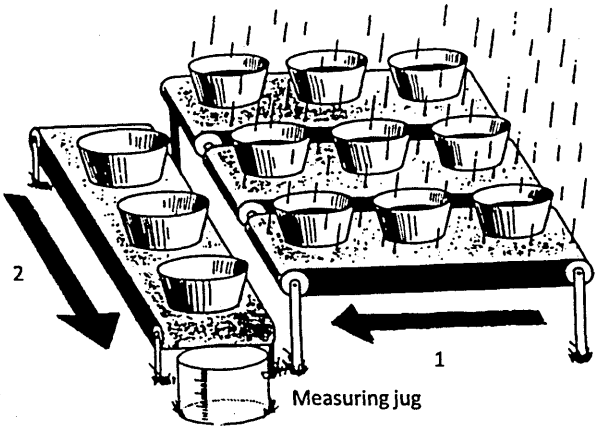

Figure 3.11: Water bucket analogy for the method of storing and moving charge through silicon. The water is collected in the buckets representing the pixels. After the water is collected the buckets are moved on conveyer belt 1 (parallel) towards the buckets on conveyer belt 2 (serial). The serial buckets are then emptied into a measuring jug, measuring the amount of water [Janesick, 2001].

The basic concept for forming a 2D array of pixels can be seen in Figure 3.12. Polysilicon electrodes are used to define the silicon into rows and "channel stops" are used to split these rows into individual columns, forming the pixel.

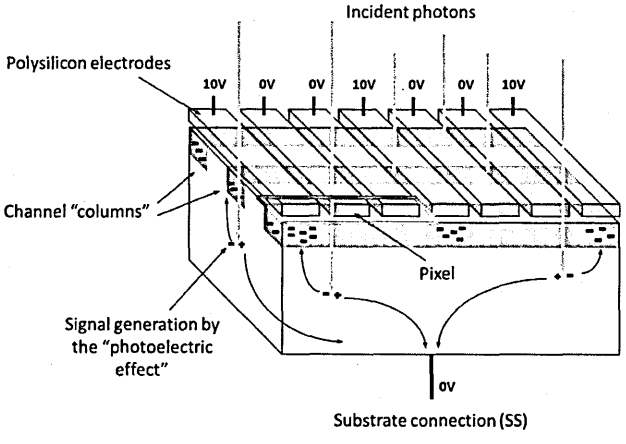

Figure 3.12: A CCD with electrodes placed over the surface to define the pixels.

The channel stops are created with a boron implant (p^+) between the separate columns in the silicon pixelated array. The implant keeps the charge packets in adjacent columns separated through changing the potential in the silicon. The pixels allow the spatial information of where the photon interaction occurred to be retained.

3.4.2 Surface and buried channel MOS CCDs

The MOS CCD uses the depletion region in a MOS capacitor to separate photo-generated e-h pairs and the electrons are stored as an inversion layer at the oxide-semiconductor interface. This is

known as a "surface channel" device but, as the charge is held at the oxide-semiconductor interface where there are a high number of trapping centres, the charge is not moved very efficiently from pixel to pixel. To avoid this Charge Transfer Inefficiency (CTI) the buried channel CCD was developed [Lutz, 1999].

To form a buried channel, a MOS CCD has an n-type doping implanted between the oxide and the p-type silicon. A p-n junction is formed within the semiconductor material and moves the charge collection point of the electrons generated in the CCD from the oxide-semiconductor interface to a point just below in the n-type silicon known as the "buried channel" (Figure 3.13). The charge is moved away from the trapping centres at the oxide-semiconductor interface, making charge transfer more efficient.

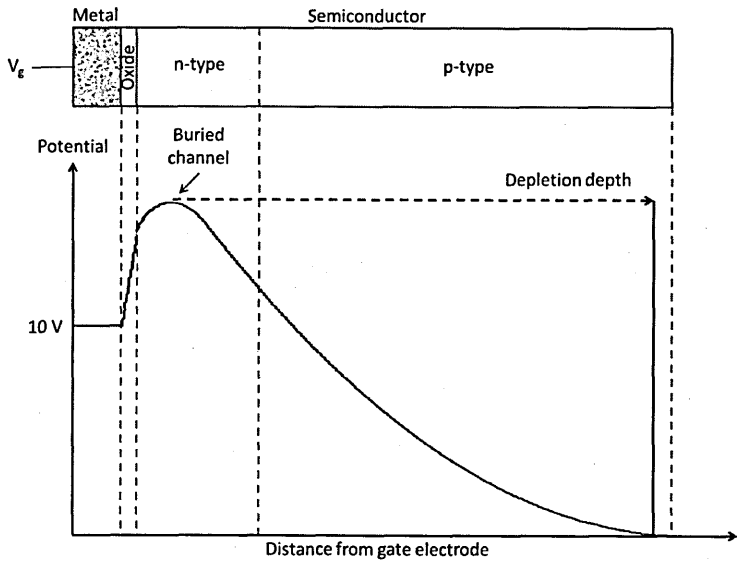

Figure 3.13: The basic doping structure of an n-channel CCD with associated potential profile where V_g is the potential placed on the gate electrode.

The potential distribution can be explained as follows. With reference to Figure 3.5 and Figure 3.3, the voltage distribution in a MOS capacitor on n-type silicon in depletion would be as shown on the left hand side of Figure 3.14(a). The voltage distribution of a p-n junction is shown on the right hand side. By merging together the two structures such that the depletion regions meet, the potential distribution shown in the bottom figure results [Burt, 1974], [Kent, 1973], [Walden, 1972].

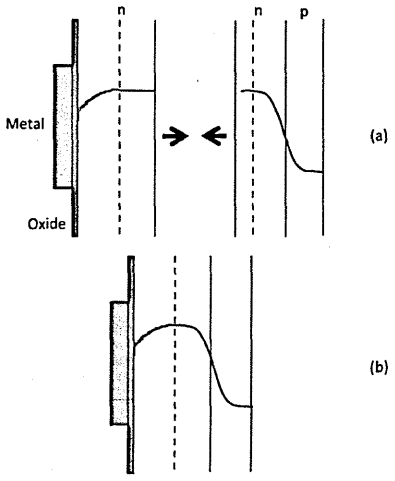

Figure 3.14: An n-channel MOS and p-n junction are shown separately (a) and combined (b). The potential profile running through the semiconductor is also shown and the method by which the CCD potential forms can be seen.

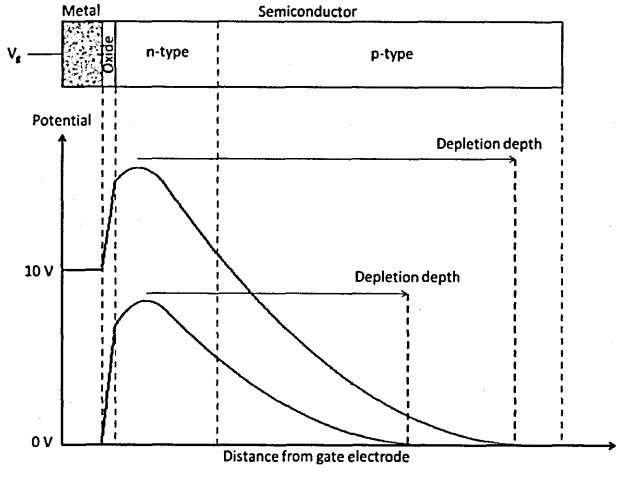

Figure 3.15: The changing potential in the MOS CCD with varying gate voltage. The electrons are collected at the peak potential which is within the n-type silicon and away from the oxide-semiconductor interface.

The potential profile across the buried channel CCD for a potential of 0 V and 10 V on the gate electrodes, is shown in Figure 3.15. Electrons generated in the silicon are collected at the peak of the potential plot which is in the n-type silicon and away from the trapping centres at the oxide-semiconductor interface. The depth of depletion is given by the point that the potential in the p-type silicon is zero. It can be seen that the depletion region is larger when a positive voltage is applied to the front surface of the device.

If the clocking amplitude of charge through the CCD is between 0 V and 10 V the difference between the peaks of the voltage potential curves determines the "bloomed full-well capacity" of the buried channel. This is a measure of how much charge the buried channel can hold before it

fills and the charge spills into neighbouring pixels (blooming) (Figure 3.16 [Janesick, 2001]). The figure is inverted with respect to voltage compared to Figure 3.15.

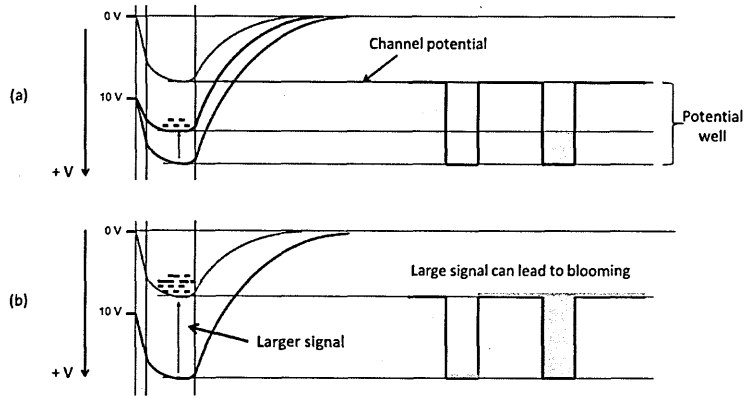

Figure 3.16: The potential for a CCD for two different signal levels is shown. As the signal in a pixel becomes larger, the potential well "fills" until it reaches "full-well". Diagram (b) shows the charge "blooming" out of the pixel as it reaches full-well.

3.5 Charge transfer

The electrons that are generated and stored in the silicon are transferred through the device towards the sampling circuit using a process called charge transfer [Holst, 2011]. Electrodes over the front surface of the device can be used to form and manipulate potential wells in the CCD. By holding one of the electrodes per pixel at a clocking voltage (typically +12 V [e2, 2006]) it is possible to collect the charge generated by photon interaction and move it through the device towards the output [Lumb 1990].

3.5.1 Full-frame array

The gate electrodes on each row of the image area are connected allowing the potentials in the pixels to be changed together, thus moving the charge through the pixel array in a process known as a parallel clocking (Figure 3.17 [Tompsett, 1972]).

The charge packet reaches the bottom of the image area and is transferred into a serial register that is made up of a 1D array which moves a single row of charge towards the output node. The charge transfer happens with similar clocking potentials as with the parallel transfer, but the entire serial register has to be read out once for each single parallel transfer. Therefore, the speed of the serial readout is the dominant restriction on how fast the CCD can be read out. In the case of Figure 3.17, three phases per pixel are used to move the charge through the image

area. By clocking the electrodes sequentially, the charge in the image section is moved in parallel through the device.

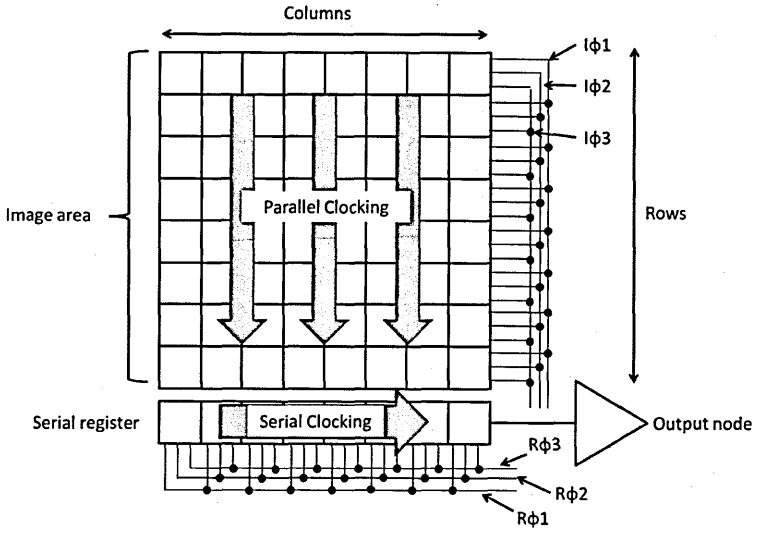

Figure 3.17: A CCD schematic with parallel clocking in the image area and serial clocking in the serial register shown. The device is clocked using a three phase electrode structure per pixel.

In a full frame device (Figure 3.17) the whole of the CCD image area can be used for photon detection [Lumb, 1990]; however, this means that the device has a small duty cycle (the time that the sensor is collecting light) as photons collected during the readout are ignored. To read out the device, the clocking process is repeated for each row in the image area. Assuming that a 3-phase device is being used, the clocking drive waveforms that would be needed are shown in Figure 3.18.

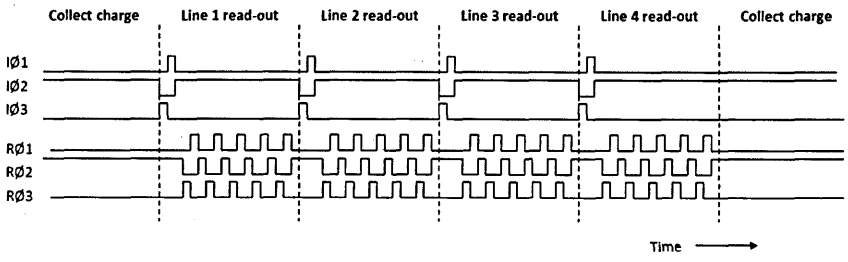

Figure 3.18: The clocking drive waveforms needed to readout the signal collected in a 3-phase CCD.

In the example from Figure 3.18 the charge is collected in the image area with Iϕ2 held high. To read out the image section the charge is moved from Iϕ2 into Iϕ3 by overlapping the clock edges and then into Iϕ1 before going back into Iϕ2 which moves the bottom row of the image section into the serial register under Rϕ2. Overlapping clocks edges are when the potential on one gate electrode is increased to +V at the same time that the adjacent gate electrode potential is held at

+V. The charge is shared between the two pixels as their clock pulses coincide. The charge is moved through the serial register through the manipulation of Rϕ2, Rϕ3 and Rϕ1 for the length of the serial register until the charge is clocked onto the output node and converted into a voltage (Section 3.5.3). The image phase clocks are then used to move the next row of the image area into the serial register so that it can be read out. To readout the device this process is repeated for each row.

3.5.2 Frame transfer array

A device that is being run in frame transfer mode has an image section and a store section. The image section is optimised for photon detection while the store section is normally covered with a shield making it insensitive to optical photons. After integrating charge, the gate potentials are used to move the charge quickly out of the image section into the store section. This frees up the image section for a new measurement and the charge accumulated in the store section can then be read out slowly to optimise the noise performance and reduce smearing (Section 3.7) (Figure 3.19 [van de Steeg, 1985], [Lumb, 1990]).

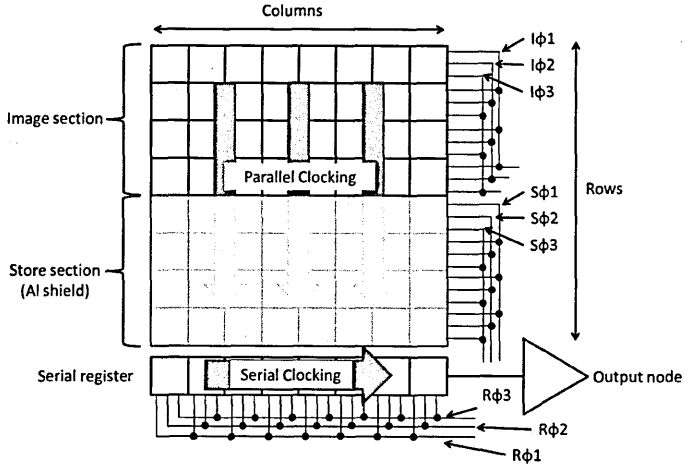

Figure 3.19: A frame transfer CCD with an aluminium shield over the store section to make the section insensitive to incident photons.

3.5.3 Output circuits

The charge accumulated in the device is moved using the gate potentials in the pixels towards the output circuit. The output circuit typically comprises a heavily doped n-type region called the "output node" with associated reset and source-follower transistors (Figure 3.20). The node has

parasitic capacitance C_n and it is on this capacitance that a charge being read out is stored before being converted to an equivalent voltage signal across a load resistor, R.

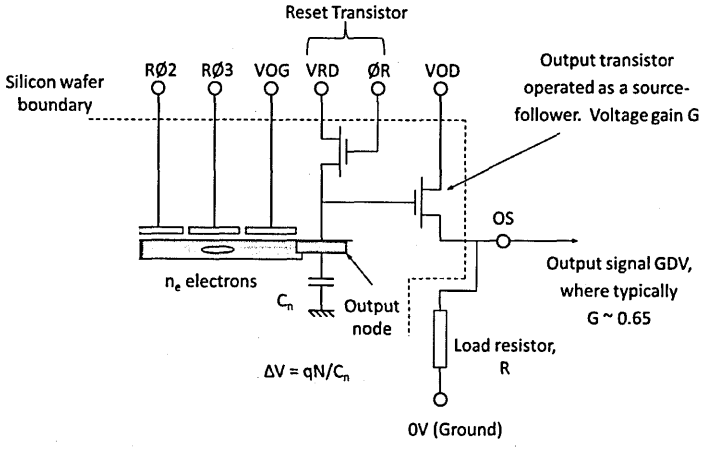

Figure 3.20: The charge packet is read onto the output node and then converted into a voltage by creating a potential difference across the load resistor, *R*. The output transistor operates as a source-follower buffer circuit. ϕR is used to reset the output node to the VRD level in between read outs. The area enclosed by the dotted line is manufactured on the silicon wafer.

The reset transistor is operated in switching mode leaving the transistor in either an on or off state depending on the potential on ϕR (the reset clock). When ϕR has a positive voltage, typically 10 V, the capacitor on the output node, C_n, is charged to a level determined by VRD (the Reset Drain potential). The potential on ϕR is then taken to 0 V and the node is left "floating" at VRD ready for the next charge packet to be read out (this is the reset operation). The output transistor is operated in analogue mode and so the signal voltage on the gate of the transistor will relate to the signal on OS (Output Source). If the voltage on the gate is V_G and that on the source is V_S, the current through the transistor is given by Equation 3.2, which is matched by the current through the load resistor, R, by Equation 3.3:

$$I_d = \frac{1}{2}\beta(V_G - V_s - V_T)^2 \tag{3.2}$$

$$I_d = \frac{V_s}{R} \tag{3.3}$$

Eliminating I_d from these equations gives the variation of V_S with V_G, namely:

$$V_s = V_G + \frac{\left[1 - \sqrt{1 + 2\beta V_G R}\right]}{\beta R} \tag{3.4}$$

For small signals:

$$\frac{\Delta V_S}{\Delta V_G} = 1 - \frac{1}{\sqrt{1 + 2\beta V_G R}} = G \tag{3.5}$$

G is described as the voltage gain, typically with a value 0.65-0.80 depending on design [Horowitz, 1989]. The source voltage therefore follows any change of voltage on the gate, but at reduced amplitude, hence the circuit is known as a "source-follower". The overall transfer characteristic is given by Equation 3.6, where C_n is the capacitance of the output node, q is the electronic charge, n_e is the number of electrons in the charge packet that is being read out and G is the voltage gain of the source-follower.

$$\Delta V_S = \frac{q n_e G}{C_n} \tag{3.6}$$

The term "responsivity", R_0, is typically used to characterise an output circuit and this is essentially the output voltage for the detection of a single electron and it is expressed as:

$$R_0 = \frac{qG}{C_n} \tag{3.7}$$

3.6 X-ray photon detection performance

3.6.1 X-ray detection

In Section 3.3 the detection of photons of different energies was discussed, with photons at energies close to the indirect band gap energy in silicon (1.11 eV) producing one e-h pair with the assistance of a phonon in the silicon lattice. Infra-red, optical and UV photons are detected in silicon this way; however, this is not the case for higher energy photons.

3.6.1.1 Quantum yield

The quantum yield for a material is a measure of the amount of energy required to generate an e-h pair in the silicon without phonon assisted transition [Janesick, 2001]. X-rays exist in the high energy region of the electro-magnetic spectrum from ~50 eV up to several MeV [Young, 2000] and as this energy is much greater than the quantum yield for silicon (3.65 eV) [Lumb, 1990], the initial photon-generated electron has enough kinetic energy to impact other electrons in the silicon lattice, exciting them into the conduction band and producing further electrons through impact ionisation. Electrons continue to be produced until the kinetic energy of the electrons already in the conduction band falls below the quantum yield. The mean number of e-h pairs

generated by the interaction in this charge cloud, n_e, is found by dividing the energy of the photon by the quantum yield. The standard deviation on the number of electrons generated by an X-ray interaction in the silicon would be equal to $\sqrt{n_e}$ if the interaction followed Poisson statistics; however, when experiments are performed to measure the distribution of e-h pairs that are generated for X-ray energy photons in silicon, the distribution of energies, and so the standard deviation, is found to be less than $\sqrt{n_e}$. The improvement in the signal's shot noise is explained by the Fano Factor and is discussed in Section 3.7.1.1.

3.6.1.2 X-ray absorption length

The absorption length, λ, is defined as "the depth into the material measured along the surface normal where the intensity of X-rays falls to 1/e of its value at the surface", [Henke, 1993]. The probability of an X-ray event interacting at a depth x in a material is given by the Beer-Lambert law:

$$P(x) = \frac{1}{\lambda} e^{-\frac{x}{\lambda}} \tag{3.8}$$

The mean interaction point for a photon is given by its absorption length, but there will be a distribution of interaction depths around this mean value (Figure 3.21).

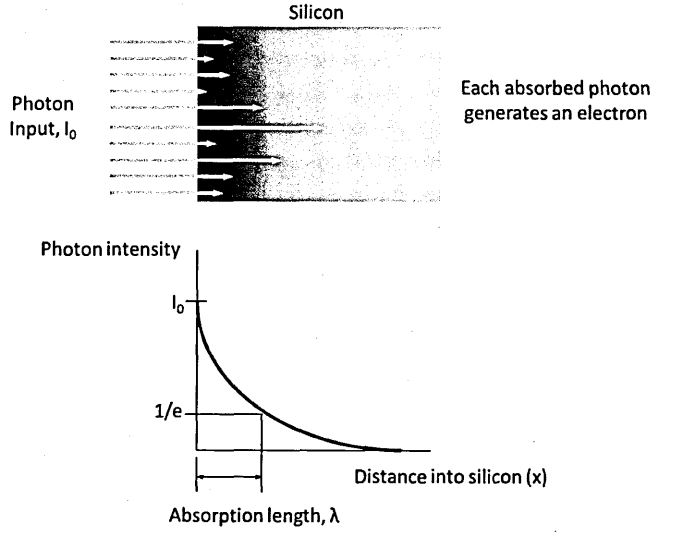

Figure 3.21: The absorption length (1/e depth) into silicon.

The mean position that the X-ray interaction will occur in silicon can be predicted from the energy of the incident X-ray. The higher the energy of the X-ray, the further into the device, on average,

the interaction will occur. However, the silicon atoms interacting with the X-rays preferentially absorb photons of energy equal to the transition energy of its electron shells. The silicon L series absorption shells have a transition energy of ~100 eV causing X-rays of this energy to be preferentially absorbed into the silicon. At an energy of ~1800 eV, which is equal to the K series transition energy, there is also preferential absorption in the silicon. The absorption profile for X-rays in silicon at increasing energy is shown in Figure 3.22 [Henke, 1993].

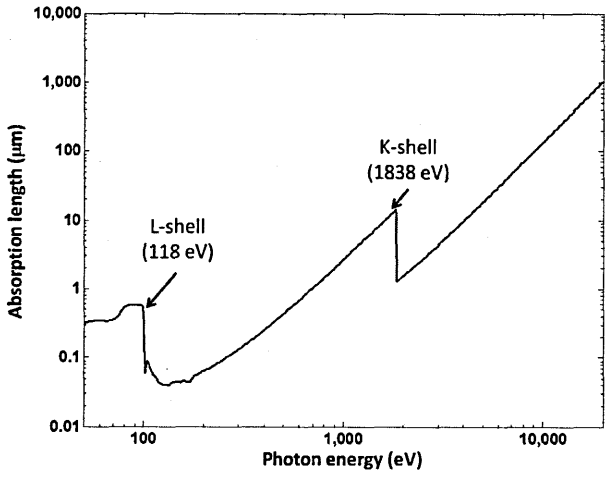

Figure 3.22: Absorption length of X-rays in silicon between 50 eV and 20 keV showing the K and L-shell absorption lines [Henke, 1993].

Figure 3.22 shows that a 1000 eV photon has an absorption length approaching 10 μm; therefore, this is the average depth at which the photons will interact with the silicon. The actual interaction position varies according to the probability function in Figure 3.21 and so to detect all of the 1000 eV photons, silicon thicker than the absorption length is required.

At 150 eV, the average X-ray interaction depth from Figure 3.22 is ~50 nm. Manufacturing a CCD that is able to detect photon interactions so close to the surface is technically difficult due to the geometries of the electrode structures and will be discussed in Chapter 4.

3.6.2 Depletion, diffusion and charge splitting at energies < 1000 eV

The use of back-illuminated CCDs for low energy X-rays detection brings a new problem. The charge cloud is generated close to the back surface of the device and has to travel through the active silicon before it can be collected in the buried channel and read out. A standard e2v back-illuminated device is ~40 μm thick and the initial photon interaction will occur within 1 μm

of the back-surface for X-ray energies <700 eV (Figure 3.22). When the charge generated by the photon in the silicon moves through the device towards the buried channel, it can diffuse isotropically outwards away from the point of interaction. If the charge cloud has a significant amount of silicon to drift through before it reaches the buried channel, the probability of the charge being split across several pixels in the silicon increases, a phenomena known as charge splitting, with the events being called "split events" [Lumb, 1990], [Bootsma, 2000], [Tsunemi, 2005]. The longer it takes for the charge to be collected in the buried channel the larger the final charge cloud. The amount of time that it takes for the charge to be collected is determined by the thickness of the silicon and the electric field strength at the photon interaction position. Thick devices with small depletion depths will allow large charge clouds to form, leading to an increase in split events (Figure 3.23).

Splitting the charge across several pixels degrades the energy resolution of the CCD as the charge has to be recombined through "off-chip" binning to reconstruct the charge cloud and have complete charge collection of the initial X-ray generated charge. "Off-chip" binning contributes a component of readout noise to the signal for each summation that occurs, thus increasing the FWHM of the X-ray spectral peaks and degrading the spectral resolution. Complete charge collection for small charge clouds split over several pixels is difficult as small signals can be easily lost in the noise [Lumb, 1990].

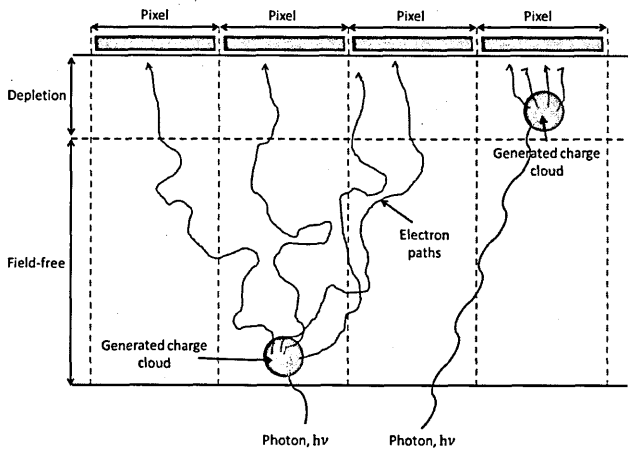

Figure 3.23: Two charge clouds interacting at different depths into the silicon. The charge clouds are able to diffuse further if they are generated in the free-field region of the active silicon producing split events.

If the X-ray interaction occurs in the depleted silicon, the charge is quickly collected in the buried channel and the charge is less likely to diffuse isotropically to form split events. The increase in charge cloud size in the field-free region of the silicon (in terms of charge cloud FWHM) is approximately equal to twice the depth of field-free silicon the charge-cloud has to travel through [Bootsma, 2000], [Janesick, 1987]; therefore, a charge cloud that travels through 10 µm of field-free silicon will have a FWHM when it reaches depletion of ~20 µm plus the original charge cloud size (Figure 3.24).

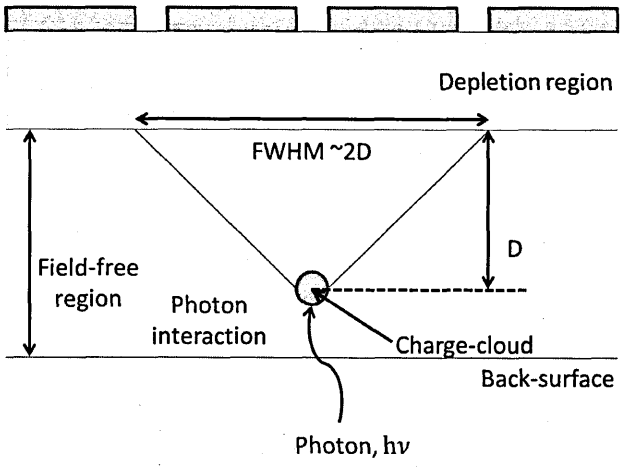

Figure 3.24: The increase in charge cloud size when the photon interaction occurs in the field-free region of the active silicon is shown. The charge cloud's size (FWHM) will increase to approximately twice the thickness of the field-free region it drifts through.

One way to reduce the split events would be to increase the electric field across the device and hence increase the depleted depth of material. The charge that is generated by photon interactions in the depletion region is quickly collected in the buried channel of the CCD making it unlikely that the charge will split. The depth, x_p, that the depletion stretches into the CCD can be found using Equation 3.9 [Howes, 1979], where ϕ_{CH0} is the empty buried channel potential (V), ε_{Si} is the permittivity of silicon (1.03 x10^{-12} F cm^{-1}), q is the electronic charge (1.60 x10^{-19} C) and N_A is the silicon acceptor donor concentration (cm^{-2}). By having a lower acceptor doping concentration (higher resistivity - Figure 3.25) or by having a larger buried channel potential the depletion will be deeper in the silicon.

$$x_p = \sqrt{\frac{2\phi_{CH0}\varepsilon_{si}}{qN_A}} \tag{3.9}$$

The buried channel potential can be increased by clocking with a higher potential on the gate electrodes or by reducing the substrate voltage. The voltages that can be used in e2v devices are limited by gate protection diodes that will trigger when the potential gets too large (normally around 17 V [Jerram, 2011]) in order to protect the device from a large current flow that could cause damage; therefore, deep depletion devices are made of low doping or high resistivity material (small N_A). The relationship between doping level and resistivity is shown in Figure 3.25.

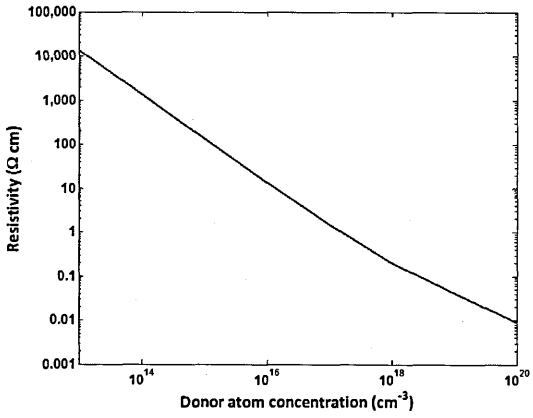

Figure 3.25: The relationship between donor atom concentration and resistivity. The higher the resistivity, the further the depletion will be driven by the clock potential.

Standard devices made by e2v have a resistivity of at least 100 Ω cm while "deep depletion" devices have a minimum of 1500 Ω cm [Lumb, 1990]. e2v also manufacture high-rho CCDs where the device can be "over-depleted" increasing the size of the depletion region and reducing the number of split events. These devices have a resistivity of greater than 3000 Ω cm [Murray, 2008].

A second way to reduce the number of split events is to have larger pixels by changing the pixel architecture or through "on-chip" binning. On-chip binning is the process by which the charge in adjacent pixels can be summed on the CCD in the charge domain, avoiding the addition of the extra component of readout noise that occurs with off-chip binning. The binning artificially forms larger "pixels", increasing the chances of the charge being collected by a single "pixel" which causes an improved energy resolution. Larger pixels will cause the CCD to have poorer spatial resolution as the point of the photon interaction will be uncertain.

3.6.3 Partial events

When detecting photons, charge can be lost to the back-surface generation/recombination centres at the Si-SiO_2 interface, Figure 3.26.

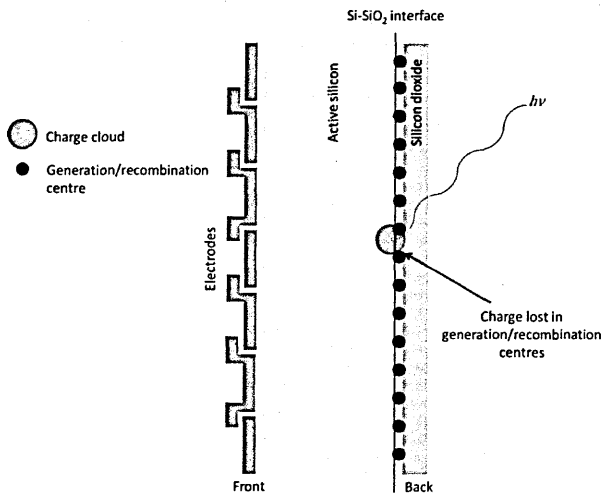

Figure 3.26: A charge cloud created at the Si-SiO_2 interface loses part of the charge to the interface generation/recombination centres.

Events that have lost charge due to these centres are termed "partial events". A partial event can occur when an X-ray interacts with the active silicon close to the back surface of the device generating a charge cloud that overlaps the passivated region, causing a proportion of the charge to be lost through recombination. The result is a reduction of the amount of charge and the charge cloud appears to have been generated by a photon of lower energy [Bootsma, 2000].

To minimise this effect, the dead-layer at the back-surface of the device needs to be as thin as possible. There are several ways to achieve this and they are discussed in Chapter 4. Partial events are usually only seen when detecting low energy photons as the interaction is close to the Si-SiO_2 interface.

Partial events can be seen if the device is operated back or front-illuminated. If the charge interacts in the silicon close to a Si-SiO_2 interface (these occur at the front and back of the device) then charge can be lost creating a partial event. Where the charge is lost is dependent on the energy of the photon and whether the device is being operated as a front or back-illuminated CCD.

3.7 Signal-to-Noise performance

Noise in a CCD is any addition to the signal that is read out from the device. It is a non-deterministic component and can take many forms. Several methods have been developed to minimise its effect.

3.7.1 Shot noise

Shot noise is the random fluctuation in the number of electrons generated from a source. For a mean of n_e electrons generated per optical photon interaction, the shot noise is Gaussian and characterised by a standard deviation of $\sqrt{n_e}$. Using the quantum yield of silicon, it is possible to predict the mean number of e-h pairs that will be generated in the charge packet [Janesick, 2001]. The noise is inherent in photon detection and so sets the theoretical limit on the possible spectral resolution of the device.

3.7.1.1 Fano Factor

In 1947, Fano showed that if single photons produced charge clouds that contain several electrons, the distribution of the number of electrons generated by the interaction would have a narrower FWHM than predicted by Poisson statistics [Fano, 1947]. The reduction is due to the co-dependence between the electrons generated from a single X-ray photon. A significant number of electrons are produced per photon interaction across the X-ray band in silicon and so the majority of these electrons are generated through impact ionisation. Each new electron is ionised from a silicon atom through this impact, so there is one less electron in the lattice to add to the charge packet. The number of electrons in the silicon is much larger than the X-ray interaction can produce, but the reduction in the number of available electrons for ionisation constrains the total number of electrons that can be produced by the interaction. The probability of generating the mean number of electrons expected from an X-ray interaction is higher than for single e-h pair production, causing the observed narrowing of the produced X-ray peak [Lumb, 1990].

The Fano factor, f, describes the reduction of the shot noise of the system, which is dependent on the material that is used to detect the photons and the photon energy. The factor has been

shown to have a slight variance with energy, but this effect is small over the energy range discussed in this thesis [Perotti, 1999]. The narrowing of the measured X-ray peak FWHM is shown in Figure 3.27.

The Fano Factor also increases the Signal-to-Noise Ratio (S/N) of the detected signal in comparison to the optical case for the same signal size due to a smaller shot noise on the input signal; however, if readout noise is the dominant noise contribution, this reduction in noise will have a small overall effect on the S/N.

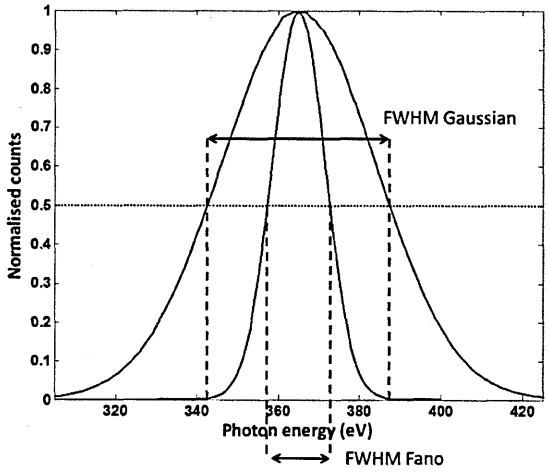

Figure 3.27: The narrowing of the shot noise peak for X-ray detection in silicon that is described by the Fano Factor.

The S/N is the ratio of the amount of generated signal to the size of the noise. If a device is used to detect both optical and X-ray photons and is cold, the readout noise can be considered to be the same in each case and the signal is equal to the number of electrons (n_e). This gives a simplified signal to noise ratio as shown in Equation 3.10, where $\alpha = 1$ for inputs where one photon generates one e-h pair (optical) and $\alpha = f$ for X-ray inputs. The result shows that, as $f < 1$, X-ray interactions have a higher S/N than optical interactions, for the same n_e, by a factor f which is equal to ~0.12 for X-rays in silicon [Lumb, 1990].

$$\frac{S}{N} = \frac{n_e}{\sqrt{\alpha n_e}} = \frac{\sqrt{n_e}}{\alpha} \tag{3.10}$$

3.7.2 Dark signal

Dark signal is the generation of electrons and holes in the silicon without a photon interaction and hence dark. The process occurs due to thermal mechanisms in the silicon and, as discussed in Section 3.3.1, mid-band traps have to exist in the silicon to enable the thermal energy in the lattice to excite electrons across the band gap. A mid-band trap is a defect in the silicon that can "trap" an electron between the valence and conduction band making thermally generated electrons more likely. The effect increases the background on the signal affecting the S/N of the device and it is an effect that would ideally not occur or be suppressed. The electrons are then collected as normal in the device and read-out. It is possible to suppress dark signal generation through the reduction of the temperature of the CCD, thus lowering the energy available to assist the thermal generation mechanism [Kittel, 2005].

The number of electrons excited into the conduction band through thermal interactions is generally expressed in units of "per pixel per second". If N electrons are generated per pixel per second then the dark current per pixel is given by $\frac{Nq}{t}$, or can be given as $\frac{Nq}{At}$ per cm^2, giving a measure of performance for the device that can be easily compared to that of other devices, where q is the electronic charge, t is the integration time and A is the pixel area. The dark current per pixel in an image can be reduced by decreasing the frame rate through increasing the readout speed.

A second method for dark current generation is from the Si-SiO_2 interface in the device. The structure of the silicon does not match the structure of the oxide, leaving "dangling bonds" that act as generation/recombination centres in the silicon. The generation/recombination centres generate electrons that are added to the charge packet, increasing the dark signal. The effect can be suppressed through cooling the device; however, it is also possible to clock the CCD in "inverted mode" while the device is still warm in order to reduce thermal electron generation, as discussed in the next section.

The final stage of the CCD manufacture process is a hydrogen passivation where the CCD is placed in a hydrogen atmosphere. The hydrogen bonds to the dangling bonds at the Si-SiO_2 interface, reducing dark signal generation; however, the passivation will dissipate over time resulting in an increase in dark signal.

When the CCD is operated at temperatures below -80 °C, the dark signal is sufficiently suppressed such that its effects can be largely ignored (< 1 e^-/hour/pixel) [Flora, 2005].

3.7.3 Inverted mode clocking

In order to suppress dark current generated at the Si-SiO_2 interface the device can be clocked in inverted mode. By increasing the substrate voltage on the CCD, holes accumulate at the front-surface of the CCD, suppressing the dark signal generated at the interface and allowing the device to be run warmer for the same dark signal as a non-inverted device (Figure 3.28). However, inverted mode clocking reduces the full-well capacity of the potentials in the device and the depletion depth [Bogaart, 2009].

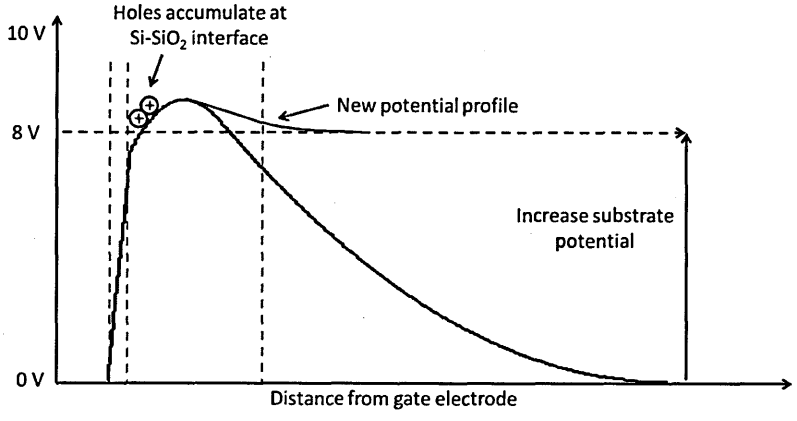

Figure 3.28: Increasing the substrate potential causes the CCD to become pinned with holes being trapped at the Si-SiO_2 interface.

3.7.4 Clock-Induced Charge

Clock-induced Charge (CIC) is the generation of electrons through the impact ionisation of holes with the silicon lattice as the CCD gate electrodes are clocked. The generated electrons add to the charge packet increasing the noise on the detected signal [Denvir, 2003].

CIC shows some temperature dependence as cooling the device causes an increase in the chance of impact ionisation as the phonons in the silicon lattice have less energy, reducing the possibility of collisions between these phonons and the holes. Fewer phonon collisions increase the probability of electrons being generated by impact ionisation; however, this effect is small [Sze, 1981]. CIC is most common when the device is run in inverted mode because, in inversion, the surface traps are empty of electrons and these traps then re-fill as the device goes into depletion. Going from inversion to depletion creates a high electric field in the silicon between the electrodes and as the holes cross the high field inter-electrode region, they are accelerated and impact ionisation can occur leading to the release of an electron [Janesick, 2001].

To avoid CIC, a CCD can be operated cold in non-inverted mode to reduce the build-up of holes under the gate electrodes. If the device requires to be operated in inverted mode, then it is possible to implement image area clocks that operate from negative to positive voltages causing the device to be inverted at 0 V on the gate electrodes. Clocking the device this way reduces the size of the electric field formed in the device when going from inversion to depletion, and CIC is reduced. It is not always possible to clock the serial register this way, especially in an EM-CCD (Section 3.8), but as the bulk of dark current generation will be from the image area, inverted mode clocking can still be beneficial. A final method of reducing CIC is to have longer rise and fall times on the clock edges. Slower clock transitions cause the change in electric field to be less abrupt, reducing the probability of impact ionisation occurring [Janesick, 2001].

3.7.5 Reset noise

To read out a photon generated charge packet, it is moved onto a capacitive output node that has been recharged to a set level determined by its bias voltage, commonly referred to as VRD (Section 3.5.3). The output node has to be reset to this level for each pixel that is read out and this is achieved through a reset clock operation; however, the level to which the output node is reset is not constant and there is a thermal fluctuation on the reset level of the device [Johnson, 1928]. The possible variation in the reset level in a pixel is shown in Figure 3.29. To

remove reset noise, CCD readout electronics can use Correlated-Double Sampling (CDS) [White, 1974].

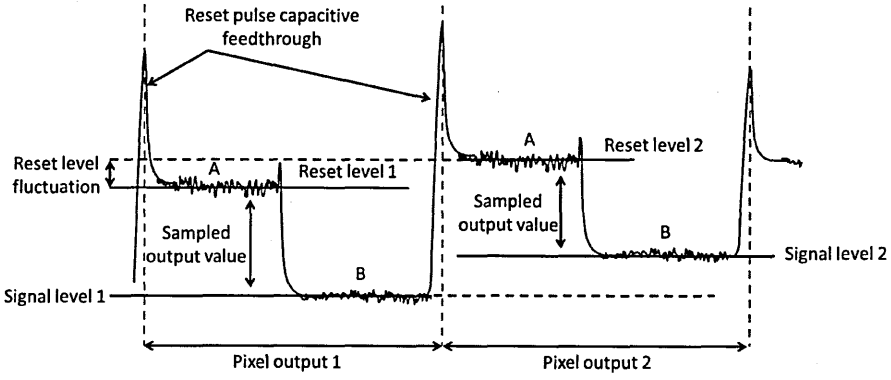

Figure 3.29: An exaggerated example of two pixels read out from a device. The different height of the reset level is indicative of reset noise.

The CDS method samples the pixel output after the reset pulse to measure the reset level (Position A in Figure 3.29). A corresponding measurement is then taken in the second half of the pixel output to determine the amount of charge in the pixel (Position B in Figure 3.29). The two main methods of CDS used in CCDs are "Clamp and Sample" and "Dual Slope Integration". Clamp and sample takes a sample of the charge after the reset pulse and again when the charge has been added to the output node capacitor, taking the difference to calculate the signal level. Dual Slope Integration takes an average of the signal for a set time period, *intT*, after the reset pulse and again after the charge has been read out (Points A and B in Figure 3.29 respectively) (Figure 3.30). During the first *intT*, charge is negatively integrated onto an op-amp integrator and then positively for the second period. The resulting charge stored on the integrating op-amp is the signal.

Dual slope integration CDS is able to minimise the effect of thermal fluctuations in the electronics and high f noise spikes, as it averages the signal over time. The larger *intT*, the lower the noise from thermal fluctuations.

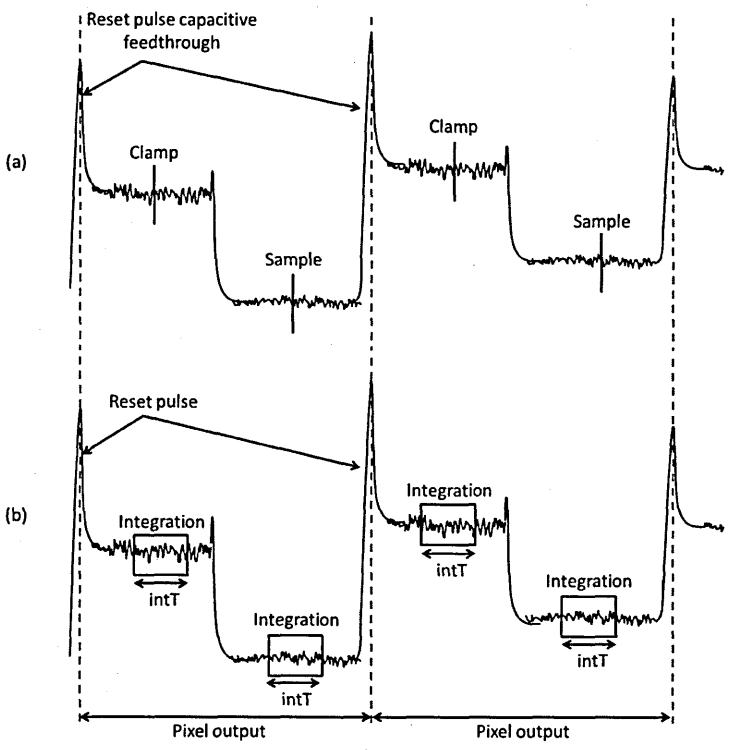

Figure 3.30: Pixel output (a) shows the positions of the measurements taken in clamp and sample CDS. The clamp is taken on the reset level of the pixel output and the sample is taken once the charge on the output node has been read out. Pixel output (b) shows the period of time that the signal level is integrated in dual slope integration CDS (*intT*).

3.7.6 Readout noise

Readout noise is caused by the random thermal motion of electrons in the output circuit that gives rise to a fluctuation in the output voltage. Electrons moving through a circuit collide with the lattice and have a thermal motion that causes thermal noise (or white noise), described by the Brownian motion of carriers. The noise was quantified by Johnson and Nyquist in 1928 (Equation 3.11), where W is the r.m.s. noise voltage (V), k is Boltzmann's constant (1.38×10^{-23} J K^{-1}), T is the absolute temperature (K), R is the resistance of the conducting path (Ω) and B is the equivalent frequency bandwidth or noise power bandwidth (Hz) [Johnson, 1928], [Nyquist, 1928].

$$W = \sqrt{4kTBR} \tag{3.11}$$

The noise is a feature of electronic circuits and is represented by the fluctuating lines in the pixel's waveforms in Figure 3.30. If dual slope CDS is being used, the random fluctuations can be averaged over a long period of time. Random signals that are averaged over time tend to zero as the length of time increases making dual slope CDS an effective way of minimising thermal noise

on the signal; however, increasing the CDS timings causes the CCD to be read out more slowly and so a compromise has to be reached between noise and speed [Kozlowski, 1999]. "Clamp and sample" CDS only takes one measurement per pixel output reducing its effectiveness of removing thermal noise. Low pass filters can be used to remove some of this thermal noise, discussed in the next section, before the CDS operation as it limits the bandwidth (B) and so minimises the noise in Equation 3.11.

The output node has an inherent capacitance that affects the responsivity of the device. If the output has a high responsivity, smaller changes in signal level will be able to be detected; however, this puts a limit on the size of the signal that can be effectively read out. The detection of large signals requires a lower responsivity to increase the dynamic range and allow the signal to be detected without saturating the output node. The larger the output node, the higher the node capacitance and the lower the responsivity (Equation 3.7). A trade-off has to be made between a highly sensitive device and one that can handle large signal levels.

3.7.6.1 Low-pass filters

In CCD bias potentials, low pass-filters are used to remove high frequency noise pickup in the wiring between the CCD and the power supply unit. The low pass filter is designed to have a cut-off frequency of 70 Hz – 160 Hz so that higher frequencies are highly attenuated. The cut-off frequency can be calculated using Equation 3.12 [Horowitz, 1989]:

$$f_c(Hz) = \frac{1}{2\pi RC} \tag{3.12}$$

The use of a low-pass filter before a clamp and sample CDS circuit will cause the change in pixel output seen in Figure 3.31.

The output signal from the low-pass filter has a lower Johnson-Nyquist noise, but the settling time for the pixel output is larger due to the time constant of the filters and more time is needed for the system to reset fully. A balance is needed between the noise level and the settling time.

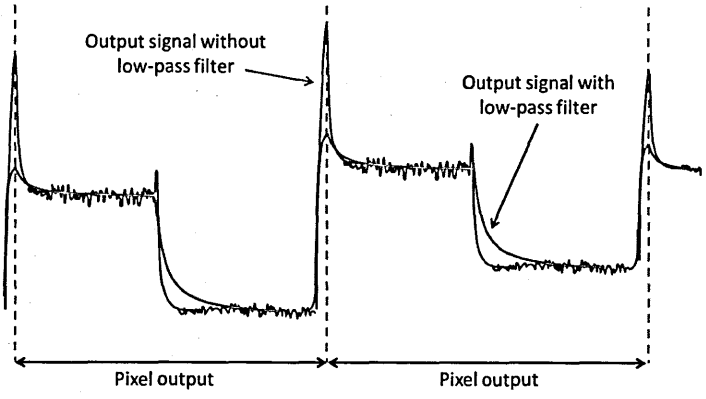

Figure 3.31: The increase in settling time in the pixel output through the use of a low-pass filter on the output waveform.

3.7.6.2 Pre-amplifier output

To increase the voltage signal read out from the CCD a pre-amplifier on the headboard can be used to amplify the signal and increase the S/N in the presence of thermal noise and electronic pick-up in the electronics.

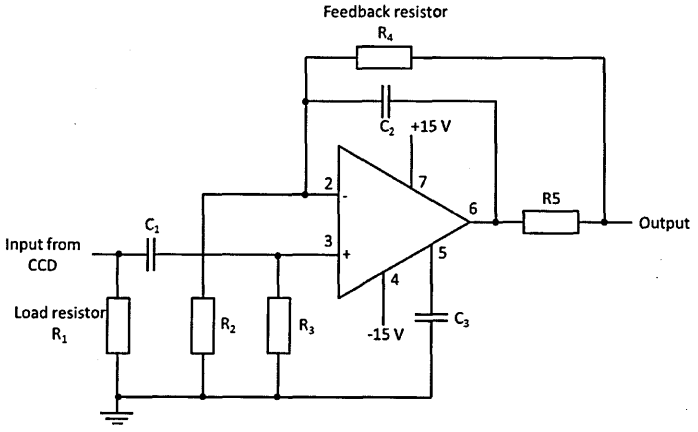

Figure 3.32: Typical simple pre-amplifier circuit for a CCD [AD829 datasheet, 2000], [Horowitz, 1989].

The serial output of the CCD is typically amplified by 11x for X-ray applications [Horowitz, 1989]. The noise effects from components in the headboard electronics are therefore reduced in proportion and effectively suppressed.

Figure 3.32 shows the pre-amplification circuit that is used which has a fast voltage response time. The external load resistor (R_1) creates the potential difference to be supplied by the CCD. The gain of the non-inverting pre-amplifier circuit can be found using Equation 3.13, with R_2 and R_4:

$$G_{pre-amp} = 1 + \frac{R_4}{R_2} \tag{3.13}$$

The resistor R_3 provides a DC path to ground for the small input current as the signal source is AC-coupled though capacitor C_1. Resistor R_5 is included for current-limiting purposes. Considering the readout schematic in Figure 3.33, the signal read out, V_s, and the noise on that signal, e_{n1}, go into a pre-amplifier.

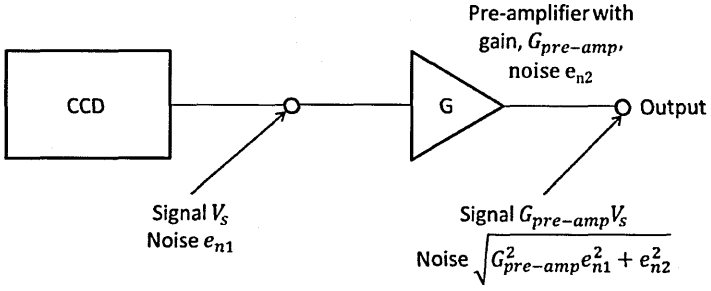

Figure 3.33: Block diagram of the readout from a CCD describe in terms of the signal, V_s, gain, G, and the noise contributions from the CCD readout, e_{n1}, and the output electronics, e_{n2}.

The S/N before the amplifier is given by Equation 3.14.

$$\frac{S}{N} = \frac{V_s}{e_{n1}} \tag{3.14}$$

The signal is then increased by the gain on the pre-amplifier and the S/N becomes:

$$\frac{S}{N} = \frac{GV_s}{\sqrt{G^2 e_{n1}^2 + e_{n2}^2}} = \frac{V_s}{\sqrt{e_{n1}^2 + \frac{e_{n2}^2}{G^2}}} \tag{3.15}$$

If the gain on the op-amp is large enough the second noise term in the denominator of Equation 3.15 becomes small and so the noise of the system is equal to Equation 3.14, showing that the gain on the pre-amplifier suppresses the noise on the output electronics.

3.7.7 Total noise

Through the optimisation of the CDS timings on the CCD readout electronics, cooling and careful clocking, it is possible to reduce the noise generated by a CCD to levels approaching shot noise when detecting large signals. To analyse the total noise on the system, individual noise sources should be considered in turn.

The number of electrons generated by the photon interaction has a shot noise, σ_{shot}, which is equal to the energy of the photon, E, divided by silicon's quantum yield ω, Equation 3.16. The noise is improved by the Fano Factor, f, when detecting X-rays (with the noise measured in electrons), as described in Section 3.7.1.1.

$$\sigma_{shot} = \sqrt{fn_e} = \sqrt{f\frac{E}{\omega}} \tag{3.16}$$

The noise on the dark signal, σ_{dark}, is a measure of the number of electrons produced per pixel per second by thermal excitations in the silicon via mid-band traps. The readout noise, $\sigma_{readout}$, is a measure of the number of electrons added to the signal through thermal fluctuations in the readout electronics, again measured in electrons.

The noise can be added in quadrature and so the total noise is given by:

$$\sigma_{total} = \sqrt{\sigma_{readout}^2 + \sigma_{dark}^2 + \sigma_{shot}^2} = \sqrt{\sigma_{readout}^2 + \sigma_{dark}^2 + f\frac{E}{\omega}} \tag{3.17}$$

The peak in the histogram of the CCD pixel values will have a Gaussian shape allowing the FWHM of the peak to be calculated using Equation 3.18:

$$FWHM = 2\sqrt{2ln2}\sigma_{total} \approx 2.355\sigma_{total} \tag{3.18}$$

A value for the combination of noises can then be found by measuring the FWHM of the photon peak. The FWHM is usually measured in eV and, to make this conversion, Equation 3.18 is multiplied by ω (the quantum yield in silicon), giving the following relation between noise the read-out signal and the FWHM of the photon peak:

$$FWHM = 2.355\omega\sqrt{\sigma_{readout}^2 + \sigma_{dark}^2 + \alpha\frac{E}{\omega}} \tag{3.19}$$

If the incident photon detected by the CCD only produces a single e-h pair per interaction then $\alpha = 1$, whereas if many e-h pairs are produced by a single interaction $\alpha = f$ (the Fano Factor).

3.8 Electron Multiplying CCDs

Electron Multiplying CCDs (EM-CCDs) take a conventional CCD and add a multiplication register after the serial register and before the output node of the device (Figure 3.34). EM-CCDs are n-channel devices as collected electrons are needed in the amplification process. The number of electrons in each charge packet is increased through impact ionisation in the multiplication register [Jerram, 2001].

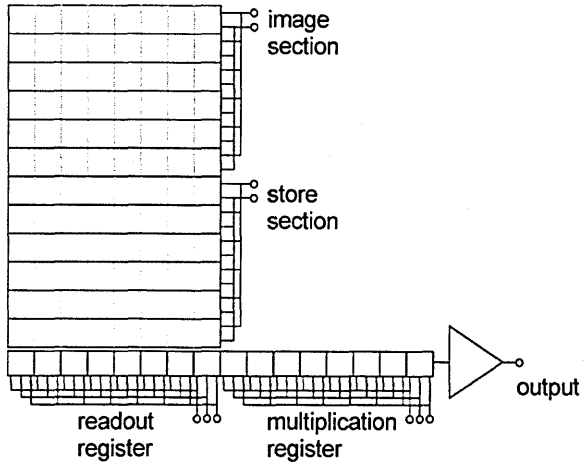

Figure 3.34: Schematic of an EM-CCD showing the multiplication register inserted between the serial readout register and the output node [Robbins, 2003].

The multiplication register contains a phase that can be clocked to a high potential (40 V – 50 V), known as Rϕ2 "High-Voltage" (Rϕ2HV). The electrons enter the high field region between the RϕDC barrier phase and Rϕ2HV and are accelerated (Figure 3.35). The accelerated electrons can ionise other electrons in the silicon lattice through impact ionisation (Section 3.3), increasing the number of electrons in the charge packet. Figure 3.35 shows the clocking scheme in the multiplication register of an EM-CCD.

The charge cloud is stored under Rϕ1 in the multiplication register (Step 1 in Figure 3.35) while the potential on Rϕ2HV is increased. To stop charge entering the Rϕ2HV phase until it has reached full potential an RϕDC phase is built into the register between Rϕ1 and Rϕ2HV. RϕDC is held at a constant low potential (~2 V) and acts as a barrier phase to the movement of the charge packet (Step 2 in Figure 3.35), but allows charge to flow when Rϕ1 is reduced to 0 V. When Rϕ2HV has reached the full applied potential, Rϕ1 is reduced to 0 V and the charge flows into

Rϕ2HV (Step 3 in Figure 3.35). Rϕ2HV is then clocked into Rϕ3 and the process repeats for all the elements in the gain register (typically ~500) [e2v, 2004].

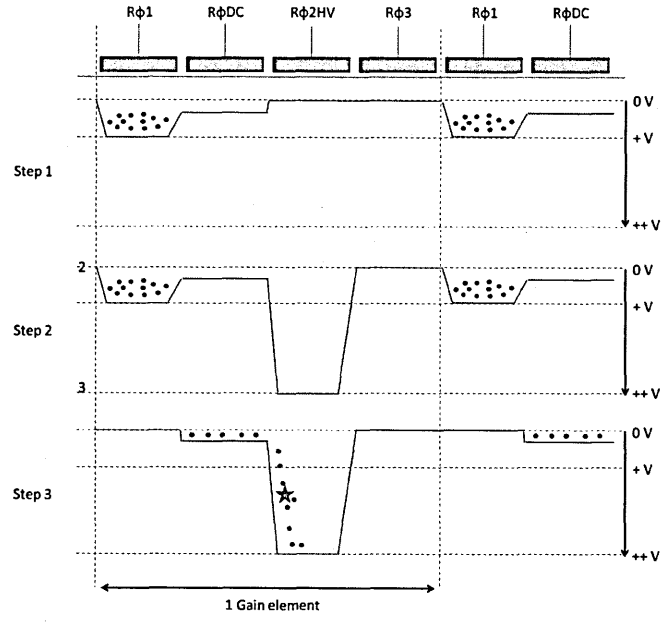

Figure 3.35: A clocking scheme showing the high potential (Rϕ2HV) and barrier potential (RϕDC) necessary to the operation of an EM-CCD. RϕDC stops the charge packet entering Rϕ2HV before it has reached full potential, maximising the chance of impact ionisation in the gain element and providing a constant field for impact ionisation in each pixel transfer.

The average gain, G, achieved by an EM-CCD is dependent on the number of gain elements in the register, N, and applied potential on Rϕ2HV. The probability of generating an additional e-h pair in a single gain element, p, and the number of elements in the multiplication register, N, gives Equation 3.20 [Jerram, 2001].

$$G = (1 + p)^N \tag{3.20}$$

Although the probability of impact ionisation occurring in a single gain element is small ($p \sim 0.015$), there are many gain elements in the multiplication register and therefore high levels of gain can be produced. For example, for multiplication registers with elements of 100, 200, 300, 400 and 500 pixels the gain is equal to ~4, ~20, ~87, ~386 and ~1710 respectively (for $p \sim 0.015$) (Figure 3.36).

The increase in signal due to the multiplication process occurs before the charge is read out from the device. Readout noise from the EM-CCD is constant regardless of signal size and so this internal amplification of the signal increases the S/N. The increase in S/N is due to the

amplification of the signal, but it can also be regarded as a suppression of noise; EM-CCDs lower the effective readout noise of an imaging system. EM-CCDs are manufactured on low resistivity silicon to increase the probability of impact ionisation at relatively small potentials. Although e2v have manufactured EM-CCDs on high resistivity silicon in the past, they required a much higher potential on Rϕ2HV to achieve the same level of gain as in a lower resistivity device which caused them to have a higher power dissipation and more complex headboard circuitry [Burt, 2012].

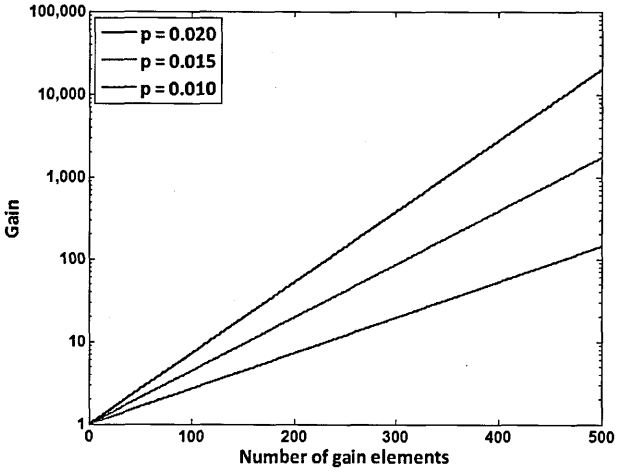

Figure 3.36: Gain register size effect on the total gain for different multiplication probabilities. The total gain on the signal increases with the number of elements in the gain register shown here for $p = 0.02, p = 0.015$ & $p = 0.01$.

3.8.1 Signal to Noise Ratio changes with photon energy and gain

The multiplication gain process is stochastic in nature and therefore the gain on the signal, as found by Equation 3.20, is an average. The noise on this signal is a function of the number of electrons in the charge cloud. The work completed by Basden et al. [2003] shows this nature of multiplication gain. The performance of an EM-CCD with a total gain of 6629 and 591 elements was predicted when there were 1, 2, 3 and 4 electrons in the charge packet. They found that the gain distribution would follow Equation 3.21, where *n* is an integer number of input photo-electrons and $p(x)$ is the probability of achieving the gain across the distribution of gain for the given photo-electron input (Figure 3.37).

$$p(x) = \frac{x^{n-1} e^{-\frac{x}{G}}}{G^n (n-1)} \tag{3.21}$$

By increasing the number of electrons, the effect on the gain distribution can be measured. The larger the number of electrons in the charge cloud, the closer to a Gaussian the gain distribution becomes. Hence with a large enough number of input electrons the gain distribution can be thought to be Gaussian giving a noise on this distribution:

$$\sigma_{gain} = \sqrt{n_e} = \sqrt{\frac{E}{\omega}} \tag{3.22}$$

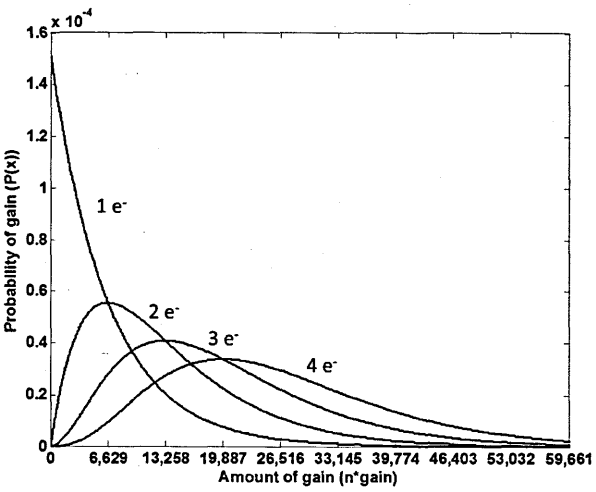

Figure 3.37: The distribution of possible levels of gain for charge cloud sizes 1, 2, 3 and 4 electrons showing that as the signal size increases the range of output signals from the multiplication register starts to become Gaussian [Basden, 2003].

If one assumes that the only noise sources in the EM-CCD are those from the readout amplifier, $\sigma_{readout}$, the shot noise on the initial photon interaction, σ_{shot}, and the noise through fluctuations on the multiplication gain, σ_{gain}, and noting that the shot noise and gain noise are equal to $\sqrt{n_e}$, for optical photons, the total noise can be given by Equation 3.23, where α is the factor acting on the incident photon generation noise (1 for optical and f for X-ray) and β is the gain factor. For devices with gain of 1, $\beta = 0$, whereas $\beta = 1$ for devices with higher levels of gain. This is an extension of the original equation for the noise in the CCD, Equation 3.17.

$$Noise = \sqrt{\alpha n_e + \beta n_e + \left(\frac{\sigma_{readout}}{G}\right)^2} \tag{3.23}$$

The signal collected in the detector is n_e and so the S/N is given by:

$$\frac{S}{N} = \frac{n_e}{\sqrt{\alpha n_e + \beta n_e + \left(\frac{\sigma_{readout}}{G}\right)^2}} \tag{3.24}$$

For large values of G ($\beta = 1$), Equation 3.24 can be simplified to:

$$\frac{S}{N} = \frac{\sqrt{n_e}}{\sqrt{\alpha + \beta}} \tag{3.25}$$

For X-ray inputs (where $\alpha = f$), the S/N becomes $\frac{\sqrt{n_e}}{\sqrt{1+f}}$ when the device is being operated with high gain, G. When $G = 1$, $\beta = 0$ for a device that detects X-rays with a small level of readout noise, the S/N is equal to $\sqrt{\frac{n_e}{f}}$ which is larger than the case with gain by a factor of $\sqrt{\frac{f}{1+f}}$. If readout noise is large enough, the case where the gain is 1 becomes more complicated. This describes the gain on the output signal from the EM-CCD; however, a more useful comparison would be of the output signal to a dark frame.

A dark frame from a cooled EM-CCD gives the readout noise from the device. By comparing it to the amplified output from the CCD the noise suppression due to the EM-CCD can be measured. The S/N described by Equation 3.24 is a measure of the fluctuations on the signal level with respect to the size of the signal, n_e. To see the effect of gain the S/N needs to be a comparison of the dark frame (readout noise) to the signal level, n_e, and is given by Equation 3.26 (Figure 3.38).

$$\frac{S}{N} = \frac{Gn_e}{\sigma_{readout}} \tag{3.26}$$

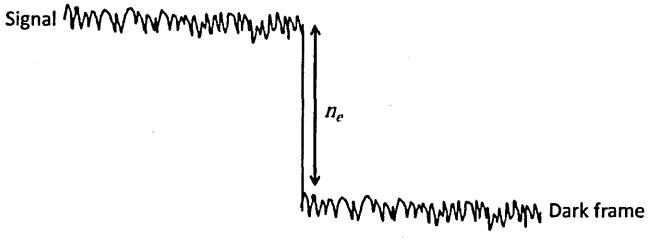

Figure 3.38: The difference between the random fluctuations of noise on a signal that multiplication gain does not suppress and the signal to background noise, which multiplication gain does suppress. The effect of gain suppressing the readout noise of the EM-CCD is found through comparing a dark reference frame with the amplified signal from the EM-CCD.

3.8.2 Excess Noise Factor for single e-h pair generation (optical) photon energies (α=1)

The gain on the detected signal is stochastic and has an associated noise that is analogous to shot noise (Equation 3.22). Adding the multiplication noise to Equation 3.16, the standard deviation of signal detected with an EM-CCD can be calculated.

$$\sigma_{total} = \sqrt{\frac{\sigma_{readout}^2}{G^2} + G\sigma_{dark}^2 + \sigma_{shot}^2 + \sigma_{multiplication}^2} \tag{3.27}$$

which, for the high gain case, σ_{shot}^2 and $\sigma_{multiplication}^2$ equal $\frac{E}{\omega}$, becomes:

$$\sigma_{total} = \sqrt{\frac{\sigma_{readout}^2}{G^2} + 2\sigma_{dark}^2 + 2\frac{E}{\omega}} \tag{3.28}$$

Robbins and Hadwen [Robbins, 2003] showed that this result for the FWHM only holds for high levels of gain (> 10x). At lower gain levels the noise on the gain amplification is lower than predicted by the Gaussian approximation, falling to zero at a gain of 1x (the case for a conventional CCD). The Noise Factor, F, is described in [Hynecek, 2001] by Equation 3.29 and, following the method described in [Robbins, 2003], allows the increase in noise on the multiplication of the signal with increasing gain to be solved analytically and tested experimentally, where σ_{out}^2 is the variance on the output signal from the CCD, σ_{in}^2 is the variance on the input signal to the multiplication register. The result is shown in Equation 3.30 and is called the Excess Noise Factor (ENF) (Figure 3.39).

$$F^2 = \frac{\sigma_{out}^2}{G^2\sigma_{in}^2} \tag{3.29}$$

$$ENF = \frac{1}{G}\left(\frac{2G + g - 1}{g + 1}\right) \tag{3.30}$$

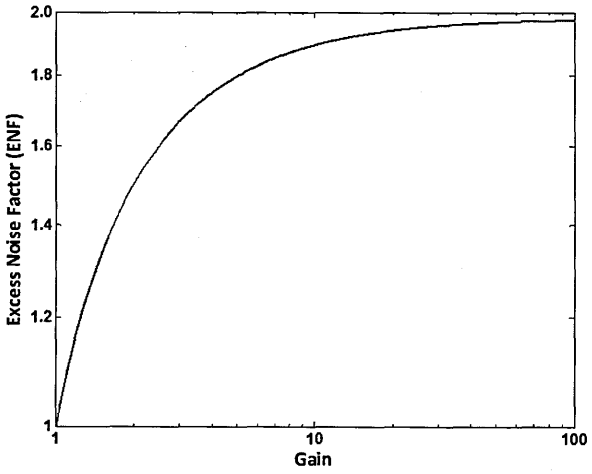

Figure 3.39: Prediction for the ENF with increasing gain. The increase in ENF with respect to gain in the multiplication register of the EM-CCD is shown at 1 with a gain of 1x to ~2 at high levels of gain (> 10x).

The result allows the FWHM of the detected photon peak to be predicted based on the energy of the incident photon and the size of the other noise sources present in the device, Equation 3.31.

$$\sigma_{total} = \sqrt{\frac{\sigma_{readout}^2}{G^2} + ENF\sigma_{dark}^2 + ENF\frac{E}{\omega}} \tag{3.31}$$

Multiplication gain improves the S/N with respect to the readout noise as the signal is amplified before it is read out. However, the Excess Noise Factor shows that there is an increase in the noise in the system due to the noise associated with the multiplication gain and the ENF also acts on dark signal as this signal is accumulated before the multiplication condition. The ENF increases the noise associated with the number of electrons in the pixel; therefore, EM-CCDs are used in Low-Light-Level environments where the shot noise is minimised.

3.8.3 Temperature dependence of multiplication gain

The gain that can be generated from an EM-CCD for a fixed potential (Rϕ2HV) is temperature dependent. The probability of additional electrons being generated by impact ionisation in the silicon is dependent on the magnitude of the phonon energy. If the phonon energy is high, the electrons are more likely to scatter off the phonons reducing the available energy to ionise further electrons [Tirino, 2003], [Sze, 1981]. Through the cooling of the silicon, the magnitude of the phonon energy falls and electrons are less likely to scatter off them, increasing the chances of impact ionisation in the multiplication register. This dependence has been measured and can be

seen in Figure 3.40 [e2v, 2004]. In order to ensure that the level of gain for a given gate potential stays constant, accurate temperature control is important.

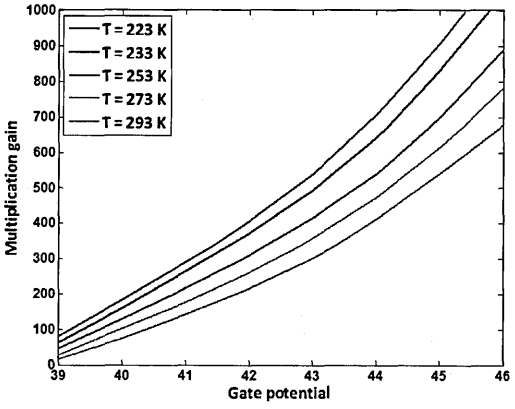

Figure 3.40: The relationship between increasing the voltage on the HV electrode in the multiplication register (gate potential) and the amount of gain is shown for different temperatures. Lower temperatures give higher levels of gain for the same amount of potential on the HV gate electrode [e2v, 2004].

3.8.4 Ageing of the EM-CCD multiplication register

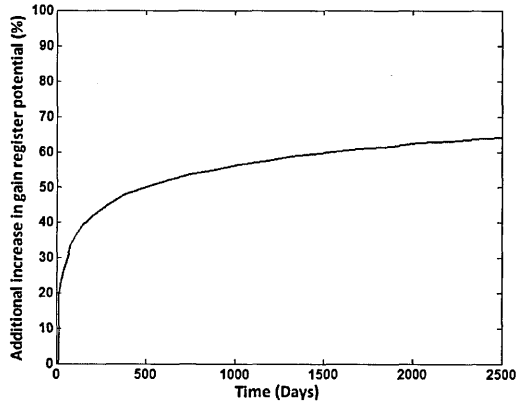

Figure 3.41: EM-CCD gain register ageing over time. The experiment was designed to keep the level of gain the same by varying the gain register potential. The change in the required potential demonstrates the ageing of the register [Evagora, 2012].

EM-CCDs are also known to experience a gain ageing effect where the amount of gain that is produced for a given potential on Rϕ2HV falls over time. The effect is most pronounced during the first few hours of running the device; therefore, e2v "burn in" the devices before they are delivered to the customer. After the initial rapid ageing the EM-CCD ages very slowly covering a 15% degradation over 2000 days (Figure 3.41); therefore, once the EM-CCD has been initially aged, the ageing effect can be largely ignored [Evagora, 2012].

3.9 Summary

Incident photons can generate electrons through the photo-electric effect and subsequently detected, with the generated signal read out from the device. Several different types of CCD electrode architecture can be used to move the charge, including two-phase and three-phase clocking. In order to produce an effective detector, the doping of the silicon has to be optimised for the specific application as the different dopants used in the CCD can affect performance. To optimise CCD performance, noise sources and their possible mitigation must be considered.

To optimise CCD performance in the work carried out in this thesis, the noise performance of CCDs and EM-CCDs must to be understood. Potential problems may occur due to the multiplication process, EM-CCD ageing, CIC and variable gain due to unstable temperature; methods of minimising the problems have previously been identified. By having a stable temperature control system and a device that has been through a "burn-in" process, ageing and gain stability can be addressed. CIC can be mitigated by not running the devices in inverted mode and by having slow clock edges.

A main theme of this thesis will be the analysis of the additional noise added to the detected signal through the multiplication process in an EM-CCD. A comprehensive understanding of this process is vital if EM-CCDs are to be considered as X-ray detectors for future soft X-ray spectrometers. The work carried out previously with respect to this noise, the Excess Noise Factor, has been reviewed allowing the adaption of the technique at X-ray energies.

Effective charge collection in CCDs is important for achieving the best spectral performance. With the detection of soft X-rays, charge collection is challenging and so the effect of incomplete charge collection must be understood allowing mitigation strategies to be implemented in experiments, such as larger pixel device, on-chip binning and large depleted regions in the active silicon.

Chapter 4: QE Improvements for soft X-ray detection

4.1 Introduction

Back-illuminated CCDs were developed in order to produce devices that had a higher X-ray Quantum Efficiency (QE) than front-illuminated CCDs for photons of low energies (<700 eV, Figure 3.22). Quantum Efficiency is a measure of the detection efficiency of a device and is given by the percentage of incident photons that are actually detected. This chapter will look in greater detail at the difference between the front and back-illuminated devices, as well as how back-illuminated CCDs are manufactured and the processes of back-surface passivation that have been developed to maximise their low energy performance.

4.2 Quantum efficiency model

To evaluate the difference between back and front-illuminated devices, a model simulating the two different types of device was made by the author in MATLAB as part of the work for this thesis. The model takes the linear attenuation coefficients, μ, of the materials of which the CCD is composed over a range of X-ray energies and uses this information to evaluate how much of the incident radiation, I_0, at each energy reaches the active silicon [Henke, 1993]. The value for μ varies with energy, are found using [Henke, 1993] and are shown for Si, SiO_2 and Si_3N_4 in Figure 4.1.

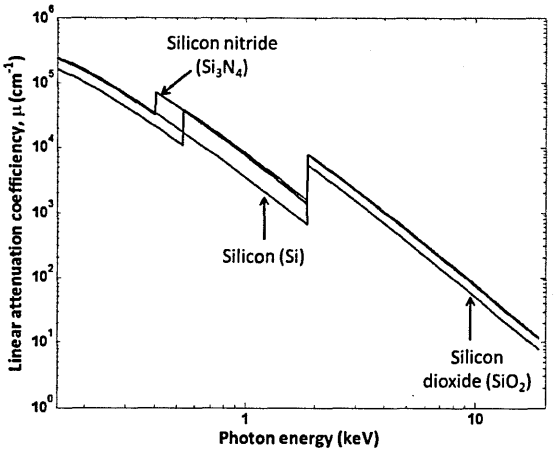

Figure 4.1: Linear attenuation coefficients of the different materials found on a CCD. The K-shell edges of nitrogen (399 eV), oxygen (523 eV) and silicon are shown (1740 eV) [Henke, 1993].

It is assumed that if the photons reach the active silicon they are detected. The thicknesses of material on the surface of a front-illuminated device were taken from Table 4.1. The native oxide on the surface of the back-illuminated device was assumed to be 5 nm [Morita, 1990], [Samson, 2000] and the dead layer caused due to the passivation of the back-surface was measured using a SIMS technique. With this information it is possible to use Equation 4.1 to predict the intensity of the incident radiation, I_0, that reaches a depth x into the device.

$$I = I_0 e^{-\mu x} \tag{4.1}$$

Using Equation 4.1 and the linear attenuation coefficients of the material in a CCD yields the Equation 4.2 for QE, where x_{dSi} is the depth of the active silicon in the device and x_{Si}, x_{SiO_2} and $x_{Si_2N_4}$ are the thicknesses of the polysilicon gate electrode, the combined depth of the SiO_2 layers and the silicon nitride dielectric respectively.

$$QE = \left(1 - e^{-(\mu_{Si} \cdot x_{dSi})}\right) \cdot \left(e^{-(\mu_{Si} \cdot x_{Si})} \cdot e^{-(\mu_{SiO_2} \cdot x_{SiO_2})} \cdot e^{-(\mu_{Si_3N_4} \cdot x_{Si_3N_4})}\right) \tag{4.2}$$

For a back-illuminated device, the gate electrodes do not have a probability of absorbing the incident photon and therefore Equation 4.2 leads to Equation 4.3, where x_{deadSi} is the dead layer between the native oxide and the active silicon generated through the passivation process discussed in Section 4.4.1. These two formulae are the basis of the plots produced for the QE in this chapter.

$$QE = \left(1 - e^{-(\mu_{Si} \cdot x_{dSi})}\right) \cdot \left(e^{-(\mu_{SiO_2} \cdot x_{SiO_2})} \cdot e^{-(\mu_{Si} \cdot x_{deadSi})}\right) \tag{4.3}$$

4.3 Front-illuminated vs. Back-illuminated

4.3.1 Front-illuminated CCDs

In a front-illuminated CCD, as the photons are incident on the device electrodes, they have to pass through the electrode structure before they reach the active silicon. The active silicon is above a thick substrate of heavily doped metallic like silicon that allows easy recombination of any e-h pairs that are generated in it (Figure 4.2).

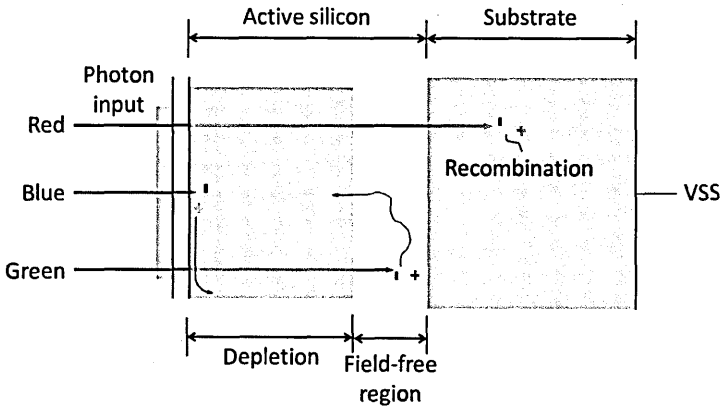

Figure 4.2: A cross-section of a front-illuminated CCD with the gate electrode shown in green and the SiO_2 and silicon nitride layers shown by the white space directly beneath the gate electrodes.

The depth that a photon penetrates into the device is dependent on the energy of the incident photon and the material the photon has to pass through. The lower energy detection limit is based on the energy of photon required for a phonon assisted transition across the band-gap and is 1.11 eV. At energies approaching this lower limit a large thickness of silicon is required to increase the probability of the photon interacting with a phonon; therefore red light penetrates further into the silicon than blue (Figure 4.2). At higher energies, the Thomson cross-section of the electrons in the silicon lattice reduces in size making collision less likely and eventually (at energies approaching 20 keV) the silicon becomes transparent to the photons. The depth of the layers that an incident photon has to penetrate in order to reach the active silicon in a typical front-illuminated device manufactured by e2v is given by Table 4.1 and shown in Figure 4.3.

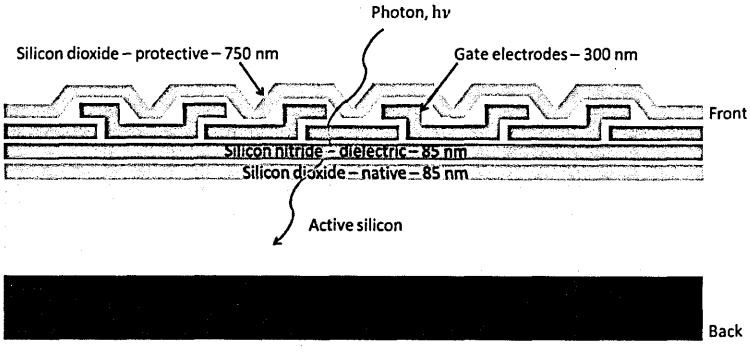

Figure 4.3: A typical front-illuminated CCD: The active silicon at the front of the device is covered by polysilicon gate electrode, a protective silicon dioxide layer and a silicon nitride dielectric (not to scale).

Table 4.1: Layers that incident X-rays have to penetrate in order to reach the active silicon in a front-illuminated device [Murray, 2008]

Layer	Thickness (nm)	Use
Silicon dioxide (SiO_2)	750	Protective layer
Polycrystalline silicon (Si)	300	Gate electrode
Silicon nitride (Si_3N_4)	85	Dielectric
Silicon dioxide (SiO_2)	85	Natural layer
Active silicon	Up to 50,000	Active material

Most X-ray applications for CCDs do not require silicon thicker than 50 μm, but this is not the case for other applications (Near Infra-Red). Using the model described in Section 4.2 the QE performance of a front-illuminated device can be predicted over a large energy range (Figure 4.4).

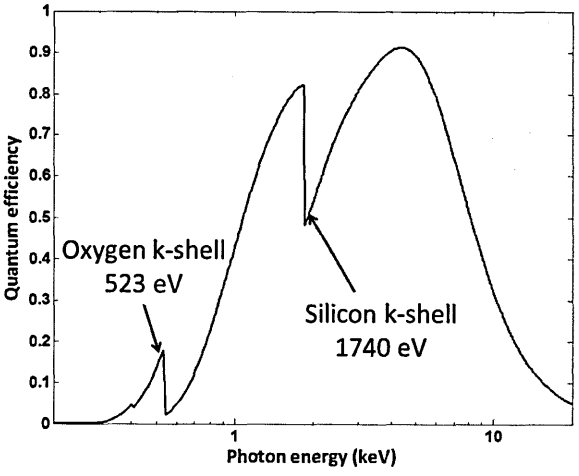

Figure 4.4: Quantum efficiency for a front-illuminated CCD over a 0.1 keV to 20 keV energy range using the values stated in Table 4.1.

Figure 4.4 shows that at energies less than 1 keV the performance of the front-illuminated devices is unlikely to be sufficient for scientific applications, as the QE is below 50%. The low QE at soft X-ray energies is one of the performance issues with front-illuminated devices that led to the development of back-illuminated CCDs. The performance of the front-illuminated CCD tails off at higher X-ray energies as the photons begin to pass through the device without interacting; the silicon effectively becomes transparent to the incident photons.

4.3.2 Back-illuminated CCDs

Back-illuminated CCDs, developed for high QE X-ray detection, are manufactured from a front-illuminated CCD that has the metallic substrate etched away, exposing the active silicon of

the device directly to the air which causes a thin native oxide to grow. The incident X-rays now only have this native oxide to pass through in order to interact in the active silicon; therefore, the QE of the device for low energy photons is potentially higher than in a front-illuminated device. There are, however, practical difficulties in realising this performance [Van den Berg, 1996].

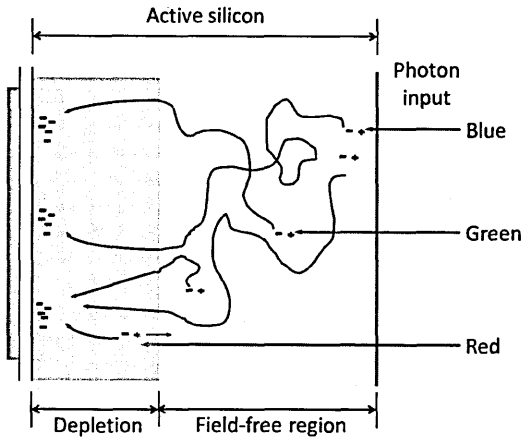

Figure 4.5: Different energy photons entering a back-illuminated device generating e-h pairs [Burt, 2011].

Figure 4.5 shows how this back-illumination approach increases the likelihood that a low energy photon will be detected in the active silicon of the device. The depletion depth, x_p, (μm) is governed by the acceptor dopant concentration, N_A (atoms cm^{-3}), the doping of the active silicon and the voltage on the gate electrodes, as shown by Equation 3.9 If the device is thicker than x_p part of the active silicon will be "field-free". Electrons that are generated in the field-free region are not affected by the electric-field in the depleted silicon and so will diffuse isotropically over several pixels and may either recombine or eventually drift into depletion leading to the X-ray events being "split" [Hopkinson, 1983]. Charge splitting can lead to problems such as incomplete charge collection and cause the energy resolution of the CCD to degrade [Van den Berg, 1996]; therefore, the section is thinned to remove the field-free region, as shown in Figure 4.6.

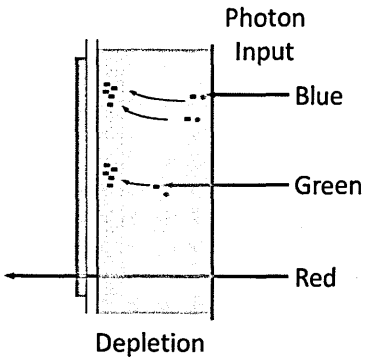

Figure 4.6: Different energy photons entering a thinned back-illuminated device generating e-h pairs.

Back thinning the CCD enables the depleted silicon to stretch all the way to the back-surface of the device, thus causing the charge to be collected faster, reducing the charge splitting, maintaining the device's energy resolution and making X-ray spectroscopy easier. However, by making the silicon thinner the upper limit on the energy of photons that the device can detect is reduced. At higher energies the X-ray photons will pass through the device without interacting. It is therefore necessary to make the device thick enough to suit the application, but not having too large a field-free area of active silicon. The depletion in the device can also be engineered to extend further into the device, allowing thicker devices to be used without sacrificing energy resolution through increasing the silicon's resistivity (Section 3.6.2).

The native oxide that grows over the back surface of the device is relatively thin compared to the electrode structure on the front of the device [Morita, 1990]; the QE of the device at low energies is improved over the front-illuminated device. Using the model in Section 4.2 it is possible to make predictions about the device's quantum efficiency over the same energy range as before (the thickness of the active silicon is taken to be the same in the front and back-illuminated devices) (Figure 4.7).

Figure 4.8 shows a comparison between the front and back-illuminated device over the "soft" X-ray energy range. With increasing energy, the performance of the back and front-illuminated devices coincide.

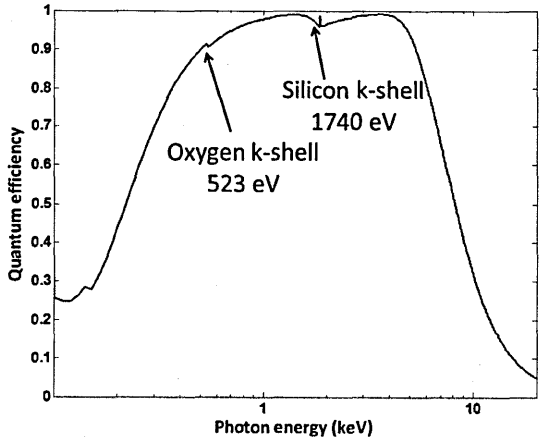

Figure 4.7: Quantum efficiency for a back-illuminated CCD over a 0.1 keV to 20 keV energy range using Equation 4.2 and the values stated in Table 4.1.

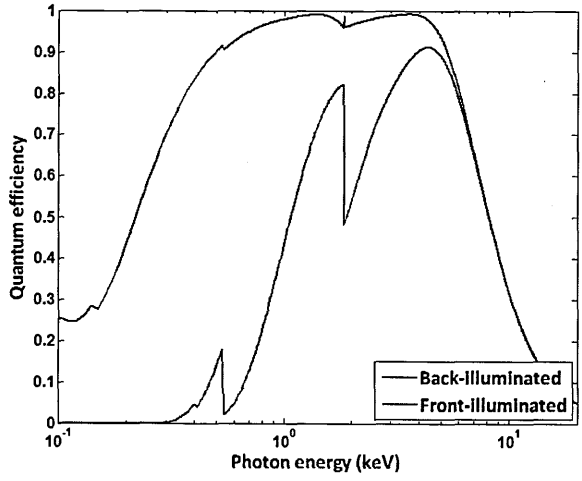

Figure 4.8: Quantum efficiency for a back-illuminated compared to a front-illuminated CCD over a 0.1 keV to 20 keV energy range using the values stated in Table 4.1.

The benefits of using a back-illuminated device over "soft" X-ray energy ranges can be seen; however, back-illuminating a CCD causes the formation of an accumulation region where generated signal can be lost, that has to be passivated through the introduction of a p^+ (highly p-type doped) "dead-layer".

4.4 Accumulation and back-surface passivation

The accumulation region that is formed close to the surface of a back-illuminated CCD affects the photon detection performance requiring this region to be suppressed through a passivation process [Amelio, 1971].

Back-illuminated CCDs have their substrate etched to minimise the thickness of silicon that the charge has to travel through before it is collected in the buried channel. Thin silicon reduces charge splitting between pixels; therefore, improving energy resolution. Once the substrate has been etched away a native oxide will form on the surface [Morita, 1990]. In silicon CCDs this layer is made up of silicon dioxide (SiO_2); however, the creation of this Si-SiO_2 boundary leads to the formation of generation/recombination centres or traps at the interface, due to the mismatch between the bonds. The centres cause additional energy states within the band-gap that allow photo-generated signal close to the back surface to recombine, reducing the UV and "soft" X-ray response [Janesick, 1985]. The native oxide also has an inherent positive charge that leads to an accumulation region being created at the surface of the CCD, drawing electrons towards the generation/recombination centres at the Si-SiO_2 interface [Amelio, 1971], [Nikzad, 1994], (Figure 4.9), resulting in a significant loss of QE.

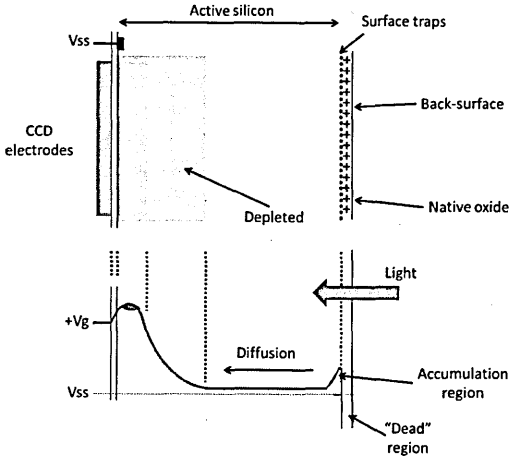

Figure 4.9: The variation of potential in a device with distance from the surface in a back-illuminated CCD. At the back-surface an increase in the potential profile is created due to the inherent charge of the native oxide.

To stop photo-generated signal from being lost at the interface states, the back-surface of the CCD is passivated. The process creates a p^+ layer on the back-surface of the device, altering its properties. Essentially, a potential step is put into the back-surface that acts as a barrier to electrons diffusing towards the generation/recombination centres, sweeping the charge towards the buried channel, causing a reduction in the amount of recombination and improving the device's QE. Any interactions that occur in this p^+ layer, or closer to the back-surface, will be unable to overcome this potential barrier and therefore will be lost to the

generation/recombination centres. The thin strip of p^+ material at the surface of the CCD is referred to as a "dead" layer and it should be as thin as possible [van den Berg, 1996] (Figure 4.10).

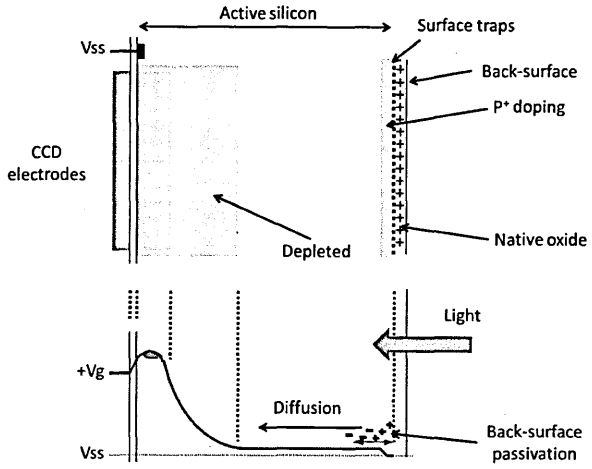

Figure 4.10: The potential in a device varies with distance from the front surface in a back-illuminated CCD. The increase in back-surface potential has been nullified through its passivation with a boron implantation.

4.4.1 Passivation processes

There are three main methods of back-surface passivation that are used commercially: chemisorption, ion implantation and Molecular Beam Epitaxy (MBE).

4.4.1.1 Chemisorption

Chemisorption techniques aim to neutralise the positive charge, acting to minimise the chance of electrons recombining through the introduction of a negative charge into the silicon dioxide layer. One way of achieving this is through a "UV flood" as shown in Figure 4.11 [Janesick, 1985], [Lumb, 1990].

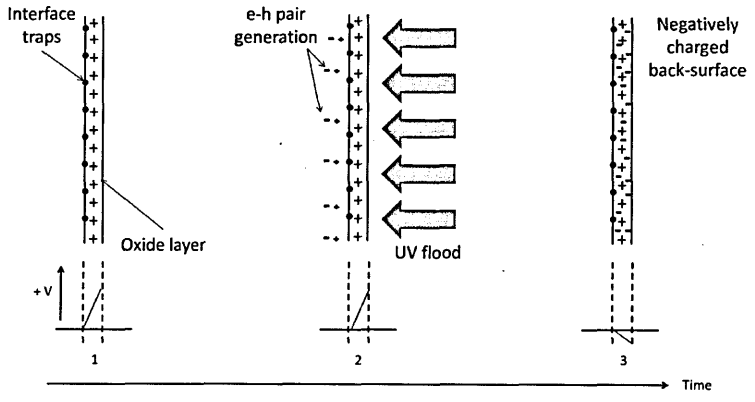

Figure 4.11: The effect of a UV flood on the potential at the back-surface of a CCD.

Exposing the back-surface of the CCD to a UV light source creates high-energy e-h pairs close to the Si-SiO_2 boundary. The electrons drift into the SiO_2 causing an oxide charging effect. Negative charge builds up in the oxide, which is then able to repel any generated electrons. The electrons are unable to reach the generation/recombination centres at the Si-SiO_2 boundary allowing them to be collected in the buried channel, increasing the QE of the device.

The chemisorption technique has two major issues. The first is that the UV charging is not permanent. Due to the proximity of the generation/recombination centres at the Si-SiO_2 interface, the electrons that neutralise the oxide layer will eventually be lost to these centres, causing the oxide to lose its negative charge. The CCD will have to be re-charged several times over its lifetime, leading to the second problem. The way the UV charge is implemented means it is impossible to repeat the charging in exactly the same way each time, producing a variation in the QE of the device, requiring time consuming recalibration.

The other techniques of back-surface passivation aim to replicate the level of passivation generated by chemisorption, but with greater stability over time.

4.4.1.2 Ion Implantation

The process of ion implantation creates a region of silicon close to the back-surface that has a higher boron doping level (p^+) than the rest of the device (p^-) (Figure 4.12).

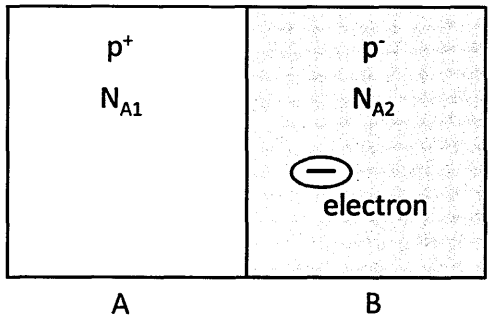

Figure 4.12: Two areas of silicon with different levels of doping. Section A, in this case, has a higher boron concentration (p^+) than section B (p^-).

In a semiconductor the number of majority change carriers, n, multiplied by the number of minority charge carriers, p, is constant and equal to the intrinsic carrier concentration, n_i, squared (1.08×10^{10} cm^{-3} for silicon at room temperature) [Hook, 1974]:

$$n.p = n_i^2 = constant \tag{4.5}$$

The doping concentration in a material, N_{A1} and N_{A2} in Figure 4.12, is equal to p; therefore:

$$n_1 N_{A1} = n_2 N_{A2} = n_i^2 \tag{4.6}$$

Rearranging Equation 4.6 gives:

$$n_1 = n_2 \frac{N_{A2}}{N_{A1}} \tag{4.7}$$

By introducing different doping concentrations into the silicon, the charge carrier concentrations will vary and affect the movement of photo-generated electrons in the silicon. The probability of the electron in *B* going into *A* in Figure 4.12 is proportional to $\frac{N_{A2}}{N_{A1}}$. If the doping concentration in section *A*, N_{A1}, increases, as the concentration in section B, N_{A2} remains constant, the number of majority carriers in section A falls and the number in section B rises and the probability of the electron moving from section *A* into section *B* reduces. The effect can also be analysed in terms of potentials, as will be shown later (Figure 4.21).

Figure 4.13 shows that the collection probability in the device can be considered to be 100% in the p^- layer, subsequently falling to zero at the silicon/silicon dioxide interface. To get the best possible QE from the back-surface it is important to minimise the value of t (depth that the boron implant penetrates into the silicon).

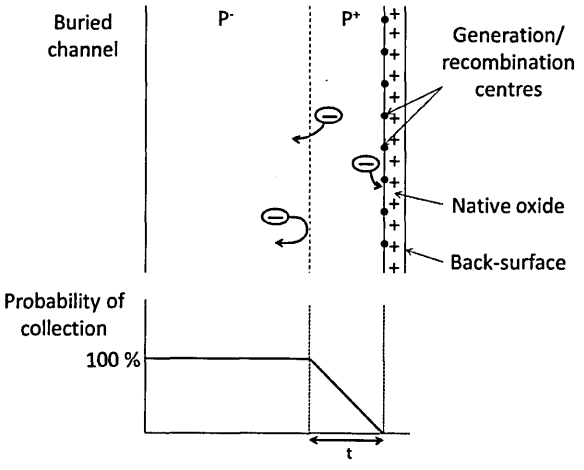

Figure 4.13: The effect of the increase in doping on generated electrons and the effect that it has on the probability that the charge will be collected by the buried channel in the CCD. The closer the interaction occurs to the generation/recombination centres the lower the probability of the electrons being detected.

The thickness of the p^+ layer, t, is ~0.05 μm and this is referred to as the "dead layer"; however, the collection probability in the p^+ layer increases with distance from the back-surface, and so the surface is not "dead".

To form the p^+ passivation layer in a back-illuminated CCD, e2v uses an ion implantation process called a "laser doped anneal" which follows these steps:

1. Boron atoms are incident onto the back surface of the CCD to implant them into the silicon. The energy of the atoms determines the average depth that the atoms will penetrate into the silicon which is the dominant contribution to the thickness of the "dead" layer. The process used by e2v to passivate the back-surface implants boron at 10 keV
2. The back surface of the device is rapidly melted using a UV laser pulse (λ = 248 nm, 30 ns pulses) to provide a shallow anneal. Boron has a high diffusivity in liquid silicon and as the silicon cools and re-crystallises the boron atoms are incorporated into the silicon lattice forming the passivation layer.

Ion implantation, while not as effective as chemisorption in terms of minimising the size of the p^+ layer, is relatively cheap and allows the passivation of multiple CCDs at one time with a permanent solution. However, as it is an ion implantation process there is an element of lattice damage associated with the implantation and this can create non-uniformities in the back of the device and create additional generation/recombination centres and defects in the silicon lattice. The thickness of this passivation layer is of the order 50 nm, but it is possible to do a selective etch on the back-surface of the device to make this layer thinner and so improve the low energy QE of the CCD (UV energies). The boron concentration with depth in a CCD with a thinner p^+ layer is shown in Figure 4.14. The surface contamination seen in Figure 4.14 is caused by the sputtering of the CCD surface when the Boron concentration was measured.

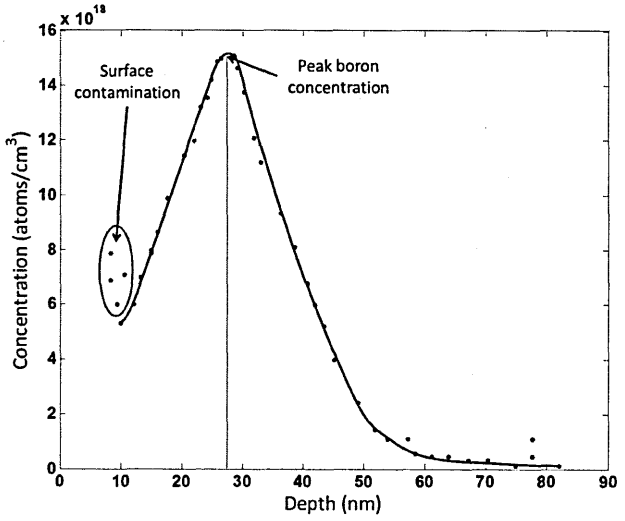

Figure 4.14: Measurement of boron concentration vs. depth made by e2v for the enhanced process back-surface passivation technique discussed later in section 4.4.1.3 [Endicott, 2010].

An earlier technique, originally developed by EEV and the Dutch Space Agency, SRON (Stichting Ruimte Onderzoek Nederland) for use on the CCDs for XMM-Newton, was to form the dead layer using Gas Immersion Laser Doping (GILD). GILD passivates the surface of a back-illuminated CCD with a thin boron implant (50 nm – 100 nm from the surface) in order to improve the soft X-ray response of the detectors [Bootsma, 2000]. GILD is implemented through the following process:

- The CCD is held in an atmosphere consisting of diborane gas (B_2H_6) and a pulsed KrF excimer laser (λ = 248 nm) is stepped over the CCD in order to dissociate the diborane gas and melt a very small layer into the silicon.
- The atomic boron penetrates into the molten silicon by liquid phase diffusion and the dopant is introduced as far as the melt depth.
- The profile of the boron doping is determined by the laser energy [van den Berg, 1996].

The GILD process is able to produce back-illuminated CCDs with dead layer of ~50 nm, but as the CCD has to be in a diborane atmosphere, it takes longer to process multiple CCDs compared with ion implantation techniques, but there is no un-annealed lattice damage created as the boron atoms do not require activation. The GILD process was only possible on a single device at a time and so has been superseded by the ion implantation technique.

4.4.1.3 Ion Implantation enhanced process

To improve the soft X-ray performance of back-illumination, e2v enhanced their ion implantation process using a technique called "anodic etching". Electrolytic techniques are used to force a thicker than normal layer of SiO_2 to form on the back-surface. In order for the SiO_2 to grow in size, silicon from the device has to be oxidised causing the SiO_2 layer to grow into the device. The SiO_2 layer can then be selectively etched away, reducing the size of the p^+ layer in the silicon. The amount of oxide that is grown can be predicted, but if too much of the silicon is etched away the passivation layer can be removed. When the etch is complete a native oxide will again form on the back surface.

4.4.1.4 Molecular Beam Epitaxy (MBE)

Molecular Beam Epitaxy (MBE) is a process used at the Jet Propulsion Laboratory (JPL) in California to pacify the surface of a back-illuminated CCD. The process has been called "delta-doping" due to the sharply-spiked dopant profile that is created in the epitaxial layer, [Hoenk, 1992]. Figure 4.15 is produced by analysing the potential step that is introduced into the silicon through the growth of a boron layer (changing the doping concentration). It is found by solving Poisson's equation for each point in the silicon.

The conduction band edge in silicon is 1.11 eV and so this energy is equivalent to zero potential in the silicon. MBE is used to grow a 2.5 nm layer of boron-doped silicon on the back-surface of a fully-processed, thinned CCD (Figure 4.16) [Nikzad, 1994].

The delta-doped layer that is grown on the device (Figure 4.16) is indistinguishable from the original lattice causing the density of defects at the substrate-epilayer interface to be small. A possible problem with this method is that the silicon deposition is performed by electron beam evaporation, which produces ~6 krad of X-ray radiation; however, this is below the damaging level for the CCD and no increase in dark current or Charge Transfer Inefficiency (CTI) is seen. X-ray damage normally manifests itself after an exposure of ~100 krad [Magorrian, 1988].

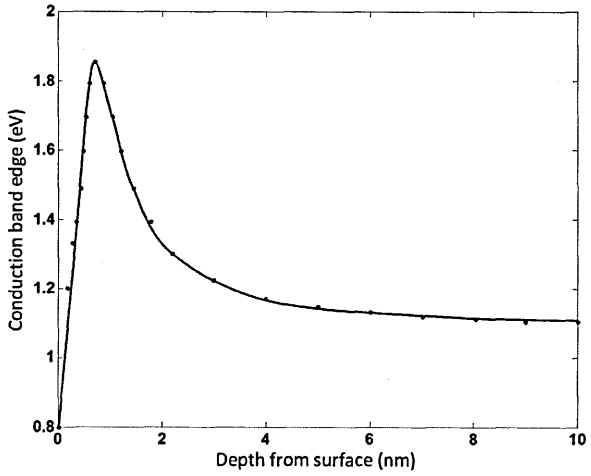

Figure 4.15: The conduction band edge energy is shown as a function of distance from the back surface of the device for a back-illuminated CCD that has been delta-doped with the peak being ~5 Å from the back-surface [Hoenk, 1992]

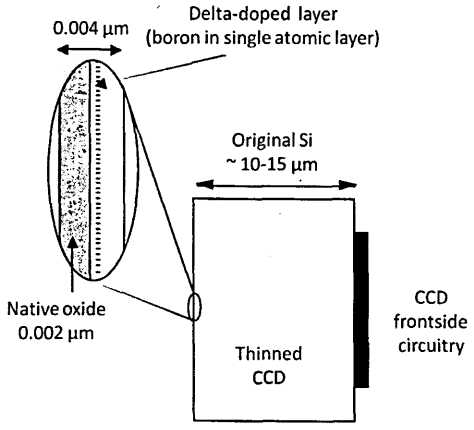

Figure 4.16: Surface of back-illuminated CCD after it has been Delta-doped with approximate dimensions given [Nikzad, 1994].

Delta-doping is the most effective method for back-surface passivation due to the thin dead-layer created [Westhoff, 2009]; however, it is costly to implement and only shows a benefit in QE over a narrow energy range in the UV due to the photon's absorption length at these energies being very close to the surface of a back-illuminated CCD.

4.5 Measuring the surface passivation for an e2v CCD97

In order to characterise the size of the p^+ layer boron implantation of an Anti-Reflection (AR) coated, back-illuminated e2v CCD97, the author took a sample to Ceram in Stoke-On-Trent. The EM-CCD was placed into a Secondary Ion Mass Spectrometer (CAMECA IMS 4F) that used an oxygen ion beam to sputter the surface of the device (Figure 4.17).

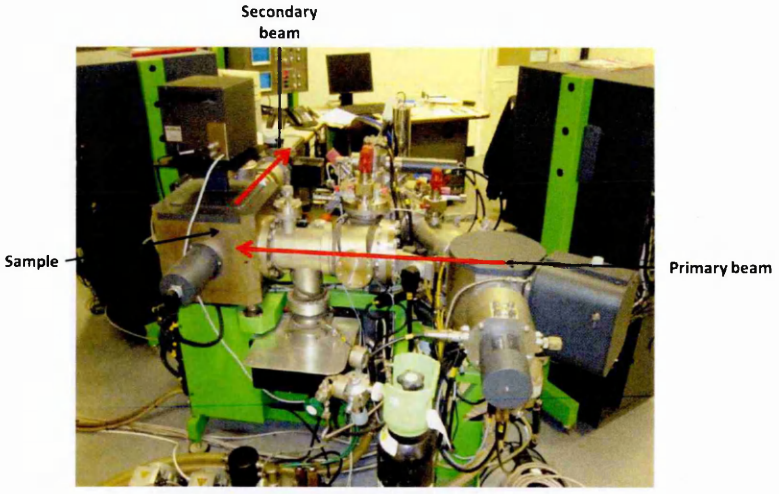

Figure 4.17: The CAMECA IMS 4F at Ceram used for the back-surface measurements.

The ions that were ejected from the CCD surface as a result of the ion beam were collected and, using a silicon sample of known boron concentration (1.648 $x10^{19}$ cm^{-2}) as a reference, the amount of boron in the silicon was measured. The known sample was calibrated using a NIST standard [Henke, 1993]. The instrument can detect boron concentrations at the parts-per-billion level. The ion beam sputtered the silicon at a constant rate allowing the depth at which the samples were taken to be calibrated using a depth profiler (stylus profilometer). The stylus is swept across the trench made by the ion beam and the vertical and horizontal positions are measured allowing the trench profile to be found (Figure 4.18).

The SIMS used an oxygen ion beam in order to reduce the ionisation potential of the boron and silicon, reducing the energy needed to produce the secondary ions. Two measurements of the back-surface were taken with different ion beam potentials: the first had a beam potential of 5.5 keV and the second had a beam potential of 3.1 keV. The lower the beam potential, the longer it takes to sputter the surface allowing higher resolution data to be taken.

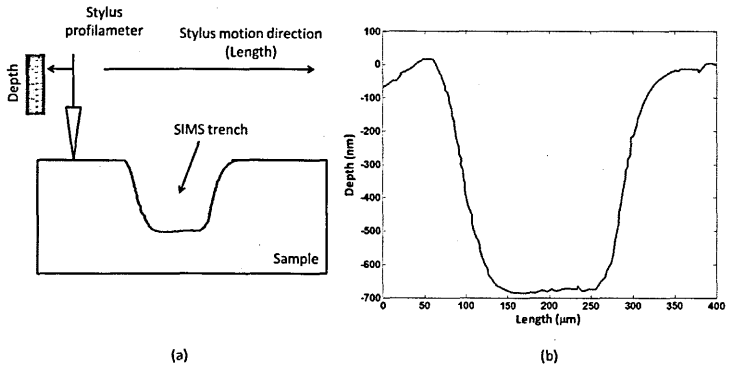

Figure 4.18: (a) Schematic of stylus scanning across the SIMS trench (b) the resulting profile of the trench from which the trench depth can be found.

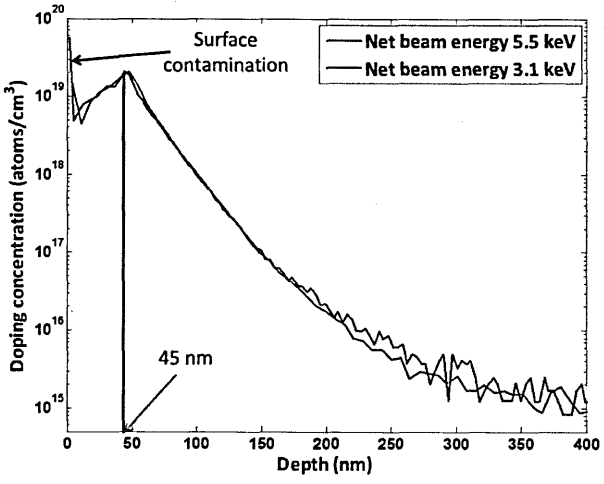

Figure 4.19: The doping profile on the back-surface of the e2v CCD97 at different beam potentials.

The two back-surface boron concentration plots, Figure 4.19, show that the peak boron concentration in the device is ~2 x10^{19} atoms cm^{-3} compared to the bulk doping level of 10^{15} atoms cm^{-3} which represents a significant increase in the doping level of the silicon. The dead layer is shown to be equal to ~45 nm in this device; however, the CCD is coated in a layer of hafnium oxide and there is some surface contamination that is making the size of the dead layer appear to be larger than it would be if the CCD was uncoated. Removing the effects of the contamination allows the position of the peak boron concentration to be estimated (Figure 4.20).

Figure 4.20 shows the dead layer extending ~40 nm into the CCD back-surface which is larger than the modelled value in Figure 4.14, but Figure 4.20 shows the result for an EM-CCD with AR coating. The device has a thicker dead-layer than predicted as it is not designed for high QE X-ray detection.

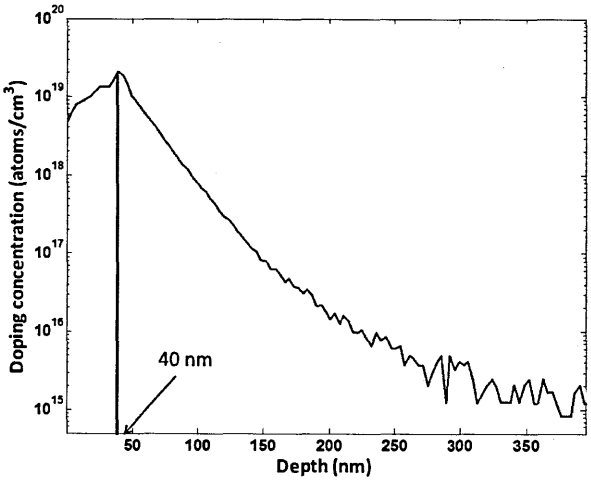

Figure 4.20: The high resolution doping profile plot with the surface contamination and hafnium oxide AR coating removed.

Through the use of the Poisson equation and the SILVACO TCAD programme, it is possible to turn this doping profile into the potential seen at the back surface of the device in comparison to the MBE result shown in Figure 4.15 (Figure 4.21). The y-axis is shown in terms of the potential in the silicon, not the conduction band edge.

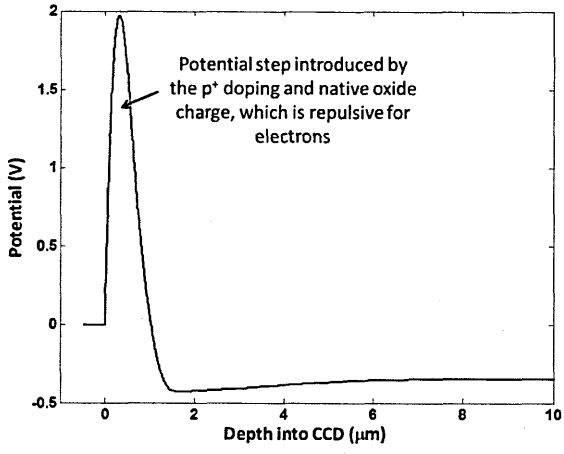

Figure 4.21: Potential step introduced to the surface of a back-illuminated CCD through the ion implantation technique with the peak potential occurring at ~40 nm. The plot is derived from the doping concentrations measured with the SIMS (Figure 4.20).

4.6 Summary

Back-illumination was developed to produce CCDs with high QE across UV and soft X-ray energy ranges. Back-illumination removes the gate electrode structure from the path of the incident radiation, reducing the thickness of material that incident X-rays has to travel through to reach the active silicon. The resulting devices have higher levels of interaction in the active silicon but,

due to the inherent positive charge of the native oxide that grows on the exposed back-surface, electrons are lost in the back-surface generation/recombination centres causing QE to fall. Back-surface passivation was developed to anneal the effect of the native oxide and so maintain the high QE possible with back-illumination. Various methods have been designed to achieve the necessary passivation with the devices used in this thesis passivated through ion implantation. When a device is passivated using ion implantation, a thin p^+ dead-layer is created close to the back-surface of the CCD that reduces QE at low soft X-ray energies; however, this layer is necessary to passivate the device.

Chapter 5: X-ray detection in the laboratory

To characterise the performance of CCDs in the laboratory requires equipment that allows the device to be cooled under vacuum and illuminated with X-ray photons. The following chapter will describe the equipment used in the laboratory, the data analysis techniques required when X-ray photon counting and the CCDs used in this thesis will be introduced.

5.1 Laboratory equipment

5.1.1 Electronics

To operate CCDs in a laboratory, each device requires a set of dedicated headboard electronics controlled using a drive electronics system, providing the clock voltages and bias potentials for the CCD and to sample the output. A "USBREM Scientific Camera System" [Holland, 2008] from XCAM™ was used to supply the USB interface to a PC, the CDS functions (in this case a 16-bit dual slope integration CDS card), the clock drive potentials and the biases (Figure 5.1).

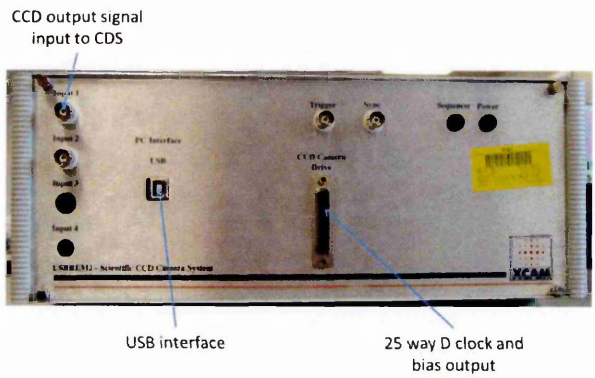

Figure 5.1: XCAM box used to control the CCD inputs and perform CDS on the CCD output.

5.1.2 Experimental chamber, vacuum equipment and cooling system

To reduce the dark signal in CCDs, they are cooled to suppress the dark current (preferably colder than -80 °C). To achieve this, the CCD has to be under vacuum to avoid ice build-up on its surface. Cooling was provided by a MegaTech™ Poly-Cold Compact (PCC) compressor and CryoTiger™ head and a Pfieffer™ Turbo pump is used to obtain a vacuum of order 10^{-5} mbar (Figure 5.2).

Inside the vacuum chamber, the CryoTiger™ head is coupled to the CCD ceramic to provide the cooling, through a copper braid from the CryoTiger™ head (made from nickel) to a copper

baseplate. A copper cold-finger and nylon support studs are then attached to the baseplate to provide cooling and support to the CCD package (Figure 5.3). The CCD is held in place using a 10G clamp [Tufnol datasheet, 1994] that has an open region to allow illumination of the active area of the device (Figure 5.4).

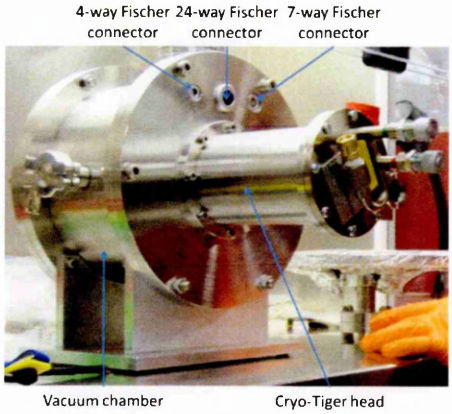

Figure 5.2: Vacuum chamber with CyroTiger™ head attached and camera head flange in place.

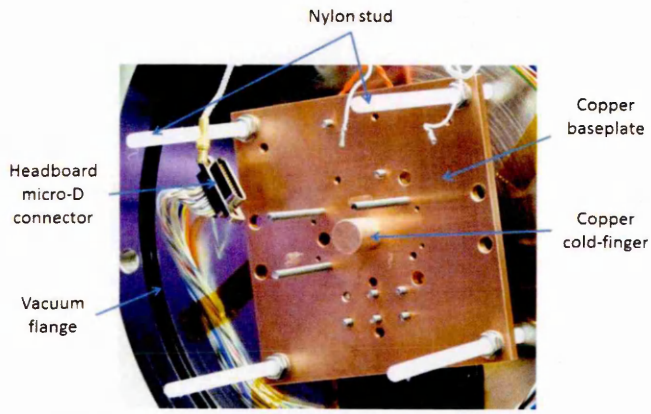

Figure 5.3: Baseplate and cold finger supported on the chamber flange with nylon stud.

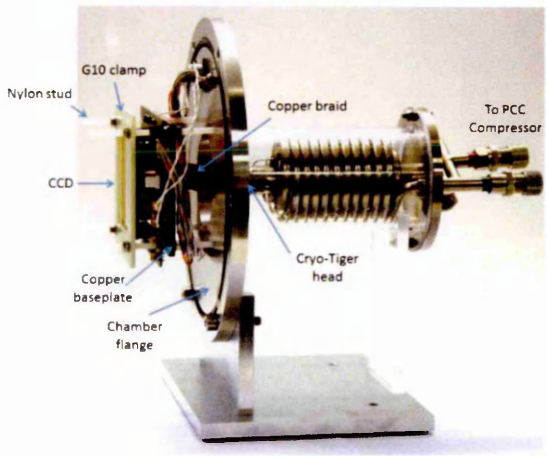

Figure 5.4: Chamber flange with a CryoTiger™ head coupled to the CCD ceramic via a copper braid, baseplate and cold-finger. The CCD is held in place with Nylon stud and a 10G clamp.

5.1.3 X-ray sources

To test the CCDs at soft X-ray energies (300 eV to 10000 eV) the equipment has to be able to generate these photons. Described below are the two main ways in which X-rays are generated in the laboratory.

5.1.3.1 ^{55}Fe

^{55}Fe is an unstable isotope of iron with 26 protons and 29 neutrons in its atomic nucleus. It decays via electron capture to ^{55}Mn with a half-life of 2.737 years [Audi, 2003]. The vacancy in the K-shell created by the electron capture is filled by an electron from a higher energy electron shell. The difference in energy between the two shells is then emitted from the atom by either Auger electrons of 5.19 keV (60% probability), K-alpha X-rays at 5.9 keV (24.4% probability) or K-beta X-rays with an energy of 6.49 keV (2.85%). The remaining 12% probability of emission is accounted for by lower energy Auger electrons and photons from other minor transitions [Esam, 2003].

Placing an ^{55}Fe source in the chamber with the CCD allows X-rays of a known energy (5898 eV K_α and 6490 eV K_β) to be incident onto the CCD with a very low background signal allowing high precision measurements of the device's performance. The sources used in the laboratory are of reasonably low activity (19 kBq) allowing individual photons to be easily measured with a typical exposure time of 1/10th second.

5.1.3.2 X-ray tube

To generate a larger range of energies than is possible with an ^{55}Fe source, an X-ray tube can be used with a variety of target materials. A tungsten filament and a target are sealed in a vacuum. By passing a potential through the tungsten filament, electrons are generated and they are accelerated towards the target by placing a potential difference between the filament and the target. The number of electrons produced is dependent on the current that is passed through the filament and the maximum energy is dependent on the potential applied (Figure 5.5).

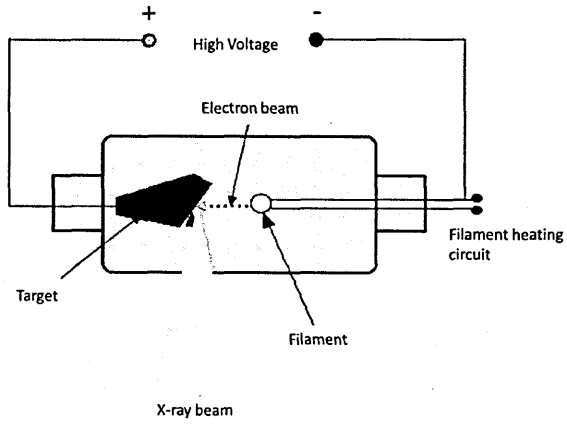

Figure 5.5: The inside of an X-ray tube with the electrons generated by a tungsten filament being accelerated by a potential into a target where X-rays are generated. Higher potentials allow higher energy electron transitions to be fluoresced (depending on the target material).

The accelerated electrons are incident on the target, creating a large amount of thermal energy [Brown, 1975]. The X-ray tube can generate photon emission in two possible ways:

The first is through the electron being deflected by the nucleus of an atom within the target material. The deflection changes the electron's direction and causes it to lose kinetic energy through the emission of a photon of energy determined by the unknown direction change. The electron then continues through the target until it is deflected by another atom and emits another photon of unknown energy, causing it to slow further. Radiation generated by this method is called Bremsstrahlung from the German for *brems* (brake) and *strahlung* (radiation) [Young, 1996]. The energy of the photon produced is dependent on the position of the electron and the atomic nucleus; therefore, Bremsstrahlung produces a continuum of energies up to the maximum energy provided by the potential between the filament and the target [Knoll, 2000] with the peak occurring at approximately 1/3 of the maximum energy (Figure 5.6).

The second method of photon generation, known as X-ray fluorescence, occurs after an incident electron directly displaces an orbital electron in the target atom. The displaced electron is replaced by an electron from a higher energy electron shell and the difference between the energy of these shells is emitted as an Auger electron or X-ray photon. The energy of the released photon is characteristic of the atomic element that the electron was released from due to the uniqueness of the binding energy of the atom [Bearden, 1967]. The X-rays generated from the

target travel into the chamber where they fluoresce a second target. Through the use of a specific target in the chamber the fluorescence lines produced can be tailored to the experiment.

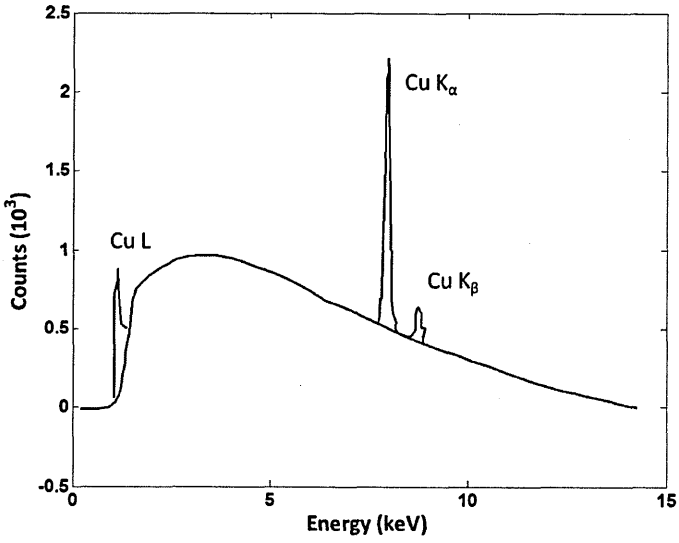

Figure 5.6: X-ray tube spectrum with a copper target showing the Cu K and L shell emissions (red) with a Bremsstrahlung background (blue).

Figure 5.6 shows the X-rays produced by fluorescence on the Bremsstrahlung background emission for a copper target. The K-shell emissions (K_α and K_β) are clearly visible at 8047 eV and 8904 eV with the L-shell emission visible at 928 eV but with a much lower fluorescence yield than the K_α emission (~8%) [Krause, 1979].

The X-ray tube has a high background signal due to Bremsstrahlung; however, if a target wheel is used in the chamber to change the target material, its tuneable flux and X-ray energy can make it ideal for testing the CCD at multiple energies without having to remove it from the vacuum chamber.

5.2 The CCDs used in this thesis study

Two different types of CCD were used in the work of this thesis. The first were conventional back-illuminated CCDs that are defined here as devices that operate without internal gain and the second were EM-CCDs that incorporate a multiplication gain register.

5.2.1 Conventional CCDs

5.2.1.1 e2v CCD30-11

The CCD30-11 is a 256 row by 1024 column array CCD with 26 μm x 26 μm pixels. It is back-illuminated with no AR coating to maximise quantum efficiency at soft X-ray energies. The device is 3-phase in parallel and serial transfer directions and the output circuit has source follower architecture (Section 3.5.3) [e2v, 2006].

Two different types of CCD30-11 were used in the course of this work. One was an enhanced back-surface process CCD and the other was made using the standard back surface process.

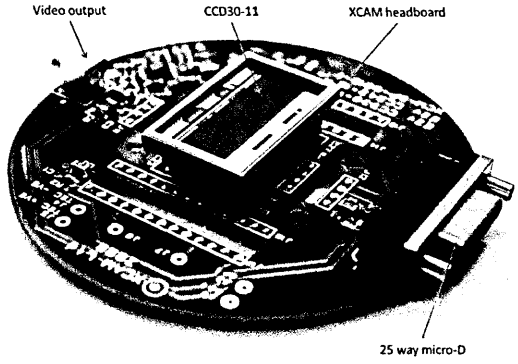

Figure 5.7: A CCD30-11 on the XCAM headboard. The 25 way micro-D interfaces the clocks and biases and the MCX jack the video output.

The headboard for the CCD30-11 (Figure 5.7) was designed by XCAM, and follows the same design as headboards shown later in the chapter (Section 5.2.1.2).

The devices were manufactured on deep depletion silicon (~1500 Ω cm) allowing the depleted region to extend close to the back-surface of the device. Charge was integrated on the device with 2 phases held at high amplitude (11 V) during integration, reducing the number of split events in the collected data.

5.2.1.2 Hamamatsu CCD S717-090N

The Hamamatsu S7170-0909N is a 512 row by 512 column array CCD with 24 μm x 24 μm pixels. It is mounted in a window frame style package so that it can be operated both front and back-illuminated and has no AR coating in order to maximise the quantum efficiency at soft X-ray energies (Figure 5.8). The device has an enhanced back-surface after passivation from ion

implantation and the parallel and serial electrode structure is 2-phase. The Hamamatsu CCD is a deep depletion device and has bulk silicon with resistivity of 3 kΩ cm to 5 kΩ cm. The device has a transfer gate to control the movement of charge from the image section into the serial register and a summing well to control the movement of charge onto the output node. Both of these structures can be used to bin charge in the parallel and serial directions respectively [Hamamatsu, 2006]. The headboard design for the device was based on the design usually used for e2v devices (Figure 5.9).

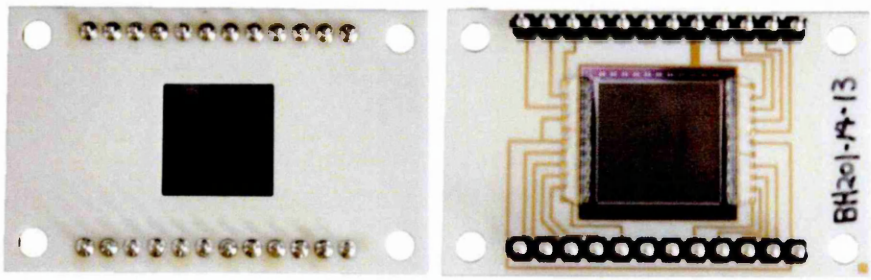

(a) (b)

Figure 5.8: The Hamamatsu device in its package, shown both back (a) and front-illuminated (b).

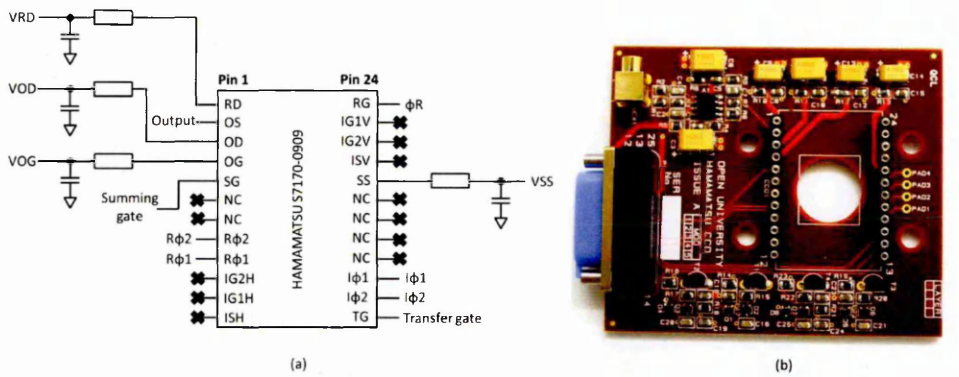

Figure 5.9: Hamamatsu headboard schematic showing low pass filters on the bias connections. Clocks are connected directly to the drive electronics and the injection structure tied to VRD to prevent spurious charge injection (a). A photo of the headboard is also shown (b).

The charge injection structure was not used in this experiment; hence, ISV and ISH (pins 12 and 21) were connected to VRD to prevent spurious charge being injected into the device. Due to the packaging of the device, an alternative mechanical jig had to be developed to provide cooling and protect the front side of the device (Figure 5.10).

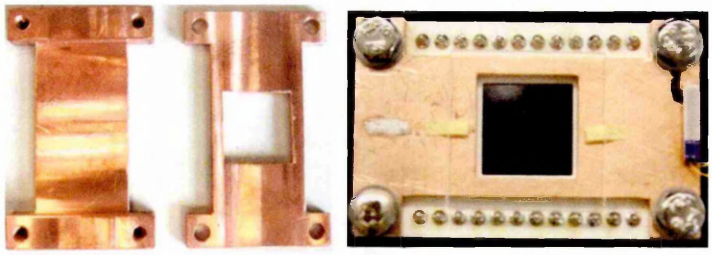

Figure 5.10: The front and back copper clamps for the Hamamatsu device to hold the CCD steady and allow it to be cooled.

The CCD ceramic is clamped between the two pieces of copper which is cooled conducting heat away from the CCD.

5.2.2 e2v EM-CCDs

The other devices used in the study were Electron-Multiplying CCDs. EM-CCDs differ from normal CCDs through the introduction of a multiplication register before the output node (Section 3.8).

5.2.2.1 e2v CCD97

The CCD97 is an e2v L3 vision (Low-Light-Level) frame transfer CCD. It has 512 row by 512 column image and store sections of equal size with 16 μm square pixels. The multiplication register contains 536 elements. The device does not have an AR coating and the store section is unshielded unlike standard CCD97s manufactured by e2v. The image and store section pixels have a 2-phase architecture and the serial register is 3-phase in order to allow for a higher potential electrode in the multiplication register [CCD97 datasheet, 2004]. The headboard was purchased from XCAM™.

The device has to be manufactured on low resistivity silicon in order to allow the multiplication register to operate efficiently. The unshielded store section of the device has a thicker oxide layer and hence dead layer than the image section of the device as it has not been optimised for photon detection; therefore, it is important, in order to optimise the running of the device, to detect incident photons in the image section and incorporate a shield to cover the store section in the clamping system.

A photo of the device on the headboard is shown in Figure 5.11 and a schematic of the device is shown in Figure 5.12. To reduce CIC when the device is inverted to surface dark current, the

clocks amplitude swing from -5 V to +7 V. This is achieved through an additional circuit board that uses MOSFET line drivers to shift the clock levels from those provided by the XCAM system. With the clocks at -5 V and the substrate at 0 V, the device is inverted, reducing the Si-SiO_2 interface dark current generation and changing the bias to +7 V brings the phase out of inversion as the charge is transferred. When the device is cold, it is not necessary to invert the CCD making CIC less of a problem. In this case the clock waveforms for the CCD are reverted back to normal 0 V to 10 V levels.

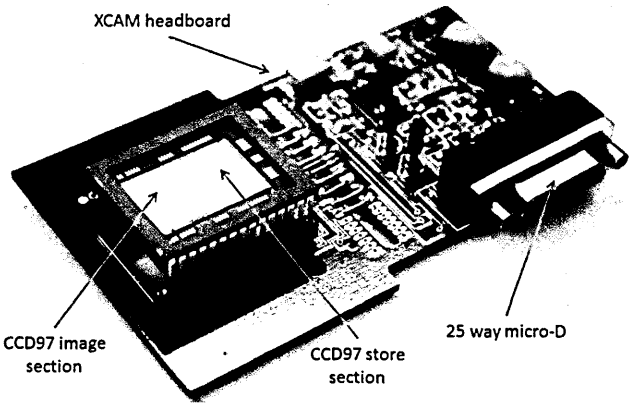

Figure 5.11: CCD97 with XCAM headboard. The 25 way micro-D interfaces clocks and biases. The image and store sections are shown.

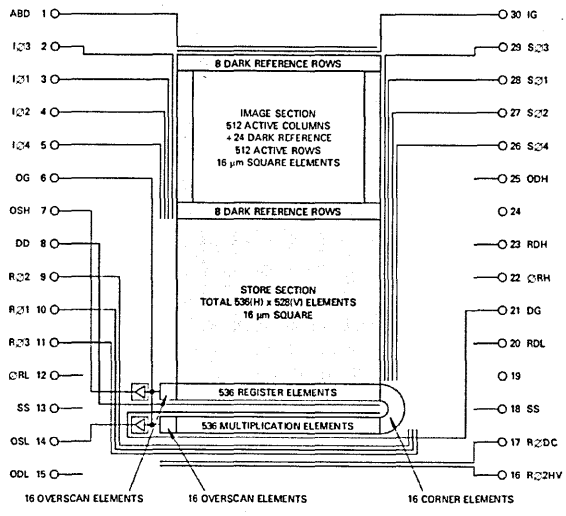

Figure 5.12: Schematic of the CCD97 showing the image and store sections, the serial register and the multiplication register before the output node [e2v, 2004].

5.2.2.2 e2v CCD220

The CCD220 is an e2v wavefront sensor with a multiplication register to reduce the effective readout noise to sub-electron levels and 8 outputs to allow fast readout (10 MHz pixel rate). The device is optimised for optical photon detection with a hafnium oxide AR coating, is a frame

transfer device and has aluminium shields over the store section (Figure 5.13). The CCD220 has a 240 row by 240 column image array that is split into 8 sections of 120 rows by 60 columns. The pixels are 26 μm x 26 μm [e2v, 2007] and there is 40 μm of (depleted) active silicon.

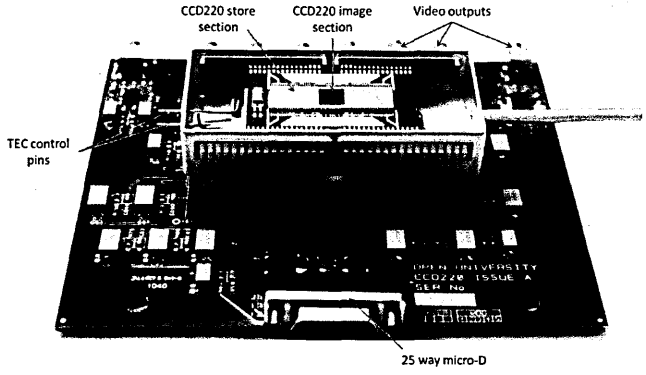

Figure 5.13: CCD220 on its headboard. The headboard is equipped with 8 output MCX jacks and a 25 way micro-D connection. The device's store section is covered in an Al shield and he image section appears blue due to its hafnium oxide AR coating.

The device is also optimised for the minimisation of split events (Section 3.6.2). Based on a design for a CCD with an integrated electronic shutter [Reich, 1993], the CCD220 has low resistivity silicon close to the front surface of the CCD to enable efficient multiplication gain and high resistivity silicon towards the back surface to enable the device to deplete further. To keep the low and high resistivity silicon separate, the p-type silicon at the p-n interface is highly doped forming a p-well that acts as a barrier between the n-type channel and the p-type bulk (Figure 5.14). At normal clocking potentials (~10 V), the depletion in the device is restricted to close to the front surface by the p-well and the device can operate like a normal EM-CCD; however, during the integration of charge the clocking potentials are held at much higher voltages (~17 V) and the depleted region "punches" through the p-well barrier, into the high resistivity silicon driving the depletion towards the back-surface. The charge that is generated in the device can then be collected quickly in the buried channel, reducing the likelihood of charge clouds splitting between pixels. By solving Poisson's equation it is possible to turn this doping profile into a potential profile [Amelio, 1971]. The plot was made using the SILVACO TCAD program.

Figure 5.15 shows how the depth of depletion in the device changes with gate voltage. At normal clocking voltages (10 V) the depletion only extends to 15 μm in the device, whereas when the

potential on the gate reaches 20 V the depletion extends towards the back-surface. The device is 40 μm thick which is approximately the depletion that is achieved at 20 V.

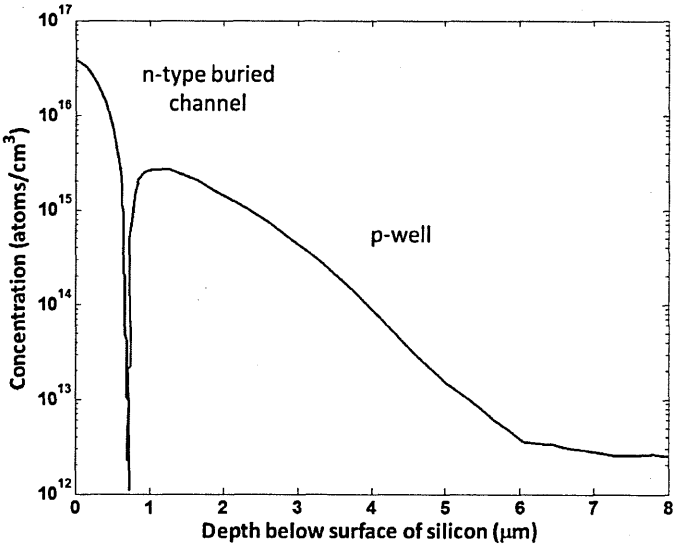

Figure 5.14: The doping profile inside the CCD220. The p-well creates a barrier between the low resistivity silicon in the buried channel and the high resistivity bulk silicon.

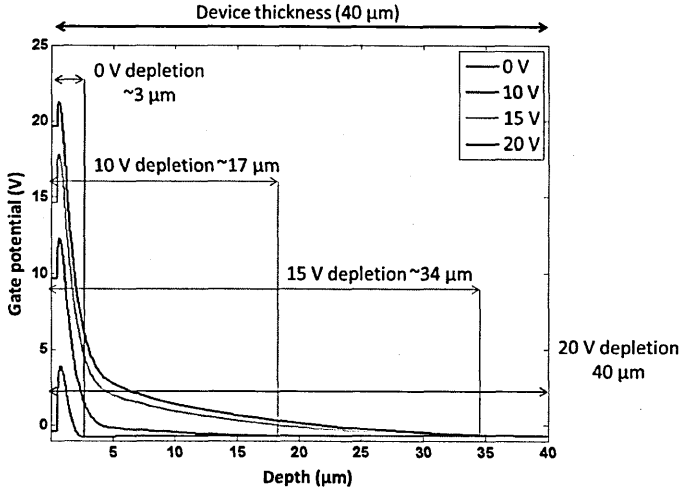

Figure 5.15: Potential profile in the CCD220 for different gate potentials. Increasing the potential on the gate electrode drives the depletion towards the surface of the back-illuminated device.

With 8 outputs running the static power dissipation could not be removed by the CryoTiger through the resistance of the unused TEC. To reduce the amount of heat that the CCD generated only 1 output was used at a time with the rest tied high to the reset drain (VRD). The schematic for the HV circuit is shown in Figure 5.16. Due to the small size of the imaging area that each output needs to read out, the image section can be read out quickly. At a 10 MHz pixel rate, a section of the device can be read out in 1/100th second.

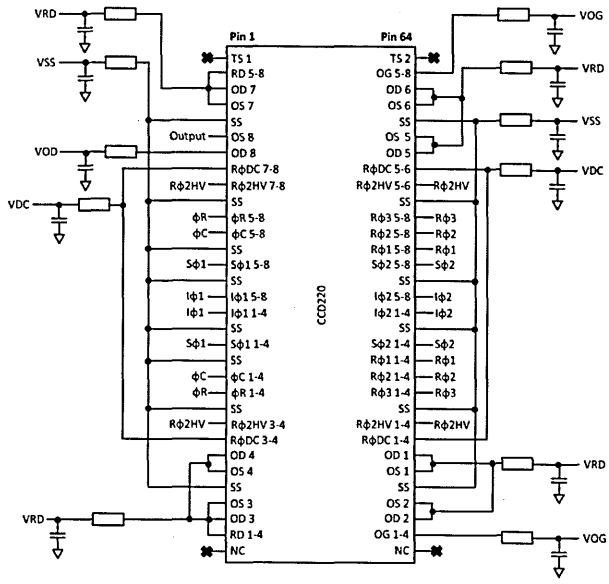

Figure 5.16: Schematic of the CCD220 headboard. The clock biases go straight to the drive electronics and the potentials are low pass filtered. Only one output is used and so all other outputs are tied to VRD.

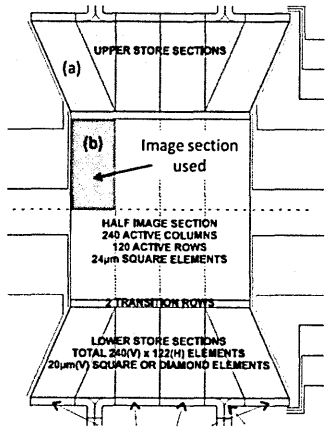

Figure 5.17: The schematic for the CCD220 showing how the image section is split into 8 different sections that are all read out through separated output circuits for high speed operation. The image section used in this thesis is marked (b) as is the store section used (a) [e2v, 2007].

The schematic for the CCD220 is shown in Figure 5.17 and the initial full read out of one of the outputs is shown in Figure 5.18. The figure shows all of the serial register and multiplication register elements and the image and store regions with some overscan. The figure is a complete readout of prescan and overscan elements that are found on the device (the dark regions) along with the store section and image section that has an increased level in dark current and so appears lighter. The image indicates that the EM-CCD is working correctly.

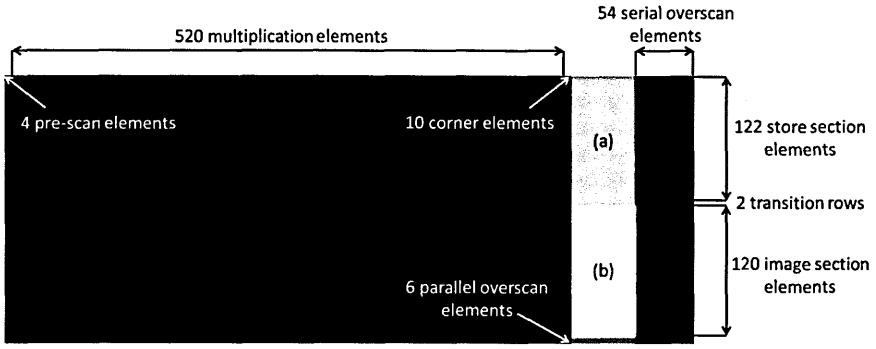

Figure 5.18: Initial readout from one of the CCD220 outputs showing the image (b) and store regions (a) along with the serial elements in the device and some overscan in the serial and parallel direction.

5.3 Comparison of the devices used in this thesis

Table 5.1: Table comparing the different CCDs used in this thesis [Hamamatsu datasheet, 2006], [e2v, 2006], [e2v, 2007], [e2v, 2007].

Device	Internal gain	Pixel Size (μm)	Pixel format (rows x columns)	Image area (mm)	Full well capacity (ke^-/pixel)
Hamamatsu	No	26	512 x 512	12.3 x 12.3	300
CCD30-11	No	26	1024 x 256	26.6 x 6.7	500
CCD97*	Yes	16	512 x 512	8.19 x 8.19	130
CCD220**	Yes	24	240 x 240	5.76 x 5.76	300

*800 ke^-/pixel in multiplication register
**500 ke^-/pixel in multiplication register

5.4 Analysis techniques for CCDs detecting X-rays

To evaluate the performance of a CCD, some basic data analysis techniques are required which form the basis of more complex analysis.

5.4.1 Event processing

Once image data has been collected, it needs to be analysed to look for X-ray events that occur in a single pixel ("isolated events"). Through performing an initial histogram on the image data on a pixel-by-pixel basis the background and X-ray are observed. Split events cause a continuum of counts between the two and are shown in Figure 5.19. The data is made up of several frames containing X-rays of a specific energy. The spectrum is from multiple X-ray events and there is no binning.

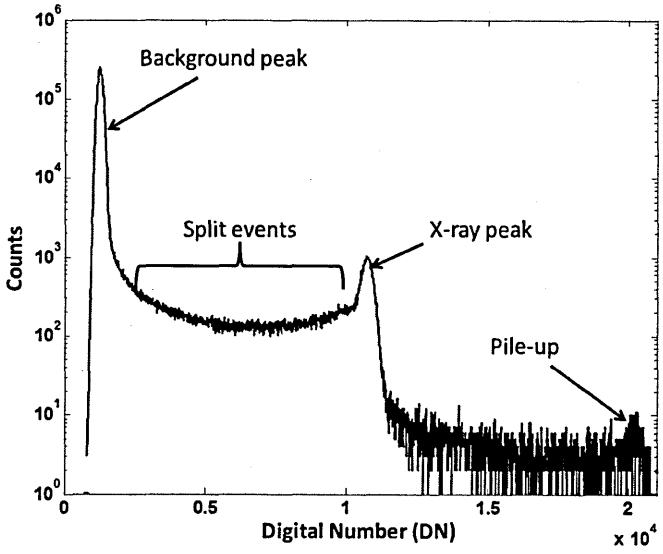

Figure 5.19: A raw spectrum of X-ray data taken with a CCD. The background peak and X-ray peak are clearly visible. Split events cause the continuum of counts between the background and X-ray peaks and multiple X-ray events per pixel appear as pile-up in the spectrum.

An algorithm was used to find events causing charge clouds collected within a single pixel (isolated events). To do this, the image array is searched for events above a threshold level and then adjacent pixels are analysed to see if they are also above the threshold. If none of the neighbouring pixels were above the threshold then the event was considered to be isolated and its position and Digital Number (DN) value were recorded. The DN is representative of the amount of charge in the pixel, Figure 5.20. The thresholding software is based upon an algorithm developed by Neil Murray for his PhD thesis and is run in MATLAB.

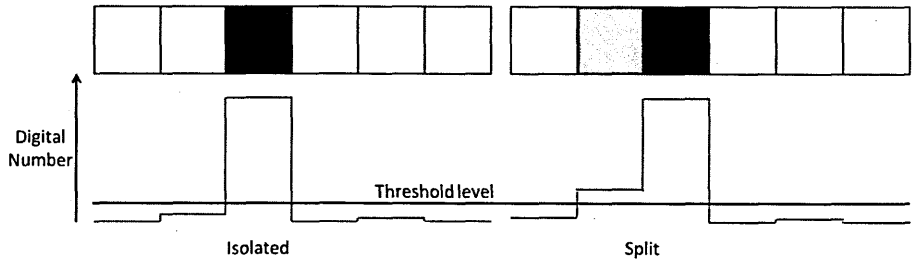

Figure 5.20: The same threshold level is shown for two 1D image readouts. The split event is detected as adjacent pixels have DN values above the threshold level (right) whereas the isolated event is surrounded by pixels with background level fluctuations (left).

A histogram of the isolated data is then produced with appropriate bins based on the dynamic range of the data and the number of isolated events found. The histogram is analysed in order to find the performance of the device. The isolated event spectrum from Figure 5.19 is shown in Figure 5.21.

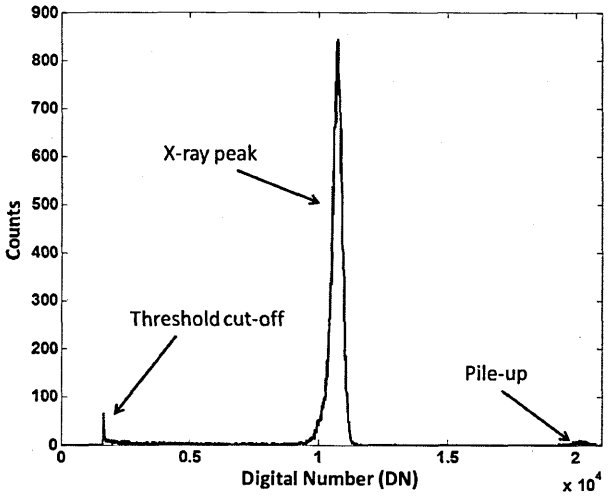

Figure 5.21: Isolated event spectrum. The split event continuum has been removed by the isolated event algorithm leaving behind events that occur in single pixels. Some pile-up events also remain.

Any pixels that have multiple X-ray events incident per frame are known as pile-up events and this creates a second peak at twice the DN of the main X-ray peak. Pile-up can be limited through adjusting the flux of the incident X-rays or the frame rate of the CCD.

Different algorithms can be used to bin the split events into single pixels creating more isolated events ("off-chip" binning). For example, if two adjacent pixels were found to have a signal level above the threshold value they could be combined into one of the pixels and the other pixel could be given the background signal level; however, this off-chip binning process adds noise to the collected signal. Each pixel has its own contribution of readout noise and by combining the pixels the readout noise has to be combined in quadrature. To avoid this problem the signal can be binned on-chip before it is read out (Section 2.4.1); however, it may be unclear how much binning is required until the device has been read out and there is a cost to spatial resolution.

5.4.2 Calibration

To turn the DN in the pixel into an energy, the data have to be calibrated. Assuming that the energy of the detected X-ray peak is known, calibration can be achieved as follows. The position of the background peak is taken to be "zero energy" and by finding the range between the background peak and the X-ray peak, a DN to eV conversion factor, the calibration, can be found (Figure 5.22).

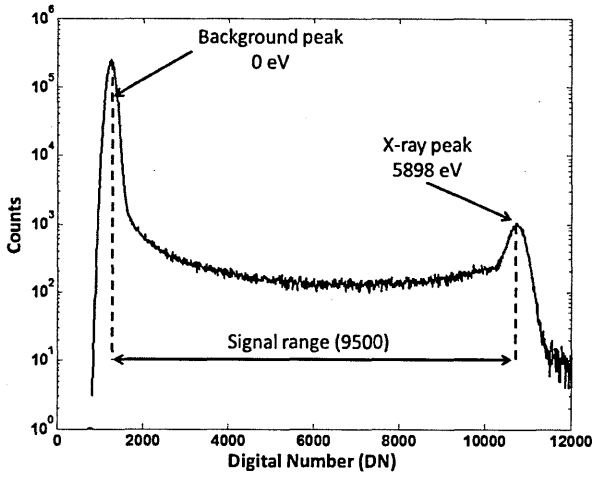

Figure 5.22: The distance between the background peak and the X-ray peak is the range. In this Figure the energy of the X-rays is 5898 eV giving a calibration of 0.621 eV/DN.

Space instruments such as the RGS on XMM-Newton (Section 2.4.1) use radioactive X-ray sources so that known energy X-rays can be used to check the calibration of the instrument allowing changes in device performance to be measured. Changes that may be seen to alter device calibration could be increases in dark current due to radiation damage or a drop in QE caused by contamination.

5.4.3 Partial Events

Partial events cause a reduction in the number of electrons in the charge packet as some electrons are lost to the back-surface (Section 3.6.3) causing a shift of the X-ray peak to lower energy in the histogram data. Higher energy X-rays will have smaller partial event fractions as the photo-generated charge will be produced further from the back-surface. Using the higher energy spectrum as a calibration, the positions at which other X-ray peaks should occur can be predicted. A comparison between the predicted position and the actual position of the X-ray peaks indicates how much charge has been lost and so gives the partial event fraction.

5.4.4 FWHM

Once the data has been calibrated it is possible to find the FWHM of the background and X-ray peaks by fitting Gaussian curves. The Gaussian fit gives a standard deviation on the signal that can be turned into a FWHM through Equation 3.18. Figure 5.23 shows the calibrated isolated event spectrum with a Gaussian fitted to it.

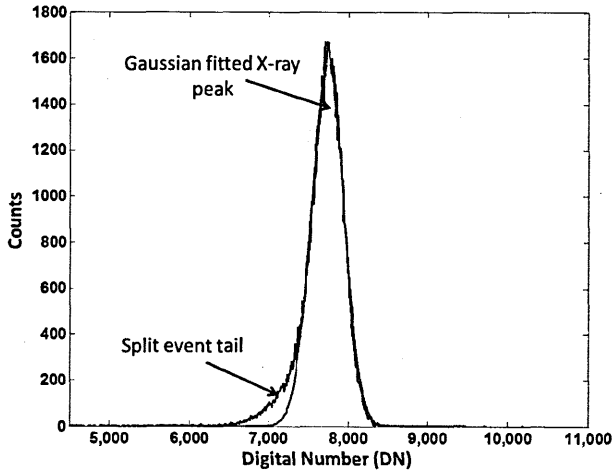

Figure 5.23: X-ray peak with Gaussian fitted. The X-ray peak doesn't match the Gaussian fit at its lower energy edge due to split events that were not identified by the isolated event search. In this case approximately 5% of events in the isolated X-ray peak are in the split event tail.

If, as in this case, a small number of the charge packets had a very small proportion of their total generated charge in an adjacent pixel the thresholding algorithm would identify the event as occurring in a single pixel. The low level charge splitting effect forms a low energy tail on the X-ray peak that doesn't agree with the Gaussian fit. If this tail is large enough it can degrade the FWHM of the X-ray peak and lead to a deterioration of spectral resolution.

The information given from the Gaussian fit can also be used to generate a breakdown of the different noise sources in the image by fitting to the background peak.

5.4.5 Measuring noise in the CCD

The noise on the image can be found from the FWHM of the background peak. By taking a region of serial overscan (Figure 5.18) and plotting a histogram, the standard deviation on the background level can be found. The background level is the readout noise from the device, $\sigma_{readout}$, as negligible dark current has had a chance to accumulate and there are no photon generated e-h pairs in the overscan causing shot noise.

The noise due to dark current, σ_{dark}, can be found through comparing the noise in the overscan to the background noise in the image. The standard deviation produced from the background peak in the histogram of the image section will be a combination of the readout noise and the

dark current, $\sigma_{combined}$. The readout noise is already known from the overscan and as noise adds in quadrature the dark current generated noise can be found:

$$\sigma_{dark} = \sqrt{\sigma^2_{combined} - \sigma^2_{readout}} \tag{6.1}$$

The shot noise on the photon-generated signal is the last dominant noise source to evaluate. The FWHM of the X-ray peak can be measured and the dark current and readout contributions to the noise are already known. The remainder of the total standard deviation, σ_{total}, on the X-ray peak must be due to shot noise:

$$\sigma_{shot} = \sqrt{\sigma^2_{total} - \sigma^2_{combined}} \tag{6.2}$$

The shot noise is equal to the square root of the number of electrons generated by the photon interaction and this is equal to the energy of the incident X-rays divided by the band-gap in silicon.

$$\sigma_{shot} = \sqrt{fn_e} = \sqrt{f\frac{E}{\omega}} \tag{6.3}$$

When optimising a device, the dark current can be minimised through cooling and the shot noise cannot be altered for a fixed signal level leaving just the readout noise to be optimised through altering the CCD readout clock timings and CDS integration periods.

5.4.6 X-ray spectra with multiplication gain

In an EM-CCD the gain changes with the changing HV gate potential, Rϕ2HV. The gain causes the range between the background peak and the X-ray peak to increase at a rate proportional to the increase in gain, reducing the "DN to eV" calibration at the same rate (Figure 5.24). The gain information can be used to plot the change of Rϕ2HV against the gain on the device (Figure 5.25).

The standard deviation on the readout noise peak in the spectrum remains the same regardless of the increase in gain (in DN); however, as the calibration is effectively reduced with increasing gain, the eV equivalent of the standard deviation on the X-ray peak is also reducing giving an effective drop in readout noise.

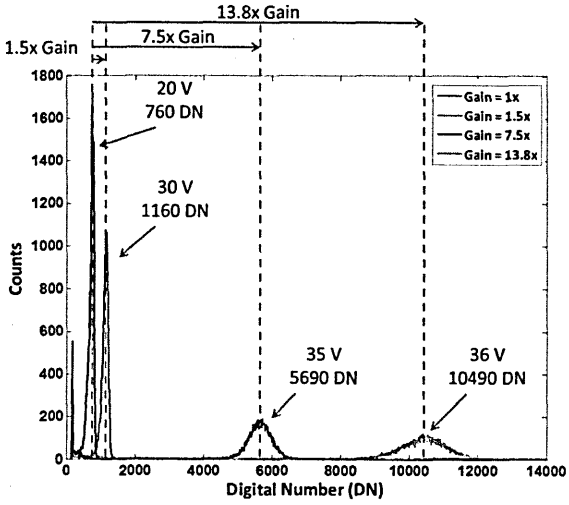

Figure 5.24: Detection of X-rays of fixed energy at increasing levels of gain. Increasing the gain increases the DN level of signal read out from each pixel which corresponds to the movement of the X-ray peak in the spectrum seen above. This can be used to calibrate the level of gain.

The accelerating potential in the EM-CCD is not equal to the potential on the RϕHV gate due to the RϕDC barrier potential that is being held at ~2 V to stop premature release of the charge packet into the Rϕ2HV potential. The barrier potential causes the accelerating potential to be lower by the potential that RϕDC is being held at; however, this is of no real consequence as the Rϕ2HV potential can be increased to compensate for the difference.

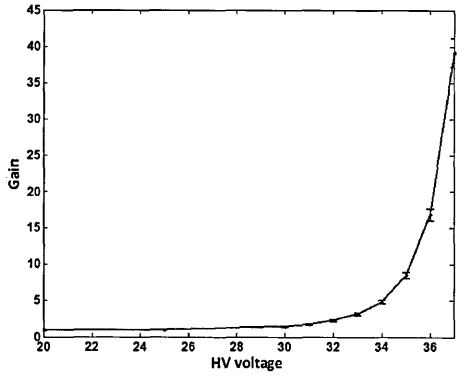

Figure 5.25: Gain calibration curve for an EM-CCD. The potential on the X-axis is the gate potential, Rϕ2HV, not the accelerating voltage (Rϕ2HV – RϕDC).

5.5 Summary

The CCDs and EM-CCDs used in this thesis required testing and characterisation in the laboratory before more precise energy experiments could be completed at off-site facilities. To perform these characterisations, devices were cooled to cryogenic temperatures in vacuum chambers. A range of X-ray energies were also required for energy calibration.

These requirements were met through the use of a CryoTiger™ for cooling, a vacuum chamber and an X-ray tube with internal target wheel with different target materials mounted onto it for X-ray fluorescence. An ^{55}Fe source was also used for quick energy calibrations.

Once the data were collected, a set procedure for its analysis was required to ensure that the results were all treated in the same way, allowing the different devices described in this chapter to be characterised and compared.

The experimental methods described in this chapter allowed the different CCDs and EM-CCDs to be tested effectively and accurately in the laboratory and these processes were adapted for use at other testing facilities.

Chapter 6: Soft X-ray testing of conventional CCDs

Future X-ray instruments desire increasing resolution, spectrally and spatially; therefore, detectors have to be produced to maximise the performance of these instruments. High spectral resolution requires a low noise system that can operate at close to Fano limited performance and the majority of X-ray events need to be collected with high QE in single events. Limiting the number of split events relies on depletion depth, device thickness, pixel size and on-chip binning; however, by increasing pixel size or binning the device will affect the spatial resolution. To test the effect of depletion depth and device thickness on the charge splitting in the CCD, three devices manufactured using different processes were evaluated.

Experiments using the PTB beamline at BESSY II in Berlin-Aldershof were conducted to investigate the soft X-ray performance of two CCD30-11 variants and a Hamamatsu S7171-0909. All of the devices have similar pixel size, allowing these experiments to draw comparisons between device performance and determine which of the two designs has the better soft X-ray performance in terms of spectral resolution and charge splitting.

The Hamamatsu device is almost twice the thickness of the e2v devices; hence, the effect of device thickness on the spectral resolution performance can be investigated. The Hamamatsu device is made on a higher resistivity material and is expected to have a larger depletion region however, as it is thicker, the benefits of this deep depletion may be nullified.

A considerable problem with soft X-ray detection in back-illuminated devices is the charge loss of the surface generation/recombination centres. With e2v implementing two different types of passivation technique and Hamamatsu using a variant of a technique used by e2v, passivation performance could be evaluated. Knowing the expected performance of different passivation methods across soft X-rays would allow improved decisions to be made when choosing which device to use for future X-ray spectrometers.

6.1 The BESSY II synchrotron facility

The BESSY II synchrotron uses a filament to generate a 70 kV electron beam that is accelerated through a microtron and synchrotron to its final energy of 1.7 GeV [Sawhney, 1997], [Thornagel, 2001]. The acceleration takes 50 ms and can be repeated at 10 Hz intervals. The accelerated electrons are then stored in the main storage ring where undulators and wigglers are used to cause the electrons to radiate synchrotron radiation of a specific energy [Keay, 1997]. To keep the electrons at a constant energy the storage ring has a series of radio frequency cavities to accelerate the electrons back up to 1.7 GeV after energy has been radiated away [Follath, 1999]. The schematic for BESSY II is shown in Figure 6.1.

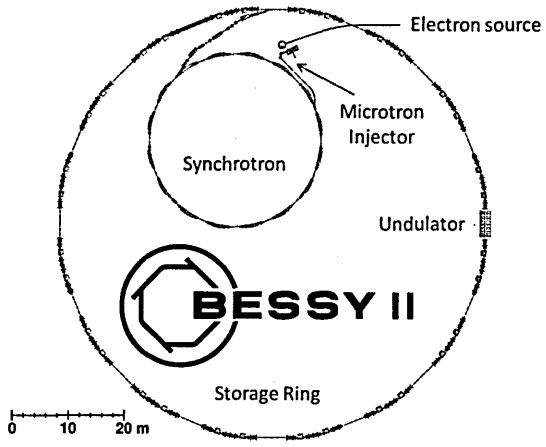

Figure 6.1: The BESSY II synchrotron facility showing the electron source, the microtron injector, the synchrotron and the storage ring with undulators to cause the electron beam to emit synchrotron radiation at a tuneable energy.

The microtron is a cyclotron in which the kinetic energy of the electrons is increased by a constant amount per revolution. It has a constant magnetic field strength which causes it to have low power consumption. From the microtron, the electrons are then injected into a particle accelerator which has a magnetic field that is synchronised with the electron beam, called a synchrotron. With each revolution, the magnetic field increases, giving the beam more energy and holding it within the confines of the synchrotron ring. When the electrons have been accelerated to 1.7 GeV they are transferred into the storage ring where they are held at a constant energy and emit synchrotron radiation. It is in this storage ring that X-rays are generated for experiments.

6.1.1 Synchrotron radiation

Synchrotron radiation is emitted when a charged particle is accelerated through a curved path similar to Bremsstrahlung that occurs in X-ray tubes (Section 5.1.3.2). The radiated energy is proportional to the fourth power of the particle speed and inversely proportional to the square of the radius of the path [Young, 2000]. Through the use of undulators, the radius of the path can be altered, causing a change in the energy of the radiation emitted allowing energy-specific experiments to be built around the storage ring [Helliwell, 1998].

6.1.2 PTB beamline

The PTB (Physikalisch-Technische Bundesanstalt) beamline is a facility based off undulator U49 at BESSY II. It consists of 9 different beamlines that use the synchrotron radiation from the storage ring, filtering and focusing it to allow X-rays of very high precision to be passed through the chambers and used for energy-specific applications [Klein, 1997]. The nine different beamlines are shown in Figure 6.2(a) and Table 7.1 with an image of the chamber setup mounted on the beamline shown in Figure 6.2(b).

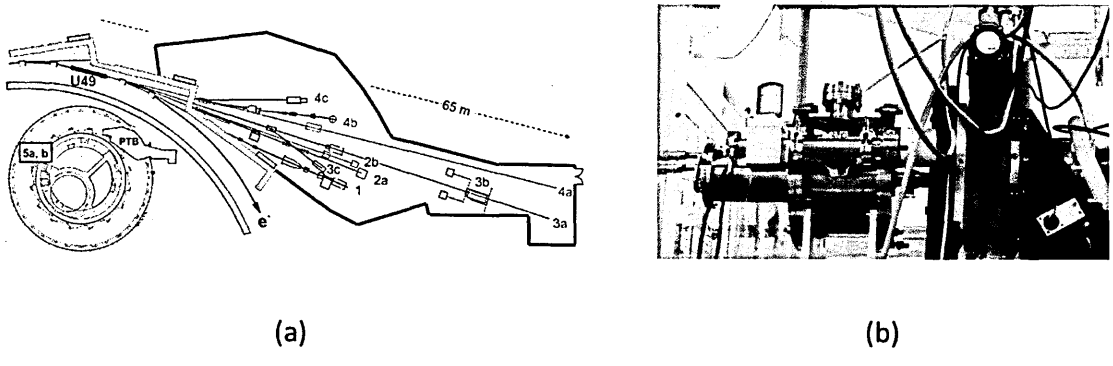

(a) (b)

Figure 6.2: The PTB facility at BESSY II showing its location around the storage ring and the locations of the 9 different beamlines (a) [BESSY, 2011]. The CCD is also shown mounted in the vacuum chamber onto the PTB beamline (b)

For the purposes of this experiment, beamline number 1 (the plane grating monochromator) was used as it allowed accurate energy control in the soft X-ray band that was proposed for use on the OP-XGS on IXO (Chapter 8). The method by which the beamline produces its highly tuneable X-rays across the energy range is shown in Figure 6.3.

Table 6.1: The different beamlines at the PTB facility at BESSY II with the range of energies at which they can be operated [BESSY, 2011].

Beamline Number	Beamline Name	Photon energy
1	Plane grating monochromator	30 eV to 1800 eV
2a	Four crystal monochromator	1.75 keV to 10 keV
2b	Fixed energy monochromator	2.5 keV
3a	Undispersed bending magnet radiation	3 eV to 35 eV
3b	Normal incidence monochromator radiation for source calibration	
3c	Deflected bending magnetic radiation (UV and EUV spectral range)	
4a	Undispersed undulator radiation	78 eV to 1860 eV
4b	Plane grating monochromator at undulation	
4c	Deflected undispersed undulator radiation	

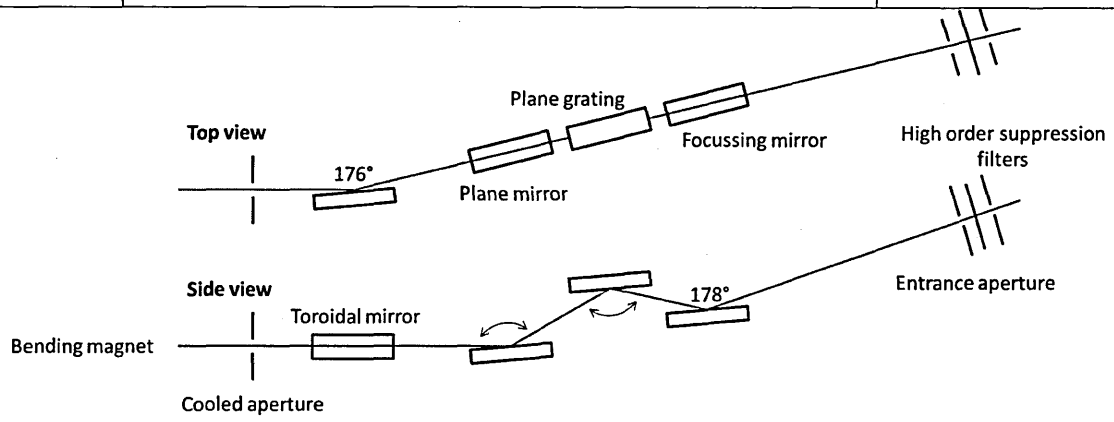

Figure 6.3: The schematic of the plane grating monochromator at the PTB beamline [Scholze, 2001].

The plane grating monochromator is optimised for radiometry and so special emphasis is put on the suppression of higher order radiation. The cooled aperture defines the incident beam from the bending magnet (U49). The natural opening from the storage ring at BESSY II is much wider than this aperture and so any residual change in the source direction, as long as it is within the aperture width, will have no effect on the incident energy and flux. The toroidal mirror is water cooled and reflects the X-ray beam at a graze angle of 2° to collimate it in the vertical direction. The plane mirror and plane grating then focus X-rays at a chosen energy onto the entrance slit where higher-order suppression filters remove other dispersed orders.

To achieve flexibility in higher order suppression the plane mirror and plane grating are scanned simultaneously allowing the entrance and exit angle at the grating to be set independently; therefore, individual photon energies can be produced at the entrance slit from a large number of grating and mirror angles, allowing the grating performance to be optimised for the energy that is required [Scholze, 2001].

Normally, BESSY II is operated in a high beam current mode with a continuous stream of electrons injected into the storage ring giving a high level of flux of generated X-rays. In this experiment it was necessary to be able to see individual photons and so the beamline could only be used when BESSY II was operating in a low current mode. During this mode of operation, a single packet of electrons is injected into the beamline every 4 hours. The low beam current mode provides a much lower flux of X-rays making photon counting possible; however, as the electron beam is not continually being injected into the storage ring in this mode of operation, the beam current degrades over time [Bootsma, 2000]. The degradation is monitored during the experiment allowing it to be calibrated, Figure 6.4.

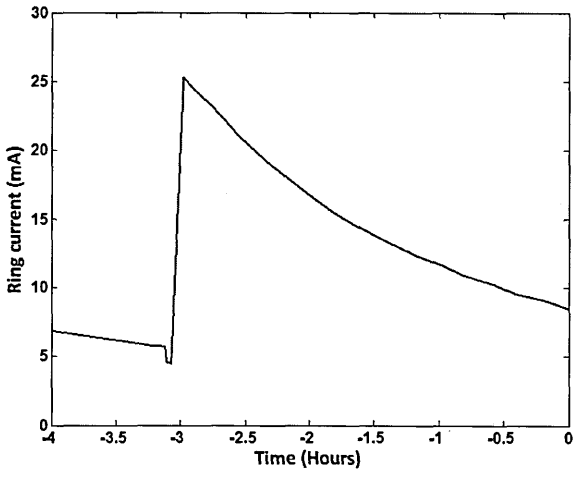

Figure 6.4: The measured degradation of the BESSY II ring current over time from initial injection at -3 hours to close to the next injection time.

Due to hydrocarbon contamination on the filters and gratings used in the beamline, 290 eV to 310 eV X-rays could not be produced; therefore, these energies had to be avoided in the experiment.

6.2 CCD30-11

Two variants of CCD30-11 were available for testing at the PTB beamline. One had been through an enhanced back-surface process that created a thinner p^+ layer in the device and the other had undergone e2v's standard back process. The back surface passivation process used was described in Chapter 4 and the devices were discussed in more detail in Chapter 5.

6.2.1 Experimental Method

The two CCD30-11 variants were taken to the PTB beamline in a portable vacuum system. The CCDs were mounted on a normal camera head setup and cooling was provided by a PCC compressor and CryoTiger™ head as described in Section 5.1. The chamber was directly mounted onto the PTB beamline using a 6 inch to 2 ¾ reducing flange and a 2 ¾ to QF25 adapter flange. The QF25 flange is built into the chamber used in the lab and the 6 inch flange interfaces to the PTB beamline.

The CCD was run in full frame mode but, as the X-ray source was always on (including during readout), the X-rays appear across the device as though the device is running in TDI mode, which produced a thin strip of X-rays down the device with a bright spot where the X-ray source is incident. The X-rays are projected as a spot due to the pin-hole that is installed in the beamline (Figure 6.5). During the short integration period, one of the image clocks is held high (11 V), driving the depletion towards the back surface and minimising the number of split events.

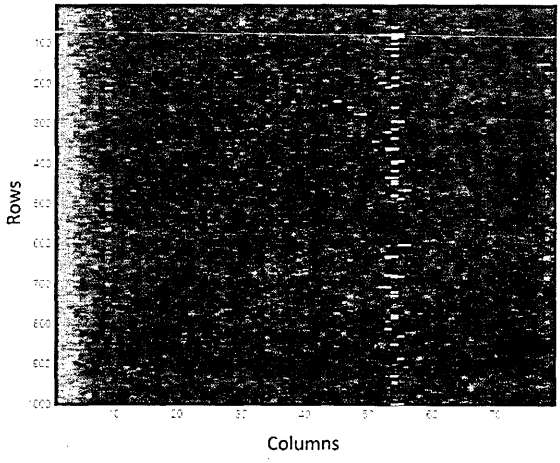

Figure 6.5: Single frame for the detection of 1200 eV X-rays in a CCD30-11. The pixels in this image are not square as the image is stretched in the x-direction to make the events more visible.

The X-ray events fell at the same point on the CCD for a particular energy (Figure 6.5) allowing a Region-of-Interest (ROI) to be set around the X-ray strip. Each frame of data produced this X-ray strip in the same ROI position; therefore, to simplify the analysis, a number of ROIs were stitched together to form a composite image of all of the data taken at that energy. The data were then analysed simultaneously while using a minimal amount of computer memory (Figure 6.6).

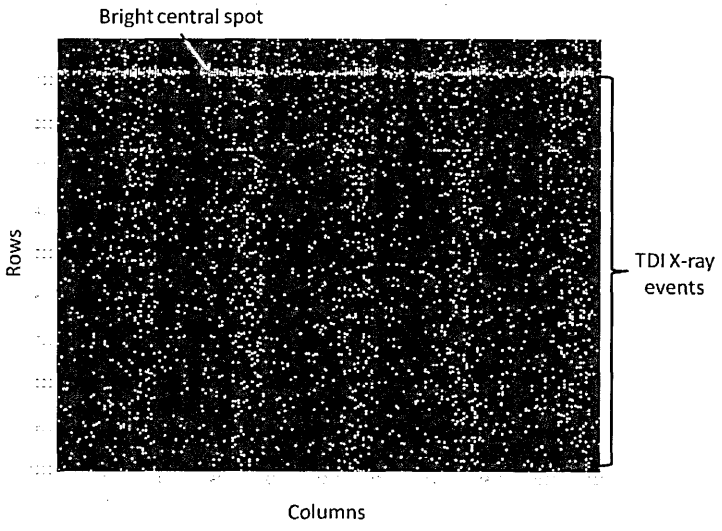

Figure 6.6: A composite image of the X-rays detected at 1200 eV using the ROI set from the first frame. The central spot is clearly visible as a line at the top of the image.

By taking several images a large number of X-rays are detected making the result statistically significant. Data were taken using both CCD30-11s at the following energies: 200 eV, 310 eV, 400 eV, 525 eV, 550 eV, 590 eV, 800 eV, 1000 eV and 1200 eV. Both devices were optimised to run at a 45 kHz pixel frequency with a noise of 5.2 electrons r.m.s. in the standard device and 4.6 electrons r.m.s. in the enhanced. The variation of the readout noise between the two devices is caused by slight differences in the respective readout circuits. The devices were cooled to -120°C to suppress the dark current.

6.2.2 Results

The results were analysed using the methods described in Section 5.4 to find the partial event fraction, the number of isolated events and the spectral resolution (FWHM) of the X-ray peak at each energy. Calculating these values allows a theoretical prediction of device performance to be made and compared with the values measured in the data.

6.2.2.1 *Partial events*

Using the data collected at 1200 eV it was possible to obtain a calibration (eV/DN) that was used to predict the location of other X-ray energies. The energy scale is calibrated from the 1200 eV data as this was the highest energy used in the experiment, hence the photon interaction will occur at the deepest point into the active silicon at this energy making charge loss to the back surface less likely. The eV/DN calibration was used to find the expected position of X-ray peaks (in terms of Digital Number) at lower energies. Any deviation that the measured X-ray peak had from this value was attributed to charge loss and the difference allows a partial event fraction to be calculated (Figure 6.7) (Section 3.6.3). The position of the black line at 310 eV is based on the 1200 eV calibration; however, the dashed blue line is the actual position of the 310 eV X-ray peak. The difference between the two lines shows that an average of 30 eV is lost (~8 electrons) from the charge packet when detecting 310 eV X-rays. The partial event fraction was analysed for each device (enhanced and standard CCD30-11 variants) and the two results were compared (Figure 6.8).

The results taken at 1200 eV used to calibrate the energy scale will have a minimised partial event fraction, but some charge will still be lost to the SiO_2 interface. The charge loss will cause the size of the partial events to be slightly underestimated but the effect is small due to the small charge loss seen; however, it will contribute to error in the experiment.

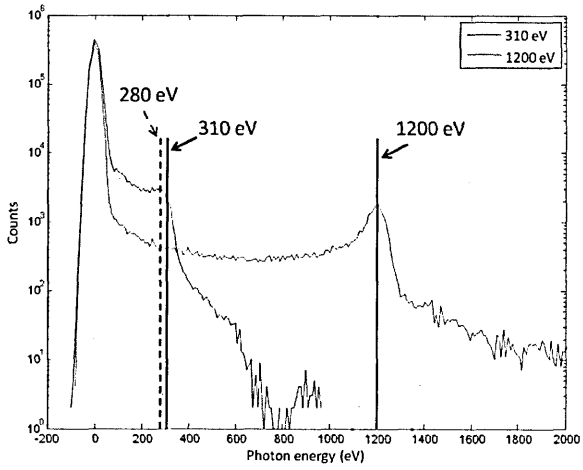

Figure 6.7: A histogram of all of the events collected for 310 eV and 1200 eV photons. The expected position of the X-ray peak according to the calibration from the 1200 eV data is shown by the black line at 310 eV. The actual peak position is at 280 eV and the difference gives the mean amount of charge lost, which in this case is equal to 30 eV.

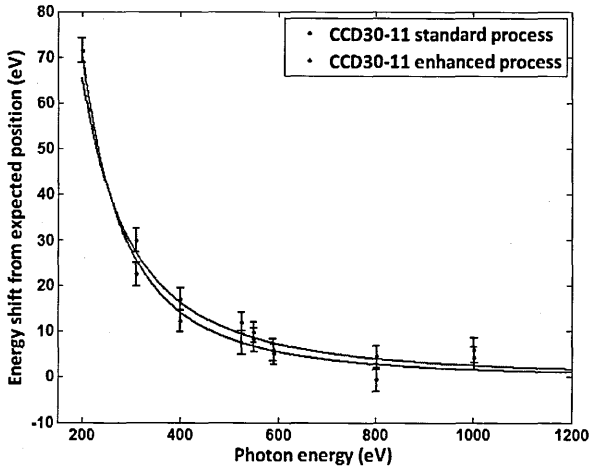

Figure 6.8: The partial event fraction as determined from the shift of the X-ray peak from the expected position as defined by the 1200 eV calibration.

Figure 6.8 indicates that the partial event fractions for each CCD30-11 variant are similar across the energy range tested, which suggest that the enhanced back-surface process does not have an effect on the number of electrons lost to the generation/recombination centres at the Si-SiO_2 interface (for 200 eV to 1200 eV X-ray photons).

Figure 3.22 shows that at 310 eV the X-rays absorption length is 100 nm, measuring the mean X-ray interaction point to be deeper into the active silicon than the typical p^+ layer thickness, which for the standard device is ~50 nm thick. The loss to the back-surface generation/recombination centres at these energies is small; therefore, the differences between the two devices will be hard to detect, giving the appearance of both devices having the same performance.

To differentiate between the enhanced process and the standard process variants, lower energy photons should be used to perform QE measurements as this will give a better indication of the p^+ layer depth in each device. If the p^+ layer is thicker, fewer photons will reach the active silicon leading to a drop in QE.

Some of the partial events that were seen could have been caused by split events. While only isolated events were used in the data analysis, if some of the events were partially split across two pixels, the splitting could have occurred below the threshold level making the event appear isolated, leading to a drop in the detected energy; however, for the split events to cause a shift in

the X-ray peak position, a large proportion of events would have to be split over several pixels and at a level that is small enough to cause the threshold algorithm to consider the events to be isolated. The small amount of charge that spread into adjacent pixels would be lost, due to the thresholding algorithm and not electron recombination, generating a partial event. Charge lost this way is normally seen as a broadening of the X-ray peak not a position shift towards lower energy; therefore, the shift is most likely to be due to partial events caused by surface recombination.

6.2.2.2 FWHM

The FWHM for each device was predicted using Equation 3.19. The shot noise is energy dependent and the dark current was suppressed by running the devices cold, so the only difference in the CCD's performance was due to variations in the readout noise. The two datasets for the experiments using the standard CCD30-11 and the enhanced CCD30-11 are shown in Figure 6.9. The difference between the two theoretical lines is due to readout noise variation in the separate output nodes. It can be corrected for by subtracting the difference between the theoretical lines from the standard CCD30-11 result. The subtraction sets the theoretical prediction of the devices to the same readout noise level. The FWHM was measured as described in Section 5.4.4 and plotted against energy for the standard and enhanced CCDs, Figure 6.10.

The figure shows that at energies above 500 eV the FWHM for the standard and enhanced CCDs are close to the theoretical prediction and at energies above 800 eV the values are as expected within errors. At energies lower than 500 eV, the FWHM starts to increase and diverge from theory. The data taken at 200 eV could not be analysed to generate a useful result as the X-ray peak was lost in the background peak (Figure 6.14). The CCD30-11 variants were on high resistivity silicon, but could not fully deplete, which caused the reduced performance at lower energies.

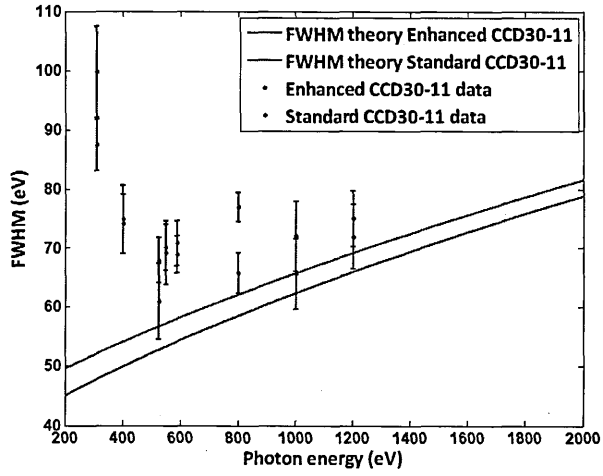

Figure 6.9: The measured FWHM of the X-ray peaks at different energies for the standard and enhanced CCD30-11s. The values are compared to the theoretical performance the devices could achieve. The readout noise for the enhanced CCD was 4.6 electrons r.m.s. and 5.2 electrons r.m.s. for the standard.

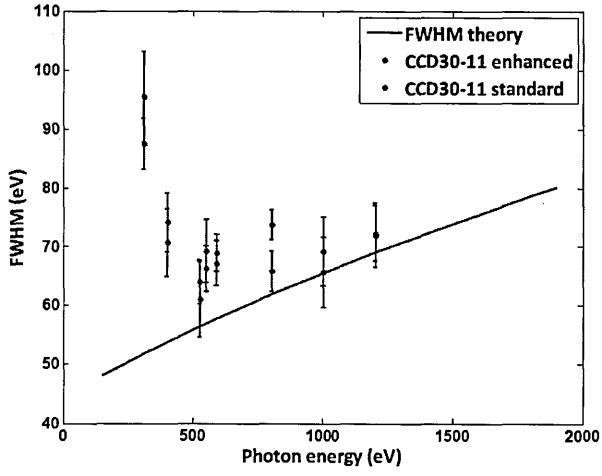

Figure 6.10: The FWHM of the detected X-ray peaks compared to the theoretical value based on readout noise and shot noise corrected to the same readout noise (4.6 electrons r.m.s.).

A similar divergence away from theoretical predictions has been seen in [Bootsma, 2000] where the effect was attributed to asymmetry in the X-ray peak (the effect is known as peak asymmetry) as well as charge splitting between pixels (Section 3.6.2). With decreasing energy the absorption length of the X-ray photons also decreases (Section 3.6.1) until a significant proportion of the incident photons interact in the dead-layer of the device. The dead-layer is not truly dead, but the amount of charge loss is proportional to the point in the dead-layer that the X-ray interaction occurs (Figure 4.13). The photons that lose charge in the dead-layer cause a second X-ray peak to form at a slightly lower energy than the main X-ray peak (Figure 6.11) and the combined FWHM of the two peaks is larger than if only the single peak were present. At the point that half of the

X-rays are detected in the active silicon and half in the dead-layer, the two peaks are of comparable size and so the greatest deterioration in FWHM will be seen (Figure 6.12).

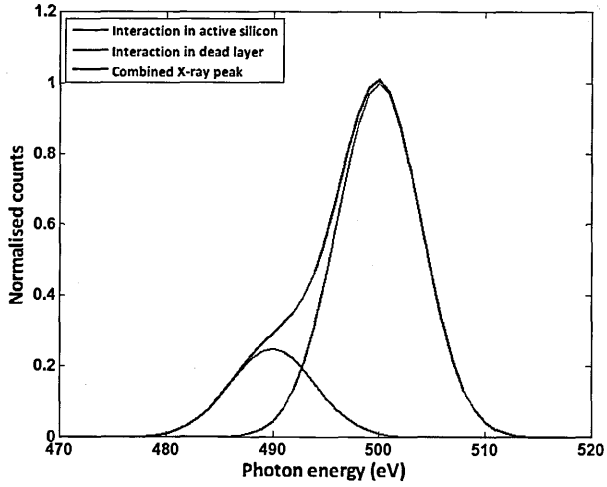

Figure 6.11: The detected photons form two X-ray peaks. One due to interactions in the active silicon and one due to interactions in the dead-layer where charge can be lost from the electron cloud. The secondary peak causes an increase in FWHM of the combined peak.

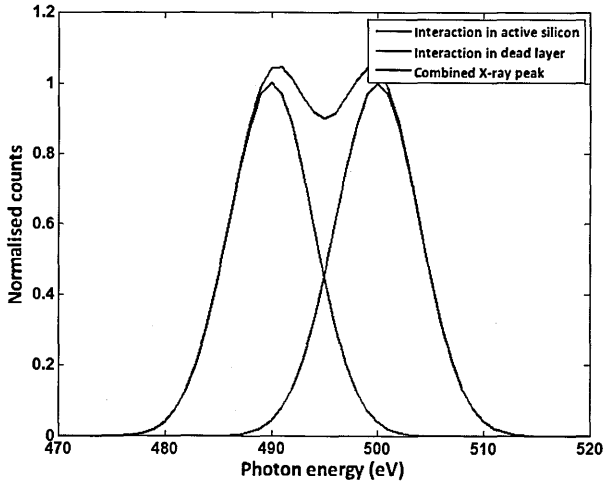

Figure 6.12: The detected photons form two equal X-ray peaks causing an even larger deterioration in FWHM.

If the energy decreases further then the lower energy peak would begin to dominate the spectrum and an improvement in FWHM should result (Figure 6.13). In the data collected, the lower energy X-rays were lost in the noise peak and so an improvement in FWHM was not seen. Through the use of an EM-CCD, the lower energy X-rays could be resolved out from this noise and so the improvement could be seen and this is planned as further work beyond the scope of this thesis.

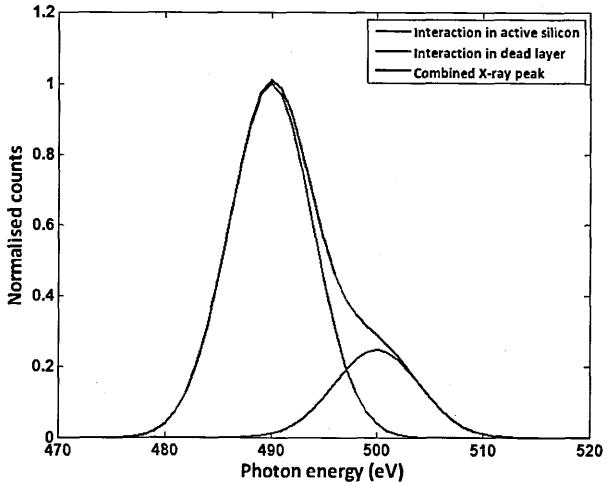

Figure 6.13: With decreasing energy, the peak formed from events that lose charge in the dead-layer will dominate the spectrum causing an improvement in FWHM.

The divergence away from the theoretical performance at lower energies is also due to the charge being split across several pixels. The isolated event search was able to remove events that were clearly split between two or more pixels; however, where the charge splitting was small, the thresholding algorithm considered the event to be isolated. The small loss of charge due to this splitting led to some events having a slightly lower DN value in the pixel than expected for that energy causing the lower energy edge of the X-ray peak to become broader, increasing the FWHM and causing the divergence from theory (Figure 6.15).

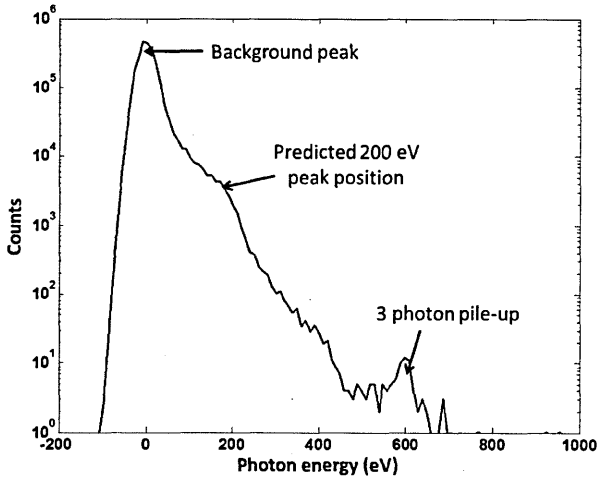

Figure 6.14: Spectrum of 200 eV photons. The X-ray peak cannot be seen as it is lost into the background peak. Some pile-up events can be seen that allow the spectrum to be calibrated.

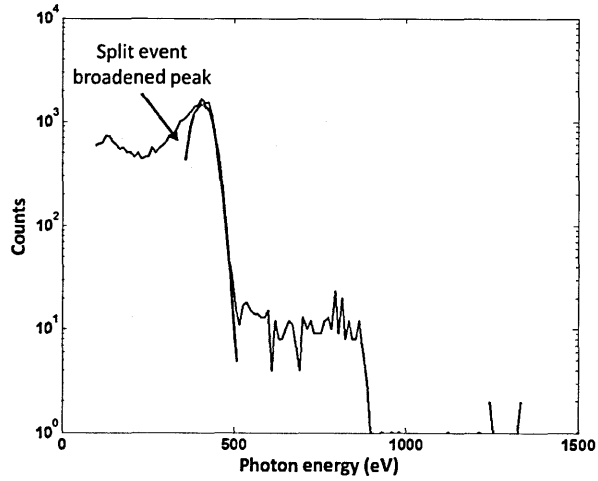

Figure 6.15: The X-ray peak for 400 eV with a Gaussian fitted to the peak and right hand edge. This shows the extra broadening that is created through split events in the image.

The performance of this experiment can be improved in the future through binning to make the pixels larger, thereby reducing the number of split events in the data and producing a "more Gaussian" X-ray peak that will follow closer to theory. A lower noise amplifier would also improve the low energy detection of the devices and devices with thinner dead-layers should see the asymmetry effect at lower energies.

The anomalous result for the enhanced device at 800 eV was due to a high flux level of X-rays on the CCD at this energy that led to high levels of pile-up and so there were fewer X-ray events to produce the X-ray peak at this energy (Figure 6.16).

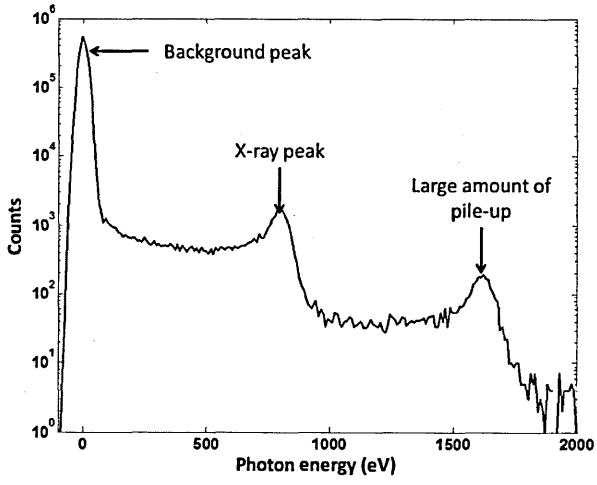

Figure 6.16: Spectrum showing the pile-up at 800 eV in the enhanced device that affected the statistics.

6.3 X-ray testing of the Hamamatsu CCD

The second experiment at the PTB beamline involved the testing of the Hamamatsu device described in Section 5.2.1.2 over a range of X-ray energies from 150 eV to 1900 eV. The Hamamatsu device was the baseline for the WHIMEx proposal and the experiment was designed to test the soft X-ray performance and QE of the device over the mission baseline energy range. The experiment also allowed the performance of different device types over soft X-ray energies to be compared.

6.3.1 Measuring the X-ray QE of the Hamamatsu CCD

To measure the QE of the Hamamatsu device, the PTB beamlines' reference diode was used to calibrate the X-ray flux incident on the CCD. Using the same setup as that used for the CCD30-11 variants, the Hamamatsu device was mounted onto the PTB beamline and cooled to -85 °C in order to suppress the dark current. The pin-hole in the beamline was changed to a slit so that more of the CCD surface could be illuminated allowing the data to be collected with fewer frames. The Hamamatsu device, as with the CCD30-11 variants, was operated in full-frame mode with the X-ray beam always on such that the slit was projected down the CCD. The beamline uses a series of gratings, mirrors and filters to produce a highly tuned X-ray energy (Figure 6.3) and because of inherent contamination, instrument deterioration and reflection efficiency the X-ray beam is not of uniform intensity across the CCD (Figure 6.17). To remove the effect of this non-uniformity the beam size has to be small enough to fall within the reference diode active area and CCD imaging area, allowing an average flux across the beam to be found. The average reading removed the non-uniformity, allowing accurate QE results to be measured. To optimise the noise performance, the CCD was read out with a pixel frequency of 34 kHz, giving a readout noise of 4.1 electrons r.m.s.

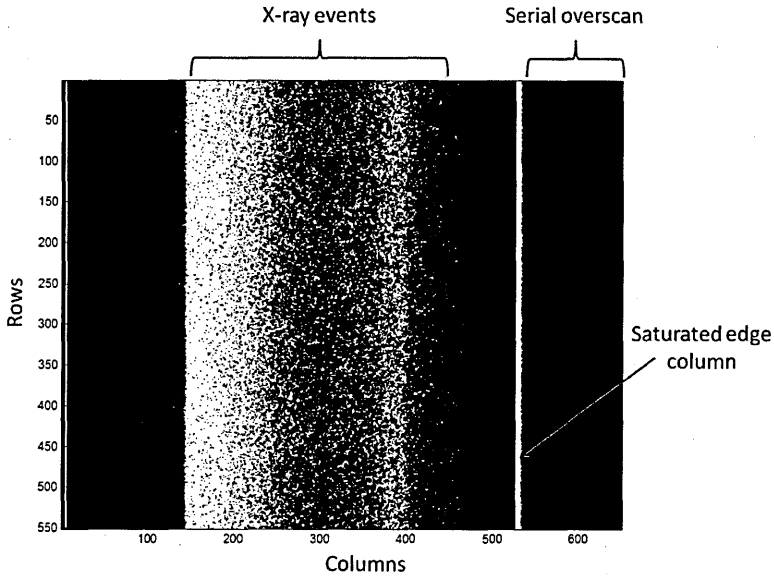

Figure 6.17: An image of a typical Hamamatsu frame with a large number of X-ray events to enable a QE measurement to be made. The CCD operates in full-frame mode and so the slit is projected as a strip down the device. The non-uniformity of the beam was removed by averaging the incident flux on the reference beam.

6.3.2 Quantum Efficiency analysis

To obtain the flux for the X-ray energies tested, a reference diode was placed in the beam before and after the data were taken, producing a current in the diode that could be measured against the background level and used as a calibration for the total number of incident photons (Figure 6.18).

To get an accurate reading from the reference diode, a higher level of X-ray flux than would be required for photon counting measurements was used. The team at the PTB beamline provided the reference diode spectral responsivity for the energies used (Table 6.2).

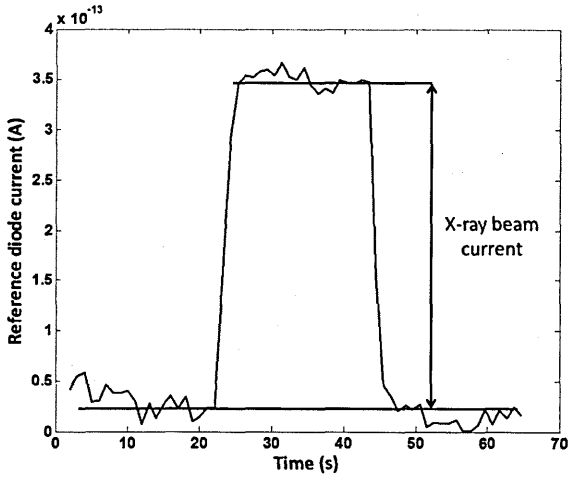

Figure 6.18: The current from the reference diode with and without X-rays being detected. The difference between the peak level and the background level give the current generated by the X-rays.

Table 6.2: The spectral responsivity of the reference diode at the energies tested in the Hamamatsu experiment (courtesy of the PTB beamline).

Photon energy (eV)	Spectral responsivity (A/W)
150	0.1417
280	0.1454
310	0.1494
400	0.1584
520	0.1702
590	0.172
800	0.1692
1000	0.1516
1200	0.1857
1800	0.1844
1900	0.177

The level of current in the diode, I_{diode} (in Amps), is divided by the known spectral responsivity, SR_{diode}, of the diode (in Amps/Watt) at the given energy to give a measurement in Watts (Joules per second). The frame readout time (FT) is known and therefore an expected number of Joules per frame, e, can be calculated. The comparison between the total energy (in eV) incident on the device, eV_{CCD}, compared to the eV calculated from the diode gives the QE :

$$QE = \frac{eV_{CCD}}{\frac{I_{diode}}{SR_{diode}} \times FT \times e} \tag{6.1}$$

Due to the beam current in the ring decaying over time between injections, the flux detected by the reference diode would decrease over time and therefore diode reference readings were taken before and after the CCD measurements to correct for the decreasing flux. The beam current was constantly monitored allowing the decay to be corrected for.

The flux on the device was also reduced at each energy to allow individual photons to be detected, in the same manner as with the CCD30-11 variant experiments. The FWHM of the detected signals could then be measured allowing the Hamamatsu energy resolution performance to be compared with the CCD30-11s at soft X-ray energies. Data were taken for the Hamamatsu device across the energy range from 300 eV to 1900 eV.

6.3.3 Results

The data were analysed using the methods described in Section 5.4 and Equation 6.1. Through the comparison of the flux incident on the CCD and the detected photons, the QE could be found. By using datasets that were at a lower photon count than the QE measurements it was also possible to scan for events that were isolated in single pixels which allowed the devices spectral resolution across the energy range to be found and a measurement of charge loss (partial event fraction) at the Si-SiO_2 interface to be made.

6.3.3.1 Quantum Efficiency

Results were taken for all of the energies described in Table 6.2, producing the results shown in Figure 6.19. Immediately it is apparent that the 800 eV and 1200 eV results are incorrect as they give a QE of better than 1. However, the measurements taken at 800 eV and 1200 eV were made as the Hamamatsu device was warming up due to a faulty cooling system causing a change in calibration and dark current over time; hence, it would appear that more X-rays have been detected than were incident on the device at these energies. The two points with QE greater than 1 would occur either because a calibration is incorrect and the data has been shifted upwards or extra charge was generated in the device at 800 eV and 1200 eV other than the photo-generated electrons. Extra electrons would be generated in a device that was warming and, as this is the case for these measurements. An increase in dark signal is considered to be the reason for the anomalous results.

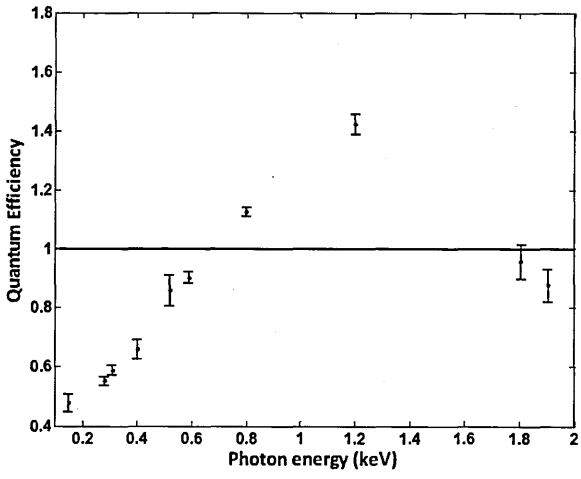

Figure 6.19: Initial results for QE measurements on the Hamamatsu device using the energies found in Table 6.2.

Ignoring these two points and using the QE model described in Chapter 4, it is possible to fit a line to these points and estimate the elemental abundances on the back-surface (Figure 6.20).

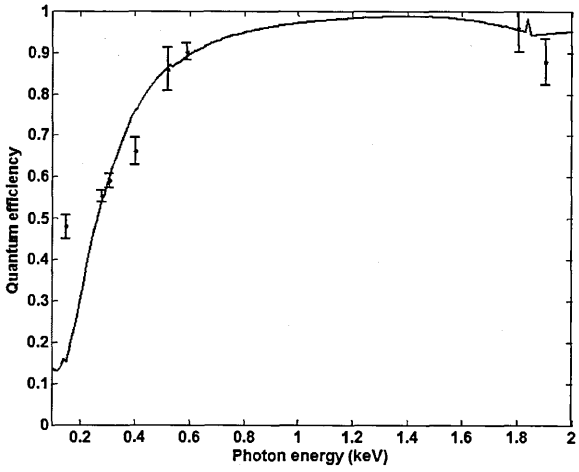

Figure 6.20: QE data point from the Hamamatsu data with the best fit QE curve.

The result at 150 eV is a long way away from the QE curve which can be explained by a probable error in the calibration. Due to the lower energy, the X-ray peak at 150 eV is partial obscured by the background peak, making an accurate calibration using the X-ray and background peak positions challenging. The estimate made on the calibration caused a miscalculation in the total flux integrated in the CCD and so an incorrect QE measurement. At 400 eV there is also some discrepancy from the QE model prediction, but due to a failure in the cooling this result was taken as the device was warming leading to inaccuracies.

Based on this result and through the optimisation of the QE model described in Chapter 4, the following materials are thought to be on the back surface of the device:

- Native oxide of SiO_2 with thickness ~4 nm
- Silicon p+ layer with thickness ~75 nm
- Carbon contamination with thickness ~2 nm

The above values are close to what would be expected for the device, although the p^+ layer is thicker than in an e2v CCD (Section 4.5). The values were found through the trial and error of layer thickness added into the authors QE model.

6.3.3.2 *Partial event fraction analysis of the Hamamatsu CCD*

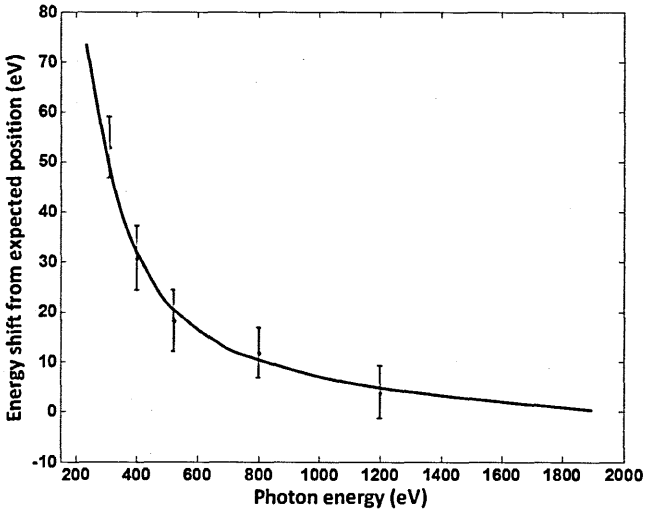

Figure 6.21: The partial event fraction for the Hamamatsu chip. The energy scale was calibrated using the results taken at 1900 eV.

The Hamamatsu device was tested to a higher energy than the two CCD30-11 variants and therefore a higher energy could be used to calibrate the energy scale for the analysis of partial events. The 1900 eV X-rays provided a more accurate baseline for comparison with the number of electrons in the charge packet. The analysis was performed in exactly the same way as for the CCD30-11 variants (Figure 6.21).

The result shows a similar trend to the CCD30-11s as the charge lost from the signal to the back surface generation/recombination centres goes up with decreasing energy. The dead-layer on the Hamamatsu device has been modelled to be thicker than on the CCD30-11s from the QE measurement which should cause the partial event fraction to increase at a faster rate with decreasing energy. The two devices are compared in Section 6.5.

6.3.3.3 *FWHM analysis for the Hamamatsu CCD*

The theoretical value for the FWHM was predicted using Equation 3.19 as the device was cold enough for dark signal to be suppressed and the readout noise could be found from the background peak. Where the device was warming, the background peak in the image area would give the combined dark noise and readout noise, allowing a theoretical value to still be predicted. The data were corrected to be at the same readout noise as in the CCD30-11 case to allow a

comparison to be made (Figure 6.22). The readout noise correction was completed using the same techniques described in Section 6.2.2.2.

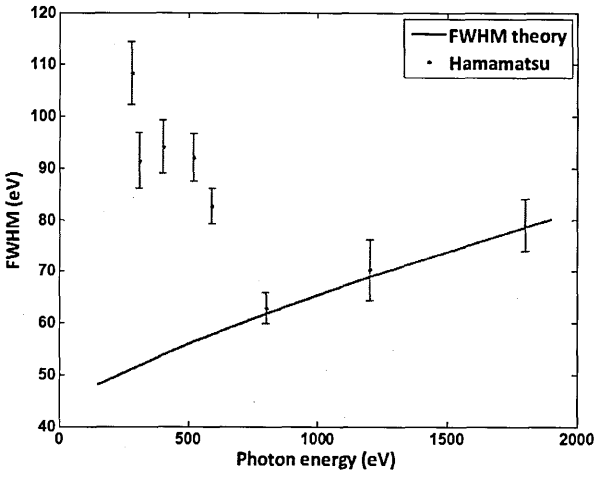

Figure 6.22: The FWHM results for the Hamamatsu device.

The Hamamatsu data matches well with theory at 800 eV and higher, but as the energy drops below 800 eV the data rapidly degrades from the theoretical prediction because of the asymmetry peak effect described in Section 6.2.2.2 and due to lower energy events splitting across pixels in the CCD, causing incomplete charge collection and a broadening of the FWHM.

6.4 FWHM comparison

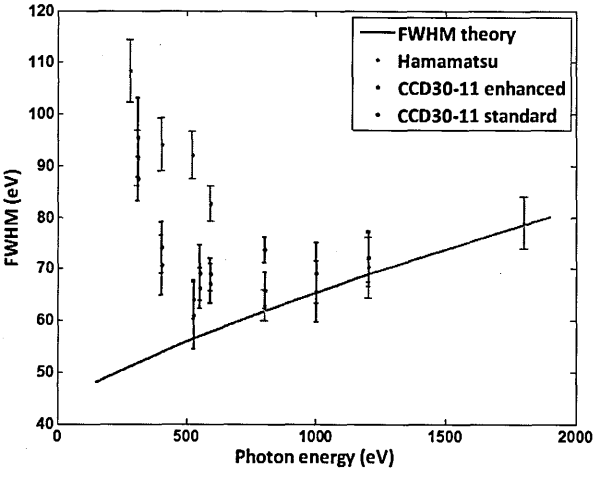

Figure 6.23: Comparison between the two CCD30-11s and the Hamamatsu device, corrected for the same readout noise (4.6 electrons r.m.s).

Neither the Hamamatsu nor CCD30-11 pixels were binned, but they are of a similar size allowing the device thickness and depth of depletion to be estimated from their spatial resolutions.

Figure 6.23 shows a comparison between the three devices. The two CCD30-11 variants stay closer to the line at lower energies than the Hamamatsu device suggesting that the two CCD30-11 variants have a thinner dead-layer so the peak asymmetry effect becomes dominant at a lower energy causing the Hamamatsu device to have higher spectral resolution degradation at lower energies. Part of the degradation may also be due to event splitting across several pixels at lower energies and this effect would be dependent on the depletion depth in the devices. Both devices are deep depletion, but the thickness of the Hamamatsu device is unknown; therefore, quantifying this effect is not possible.

6.5 Partial event fraction comparison

The Hamamatsu device was modelled from the QE data to have a dead-layer of ~75 nm which is thicker than the two CCD30-11 variants. The extra thickness of dead-layer, as it is starting to approach the absorption length of the lower energy X-rays, should cause an increase in the partial event fraction (Figure 6.24).

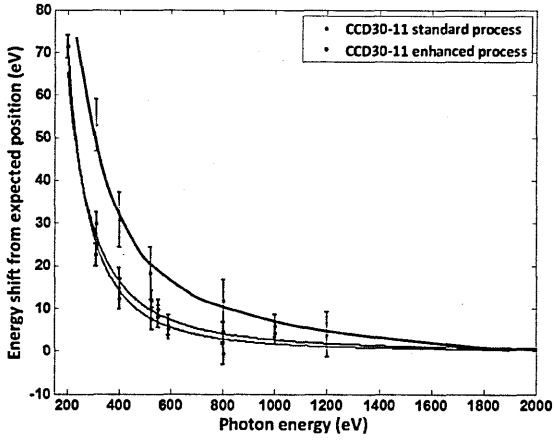

Figure 6.24: Partial event fraction comparison between the CCD30-11 enhanced and standard devices and the Hamamatsu CCD showing the Hamamatsu CCD with a higher partial event fraction than the CCD30-11s at lower energies.

The thicker dead-layer causes an increase in the partial event fraction seen in the device; however, as the absorption length of the lowest energy X-rays detected is still larger than the dead-layer thickness, this effect is not very pronounced. Through an investigation at lower X-ray energies and in the UV energy range, the effect of the thicker dead-layer could be better observed. The result supports the model of the back-surface of the CCD, developed from the QE

data, showing it with a thick (~75 nm) dead-layer providing confidence with the analysis. The errors on the Hamamatsu data are larger than for the CCD30-11s as the experiment was designed for QE evaluation, minimising the number of single photons that could be analysed and so reducing the available statistics.

6.6 Summary

The enhanced and standard CCD30-11 variants and the Hamamatsu device were tested at the PTB beamline at BESSY II to investigate their performance at the soft X-ray energies at which a high resolution X-ray grating spectrometer such as the OP-XGS would be expected to work. Generating a broad band of X-ray energies requires the use of a synchrotron facility and, to be able to photon count the X-rays, the beam needs to be working in a low current mode.

The QE of the Hamamatsu device was investigated across the X-ray energy band and the composition of the back-surface was found from this result. The experiment was compromised at some energies due to a failing in the cooling equipment, but by excluding those data a satisfactory result was obtained. The experiment was able to make an estimate of the dead-layer thickness of the device as ~75 nm, compared to ~45 nm measured in the CCD97 (Section 4.5). As the CCD30-11s were passivated with the same process as the CCD97 they are assumed to have a similar dead-layer thickness.

The results for the partial event fraction on all three devices supports the theory that the Hamamatsu device has a thicker dead-layer than the CCD30-11s as the partial event fraction increases at a larger rate in the Hamamatsu device.

The degradation in spectral resolution in the devices is due to event splitting and peak asymmetry. With a thicker dead-layer the peak asymmetry effect in the Hamamatsu device become dominant at a lower energy than in the CCD30-11s and this explains the result found. There will also be a degradation caused by event splitting. The Hamamatsu is thicker than the CCD30-11s, but has a higher resistivity; hence, depletion may be driven to similar distances from the surface. This would cause the event splitting effect to be similar in each device. Without

more data it is impossible to investigate the difference between the depletion depths in the CCDs. Future work could involve a QE study from UV energies into high energy X-rays. This would allow a detailed map of dead-layer thickness and active silicon thickness to be made allowing more accurate conclusions to be drawn. The use of an EM-CCD to study the effect of peak asymmetry may also be possible as they are able to suppress the readout noise of the device. It may also be possible to include these effects into the theoretical FWHM model to test how event splitting and peak asymmetry may effect spectral resolution degradation. Some of the results are summarised in Table 6.3.

Table 6.3: A summary of the three devices used in the experiment described in this chapter. The results are for selected energies and cover spectral resolution and charge loss to the Si-SiO_2 interface.

		Spectral resolution (FWHM)			**Charge loss (Partial event)**		
Device	**Variant**	**1200 eV**	**800 eV**	**400 eV**	**1200 eV**	**800 eV**	**400 eV**
CCD30-11	Standard	72 eV	66 eV	74 eV			17 eV
CCD30-11	Enhanced	72 eV	74 eV	71 eV		4 eV	18 eV
Hamamatsu	n/a	70 eV	63 eV	94 eV	4 eV	12 eV	31 eV

Chapter 7: The Modified Fano Factor

The remainder of this thesis focuses on the noise generated through the gain process in an EM-CCD and the effect that this has on the spectral resolution achieved at soft X-ray energies. The analytical solution for the Modified Fano Factor in this chapter follows the method described in [Robbins, 2003] for the Excess Noise Factor (ENF) (Section 3.8.2) and this result is tested using a Monte Carlo simulation of the gain register and verified experimentally in the lab using ^{55}Fe. The resulting factor that describes the energy degradation with increasing levels of gain is termed the Modified Fano Factor. Understanding the spectral degradation that occurs through the use of multiplication gain is important for instruments that use the resolving capability of CCDs to separate out orders, such as the Reflection Grating Spectrometer (RGS) on XMM-Newton.

To verify that the Modified Fano Factor holds for low X-ray energies, two further experiments were completed using the PTB beamline at BESSY II and an experiment was completed in the laboratory using Al K-shell fluorescence (1487 eV). The work in this chapter has been described previously in the authors papers [Tutt, 2011], [Tutt 2012] and, where applicable, this analysis is duplicated.

7.1 Introduction to the Modified Fano Factor

In Chapter 3 the Excess Noise factor was introduced and it was shown that the resolution of an EM-CCD when detecting optical photons could be given by Equation 7.1 (Section 3.8.2).

$$FWHM = 2.355\omega\sqrt{\left(\frac{\sigma_{readout}}{G}\right)^2 + ENF(\sigma_{dark}^2) + ENF\frac{E}{\omega}} \tag{7.1}$$

Equation 7.1 describes how the ENF affects the noise on the amplified signal at optical photon energies. If n_e electrons are generated in the device, the shot noise on the signal is equal to $\sqrt{n_e}$ and, as multiplication gain is a stochastic process, the noise generated on the amplified signal is described by a Gaussian distribution and so is also $\sqrt{n_e}$ at high levels of gain. The value for n_e is found from the energy of the incident photon and the quantum yield of silicon at that energy,

Section 3.6.1.1. The combined noise on the photon detection and gain is given by $\sqrt{2\frac{E}{\omega}}$ and so the ENF is equal to 2. A similar process can be followed with X-ray photons. The shot noise on the incident photons is now given by $\sqrt{fn_e}$, but the gain amplification noise is still $\sqrt{n_e}$ at high levels of gain. The combined noise at high levels of gain is given by $\sqrt{fn_e + n_e}$ which is equal to $\sqrt{n_e}\sqrt{1+f}$. This gives a value for the Modified Fano Factor, F_{mod}, of $(1 + f)$ and Equation 7.1 becomes:

$$FWHM = 2.355\omega\sqrt{\left(\frac{\sigma_{readout}}{G}\right)^2 + ENF(\sigma_{dark}^2) + F_{mod}\frac{E}{\omega}} \tag{7.2}$$

F_{mod} varies from f at a gain of 1, where there is no amplification, to $(1 + f)$ at high levels of gain, making F_{mod} smaller than the ENF, but as X-ray photons generate a large number of e-h pairs per photon interaction the factor is applied to a larger signal than in the optical case, making the effect more significant. F_{mod} only applies to X-ray generated signal; therefore, the ENF is applied to any dark current passed through the multiplication register. The goal of this chapter is to find what happens to F_{mod} between the gain of 1 and the high gain situation over a range of X-ray energies.

7.2 Analytical solution for the Modified Fano Factor

The Excess Noise factor is a specific form of the measurement of the ratio between the variance on the input and output signal from an EM-CCD. The general case for any device with a Fano factor, f, is derived from the original definition (Equation 7.3). F^2 is a measure of the additional noise introduced by the gain register, where G is the gain on the signal, σ_{in}^2 is the variance on the input signal and σ_{out}^2 is the variance on the output signal.

$$F^2 = \frac{\sigma_{out}^2}{G^2\sigma_{in}^2} \tag{7.3}$$

Following a similar method as described by Robbins et al., [Robbins, 2003] and by assuming that the device is run cold enough for dark signal to be suppressed and considered negligible, it is

possible to quantify F^2, including the Fano factor and this can be used to define the Modified Fano Factor, F_{mod}. The analysis starts with Equation 7.4, where σ_G^2 is the variance on the gain, $\langle n_{out} \rangle$ is the mean number of output electrons from the multiplication register and $\langle n_{in} \rangle$ is the mean number of input electrons into the multiplication register.

$$\frac{\sigma_{out}^2}{\langle n_{out} \rangle^2} = \frac{\sigma_{in}^2}{\langle n_{in} \rangle^2} + \frac{\sigma_G^2}{G^2} \tag{7.4}$$

The variance on the output signal from the multiplication register can be defined as:

$$G\langle n_{in} \rangle = \langle n_{out} \rangle \tag{7.5}$$

Assuming that the multiplication probability is constant and that successive trials are independent, the gain process can be described using a Binomial distribution. If g is the probability of multiplication per gain element then the variance on the added electrons, σ_{added}^2, can be described by:

$$\sigma_{added}^2 = \langle n_{in} \rangle g(1-g) \tag{7.6}$$

The variance on the gain is thus given by:

$$\sigma_G^2 = \frac{\sigma_{added}^2}{\langle n_{in} \rangle^2} = \frac{g(1-g)}{\langle n_{in} \rangle} \tag{7.7}$$

When combined with Equations 7.4 and 7.6, this gives the variance on the amplified signal:

$$\sigma_{out}^2 = (1+g)^2 \sigma_{in}^2 + \langle n_{in} \rangle g(1-g) \tag{7.8}$$

If looking at a Fano-limited system, standard Poissonian statistics do not apply; therefore, for X-ray processes, $\sigma_{in}^2 \neq \langle n_{in} \rangle$. It was found by Fano, [Fano, 1947], that Equation 7.9 was true when detecting X-ray energies, where f is the Fano factor and σ_{in}^2 is the Fano modified variance.

$$\sigma_{in}^2 = f\langle n_{in} \rangle \tag{7.9}$$

The Fano adjustment on the input variance led to a development in the expression for σ_{out}^2:

$$\sigma_{out}^2 = \langle n_{in} \rangle \{ f(1+2g+g^2) + g(1-g) \} \tag{7.10}$$

Equation 7.10 gives the noise on the signal from the first gain element in the EM-CCD multiplication register and so it becomes the input noise on the second gain element with a mean

input noise of $\langle n_{in}\rangle(1+g)$. Through the substitution of these values into the original expression for σ_{out}^2 (Equation 7.8) it is possible to find the output noise for the second element:

$$\sigma_{out}^2 = \langle n_{in}\rangle(1+g)\{f(1+3g+3g^2+g^3)+g(1-g)(1+(1+g))\} \tag{7.11}$$

The result from Equation 7.11 then becomes the input noise to the third element with a mean input signal of $\langle n_{in}\rangle(1+g)^2$:

$$\sigma_{out}^2 = \langle n_{in}\rangle(1+g)^2\begin{Bmatrix} f(1+4g+6g^2+4g^3+g^4)+ \\ g(1-g)(1+(1+g)+(1+g)^2)\end{Bmatrix} \tag{7.12}$$

The series can be generalised to give an expression for the N^{th} element:

$$\sigma_{out}^2 = \langle n_{in}\rangle(1+g)^{N-1}\left\{f(g+1)^{N+1}+g(1-g)\sum_{k=0}^{N-1}(1+g)^k\right\} \tag{7.13}$$

where:

$$\sum_{k=0}^{N-1}(1+g)^k = \frac{1-(1+g)^N}{-g} \tag{7.14}$$

The total gain in the multiplication register is given by Equation 7.15 for a gain register consisting of N element.

$$G = (1+g)^N \tag{7.15}$$

which allows Equation 7.13 to be simplified to:

$$\sigma_{out}^2 = \langle n_{in}\rangle\frac{G}{(1+g)}\{fG(1+g)-(1-g)(1-G)\} \tag{7.16}$$

Applying this equation for σ_{out}^2 to Equation 7.3 it is possible to find an expression analogous to the Excess Noise Factor equation (Equation 3.30), but with $\sigma_{in}^2 = f\langle n_{in}\rangle$:

$$F^2 = \frac{1}{f}\frac{\{fG(1+g)-(1-g)(1-G)\}}{G(1+g)} \tag{7.17}$$

In photon energy regimes below 4 eV where single e-h pairs are produced per photon interaction and therefore, $f = 1$, Equation 7.17 simplifies to the equation for the ENF and agrees with [Robbins, 2003]:

$$ENF = \frac{1}{G}\left(\frac{2G + g - 1}{g + 1}\right) \tag{7.18}$$

Equation 7.17 gives a measurement of the increase in the width of the X-ray peak (FWHM) after the initial X-ray interaction and so is just the noise generated by the gain process, the Noise Factor for multiplication gain. To find an expression that takes the initial shot noise on the detected signal and the multiplication noise into account requires the multiplication of the Fano Factor with Equation 7.17, giving an equation for F_{mod}:

$$F_{mod} = \frac{\{fG(1 + g) - (1 - g)(1 - G)\}}{G(1 + g)} \tag{7.19}$$

At high levels of gain, G becomes the dominant term in the equation as g is small and F_{mod} tends to $(1 + f)$ as predicted in Section 7.1. Plotting the results from Equation 7.19 against increasing gain it is possible to see how the Modified Fano Factor should vary, Figure 7.1.

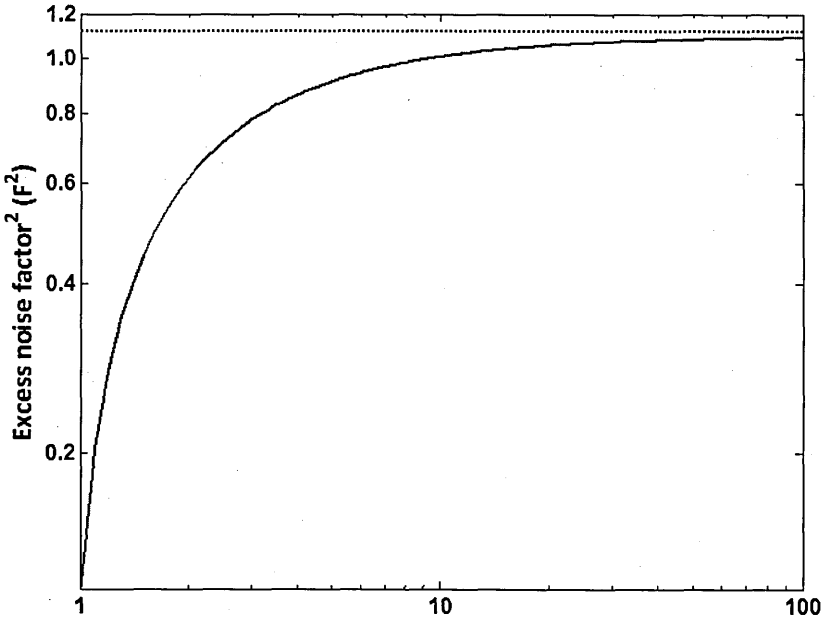

Figure 7.1: Modified Fano factor as a function of increasing gain showing that at high gain F_{mod} tends to (1 + f) which is shown by the red horizontal line.

The Modified Fano Factor is defined by:

$$F_{mod} = \frac{\sigma_{out}^2}{G^2\langle n_{in}\rangle} \tag{7.20}$$

To include the initial shot noise in the noise factor, the mean number of incident electrons is required, which leads to Equation 7.21.

$$F_{mod} = F^2 f \tag{7.21}$$

The Modified Fano Factor is a useful measure of EM-CCD spectral resolution because it quantifies the energy dependent noise on the signal into a single term.

7.3 The Modified Fano Factor Monte Carlo Simulation

To support the findings of the analytical analysis, a Monte Carlo model of the EM-CCD multiplication register elements was developed in MATLAB by the author. The model's purpose was to confirm the result of the analytical solution and to allow the uncertainty on small signals to be modelled. Each pixel of the modelled EM-CCD is considered to contain an isolated, 300 eV, X-ray event and the device is cooled to -120 °C to suppress the dark current generation. An energy of 300 eV was chosen as it is the lower energy of the Reflection Grating Spectrometer (RGS) on XMM-Newton and therefore the lowest energy soft X-ray that is currently being collected in a space application with a CCD [den Herder, 2001]. The lower end of the RGS energy range was chosen to test the detectability of the signal with the smallest charge cloud that would be generated. Through the randomisation of the number of electrons in each pixel within a Gaussian distribution of mean $\langle n_{in}\rangle = 82$ electrons and variance $f\langle n_{in}\rangle$, the shot noise on the input signal could be generated. Every electron in each pixel is then moved through N gain elements where each element has a probability, g, of generating another electron through impact ionisation (Equation 7.15) and whether an electron was added to the charge packet during a transfer was governed by the Monte Carlo process. The final variance on the output signal can then be calculated and thus the Modified Fano Factor, F_{mod}, for a system with any Fano factor, f, can be determined.

To test the accuracy of the Monte Carlo simulation and in turn the analytical solution, the Monte Carlo Simulation was used to predict the behaviour of an EM-CCD detecting optical photons ($f = 1$). Figure 7.2 shows the model used by Basden et al., [Basden, 2003] (Section 3.8.1), for an EM-CCD detecting 1, 2, 3 and 4 electrons. The points on the figure show the results of the Monte Carlo simulation made for this paper and the lines are generated using Equation 7.22.

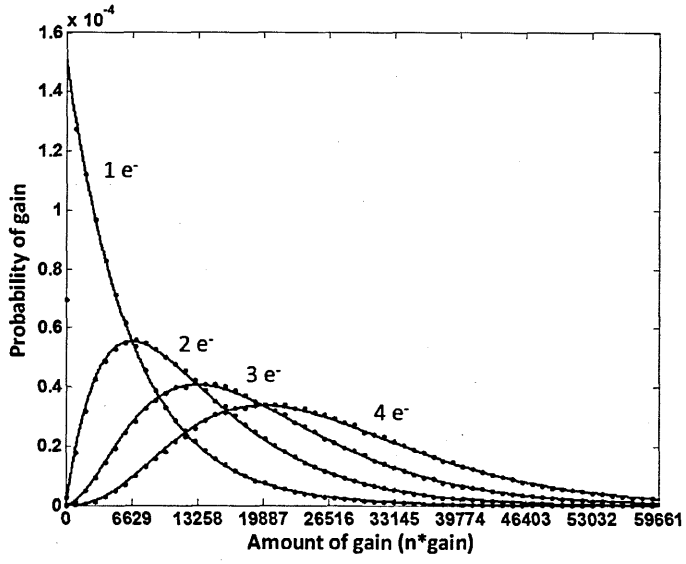

Figure 7.2: The Monte Carlo simulation predicting the range of gain for low signal levels.

$$p(x) = \frac{x^{n-1}e^{-\frac{x}{G}}}{G^n(n-1)} \tag{7.22}$$

Equation 7.22 allows the probability, $p(x)$, of getting a certain number of output electrons from the multiplication register to be found and so the effect of putting 1-4 electrons, x, through a 591 gain elements, N, with a total gain, G, of 6629 can be modelled and compared with the results found in Basden et al., [Basden 2003]. The probability of creating an electron through impact ionisation in a single element of the multiplication register, g, can be found from Equation 7.15. It can be seen that the points from the Monte Carlo simulation fall on the lines generated from Basden et al. increasing the confidence in the simulation.

The second benchmarking test used the model to predict the Excess Noise Factor behaviour in optical photon conditions. The test comprised of setting the Fano factor to 1 in the Monte Carlo Simulation (single e-h pair production per incident photon) and running the Gaussian distribution

of electrons through the model at varying levels of gain. Theory predicts that the Excess Noise Factor, F^2, will vary with gain as has been shown by Equation 7.18 [Robbins, 2003].

The results obtained from the Monte Carlo model can be compared to the plot formed by Equation 7.18 with varying gain, helping to build confidence in the model.

Both benchmarking methods for the Monte Carlo model show a good relationship with theory, therefore, confidence in the model is high.

7.3.1 Monte Carlo simulation prediction of the Modified Fano Factor

With the Monte Carlo simulation proving accurate at optical energies, it was then possible to use the same model to make predictions about X-ray energy behaviour ($f = 0.115$). X-rays of energy 300 eV and 5898 eV were put into the model and F_{mod} was found for a variety of levels of gain. Plots of gain against F_{mod} were made to compare the simulation to the analytical model.

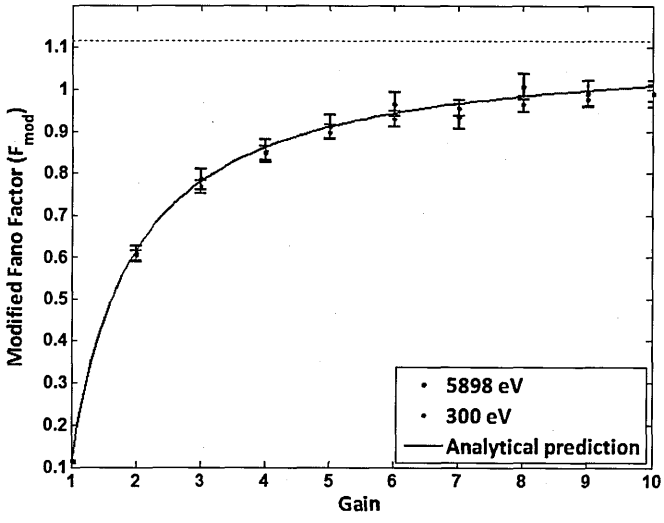

Figure 7.3: Comparison between the Modified Fano Factor predicted analytically and the prediction made using Monte Carlo simulation. The result will tend to (1+f) at high levels of gain shown by the red horizontal line.

The plots show that for an increasing level of gain and across a range of energies, there was an increase of the total noise in the system, due to the multiplication register, that tends towards $(1 + f)$ at high gain, providing further verification of the model and analytical solution.

7.4 Experimental verification of the Modified Fano Factor

The aim of the first experiment was to detect the manganese K-alpha X-ray emission with varying levels of multiplication gain at 5898 eV. The high energy Mn K-alpha emission produced by the ^{55}Fe source would be expected to penetrate deep into the device before interaction with the silicon (>20 µm [Henke, 1993]), minimising the field-free region the X-rays travel through and causing more X-ray events to be collected in single pixels. The reduction of split events should lead to an accurate prediction of the Modified Fano Factor without the need of event reconstruction and across all levels of gain.

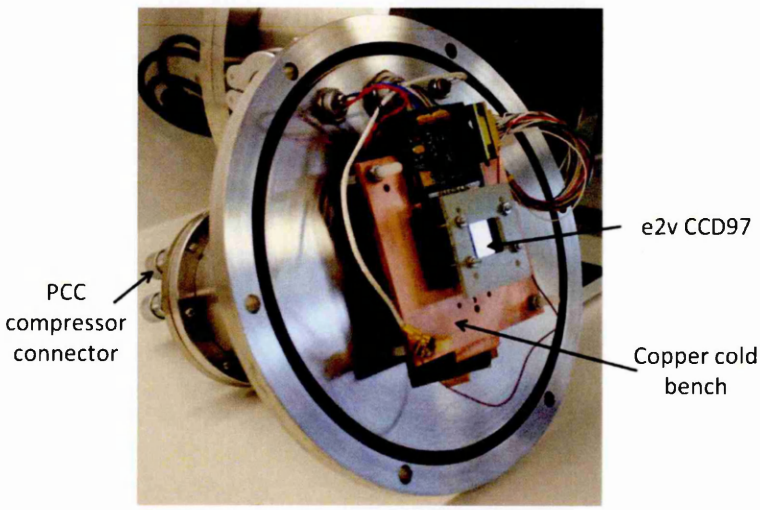

Figure 7.4: The CCD97 is shown mounted on a copper cold bench to provide cooling and on a vacuum chamber flange so that the experiment can be performed under vacuum.

The CCD97 was placed in a chamber with an ^{55}Fe source, at a pressure of 10^{-4} mbar and cooled to -115 °C in order to suppress the dark current generated (Figure 7.4). The X-rays incident on the CCD over a 0.1 second integration time and 500 frames were recorded per gain setting allowing the FWHM of the Mn K-alpha and background noise peaks to be measured. The experiment was performed over a range of gain voltages (11 V to 34 V, gain of 1 and 15 respectively) in order to get a measurement of the effect of gain on the FWHM of the signal. It was not possible to increase the voltage above 34 V as the X-ray data started to saturate the ADC of the processing equipment, limiting the experiment to modest levels of gain.

7.4.1 Experimental result compared with analytical calculation

It was possible to produce a plot of the Modified Fano Factor against the gain of the system to test the F_{mod} hypothesis (Figure 7.5).

The Modified Fano Factor was found by re-arranging Equation 7.2, remembering that $\sigma_{dark}^2 = 0$:

$$F_{mod} = \left(\frac{FWHM^2}{2.355^2\omega^2} - \left(\frac{\sigma_{readout}}{G}\right)^2\right)\left(\frac{\omega}{E}\right) \tag{7.23}$$

The FWHM can be found from the analysis of the X-ray peak and $\frac{\sigma_{readout}}{G}$ can be found from the background peak as described in Section 5.4, allowing the data points on Figure 7.5 to be found.

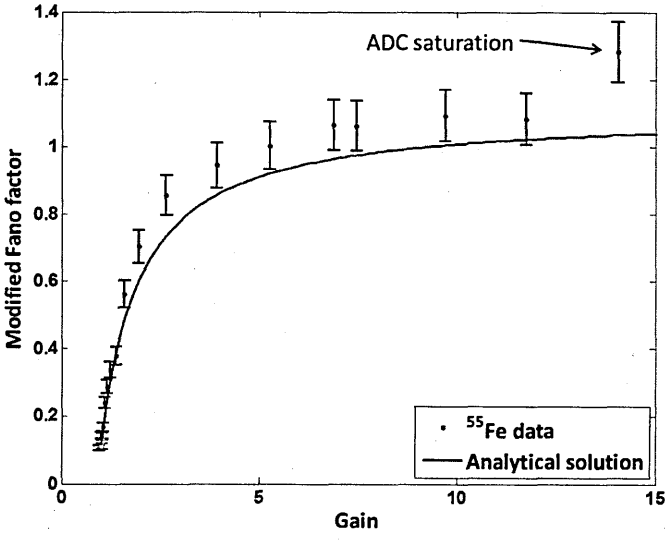

Figure 7.5: Plot showing the increase in the Modified Fano Factor with increasing gain. The result is compared to the line produced by the analytical solution.

The result does not verify the Monte Carlo model and analytical prediction for the Modified Fano Factor at X-ray energies as the points do not fall on the line generated by the analytical solution. The result follows the required shape, but the higher than predicted curve for the Modified Fano factor suggests the X-ray peaks were broader than theory predicts. At a gain of 15, the experimental data moves away from the theoretical model as the ADC nears saturation. Figure 7.6 shows the ^{55}Fe X-ray peak for two different levels of gain with the broadening of the peak clearly visible. The use of gain causes an increase in σ and a corresponding increase in the FWHM.

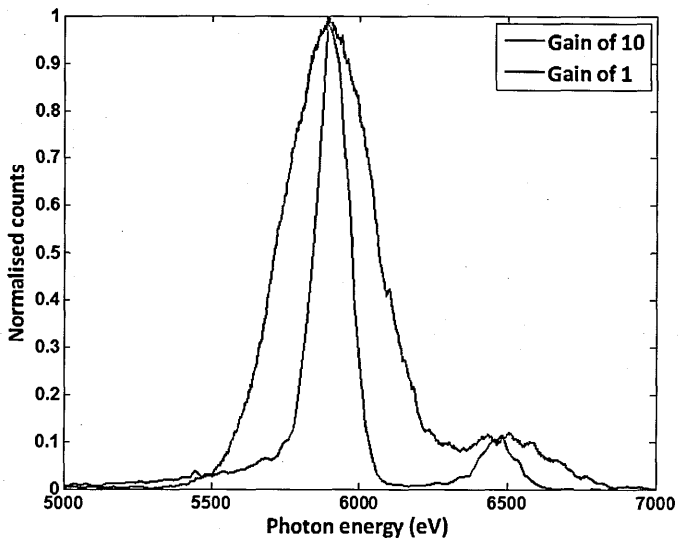

Figure 7.6: Comparison between the ^{55}Fe X-ray peak at a gain of 1x and a gain of 10x in the multiplication register.

The results for the Modified Fano Factor (Figure 7.5) do not fall exactly on the line for the theoretical prediction made using the analytical solution. The error is attributed to the splitting of the charge cloud between neighbouring pixels affecting the charge collection efficiency and, through the use of binning on future data, this could be evaluated. It may also be possible to add the split event effect into a future Monte Carlo simulation to see if the difference is due to event splitting. The systematic error may also be due to inconsistencies with the Fano Factor. Theory puts the Fano Factor at 0.115 and this was the factor that is used in the model; however, experiments have not been able to verify this value at the energy ranges used making it possible that the Fano Factor was underestimated leading to a better than possible prediction for the Modified Fano Factor and creating the error on the data [Owens, 1996], [Janesick, 1988]. A separate study would be required to investigate this potential variation in the Fano Factor. The result found for the Modified Fano Factor using Mn K-shell X-rays was then investigated further with lower energy photons in an attempt to validate the theory.

7.5 Problems faced when detecting soft X-rays

In Section 3.6, low energy X-rays are shown to interact in the silicon close to the surface of a back-illuminated device. If the depletion in the CCD used to detect the incident X-rays is not close to the surface of the CCD the generated electrons are able to drift through a field-free region of

silicon, causing the charge cloud to grow in volume and split over several pixels. The Modified Fano Factor is found experimentally using the FWHM of the X-ray peak and so any increase in the size of the peak due to event splitting and incomplete charge collection will lead to an over-estimate of the factor. To counter this problem in the devices, on-chip binning was used to increase the effective pixel size and with the CCD220 deep depletion was also possible.

7.6 Soft X-ray detection at BESSY II

7.6.1 Experimental setup

The experiments for both of the devices were completed in the same way. The EM-CCD was mounted on a copper cold finger in a vacuum chamber as with the experiment in the lab with the ^{55}Fe source. The cooling for the device was supplied using a PCC compressor and CryoTiger™ head from MegaTech™ ltd. The CCD97 was cooled to -120 °C to suppress the dark current generated by the device to a negligible level [Tutt, 2010], but the CCD220 was cooled to only -50 °C (the lowest possible with the available equipment). Only being able to cool to -50 °C allowed a significant amount of dark current to be generated; therefore, it had to be accounted for in the data analysis. The dark current posed a more significant problem at higher levels of gain as the multiplication process caused an increase in the dark signal as well as the X-ray photon signal. The expected dark current generation is shown in Figure 7.7. The formation of larger pixels through binning also caused an increase in the dark signal collected per binned pixel and at -50 °C the CCD220 had 0.04 electrons generated per binned pixel per second. The CCD97 at -120 °C had a negligible dark signal of the order 10^{-11} electrons per pixel per second. In the experiment with the CCD220 the pixels were binned asymmetrically (3x2) to make the pixels as large as possible, but as the device only has a small imaging area (120 rows by 60 columns) asymmetric binning maintained a reasonable level of spatial resolution.

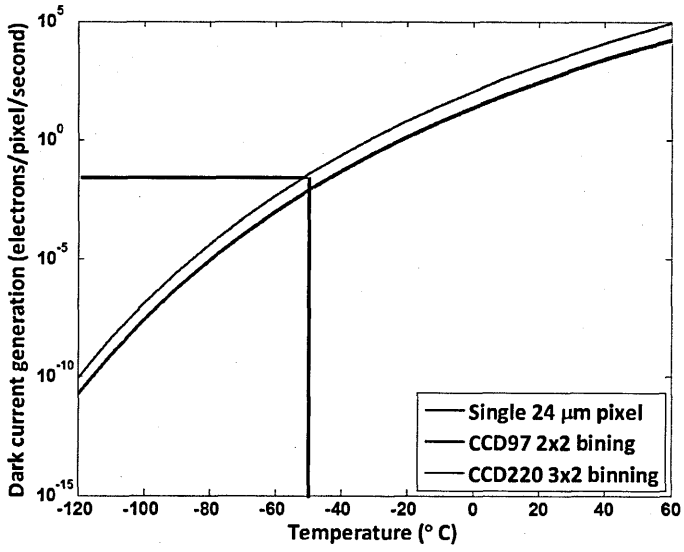

Figure 7.7: Dark current generation (electrons per pixel per second) is shown for a single pixel of 24 µm along with the generation for the e2v CC97 with 2x2 binning and the CCD220 with 3x2 binning. The operating temperature of the e2v CCD220 during the experiment (-50 °C) is marked [e2v, 2004].

Avalanche gain is temperature dependant [Crowell, 1966] making it important to keep the temperature of the EM-CCD constant. The potential was varied from 20 V (taken as G = 1) up to the voltage where the 16-bit ADC of the readout electronics becomes saturated. The FWHM of the detected X-rays and noise peak could then be measured and Equation 7.24 used to calculate the value for the Modified Fano Factor, F_{mod}, at that level of gain, G [Janesick, 2007]. The FWHM is in eV and all noise quantities are measured in electrons.

$$F_{mod} = \left(\frac{FWHM^2}{(2.355\omega)^2} - \left(\frac{\sigma_{readout}}{G}\right)^2 - F_{dark}^2 \sigma_{dark}^2 \right) \left(\frac{\omega}{E}\right) \tag{7.24}$$

Fitting a Gaussian to the X-ray peak and the noise peak allowed the FWHM and $\frac{\sigma_{readout}}{G}$ terms to be found respectively. The CCD97 was cold enough to sufficiently suppress the dark current, $\sigma_{dark} \approx 0$, but as the CCD220 device was warmer, the dark current had to be taken into account. The contribution from the dark current can be calculated by measuring the background level of the image and the overscan regions. Figure 7.8 shows the raw spectrum from an image taken at a gain of 10x where the overscan and image background peaks are clearly visible. The two peaks can be looked at separately to calculate their noise contribution.

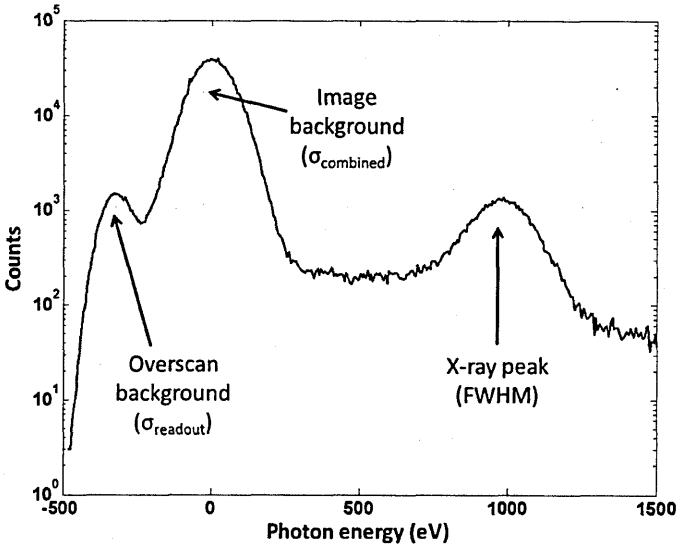

Figure 7.8: The signal levels of the overscan and image are clearly visible in this spectrum. Looking at each area in isolation allows the peaks to be fitted and the contribution to the noise of the readout and the dark current can be found.

The overscan background peak shows the contribution of noise from the readout of the device, $\sigma_{readout}$, and the background from the image area will give the combined readout and dark current noise, $\sigma_{combined}$. Errors add in quadrature allowing the noise on the dark current to be found using:

$$\sigma_{dark} = \sqrt{\left(\sigma^2_{combined} - \sigma^2_{readout}\right)} \tag{7.25}$$

The noise on the image background peak is a combination of the dark current and readout noise and so is sufficient for the calculation of F_{mod}. The effect of the gain on the signal is also taken into account through the measurement of the FWHM and therefore for the CCD220, the Modified Fano Factor becomes:

$$F_{mod} = \left(\frac{FWHM^2}{(2.355\omega)^2} - \sigma^2_{combined}\right)\left(\frac{\omega}{E}\right) \tag{7.26}$$

7.6.2 Results

The results found for the Modified Fano Factor in the first experiment at the PTB beamline using the CCD97 to detect 1000 eV X-rays are shown in Figure 7.9. The data points, while being lower than the result expected from the ENF, are above the theoretical prediction of the Modified Fano

Factor. The results are unable to verify the Modified Fano Factor due to spectral resolution degradation caused by charge splitting and incomplete charge collection.

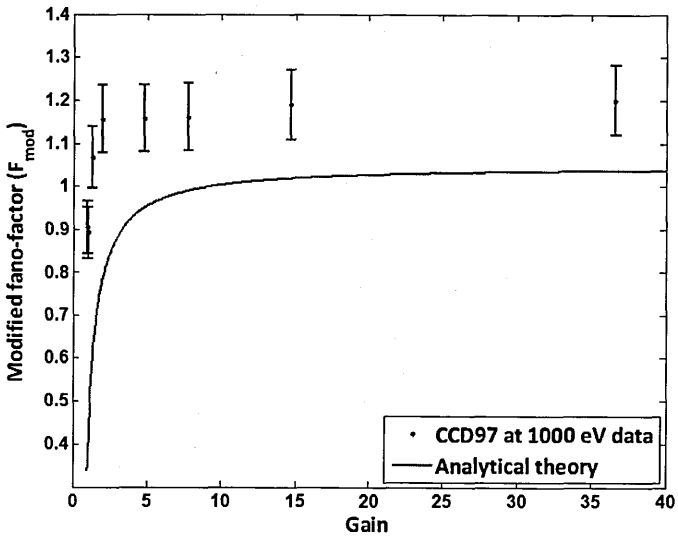

Figure 7.9: The result for the Modified Fano Factor at 1000 eV when detected using a CCD97 with 2x2 binning.

Using the deep depletion properties of the CCD220, the charge generated in the active silicon of the device could be collected in the buried channel faster than in the CCD97, reducing the size of the charge cloud. By increasing the pixel size through asymmetric binning, it was possible to collect a large proportion of the generated charge in a single pixel, leading to the result shown in Figure 7.10.

The result is a good match to the analytical theory and provides verification of the Modified Fano Factor at soft X-ray energies. The result also provides confirmation that the experiment with the CCD97 was affected by spectral resolution degradation due to incomplete charge collection. A comparison plot of the CCD97 and CCD220 data when detecting 1000 eV photons can be seen in Figure 7.11.

A final experiment conducted in the lab using Al K-shell fluorescence to generate the X-rays (1487 eV) and with the CCD220, was performance as a test of the Modified Fano Factor. The result of this experiment can be seen in Figure 7.12.

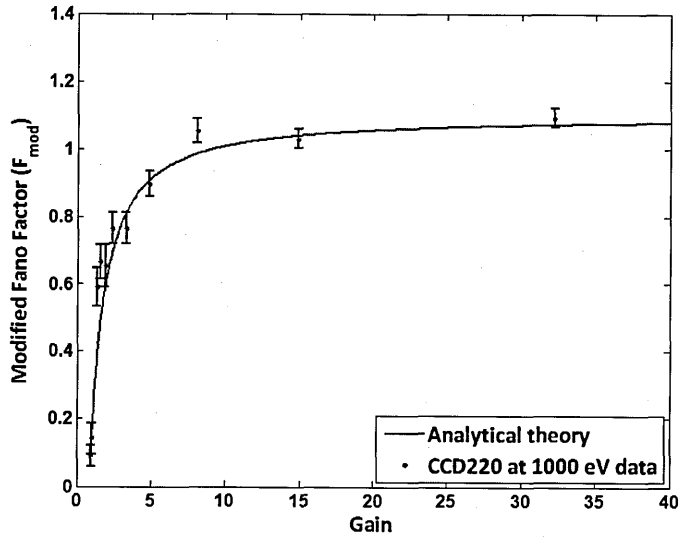

Figure 7.10: The result for the Modified Fano Factor at 1000 eV when detected using a CCD220 with 3x2 binning.

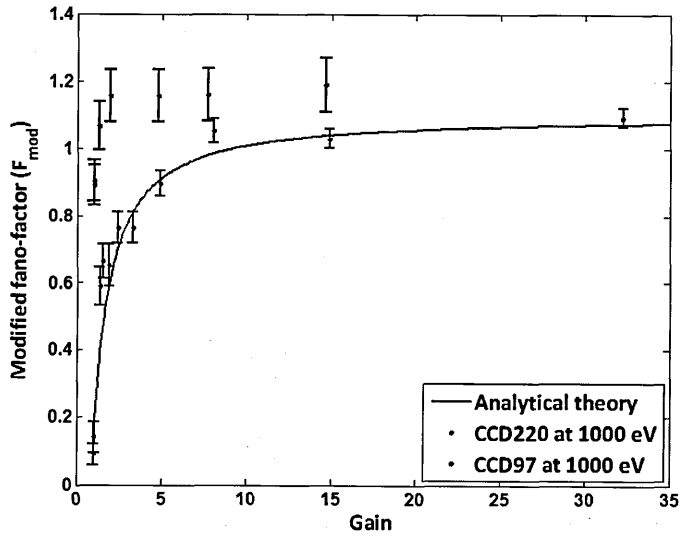

Figure 7.11: Comparison between the CCD220 data and the CCD97 data taken on the same beamline with 1000 eV X-rays.

The result also verifies the Modified Fano Factor at soft X-ray energies providing confidence in the model.

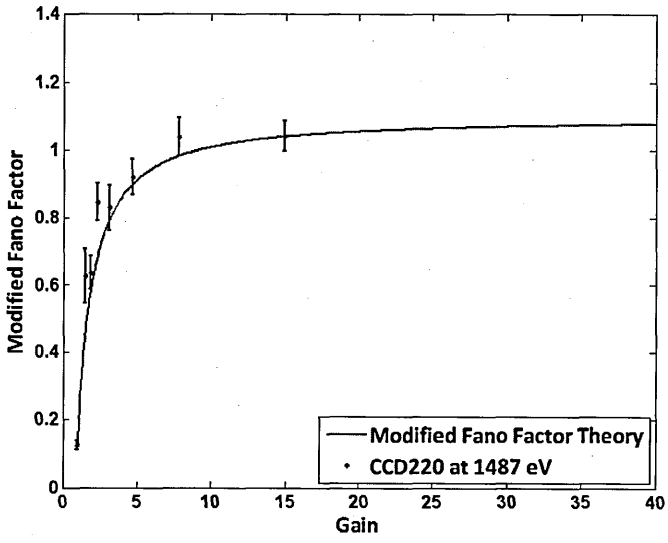

Figure 7.12: The result for the Modified Fano Factor at 1487 eV when detected using a CCD220 with 3x2 binning.

7.6.3 Discussion

7.6.3.1 X-ray damage in CCDs

The interaction of highly energetic X-ray photons in silicon can produce permanent changes in the device; especially if the interaction occurs in the oxide layers that surround the electrode structure through the creation of traps in the oxide layer [Clarke, 1994]. The X-ray damage caused by the X-rays manifests itself in four ways:

1) An increase in dark current from the Si-SiO_2 interface.
2) The oxide becomes charged causing a voltage shift in the operating biases.
3) Charge Transfer Efficiency (CTE) degradation.
4) Trap formation [Meidinger, 2000].

In this experiment, a substantial increase in the dark current would lead to an increase in the noise on the system and could affect the result; therefore, the effect must be considered. If a device is inverted, the increase in dark current can be suppressed, but in this experiment the device was run non-inverted [Westhoff, 2009].

It has been shown that, in a Front-illuminated device, radiation damage effects occur after ~10^5 rad [Magorrian, 1988] and this experiment to investigate the Modified Fano Factor was conducted at a low X-ray flux level to allow photon counting (10,000 X-rays per gain level). Over the course of the experiment an insufficient number of X-rays were incident onto the CCD to

achieve the necessary level of radiation damage to cause any effects discussed above [Beutier, 2008].

7.6.3.2 Generation/recombination centre charge loss

Charge that is generated close to the surface of a back-illuminated CCD by the interaction of a low energy X-ray can be lost to the generation/recombination centres present [Bootsma, 2000], especially if the device is not deep-depleted and the generated electrons can drift in a field-free region [Lumb, 1983]. The resulting partial event would affect the value found for the Modified Fano Factor. In this experiment, the device was operated at an integration potential that caused the depletion to be driven towards the back surface of the CCD minimising charge loss. To investigate this effect, the integration voltage on the CCD was varied from normal clocking voltages (10 V) to the integration voltage used in the experiment (17 V). By measuring the position of the X-ray peak at each voltage the charge loss could be estimated. If signal is lost from the charge cloud, the position of the peak would be at a lower energy than would be expected. The energy scale is calibrated using the X-ray peak position with an integration voltage of 17 V. The result of this investigation is shown in Figure 7.13.

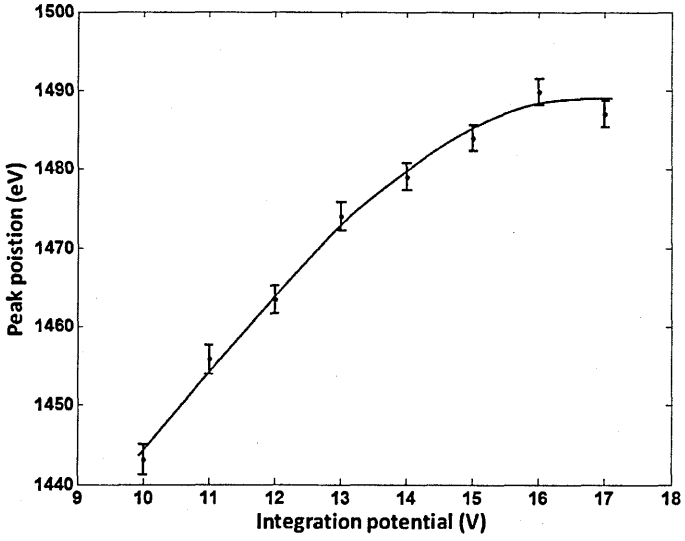

Figure 7.13: The calibrated X-ray peak position from increasing integration voltage for 1487 eV. The energy scale is calibrated using the X-ray peak position with an integration voltage of 17 V.

The result shows that when the depletion is not driven to the back-surface, charge is lost to the generation/recombination centres resulting in a fall in the X-ray peak position; however, at the

integration voltage used in this experiment the curve is flattening off suggesting that the depletion stretches to the back-surface and charge loss is minimised. During the experiment the integration voltage was kept constant and so charge loss to the centres would be equal across all of the measurements. A constant experimental method and large integration voltage enables the charge loss effect to be mitigated.

7.6.3.3 The diffuse X-ray events in the device

The data also showed that, while most of the X-ray events were point like isolated events, some X-ray events appeared as very diffuse clouds that became more visible at higher levels of gain (Figure 7.14). Most of the diffuse X-ray events seemed to occur in the parallel overscan. The diffuse X-ray events occur when photons are incident onto the CCD as it is being read out. The clocks at this time are running between 0 V and 10 V and so the depleted depth in the silicon is greatly reduced from the integration case. A large field-free region forms in the active silicon and, as the device is ~40 μm thick, the charge cloud increases in volume and splits over many pixels. The data is taken without any binning.

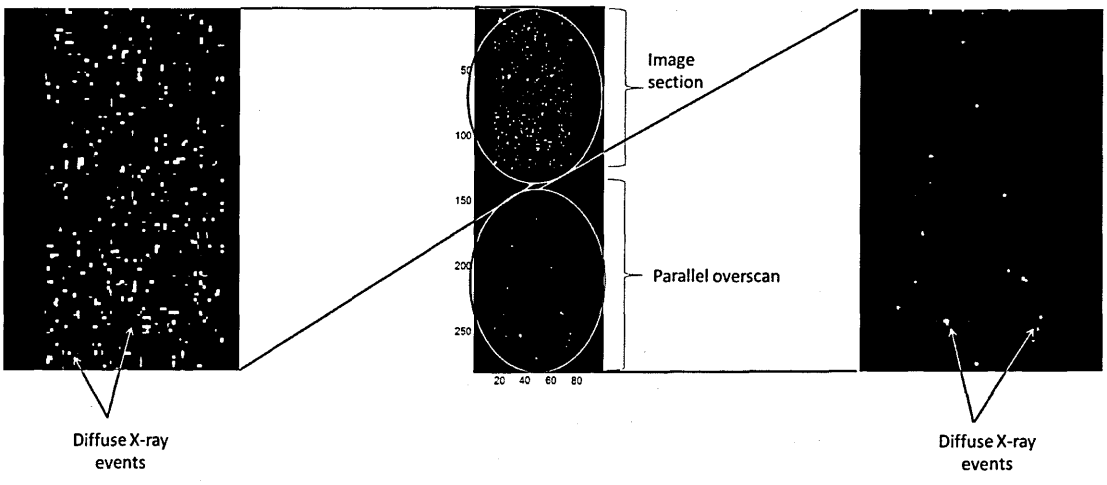

Figure 7.14: The readout from the CCD220 showing diffuse X-ray events mostly in the parallel overscan. In this image the pixels are un-binned.

7.6.3.4 High gain surface-channel effects

At high levels of gain, before the ADC becomes saturated, a "surface channel" effect was seen in the image. The effect can be seen where the X-ray events in the image seem to have deferred charge tails in the direction of serial readout (Figure 7.15).

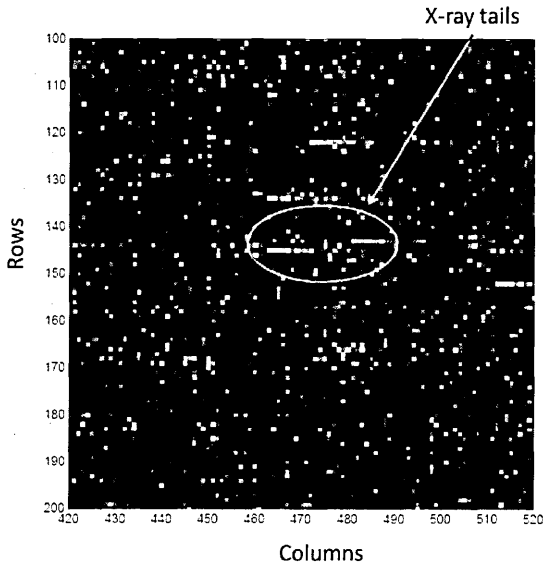

Figure 7.15: X-ray events can be seen to have a tail behind them in the readout direction.

The effect occurs due to the large amount of charge in the multiplication register when the gain is high. With increased charge levels in multiplication register due to the gain process, the charge packet sits closer to the Si-SiO_2 interface in the buried channel. Eventually the charge packet position reaches the Si-SiO_2 interface, is exposed to the traps caused by the "dangling bonds" (Section 3.7.2) and is trapped and then re-released into a later pixel, creating the charge tail. The device behaves like a surface channel CCD leading to a reduction in the transfer efficiency and reducing the spatial and spectral resolution of the collected signal. A large amount of signal is required in the charge packet to see this effect; therefore, at lower energies the effect does not manifest itself.

7.6.3.5 Spectral resolution predictions for EM-CCDs at X-ray energies

The effect of the Modified Fano factor on the degradation of the FWHM of the X-ray peak when detecting the signal with an EM-CCD has been discussed, but what is the practical application of this information? Using the Modified Fano Factor as described in this chapter it is possible to predict the spectral resolution using an EM-CCD at a specific energy and gain. The analysis in this chapter has assumed that all X-ray events are single pixel events for simplicity, but even though this is not normally the case, it offers a useful guide for the use of EM-CCDs at X-ray energies.

The EM-CCD is designed to suppress readout noise by amplifying the output signal; therefore, it is expected to perform better than a conventional CCD (or an EM-CCD being operated with a gain of 1) in experiments where readout noise is dominant. Shot noise is a function of energy, hence, as the energy increases, it becomes the dominant source of noise and so it is expected that an EM-CCD would begin to perform worse than a conventional CCD at higher energy. The ability to predict the cross-over point between when an EM-CCD and a conventional CCD have the best spectral resolution performance allows a decision about the type of device to use in a particular experiment to be made.

The determination of device performance depends on the temperature that the device is being operated at, the readout noise of the device's electronics and the energy of the detected photons and can be calculated using Equation 7.2. In the following examples, as in the rest of the chapter, it was assumed that the device was cold enough that the dark current generation was effectively suppressed and so ignored. It was also assumed that the readout noise of the EM-CCD and the conventional CCD are the same in each case so that the effect of the Modified Fano Factor is the only determining influence on the FWHM of the detected X-ray peak.

At low levels of readout noise (5 electrons r.m.s.), shot noise becomes dominant at low energy levels. Figure 7.16 shows that by suppressing readout noise, a conventional CCD will be better at resolving the X-ray photons at energies above 100 eV than an EM-CCD.

With a higher readout noise (10 electrons r.m.s.), the energy can get to a much higher level before the system becomes shot noise dominated (Figure 7.17). High levels of gain (>10x) give an improvement in spectral resolution up to 400 eV, compared with a conventional CCD, which is easily in the detectable energy range of a back-illuminated CCD. By running the EM-CCD with a low gain of 2 gives a benefit in spectral resolution up to 500 eV due to the way that the Modified Fano Factor varies at low levels of gain. However, at energies over 500 eV, the conventional CCD starts to give an improvement in resolution. Readout noises of 5 electrons r.m.s. and 10 electrons

r.m.s were chosen as typical noise values to give an idea of the spectral resolution performance of devices in the readout noise range in which they typically operate [Tutt, 2011].

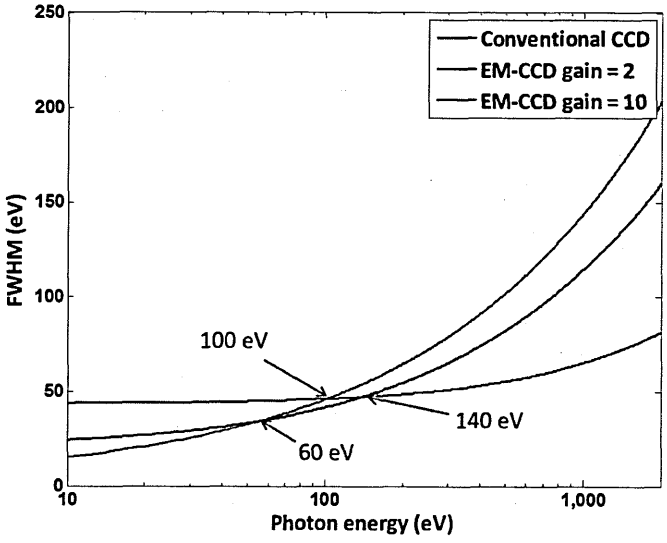

Figure 7.16: A prediction of the spectral resolution (FWHM) of a conventional CCD and an EM-CCD with a gain of 2 and 10 at soft X-ray energies. The readout noise is 5 electrons r.m.s.

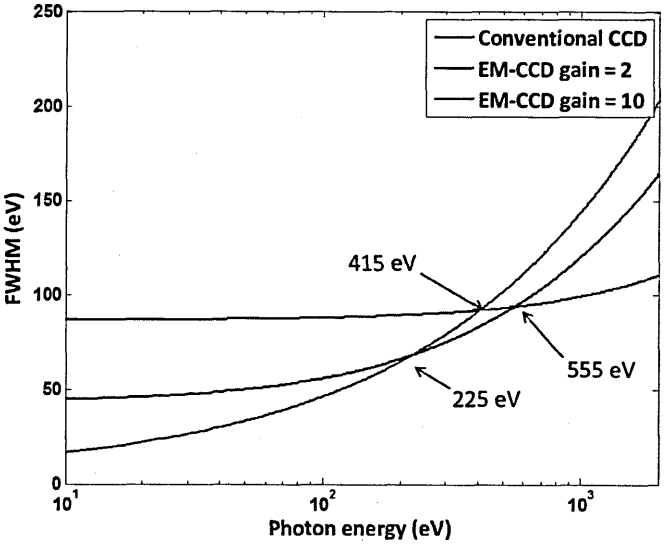

Figure 7.17: A prediction of the spectral resolution (FWHM) of a conventional CCD and an EM-CCD with a gain of 2 and 10 at soft X-ray energies. The readout noise is 10 electrons r.m.s.]

If events that occurred in multiple pixels were considered in the model, the effect of off-chip binning would lead to an increase in the noise floor of the conventional CCD (Section 3.6.2). However, as the cause of the increase in the noise floor is the addition of readout noise from the combined pixels, the effect would not be seen in the EM-CCD as readout noise is suppressed.

7.7 Summary

The results from the CCD220 at all energies tested are in very good agreement with the theoretical value for the Modified Fano Factor. The results show that when the device is deep-depleted and the pixels are made larger using on-chip binning, the effect of multiplication gain is consistent with that predicted by theory. The reduction in the size of the field-free region that the X-rays travel through increases the probability that all of the charge will be collected in a single pixel. Charge splitting in the device has been shown to be the cause of the larger than expected values for the Modified Fano Factor when detecting 1000 eV X-rays in a CCD97. The final experiment conducted in the laboratory was also able to show that the Modified Fano Factor was correct at 1487 eV through the fluorescence of the Al K-shell and so confidence in this factor over soft X-ray energies is high. The result when using the CCD97 to detect 5989 eV photons is close to verifying the Modified Fano Factor, but as the device has small pixels that were not binned, charge splitting led to the X-ray peak being broader than predicted by theory.

The experiments described above have shown that the theory for the Modified Fano Factor holds true for 1000 eV and 1487 eV photons and at 5898 eV the result can be seen to follow theory closely allowing this factor to be used to aid the development of future X-ray spectrometers, allowing EM-CCDs to be used effectively for the detection of low energy X-rays. The analysis shows that EM-CCDs give the most benefit with X-ray detection in a noisy system. If the readout noise is dominant the ability of an EM-CCD to suppress this noise by amplifying the signal before it is read out will be beneficial to the experiment. If a system becomes less readout noise dominated, the ability of an EM-CCD to suppress the readout noise becomes less useful; therefore, conventional CCDs start to become the more attractive devices to use in terms of noise reduction. However, the EM-CCD will also enable photons of low energy to be detected in the device. For X-ray energies below 300 eV it is difficult to detect the whole of the generated charge cloud, especially if it is split over many pixels. An EM-CCD is able to amplify this signal and so increase the detection efficiency.

To choose a device for an experiment at X-ray energies it is necessary to balance the effect of readout noise suppression with the increase in the energy dependant noise of the device, as well as considering how easily the X-rays will be to detect above the noise in the system. It can be seen from Figure 7.17 that with small amounts of gain, the increase in FWHM of the detected X-ray peak can be minimised, but the readout noise is still partially suppressed. There will also be an increase in the detectability of the incident X-rays and so the application of gain in the right situations can be beneficial.

EM-CCDs can be operated at a gain of 1 or through a separate, no gain, output amplifier avoiding the effect of the Modified Fano Factor and only introducing a gain when the experiment would benefit from increased detectability and readout noise suppression.

The work in this chapter has shown how the Excess Noise Factor for optical photon detection can be extended to a more general case for materials and energies that have different Fano factors, specifically for X-ray detection in silicon. The work on the Modified Fano Factor has demonstrated that EM-CCDs can be used on X-ray spectroscopy systems at energies <1 keV and particularly when system noise or readout speed is a concern.

The ability to read out a device faster without a detrimental effect on the noise of the system can have major benefits. Faster readout speeds increase the detector's tolerance to straylight and so thinner optical blocking filters can be used. The Al that is typically used on filters will also attenuate low energy X-rays, hence, faster readout speeds and thinner filters will allow more of the incident X-rays to reach the active silicon of the EM-CCD, increasing QE and potential science yield. This advantage should cause EM-CCDs to be the detector of choice for future soft X-ray spectrometers. The concern in the scientific community is that EM-CCDs are not a well-established detector technology and may suffer major radiation damage effects if used in space. To make EM-CCDs the detector of choice for future missions work has to be done to increase their TRL by testing them in space-like conditions and out to end-of-life radiation damage levels. If a spectrometer can be designed to accommodate the decrease in spectral resolution caused by

using multiplication gain then, in the opinion of the author, an EM-CCD should always be the first choice of detector so long as it is shown that the device has similar performance in space applications.

Chapter 8: Contribution to the International X-ray Observatory

8.1 Author's contribution:

The author's contributions to the Off-plane X-ray grating spectrometers on the International X-ray Observatory are as follows:

- Analysing the pointing requirement of the instrument to allow for camera array self-calibration.
- Camera array layout, CCD overlap and CCD redundancy.
- Stray-light tolerance and optical filter thickness.
- Contamination of the instrument on the ground and in space.
- A thresholding study to optimise instrument resolution.
- The use of EM-CCDs as the focal plane detector.

8.2 Introduction

The International X-ray Observatory (IXO) was a science mission being designed to help with the understanding of galaxy evolution, supermassive black holes, large scale structure, chemical element creation, matter under extreme conditions and life cycles of matter and energy in the Universe [Barcons, 2010]. It was a mission aiming to look at matter under extreme conditions and this chapter will look at the development of the instruments that were designed to allow IXO to provide insight into these phenomena. In particular this chapter will concentrate on the Off-Plane X-ray Grating Spectrometer (OP-XGS) on IXO. An artist's impression of IXO is shown in Figure 8.1.

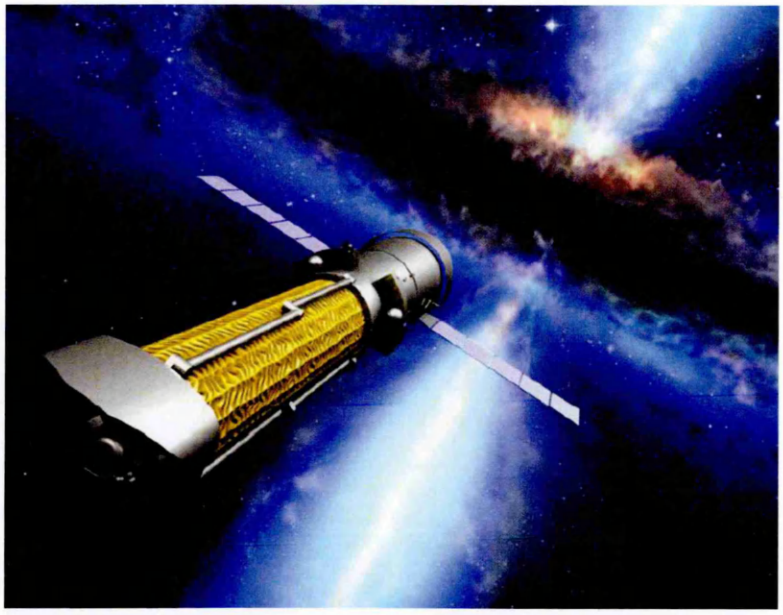

Figure 8.1: Artist impression of the International X-ray Observatory [Barcons, 2010].

8.3 IXO – A brief history

The first Cosmic Vision 2015-2025 call for Mission Proposal was issued by ESA and led to XEUS (X-ray Evolving Universe Spectrometer) being initially selected as an L-class mission candidate; however, a subsequent Phase 0 study concluded that the mission was not feasible within the L-class mission budget envelope [Barcons, 2010].

A coordination group involving ESA, NASA and JAXA was established in 2008 to explore the possibility of a joint mission merging XEUS and the NASA-led Constellation-X. The group proposed a joint study to be submitted to the NASA decadal and ESA Cosmic Vision programs to look at the IXO mission in collaboration with JAXA [Barcons, 2010].

8.4 Science Goals

IXO was a facility-class mission concept that aimed to address the leading astrophysical questions in the "hot Universe" through its breakthrough capabilities in X-ray spectroscopy, imaging, timing and polarimetry. Many of the following science issues require a panchromatic approach which would have been possible with IXO's proposed energy range that covered 0.1 keV to 40 keV [Barcons, 2010].

8.4.1 Black holes

IXO would measure a fundamental property of black holes, their spin, which is driven by galaxy formation and evolution for super-massive black holes and by the nature of core collapse for stellar mass black holes. IXO would reveal the physics of accretion near the last stable orbit, measuring General Relativistic effects in the strong field limit [Nandra, 2010], [Miller, 2010], [Fabian, 2010], [Brenneman, 2010].

8.4.2 Neutron stars

IXO would determine the mass-radius relationship for Neutron stars and so would help to constrain the equation of state and QCD (Quantum Chromo-Dynamics) models of matter at these densities. For neutron stars with ultra-high magnetic fields (magnetars), IXO's polarimeter would measure the predicted QED (Quantum Electro-Dynamics) effects [Paerels, 2010].

8.4.3 Galaxy clusters

IXO would measure the velocity structure, mass and metallicity distribution of the dominant baryon component, the hot intra-cluster gas, which would provide a deep understanding of evolution of large-scale structure and samples of clusters at various redshifts, providing important and independent constraints on the Standard Cosmological Model (SCM) and dark energy [Vikhlinin, 2010].

8.4.4 The Cosmic Web

The Cosmic Web is where half of the baryons in the local Universe are expected to reside. IXO would be able to detect these baryons and so test the predictions for the formation and topology of the Cosmic Web [Bregman, 2010], [Arnaud, 2010], [Cash, 2011], [Lillie, 2011], [Danforth, 2008].

8.4.5 Feedback mechanisms

IXO would yield insight into feedback mechanisms in the Universe on many scales, through the study of supernova remnants, outflows in starburst galaxies and AGNs across cosmic time [Fabian, 2010], [Miller, 2010].

8.5 Instruments

The majority of the instruments on IXO would have been mounted on the Moveable Instrument platform (MIP) allowing the instrument in the focal plane of IXO to be changed depending on the observation target. The X-ray Grating Spectrometer readout camera array was located on the Fixed Instrument Platform (FIP) away from the main focus of the telescope (Figure 8.2). The baseline mission could be accomplished with a payload comprising the following instruments.

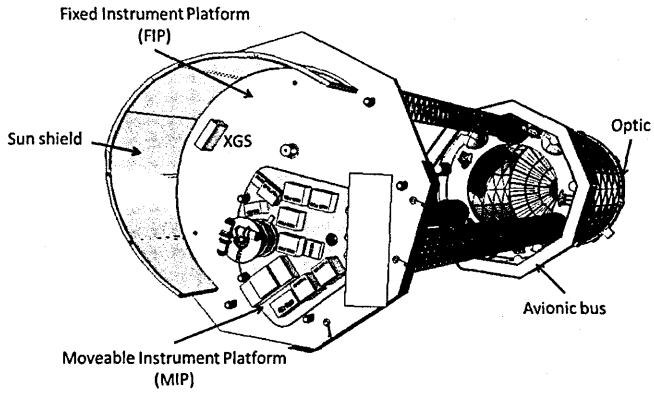

Figure 8.2: The majority of the instruments on IXO would sit on the Moveable Instrument Platform (MIP) with the XGS readout camera on the Fixed Instrument Platform (FIP).

8.5.1 The IXO optic

The IXO optic was designed to have a large area (~3 m^2), high reflectance and throughput and an angular resolution of less than 5 arcsecs Half Power Diameter (HPD) at the focus. To make this possible it would use a Wolter-I optic design (Section 2.3.6) either a Slumped Glass Optic (SGO) or Silicon Pore Optic (SPO) manufacturing process.

The slumped glass optic, proposed by a group from the USA, is formed from mirror segments that would be manufactured by placing glass on shaped and polished mandrels. The glass is then heated until it slumps to take up the shape of the mandrel. The mirror would be made up of 360 concentric mirror shells, the inner shells having a diameter of 750 mm and the outer shell 3.2 m.

The silicon pore optic, proposed by a European group, uses a standard semiconductor wafer technology process to produce rectangular plates that have thin ribs on one side and thin membranes between the ribs. The plates are bent into the required shape and several plates are stacked to create a stiff pore structure. The stacks are then mounted into a tandem structure

creating an approximate Wolter I geometry. One of these stacks is shown in Figure 8.2 [Barcons, 2010].

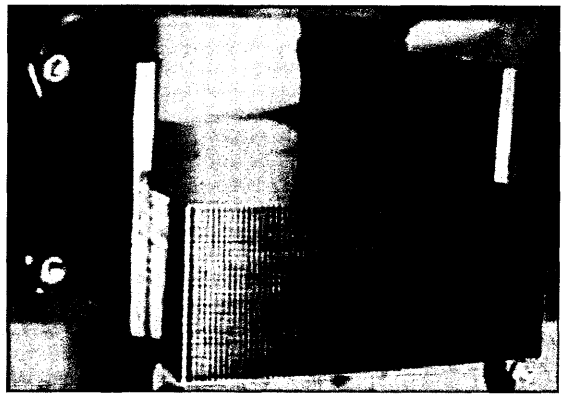

Figure 8.3: A single stack for the silicon pore optic [Barcons, 2010].

8.5.2 Wide Field Imager (WFI)

The Wide Field Imager (WFI) was proposed as an imaging spectrometer with a large field of view (18 arcmin x 18 arcmin) that aimed to provide images in the energy band 0.1 keV to 15 keV simultaneously with spectral and time resolved photon counting and a resolution of 50 eV at 300 eV and less than 150 eV at 5.9 keV. The instrument would have been made of an array of DEPFET (Depleted p-channel FET) active pixels (Section 2.3.9.8) integrated onto a common silicon bulk [Barcons, 2010].

8.5.3 Hard X-ray Imager (HXI)

The Hard X-ray Imager (HXI) would be mounted beneath the WFI to extend the energy coverage up to 40 keV. The HXI detector would be made up of 3 layers, 2 of silicon and 1 of cadmium telluride. Due to its position behind WFI, both XHI and WFI would share the same focal plane and the PSF on HXI is enlarged by 1.25 mm in diameter due to the de-focusing of the point spread function. The HXI would have covered the energy range from 10 keV to 40 keV with an energy resolution better than 1 keV (FWHM) at 40 keV and a Field Of View (FOV) of 12 x 12 arcmin^2. Silicon becomes transparent to X-rays in the energy band above ~30 keV, so the inclusion of cadmium telluride detectors is crucial to the high energy response of the instrument [Barcons, 2010].

8.5.4 X-ray Microcalorimeter (XMS)

The X-ray Microcalorimeter (XMS) (Section 2.3.9.5) was designed to provide spectra with an spectral resolution of ~2.5 eV in the energy range 0.2 keV to 10 keV for the central detector and 10 eV for the wider-field outer section, simultaneously with images of a modest field of view and with time resolved photon counting. Arrays of absorbers would be read out by Transition Edge Sensors (TES) Time Domain Multiplexing (TDM) or Frequency Domain Multiplexing (FDM). The instrument would have been cooled to ~100 mK [Barcons, 2010]. Cryo-cooled instruments have not had a large amount of success on past space missions and so the XMS was relatively high risk [Mitsuda, 2007].

8.5.5 High Time Resolution Spectrometer (HTRS)

The High Time Resolution Spectrometer (HTRS) was designed to provide spectra with resolving power $\frac{E}{\Delta E}$ of 5 to 50 in the energy range 0.5 keV to 10 keV at high time resolution (10 μs) and with a high count rate capability (2 MHz). The HTRS was based around an array of silicon drift diodes and would give IXO the ability to observe bright galactic X-ray sources (e.g. X-ray binaries, magnetars) which can generate up to 1 million counts per second (equivalent to about 5 times the intensity of the Crab nebula). The HRTS would also provide better than 200 eV spectral resolution at 6 keV together with microsecond time resolution for photon energies between 0.3 keV to 10 keV [Barcons, 2010].

8.5.6 X-ray Polarimeter (XPOL)

The X-ray Polarimeter (XPOL) was designed to provide polarisation measurements simultaneously with angular measurement (5 arcsec), spectral measurements ($\frac{E}{\Delta E}$ of ~ 5 at 6 keV) and timing at few μs level using a designed based on a Gas Electron Multiplier (GEM) (Section 2.3.9.3). A GEM is a counter with proportional multiplication that is finely subdivided allowing it to recognise tracks and so derive the ejection direction of the primary photoelectron. The track also provides the impact point with a precision of ~150 μm FWHM, largely oversampling the PSF. A major effect which decreases the position sensitivity is the blurring due to the absorption of photons from an inclined beam at different heights in the gas [Barcons, 2010].

8.5.7 X-ray Grating Spectrometer (XGS)

The XGS instrument was required to have a resolution $\frac{E}{\Delta E}$ of > 3000 over the 0.3 keV to 1 keV energy range and an effective area of >1000 cm^2 [Barcons, 2010]. Two parallel studies were performed on competing instrument designs, the Critical Angle Transmission Grating Spectrometer (CAT-GS) and the Off-Plane X-ray Grating Spectrometer (OP-XGS).

8.5.7.1 Critical Angle Transmission Grating Spectrometer (CAT-GS)

The CAT-GS was a wavelength dispersive spectrometer for high-resolution spectroscopy. One or two transmission gratings are placed behind the main mirrors in the convergent telescope beam and the readout camera array is placed on the fixed instrument platform. The transmission gratings disperse the X-rays according to wavelength and focus them into a spectrum that is recorded by the camera. The grating facets are blazed in order to maximise the diffraction efficiency of the grating allowing the target effective area of the instrument to be achieved (Section 2.3.7) [Barcons, 2010].

8.5.7.2 Off-Plane X-ray Grating Spectrometer (OP-XGS)

The focus of the remainder of this chapter is the OP-XGS.

8.6 The Off-Plane X-ray Grating Spectrometer (OP-XGS)

The OP-XGS was designed to provide high spectral resolution $\frac{E}{\Delta E}$ > 3000 at lower energies, 0.3 keV to 1 keV, as a complement to the X-ray Microcalorimeter system [Barcons, 2010]. The OP-XGS team was formed from individuals from the Open University (CCD camera array - UK), MSSL (CCD readout electronics - UK), Leicester (Advisory role - UK), University of Iowa (Gratings - USA), University of Colorado (Gratings - USA) and Northrup Grumman (Instrument structure design - USA).

8.6.1 Science case for the OP-XGS

The OP-XGS was a vital tool in achieving several of IXO's science aims. IXO aimed to observe early Active Galactic Nuclei (AGN) feedback mechanisms and these high-z AGN will have their diagnostics in the soft X-ray band. Feedback mechanisms are important in galaxy formation and

in the formation of central massive black holes. To spectrally observe this initial 'blowout' in the galaxy requires high spectral resolution so that the kinematics of the wind as well as the ionisation state, metallicity and column density can be accurately measured. Many of these diagnostics occur in the grating band [Barcons, 2010].

When it comes to studying matter under extreme conditions, the neutron star EOS is important. To study these objects it is necessary to look at accreting matter and the Doppler shift line profile of the absorption lines [Paerels, 2010]. To measure these features, high resolution is necessary and many of these features are expected to occur at soft X-ray energies.

Accretion disk emission lines are dominant below 2 keV with most existing below 1 keV. To measure the relativistic broadening of these emission lines will need an instrument such as the XGS [Barcons, 2010].

Finally, to observe the missing baryonic content of the Universe that is thought to reside in the WHIM (Warm Hot Intergalactic Medium), high resolution absorption line spectroscopy of highly ionised abundant elements (C, N, O) in AGN outflows is required and these energies all occur in the OP-XGS bandpass [Bregman, 2010], [Cash, 2011], [Lillie, 2011].

8.6.2 Basic Instrument design

The OP-XGS consists of an array of reflection gratings in the off-plane mount and X-rays are diffracted onto a dedicated CCD array. Light intersects the surface of the grating at grazing incidence 2.7° and nearly parallel to the groove direction, maximising the illumination efficiency on the gratings. The groove profile on the gratings can then be blazed to preferentially diffract light to only one side of the zero order, increasing the efficiency further. The gratings also only intersect a small part of the X-ray beam, allowing the instrument to sub-aperture part of the telescopes PSF giving the instrument a higher angular resolution than if the whole of the PSF was used. The diffracted X-rays are then dispersed onto a CCD camera array where the position that the X-ray hits determines the X-ray's energy. The CCD camera array is mounted onto the Fixed Instrument Platform (FIP), but the gratings can be mounted at different positions on the telescope

so the design of the instrument was subject to an accommodation study [Barcons, 2010] (Figure 8.4).

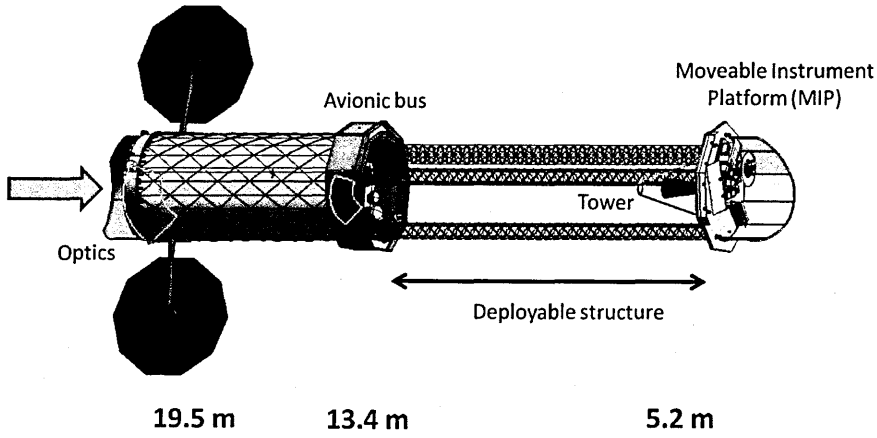

Figure 8.4: The accommodation study for the OP-XGS gratings on IXO. The Figure show possible mounting positions behind the optics (19.5 metre throw), on the avionic bus (13.4 metre throw) and on a tower structure (5.2 metre throw).

8.6.2.1 Off-Plane Gratings

Off-Plane gratings cause the diffracted X-ray to be dispersed across the direction of the incident X-ray in a cone around the zero order position; hence, it is also known as conical diffraction Figure 8.5 [Cash, 1991].

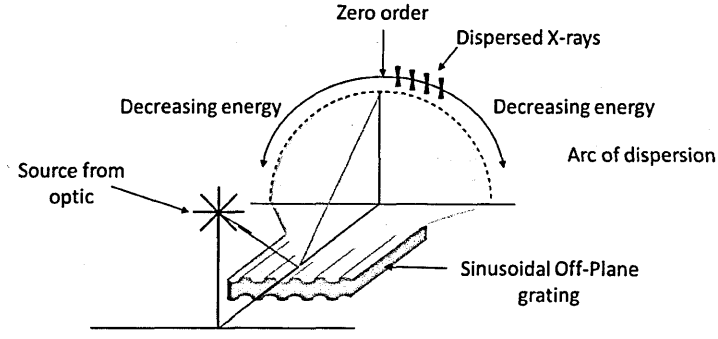

Figure 8.5: The conical dispersion created by a sinusoidal grating with the X-rays incident onto the grating at a graze angle of 2.7°.

The X-rays need to be at grazing incidence to the grating to maximise the reflectivity of the grating.

Once the X-ray is incident on the sinusoidal grating it is dispersed according to its energy along the length of the instrument until it is incident on the FIP. The amount of dispersion, and hence resolution, is dependent on the groove density on the grating, d (grooves mm^{-1}), and on the distance between grating and the CCD array, L (mm), (known as the 'throw').

$$x_{dispersion} = \frac{10^7 cos(\alpha)}{Ld} \quad (8.1)$$

The angle, α, is the angle to the vertical that the X-rays have when incident on the grating (Figure 8.6).

Blaze is a feature that can be given to gratings in order to maximise throughput (Section 3.2.7). With a sinusoidal grating, the X-rays are dispersed approximately equally to both sides of zero order (the zero dispersion position as if the grating were a mirror) (Figure 8.5). To collect all of the incident photons dispersed by the gratings, two CCD camera arrays are required; however, if blaze is used a single camera array can be used [McEntaffer, 2009].

Manufacturing the grating with an angle on the facets (blaze) makes it possible to preferentially disperse the incident X-rays to one side of zero order, maximising throughput and allowing the target effective area of the instrument to be achieved.

Figure 8.6 gives a representation of how the blazed Off-Plane grating will work. The gratings are shown as extending to the focal plane which is not the case for the instrument, but is shown to explain the radial nature of the grooves. The X-rays that come from IXO's optic are converging to a focal point at the far end of the telescope; hence, the focus of the beam at the end of the grating closest to the optic will be less than at the near end of the grating making radial grooves necessary.

If the grooves on the grating were not radial and focussing at the same rate as the converging beam, spherical aberrations would be created, reducing the resolution of the instrument [Cash, 1991].

Off-Plane gratings offer several advantages over the On-Plane equivalent. These include:

- Full groove illumination
- Scatter out of dispersion plane
- Tighter stacking of gratings

However, as the Off-Plane gratings need to be radially ruled they are more difficult to manufacture with a high groove density than their On-Plane counterparts.

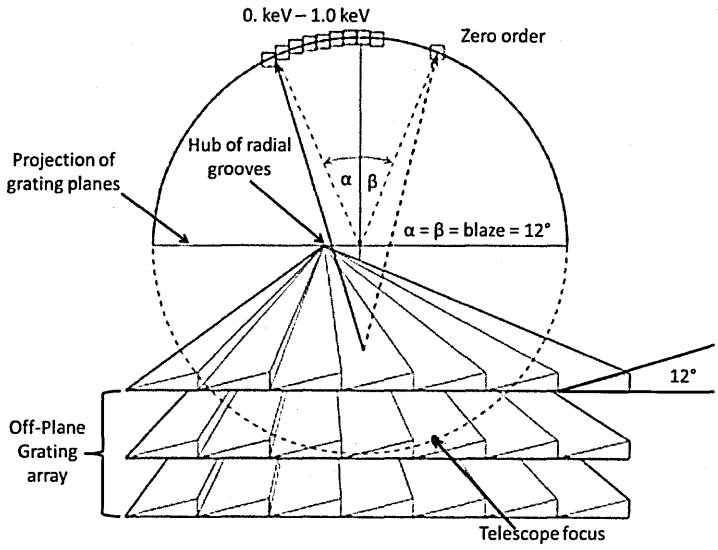

Figure 8.6: Blazed Off-Plane Grating dispersing X-rays preferentially to the left of zero order. The gratings are shown extending to the telescope focus with radial grooves to correct for the converging telescope beam. The red solid line show a single photon ray trace from the grating reflection to the detector on the focal plane and the dotted red line shows a single ray which is not diffracted travelling from the grating to the zero-order [McEntaffer, 2009].

An On-Plane grating has a shadow that is created by the groove edge over the next groove on the grating which is inherent to the grating orientation and can only be corrected for by rotating the grating through 90° into the Off-Plane configuration (Figure 8.7). In the Off-Plane case, as the grooves are in the direction of X-ray travel, the whole of the grooves can be illuminated increasing the grating throughput.

Any roughness on the grating surface will cause the incident X-rays to be scattered and this scatter occurs in the plane of the X-ray direction of travel (On-Plane). The resolution of the instrument is based on the position of the X-ray photon in the dispersion direction. In the On-Plane case, this scatter causes degradation in the resolution; however, in the Off-Plane case the scatter is in the cross-dispersion direction and so the effect on the instrument resolution is minimal which relaxes the smoothness requirement on the grating surface.

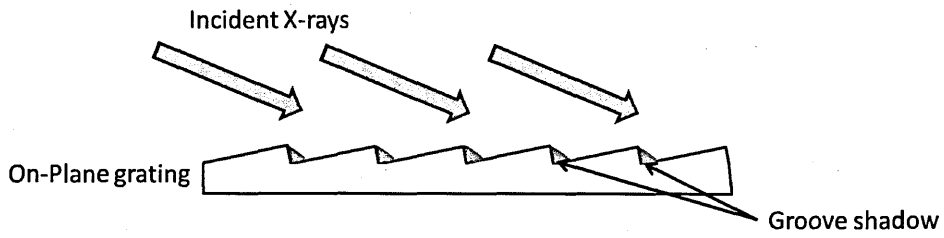

Figure 8.7: Incident X-rays onto an On-Plane grating form a shadow region preventing full groove illumination and reducing the grating's effective area.

Off-Plane gratings disperse the X-rays in a cone about the zero-order and so the specular, zero-order, reflection off the X-rays determines the separation needed between the gratings. On-Plane gratings, due to their dispersion in the plane of the reflection, have to be stacked further apart than the width determined by the zero-order position. Therefore, fewer gratings can be placed in the same space as for Off-Plan gratings, producing an instrument with a smaller effective area.

8.6.2.2 Sub-aperturing

The IXO optic focuses an X-ray beam onto the focal plane with a PSF of 5 arcsec [Barcons, 2010], which is too large for the XGS to achieve the necessary resolution; however, through the use of sub-aperturing it is possible to only sample part of the PSF, allowing a higher resolution to be achieved.

The sub-aperturing process occurs because only a part of the converging beam from the telescope is incident on the grating surface. Through under sampling the PSF, the X-rays project a bow-tie shape onto the grating array with the narrow centre identifying the X-ray energy. The range of possible positions that the photon can fall onto is small, increasing the effective angular resolution of the optic [Cash, 1991].

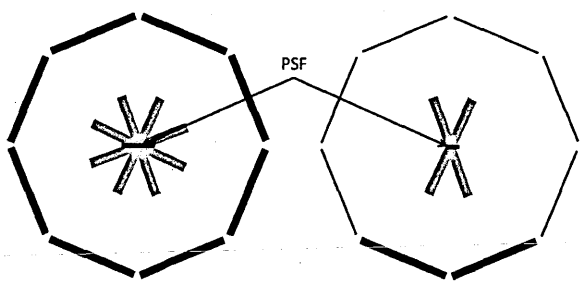

Figure 8.8: With all of the optic being used to generate an image (a) the PSF created is circular. Through sub-aperturing part of the beam (b) only part of this PSF is used and so the possible photon interaction positions are minimised.

Figure 8.8 shows the change in the shape of the PSF on the focal plane when the whole of the X-ray beam is used and when the beam is sub-apertured, forming the bow-tie shape on the focal plane. Through ray-tracing, it was possible to simulate this effect for Off-Plane gratings (Figure 8.9).

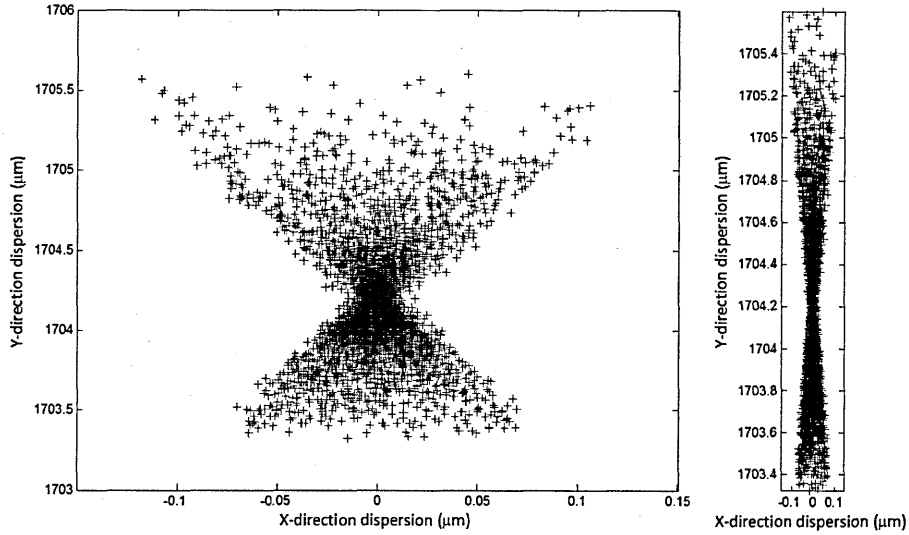

Figure 8.9: The bow-tie shape above was created through a ray-trace simulation of the grating. Image (a) is expanded in the X-dispersion direction to better show the bow-tie shape. Image (b) shows the shape of the bow-tie with the same scale on the X and Y axis [Cash, 2010].

The dispersion created by the grating is in the X-direction. It can be seen that in the X-direction, the possible positions on which an X-ray of a given energy can fall are much smaller than in the Y-direction and, as the X-direction determines the instrument's resolution, this small dispersion (caused by sub-aperturing) is essential in achieving the instrument resolution target.

8.6.2.3 Pointing requirement

To achieve the required resolution, information about the direction the telescope is pointing is required to a high accuracy. The star tracker is able to accurately give the direction that the optic of the telescope is pointing with a 2 Hz time resolution [Barcons, 2010]; however, between the optic and the CCD camera array is 20 m of oscillating telescope structure.

The OP-XGS is able to self-calibrate the position of the dispersed spectra using the zero order monitors; however, in low photon environments it is possible that zero-order will not receive any photons. The following study, performed by the author, was to determine the number of

zero-order hits that the instrument requires in order to self-calibrate and so an estimate on the brightness of source that the instrument can observe at high resolution can be made. If the pointing knowledge of the telescope can be highly constrained then a zero-order calibration may not be necessary, but it is assumed that in a worst case scenario telescope pointing will not be adequate.

Using the 4000 photons that make up the zero-order bow-tie shown in Figure 8.9 an assessment is made of how well the position of the centre of this bow-tie is constrained with a varying number of photons.

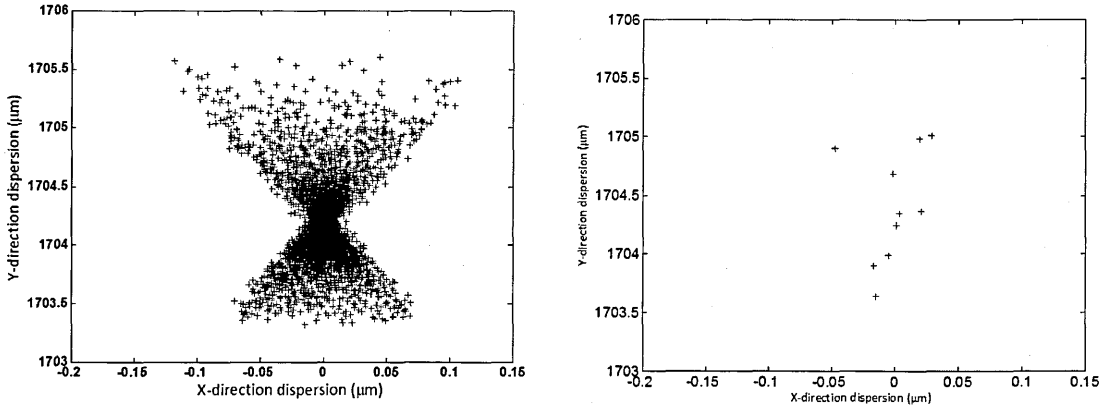

Figure 8.10: The 4000 count zero-order ray-trace (a) and 10 photons from this trace selected at random (b).

Taking 10 photons at random, Figure 8.10(b), forms the first set. The resolution of the instrument is dependent on the dispersion direction (x-axis), so this is the only dimension that is considered. The most extreme points in the x-dispersion from the full zero-order plot are -0.1182 mm and 0.1061 mm and the most accurate position for the central position of the bow-tie can then be found through the following steps.

1. Assume the central position is at the far left extreme in the X-direction (-0.1182 mm)
2. Calculate the distance of each of the random 10 photons from this position (squared values to ensure all values are positive).
3. Move the central position 0.001 mm to the right and repeat step 2.
4. Terminate operation when the far right extreme (0.1061) has been reached.

Plot the x-position against the squared distance from this position and the minimum will indicate the most likely position for the centre of the bow-tie (Figure 8.11).

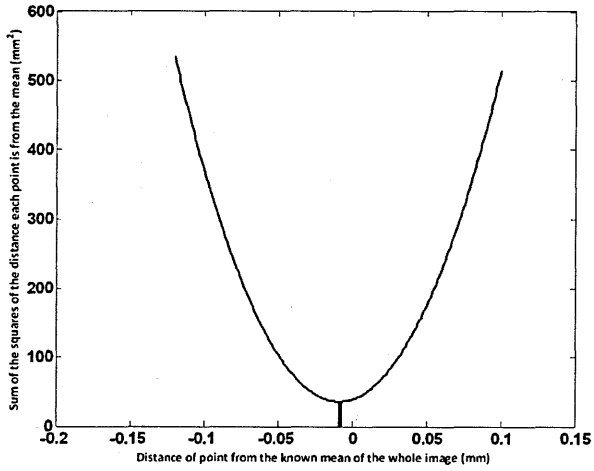

Figure 8.11: Plot of X-position against sum of the squares of the distance of each of the random 10 photons from the X-position.

There are 4000 photons in the data set and so this process can be repeated for the remaining 3990 sets of 10 random photons. Taking the standard deviation of all of these sets (in this case 400 sets of 10 photons) and an error on the position of the centre of the zero-order for 10 photons is generated. Repeating this process for a various number of random photons per set (i.e. 1 random photon 4000 times or 4000 random photons once) leads to a plot of the uncertainty of the zero-order position against the number of photons in the zero-order (Figure 8.12).

The error-bars are larger with a high number of photons in a set as the number of photons in the total dataset is fixed and so any calculation made with a set larger than 2000 can only have one iteration of the process.

The result is based on unity integration time, but as the star-trackers have a 2 Hz pointing knowledge, the effect of different integration times was also evaluated (Figure 8.13).

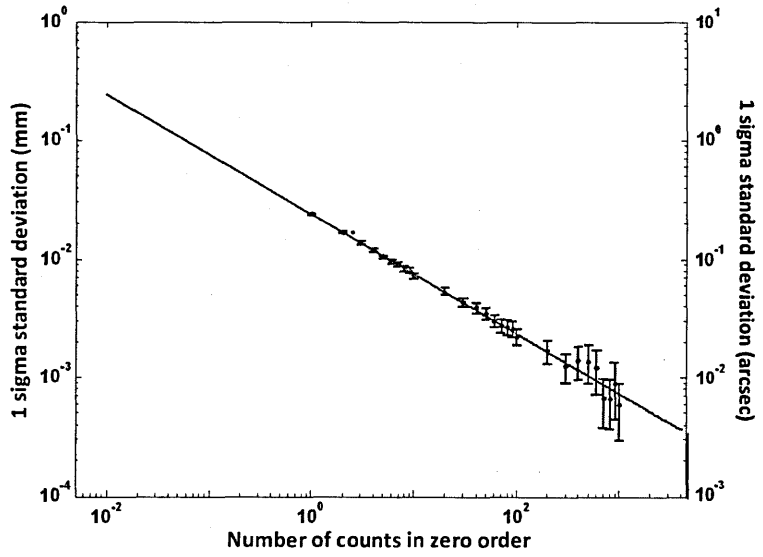

Figure 8.12: The uncertainty of the zero-order position based on the number of counts in the zero-order.

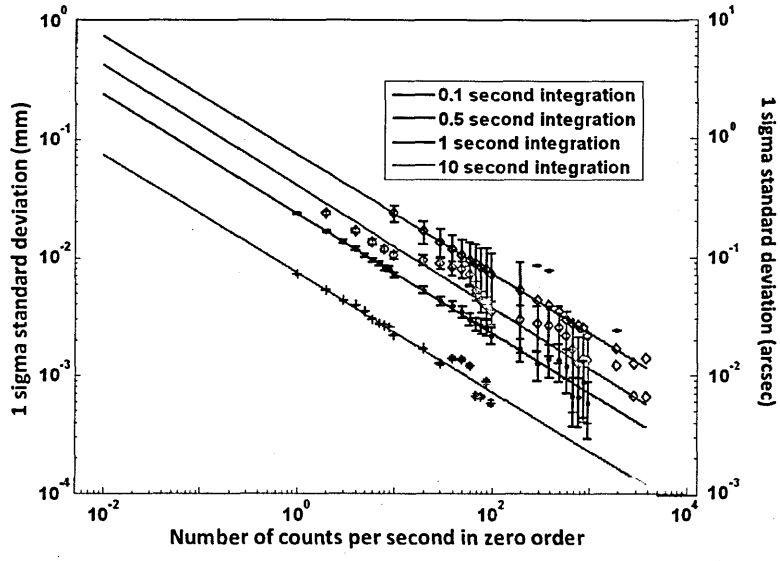

Figure 8.13: The uncertainty of zero-order position based on the number of counts in the zero-order at different integration times.

The longer the instrument can integrate for, the larger the number of zero-order counts and so the zero-order position can be determined with greater certainty; however, if the pointing is only known to 0.5 second accuracy, a longer integration time may lead to a blurring of the zero-order, decreasing its positional knowledge.

The pointing accuracy that is required of the instrument is dependent on the position of the grating array. For the avionic bus position (13.4 m from the CCD array) the necessary accuracy is 1.5 arcsec (3σ) and on the tower (5.16 m from the CCD array) the necessary accuracy is 0.5 arcsec

(3σ). Placing these values on Figure 8.13 allows the number of counts needed in zero-order to be able to achieve the telescope resolution to be found (Figure 8.14).

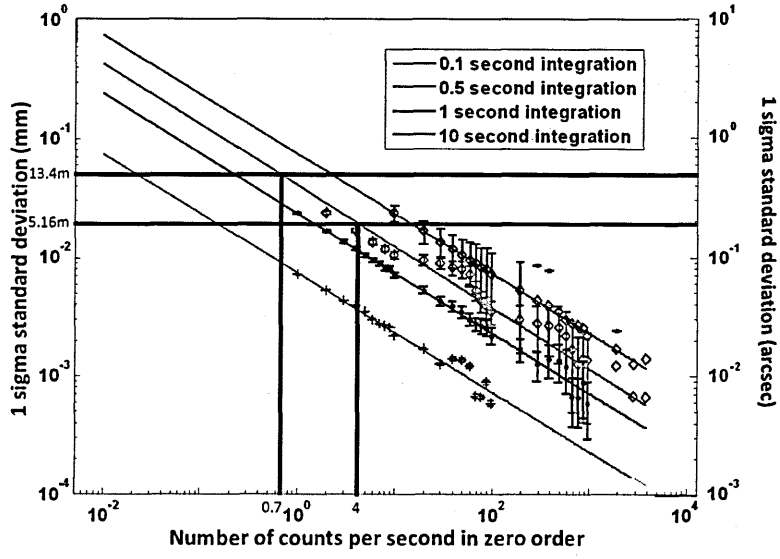

Figure 8.14: The uncertainty of zero-order position based on the number of counts in the zero-order at different integration times with the necessary zero-order accuracy for the tower and avionic bus grating positions marked.

For accurate zero-order position information at the tower position and with a 2 Hz pointing knowledge, 4 counts per second are required in zero-order, whereas at the avionic bus position less than a count a second is required. By taking one count per second in zero-order as equivalent to ~2×10^{-11} erg cm^{-2} s^{-1} the brightness of source that can be observed with the instrument using zero-order as a calibration for the spectrum position can be determined. It is assumed that ~10% of the photons incident onto the gratings are reflected straight through to the zero-order based on the grating groove density and blaze geometry [Barcons, 2010].

Figure 8.15 shows the relationship of the number of sources, N, with a given flux level, *S*, based on ROSAT data [Ebeling, 1997] giving an idea of the number of sources expected for a given flux. Using the flux required for a zero-order calibration at the tower height of 5.16 m it is clear that most of the X-ray sources are too faint for the instrument; therefore, different calibration methods are needed. The result is a worst case scenario in terms of the pointing knowledge of the instrument and so, if the pointing knowledge is better than the 2 Hz offered by the star-trackers then fainter sources will be able to be resolved. If the instrument at the centre of the telescope focus (the WFI for example) can be used for zero-order calibration of the OP-XGS,

sensitivity could be greatly improved. A final option would be to introduce some flat mirrors into the telescope design instead of gratings to increase the zero-order reflection and so number of photons in the zero order; however, this will lead to a drop in the instrument's effective area.

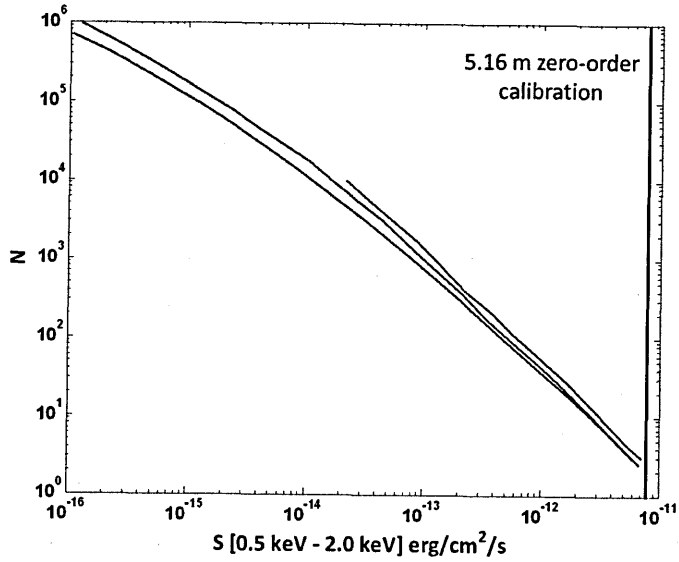

Figure 8.15: LogN - log S plot for X-ray sources in the 0.5 keV to 2.0 keV range [Ebeling, 1997].

8.6.3 Camera design

The dispersed X-rays are detected by a camera array that was designed by the team at the Open University with the CCD layout forming part of the work performance for this thesis. The design for the camera array has been through several iterations. Initially, based on the avionic bus grating position, the spectrum was going to be collected across a single array of CCDs.

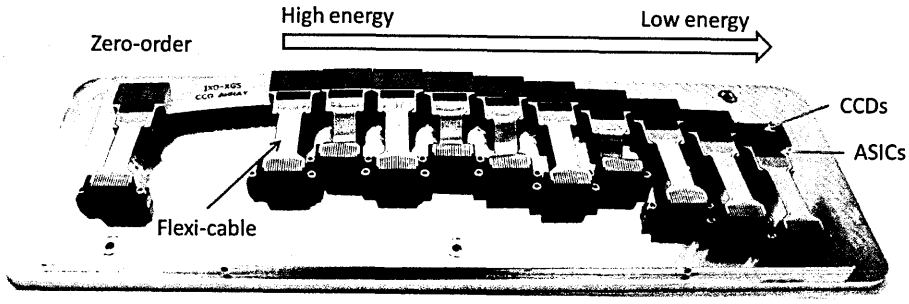

Figure 8.16: Model of initial iteration of the OP-XGS CCD array showing the zero-order monitor and the CCD array designed to detect the dispersed X-rays. Higher energy X-rays are dispersed less than lower energies.

Figure 8.16 shows the conical dispersion that is indicative of the off-plane orientation of the gratings. The zero-order CCD is used for spectrum calibration and is in the specular reflection position on the array. Higher energy X-rays are dispersed less than low energy X-rays and the CCD

array follows the curve that is created by the conical dispersion. There is some off-chip processing close to the CCD in the form of Application Specific Integrated Circuits (ASICs) and then flexi-cables take the data to the main electronics; however, this design has a low level of redundancy. If a single CCD fails a whole energy range will be lost and the dead space between the CCDs will lead to a small energy band that will not be covered by the CCD array. To minimise this affect the CCDs were designed to overlap, reducing the dead space by half which is possible as the depth of focus of the telescopes optic is larger than the thickness of the CCD packages [Murray, 2010] (Figure 8.17).

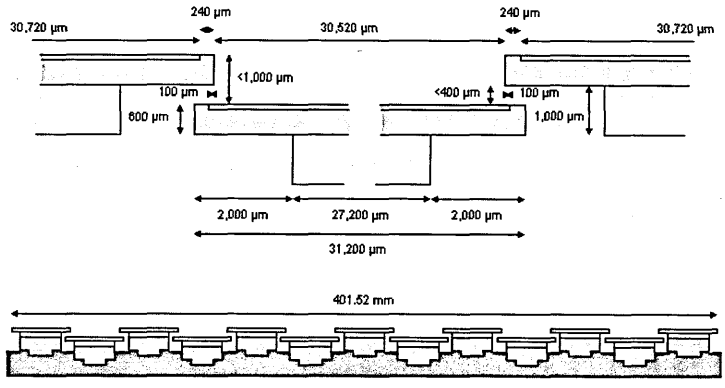

Figure 8.17: Schematic to show the overlapping CCD edges in the OP-XGS camera array in an attempt to minimise dead space between CCDs [Murray, 2010].

Through the development of the tower concept, it was decided that each grating module should project its own spectrum onto the CCD array in slightly different positions on the camera to create redundancy in the instrument. Initially there were going to be 4 grating modules and so 4 spectra on the CCD camera array which led to two different possible CCD camera array layouts (Figure 8.18).

The configurations in Figure 8.18 develop some redundancy in the system. If a CCD fails, the spectra are projected onto the array in such a way that a different energy will be lost in each spectrum, so a single CCD failure will only cause certain energies to have a 25% drop in effective area, not a complete failure at that energy.

(a)

(b)

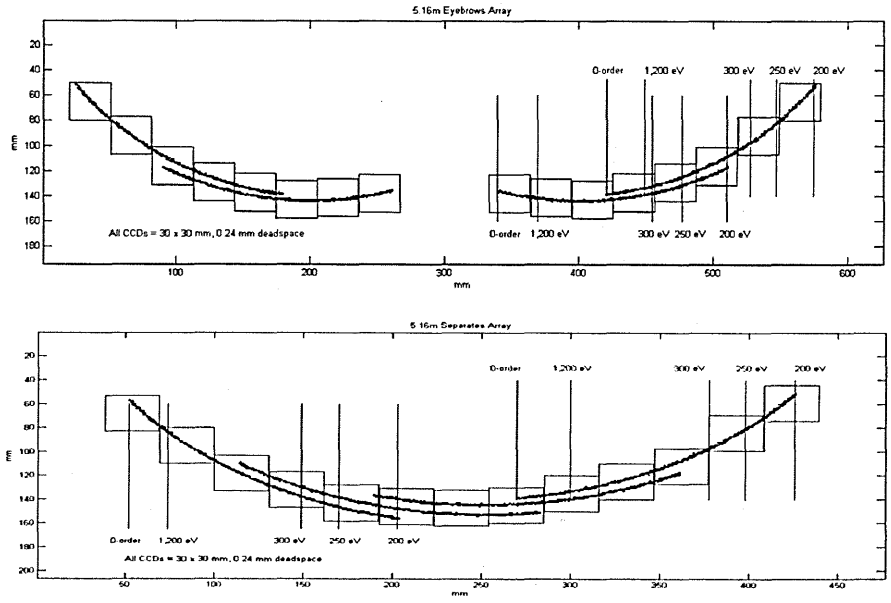

Figure 8.18: 'Eyebrow' CCD pattern for 4 spectra CCD readout (a) and the 'overlapping' orientation for the same number of spectra (b)

The final instrument design moved towards a 6 module grating array in order to achieve the necessary effective area so 6 spectra had to be accommodated by the camera array.

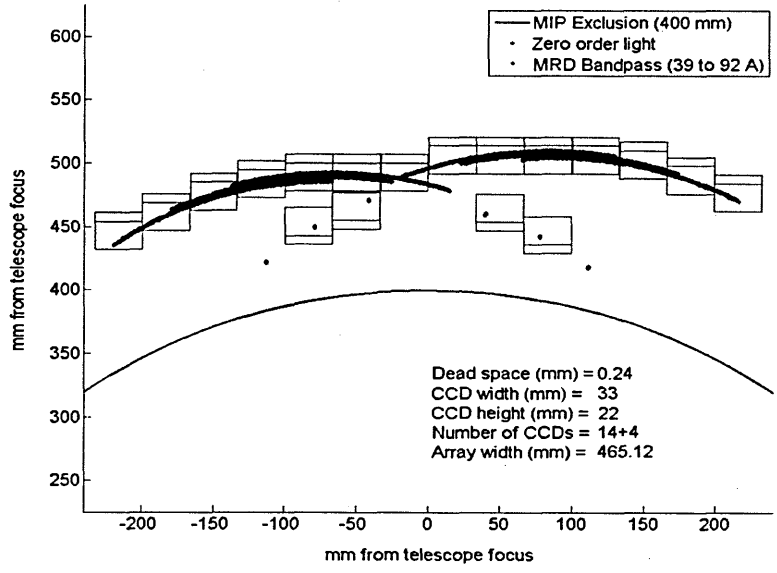

Figure 8.19: Final CCD camera array layout for a 6 module grating array with 3 spectra per CCD array [Murray, 2010].

Figure 8.19 shows the final CCD camera array layout design for the OP-XGS with 3 spectra being projected in each direction from the zero-order position. Of the 6 spectra, 4 have zero-order monitors, but if extra zero-order knowledge was required a further two CCDs could be added to the design. The design now has increased redundancy as a single CCD failure now leads to a $1/6^{th}$ drop in the effective area of a certain band of wavelengths. It also helps to spread the dead space

on the CCDs to different parts of the energy spectrum, so that there is more balance between all of the energies detected by the array. Fully package in the shielding and cooling assembly the OP-XGS camera array would look like Figure 8.20.

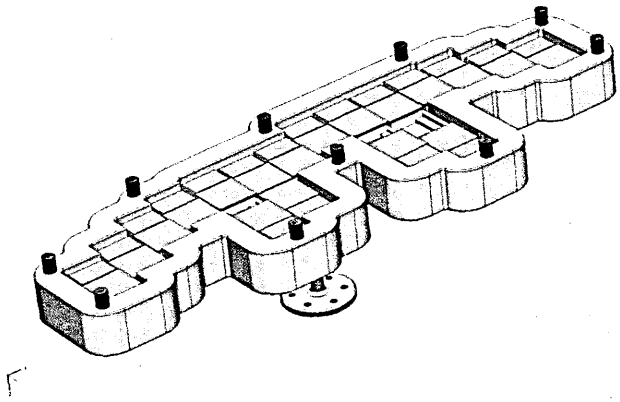

Figure 8.20: CAD drawing of OP-XGS CCD array complete with shielding and cooling assembly [Murray, 2010].

8.6.4 Effective area

The effective area of the telescope is made up of three main constituents

1. The throughput from the telescope optic
2. The throughput from the grating
3. The QE of the CCD

The optic and grating throughput was calculated using data from ESA and a ray-trace model from the University of Colorado. The CCD QE was predicted by the author using the QE model described in Chapter 4.

8.6.4.1 Telescope optic

The X-rays incident onto the optic will be reflected and focused using a Wolter I orientation. Each reflection will result in a loss of X-rays as they are not 100% efficient. The optic is the first structure that the X-rays come into contact with so maximising the optics reflectivity ensures that the throughput of the system is as high as possible.

With both the slumped glass and the SPO designs for the optic, structure is needed for the mechanical support of the mirror segments. The segments will block X-rays that are incident onto

them, reducing the throughput and the telescope effective area. The minimisation of support structure, while maintaining structural integrity to survive launch is vital in the optic design.

8.6.4.2 Gratings

The grating is also a reflective surface; hence, it has similar reflectivity problems to the optic. The gratings are iridium coated and this gives a reflectivity shown by Figure 8.21 [Henke, 1993].

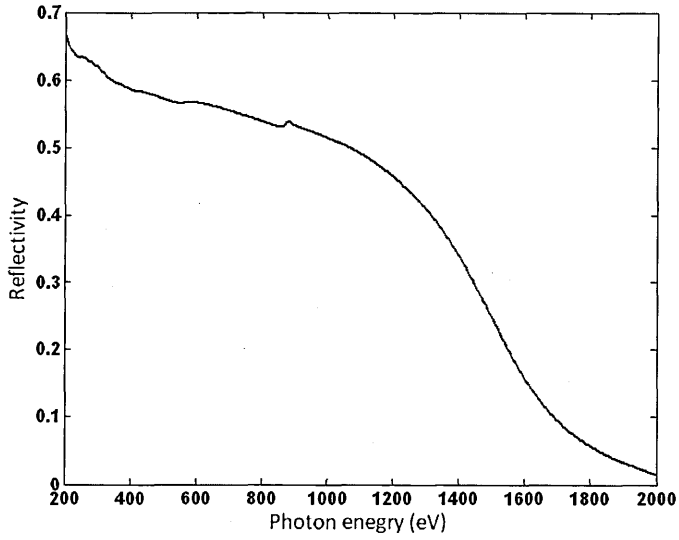

Figure 8.21: Reflectivity of X-rays in the 200 eV to 2000 eV energy range from an iridium coated grating at a 2.7° graze angle [Henke, 1993].

At higher energies the reflectivity of the grating tails off, but in the OP-XGS energy range the reflectivity is reasonably high and stable. It could be increased further by reducing the graze angle of the grating, but this makes the positioning of the CCD array more complicated due to the position of the MIP.

8.6.4.3 CCDs

CCDs contribute to the overall effective area loss in the instrument in the following ways:

- The QE of the CCDs
- The dead space between the CCDs
- The filters that are used on the device.

8.6.4.4 Total Effective area

To find the total effective area of the instrument the author of this thesis was required to calculate the effect of different filter types on the CCDs QE and combine it with the optic and grating effects. The calculation led to requirements on filter thickness if the OP-XGS was to meet its baseline performance specifications for the duration of its lifetime. The author was able to take the initial effective area of the section of the optic that focuses X-rays onto the grating and calculate all of the losses that the X-rays go through before they are detected in the CCD, which gave the effective area of the instrument at that energy. The effective area across the OP-XGS bandpass and can be seen in Figure 8.22. The black line shows the effective area performance possible using an unfiltered back-illuminated CCD and hence shows the theoretical maximum. The red line shows the effective area performance for the propose CCDs with thinner filters based on being able to tolerated 10x more optical light (Section 8.5.5). The green line shows the effect of having dead space between the CCDs with the thinner filter. The camera array has been designed to minimise the loss caused by this affect (Section 8.5.3); however, it cannot be entirely removed. The blue shows the effective area if the RGS thin filtered CCDs were used on the OP-XGS.

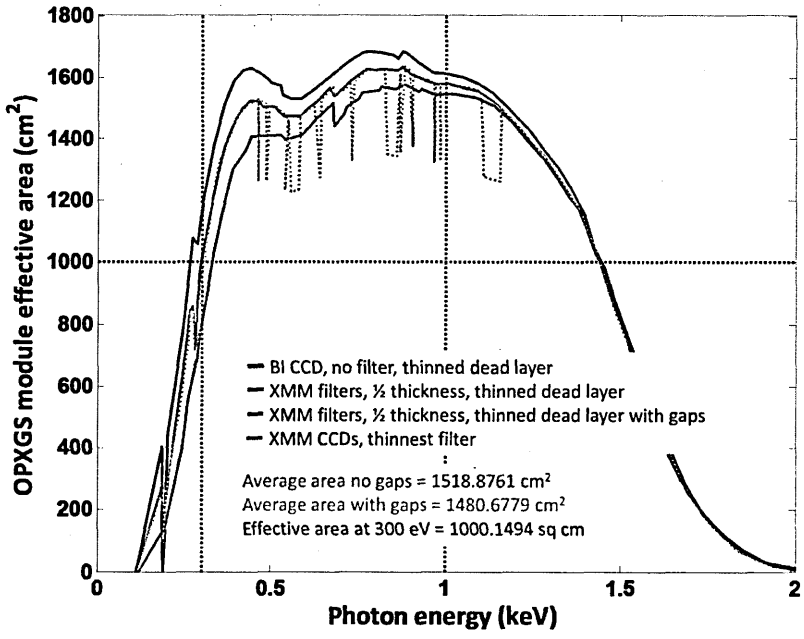

Figure 8.22: The effective area across the OP-XGS energy range with a variety of filter and dead layer combinations in comparison to the XMM RGS filters.

Figure 8.22 shows that, if it is possible to use the current design of instrument with filters that are half the thickness of the RGS filters and with enhanced back-surface CCDs (Section 4.4.1.3), it is possible to meet the OP-XGS baseline effective area requirement across the 300 eV to 1000 eV energy range.

8.6.5 Stray light requirement and filters

The telescope will contain stray light that increases the background of the instrument affecting the low energy response and so the stray light tolerance has to be analysed and filters used if necessary. Using the thickness of filters that are required to allow the instrument to meet its baseline effective area performance, the stray light performance of the OP-XGS was investigated by the author.

Through the use of the QE models used earlier in this thesis (Section 4.2) it was possible to model the use of filters on the QE of the CCD over the OP-XGS energy range; however, this model does not extend into optical energies. Fortunately the work that was carried out for the RGS on XMM-Newton could be extended for the OP-XGS [den Herder, 2001], [Brinkmann, 1996].

8.6.5.1 Reflection Grating Spectrometer on XMM-Newton

The RGS had three different Al filters on the CCDs' depending on the CCDs position in the camera array. The CCDs that were used to detect lower energy X-rays had the thinnest filters, the central CCDs had a slightly thicker filter and the high energy CCDs had the thickest filters [den Herder, 2001], [Brinkmann, 1996] and hence, the QE was maximised at lower energies where the absorption depth of the X-ray photons is smaller (Figure 8.23).

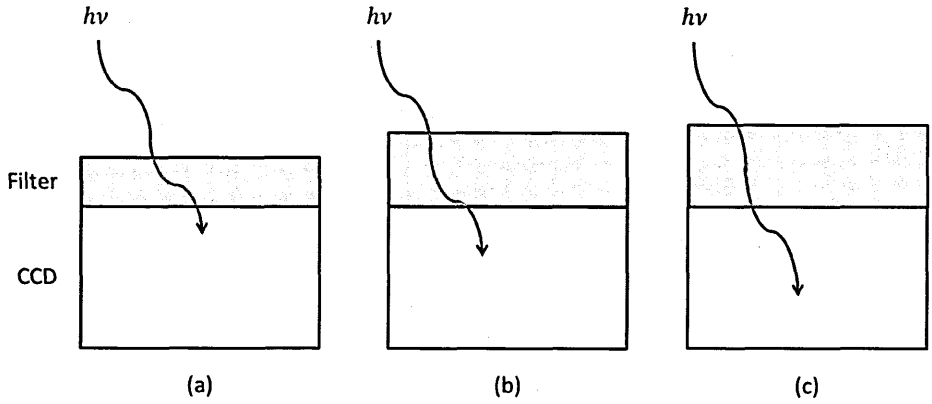

Figure 8.23: A diagram to show the relative thicknesses of the RGS filters on the CCDs. Filter (a) is 45 nm thick and is applied to the CCDs detecting the lowest energy photons (the four CCDs furthest away from the optical axis), filter (b) is 68 nm thick (the next three CCDs) and filter (c) is 75 nm thick and is on the devices that detect the highest energies (the two CCDs closest to the optical axis).

The attenuation of optical light that these filters provide can be seen in Figure 8.24. The CCD array on the OP-XGS will be 10x larger than on the RGS, but the OP-XGS CCDs will be read out 100x faster than the RGS CCDs (9 frames s^{-1} and 1 frame every 9 second respectively [Barcons, 2010], [den Herder, 2001], [Brinkman, 1996]). The thinnest filter used on the RGS will be the OP-XGS baseline with potential for the production of thinner filters to help the CCD QE and so instrument effective area. The effect of having a 45 nm Al filter on the CCDs with a 26 nm MgF_2 protective layer between the silicon and the Al on the QE is shown in Figure 8.25. The protective layer acts as an electrical insulator between the Al shield and the silicon [Bootsma, 2000].

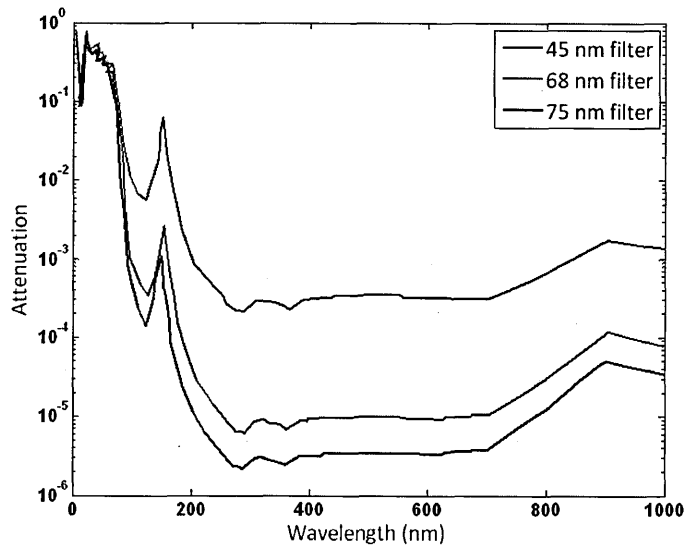

Figure 8.24: The attenuation of optical light for three different thicknesses of Al based on the RGS filters [Ness, 2009].

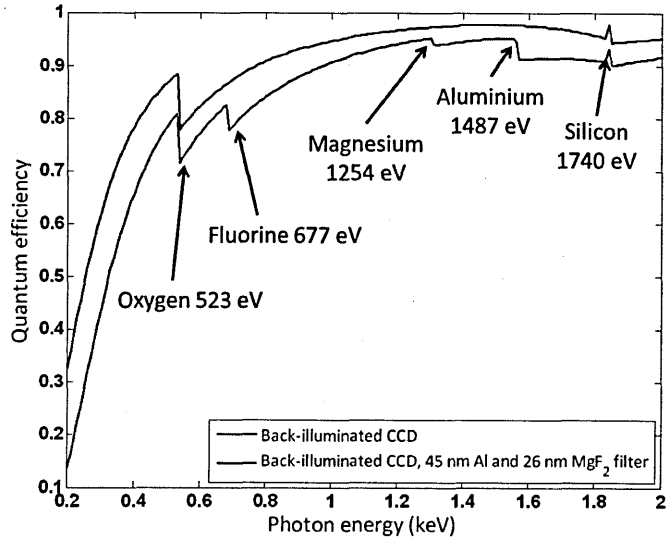

Figure 8.25: QE plot for a back-illuminated CCD with and without a filter. The extra edges caused by the filter are labelled.

The major impact of the filter on the CCD is at the low energy end of the bandpass. To improve the low energy response of the instrument, the thickness of these filters needs to be minimised.

8.6.5.2 Straylight tolerance

Using the 45 nm Al filter it was possible to calculate the straylight tolerance of the CCDs using Equation 8.2, where S is the total straylight (electrons pixel^{-1} frame^{-1}), S_0 is the tolerable extra signal in the image from straylight, QE is the QE of the CCD at the wavelength under investigation, T is the optical transmission, ft is the frame rate, PA is the pixel area and B is the baffle light rejection.

$$S = \frac{S_0}{(QE \times T \times ft \times PA \times B)} \tag{8.2}$$

Some typical values are shown;

- S_0 ~ 1 electron pixel^{-1} frame^{-1}
- T ~ 5x10^{-4} (from Figure 8.24)
- ft = 0.11 (9 frames per second)
- QE ~ 0.8 (optical QE)
- PA = 7.5x10^{16} m^2 (15 µm x 50 µm pixels)
- B = 1 – 10%

Therefore, the straylight tolerance for the instrument is $4x10^{9}B^{-1}$ photons cm^{-2} s^{-1} inside the telescope tube. The baffle factor, B, was not subject to sufficient study and so remains an unknown. The result can be expressed in terms of photons as, for optical applications, one incident photon generates one e-h pair.

Based on this information, the filters could be developed to be thinner. A thin filter has a greater chance of having pin-holes in the Al, causing the stray light attenuation to be non-uniform affecting the quality of the data produced. Such thin filters have a lower Technology Readiness Level (TRL) than the filters already flown on RGS and so the RGS filters remained the baseline.

8.6.5.3 Thin filter study

Using the data for the RGS filters (Figure 8.24) it is possible to extrapolate a plot of filter thickness against attenuation for 500 nm photons (Figure 8.26). The focusing of the IXO optic and the area of the OP-XGS CCDs meant that there is 10x more collecting area on the OP-XGS than on the RGS; however, as the OP-XGS was being run 100x faster, the system could tolerate 10x more stray light.

From Figure 8.26 the thickness that has 10x less attenuation can be found and this was set as the target thickness of the CCD filter. An Al filter of 30 nm will provide a 10x drop in optical attenuation and so this thickness of filter could be used on the OP-XGS and still keep the instrument within stray light tolerances. The effect of this thickness of filter on QE is shown in Figure 8.27.

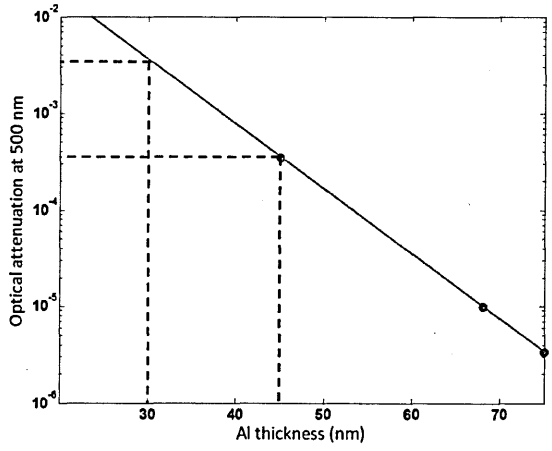

Figure 8.26: The optical attenuation lengths for the different filters used on the RGS are used to extrapolate the thickness needed for a 10x decrease in optical attenuation

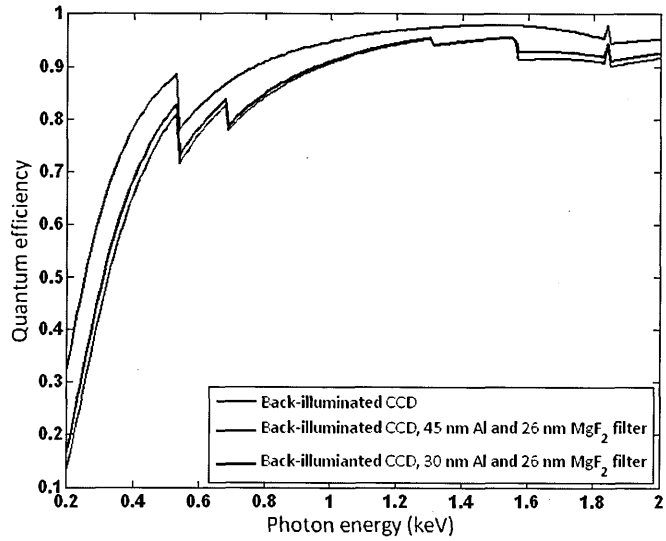

Figure 8.27: The QE for a back-illuminated device without a filter, with a 45 nm and with a 30 nm filter.

The thinner filter causes an improvement in the QE of the device, especially at the lower end of the bandpass and it would help the instrument achieve the effective area requirement.

Finally, as the authors work suggested that effective area could be maximised through the thinning of the MgF_2 layer, the idea was proposed to e2v technologies and the possibility of halving the MgF_2 layer was found to be technologically viable and implemented in the baseline design. Figure 8.28 shows the effect on QE of having a 30 nm Al filter with a 13 nm MgF_2 protective layer.

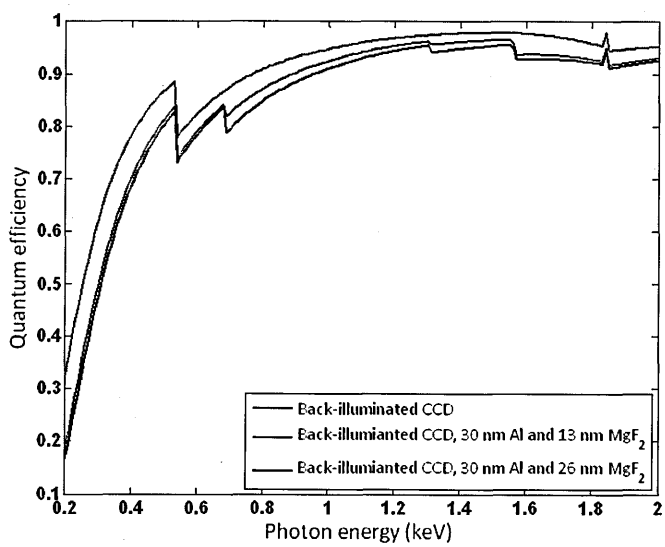

Figure 8.28: The QE for a back-illuminated device without a filter, with a 30 nm Al and 13 nm MgF_2 filter and with a 30 nm Al and 26 nm MgF_2 filter.

Figure 8.28 shows that the thinner MgF_2 protective layer between the silicon CCD and the Al filter will have a benefit on the CCD QE in the mid-range energies up to the 1 keV maximum energy of the instrument which will help the OP-XGS achieve the required effective area.

8.6.6 Contamination

A major part of the author's contribution to the OP-XGS study was to look at the effect of contamination from start of build to predicted end of life levels. The types of contamination that would have an impact on the instrument are covered in two groups, molecular and particulate.

8.6.6.1 Molecular contamination

When a CCD is running at the temperature that would be used on IXO (-80 °C) any incident molecule on the surface of the devices can be assumed to "stick" and never be removed as a worst case situation. The CCD is also the coldest object in the immediate spacecraft environment and so can be considered to be a cold trap that will attract all of the molecules present. On the ground the CCDs can be run in a clean, dry environment and heat cycled removing any contamination build up, leading to the assumption that molecular contamination is an in-flight concern. Increased level of control of the CCD's environment on the ground allows molecular contamination effects to be minimised.

In orbit molecular contamination occurs from outgassing of all surfaces in the satellite. Any volatiles in the surfaces will vaporise, forming a gas pressure in the telescope tube. The volatiles are the source of molecular contamination on the CCDs and the modelling of the effect they cause allows instrument degradation over its lifetime to be predicted.

The OP-XGS is targeting low energy X-rays; therefore, the molecular contamination that will have the largest effect on the instrument will be hydrocarbons and water due to their K-shell absorption energies [Henke, 1993]. The molecules present will have a major effect on the carbon edge performance of the detectors (277 eV) and the oxygen edge (523 eV), degrading their QE, reducing the effective area of the instrument and affecting the potential science yield.

Through the prediction of the contaminating molecules in the telescope, the contaminant level that can be tolerated by the instrument can be found using the author's QE model and adapting it to different molecules (hydrocarbons and ice).

The hydrocarbon molecule that was analysed was C_8H_8 and the drop in QE across the OP-XGS energy range was modelled for different thicknesses of this molecule. C_8H_8 was chosen as it is an unoxygenated hydrocarbon that is of typical size of what could be expected in the spacecraft environment (it is representative). By making a prediction across the OP-XGS energy range for the QE of the device with a uniform layer of the hydrocarbon across the CCD, the average QE drop across the bandpass can be found (Figure 8.29).

The degradation of QE due to contamination on the CCDs is quantified by finding the thickness of molecular contamination that is needed to create a 10% and 50% drop in QE. In the case of a hydrocarbon (C_8H_8) across the OP-XGS bandpass, a 10% drop in QE requires 148 nm and a 50% drop in QE requires 1300 nm of C_8H_8; however, this does not represent the effect at the carbon edge where the most severe QE degradation will occur (Figure 8.30).

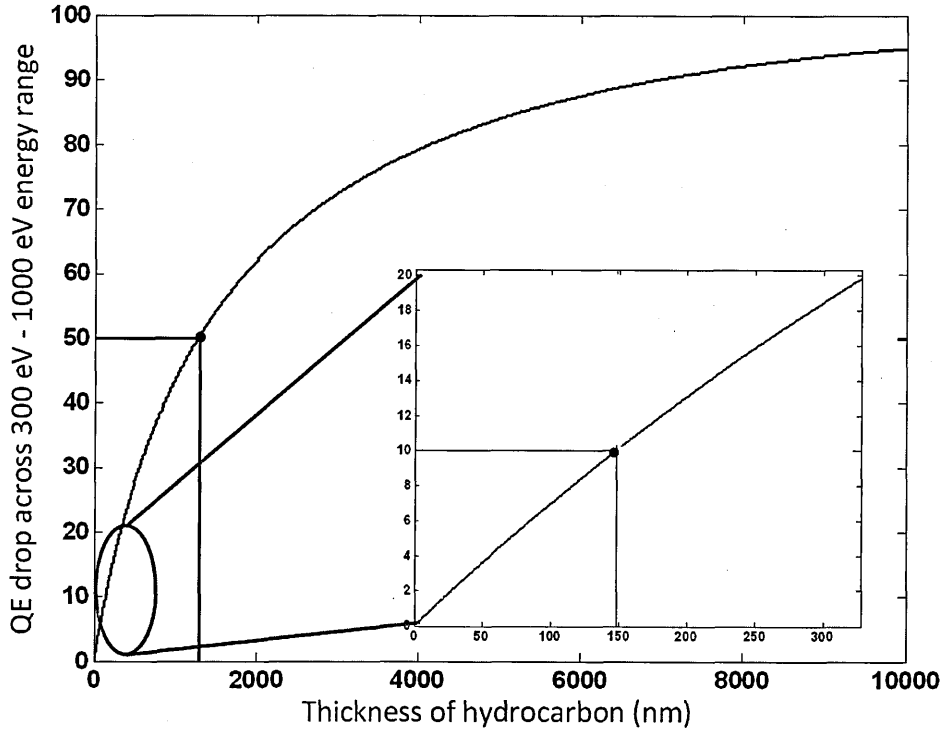

Figure 8.29: The average QE drop across the 300 eV - 1000 eV energy range is shown for varying, uniform layers of C_8H_8.

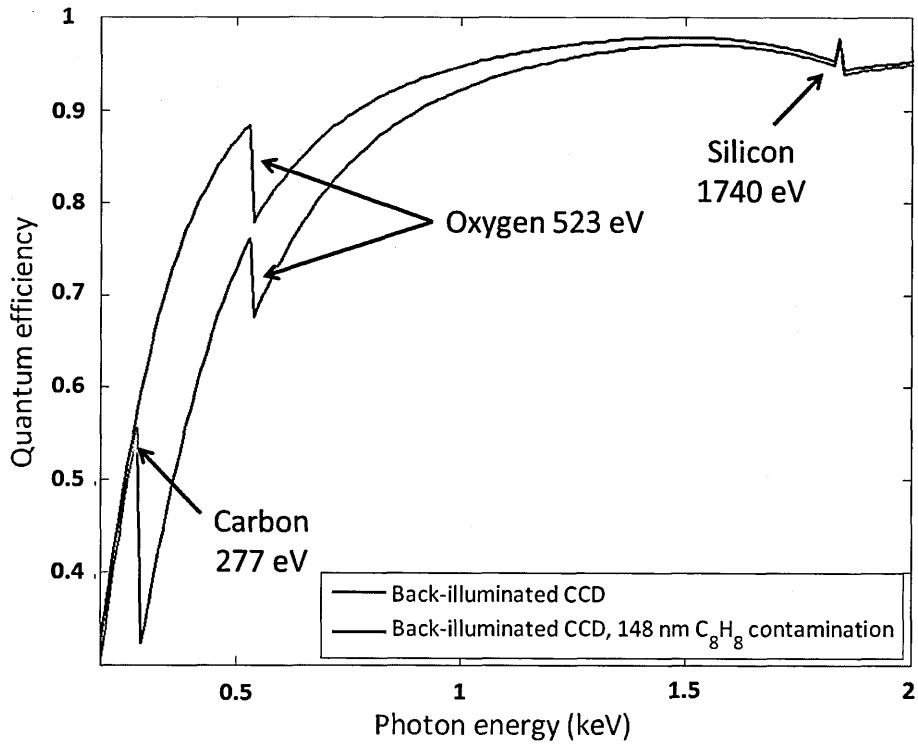

Figure 8.30: QE for a back-illuminated CCD for a perfect device and for a device with 148 nm of hydrocarbon on the surface.

Figure 8.30 shows that when considering the effect of contamination on the CCDs, the worst case situation has to be considered. While at 148 nm of contamination there is only a 10% drop of QE over the bandpass, the QE at 300 eV drops by over 40%. Instead of looking at the effect across the energy range the QE drop at the lower end of the bandpass needs to be assessed (i.e. at 300 eV).

Figure 8.31 shows that at the lower edge of the OP-XGS bandpass (300 eV) the thickness of hydrocarbon contamination that would cause a drop of 10% in QE is only 27 nm and for a 50% drop in QE is 180 nm.

The drop in QE due to contamination causes an effect on the whole system as the effective area of the instrument drops. Therefore, as the requirement of the instrument is to have an effective area above 1000 cm^2 at the end of the mission lifetime for the 300 eV to 1000 eV energy range, a limit is put on the level of contamination build-up that is allowed. A similar process as performed for the hydrocarbons was then followed for water in the telescope.

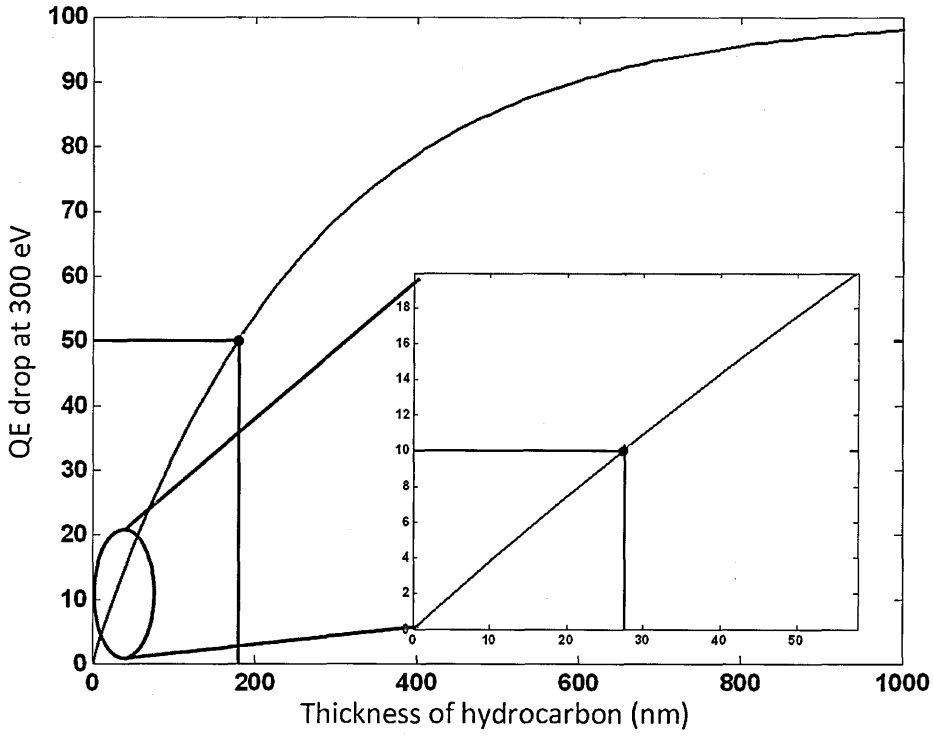

Figure 8.31: The QE drop at 300 eV is shown for varying, uniform, layers of C_8H_8.

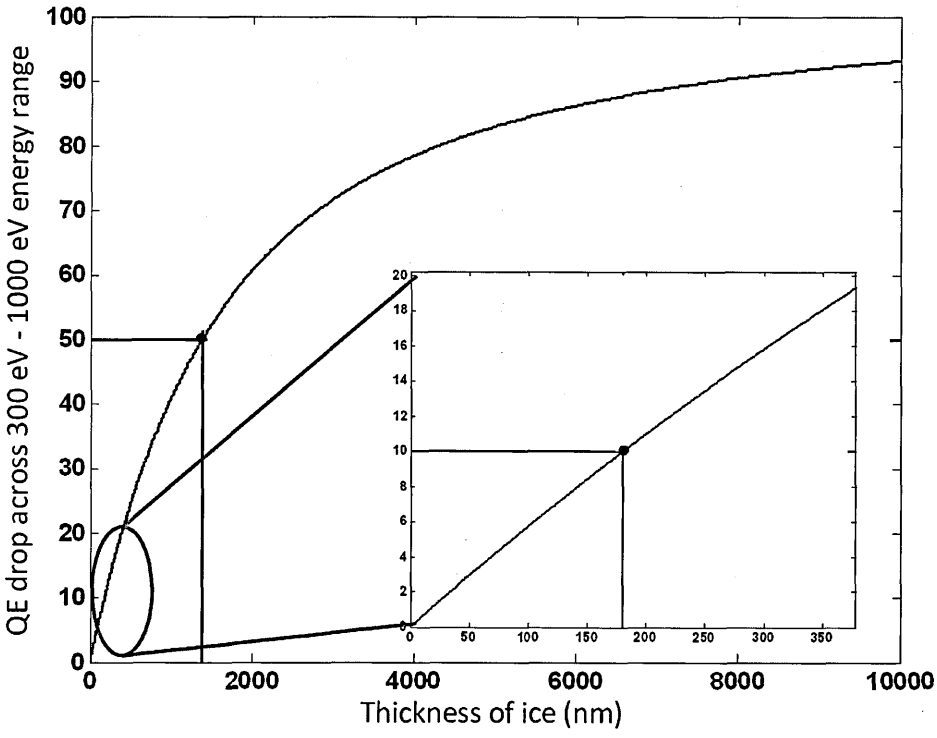

Figure 8.32: The average QE drop across the 300 eV - 1000 eV energy range is shown for varying, uniform, layers of ice water.

Figure 8.32 shows the effect of ice water across the OP-XGS energy range on the average QE of the CCDs. A 10% average drop in QE occurs with 180 nm of ice and a 50% drop in average QE with

1390 nm of ice. The result shows that ice has less of an effect than hydrocarbons on the average QE across the bandpass, but it is expected that the largest drop in QE would be at the oxygen K-shell edge (523 eV) (Figure 8.33) [Henke, 1993].

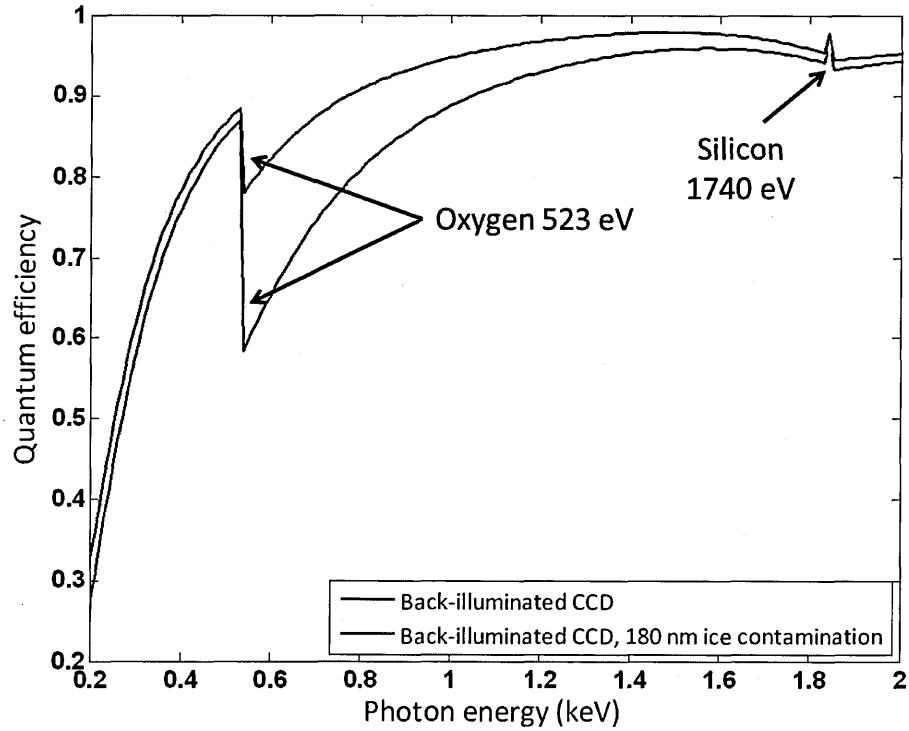

Figure 8.33: QE for a back-illuminated CCD for a perfect device and for a device with 310 nm of ice on the surface.

Similarly with the hydrocarbon analysis, the drop of QE at the oxygen edge has to be evaluated to ensure that the QE across the bandpass is high enough to keep the effective area of the instrument above 1000 cm^2. The QE drop at the oxygen edge for different thicknesses of ice water is shown in Figure 8.34.

Figure 8.34 shows that at the oxygen edge the amount of ice needed for a 10% drop in QE is 65 nm and a 50% drop in QE is achieved at 440 nm. The results for molecular contamination are summarised in Table 8.1.

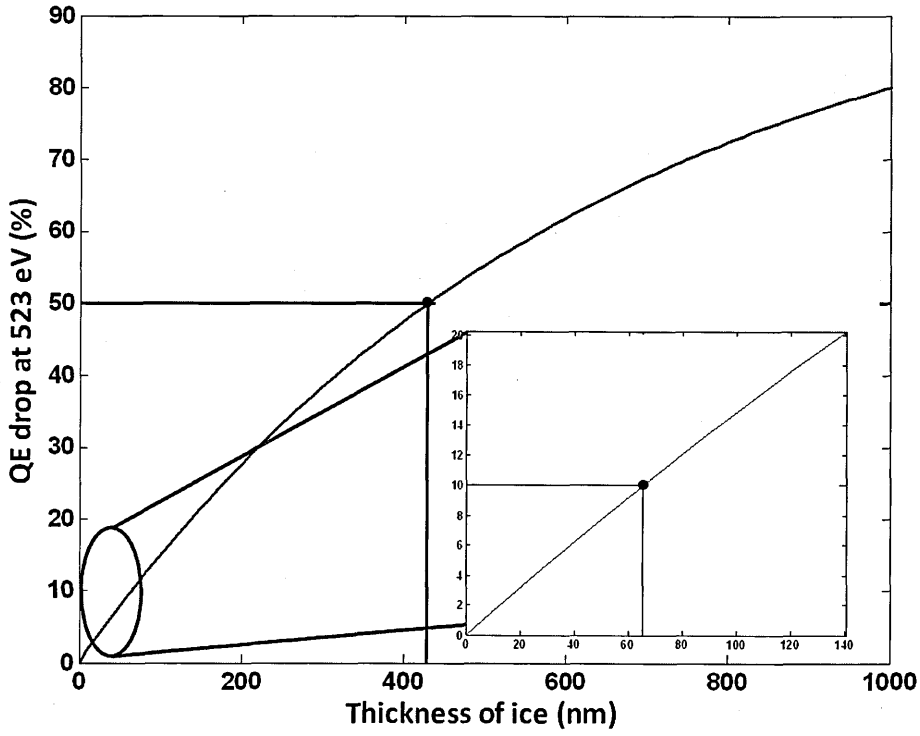

Figure 8.34: The QE drop at 523 eV is shown for varying, uniform, layers of ice water.

Table 8.1: Summary of the effect of different types of molecular contamination on the QE of the CCDs over the bandpass and at specific energies depending on the contamination type.

	Average QE drop		Carbon or Oxygen edge QE drop	
	10%	50%	10%	50%
C_8H_8	148 nm	1300 nm	27 nm	180 nm
Water	180 nm	1390 nm	65 nm	440 nm

Table 8.1 shows that ice has less of an effect on the QE of the device than a hydrocarbon, but as they act on different parts of the OP-XGS energy range they both have to be considered and controlled so as not to degrade the instrument's performance to below its baseline specification over its lifetime.

To evaluate the accumulation of a molecular contaminant, the partial pressures in the telescope tube have to be investigated. Using experience from the RGS instrument on XMM-Newton it is possible to infer information about the IXO spacecraft environment. Through the use of calibration sources on the instrument, the RGS team was able to measure the increase of carbon-based contamination on the instrument [den Herder, 2001], [Brinkman, 1996],

[Pollock, 2008] (Figure 8.35). Early in the instrument's mission, the contamination build-up rate was at its highest expected from an outgassing spacecraft. Over time, the contamination build-up slowed and predictions of likely build-up over instrument lifetime could be made. In 5 years, operating in the same conditions as the RGS, the OP-XGS might be estimated to accumulate 130 nm of carbon which is enough to reduce the overall QE by less than 10%, but will lead to a significant drop at the carbon edge. In 10 years the build-up will be 180 nm which is equivalent to a 50% drop in QE at the carbon edge and this needs to be factored into the instrument design so that the margins in the effective area are large enough to accommodate this drop in QE due to molecular contamination.

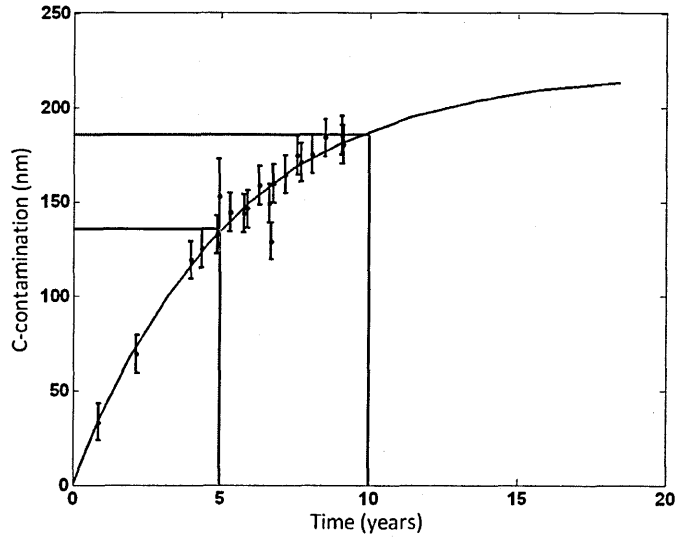

Figure 8.35: Carbon contamination build-up rate based on RGS calibration data over its lifetime [Pollock, 2009].

Molecular build-up on the gratings could affect the reflection properties of the surface and so would require study, but it was assumed that it had a negligible effect on the instrument compared to the build-up on the CCDs.

To minimise the molecular build-up on the CCDs, it was proposed that the devices be kept warm for the first few months in orbit in order to let the spacecraft outgas and that a door be in place over the CCD array. When required the CCDs are cooled to their operating temperature and the door opened. By keeping the CCDs covered for the first few months of the mission, the devices will not be exposed to the telescope environment during the period of fastest outgassing. The

CCDs would then have less hydrocarbon and water build-up, device QE would remain higher for longer and the effective area of the instrument would stay well above the baseline for the mission duration.

8.6.6.2 Particulate contamination

All spacecraft assembly facilities contain particulates and if they fall onto the instrument surface can cause contamination. An important factor to consider when it comes to particulate contamination is the particle fallout (PFO) rate. This is the rate at which particles will fall onto a horizontal surface and determines the rate at which particulate contamination will build-up [Borson, 1982]. To assess the effect of particulate build-up on the instrument, the separate surfaces need to be considered. Silicon dioxide was modelled as the particle that causes the contamination and was assumed to have a diameter of 5 nm. SiO_2 was chosen as it is a good representation of the contamination type that the instrument would be exposed to during assembly and it was easy to simulate with the author's existing model.

The gratings reflect and disperse incoming X-ray photons in a grazing incidence orientation; therefore, any particulate contamination will cause scattering or absorption of the incoming X-rays. If the X-rays are scattered, the throughput of the instrument will be affected, but as the scatter will be in the cross-dispersion direction, resolution degradation will be minimised. If the X-rays are absorbed then the throughput of the grating will fall reducing the effective area.

Absorption and the reduction of throughput are dependent on the geometry of the particles and X-rays as well at the absorption length. The absorption length of X-rays in SiO_2 is shown in Figure 8.36.

Based on Figure 8.36, it is assumed that all of the X-rays incident onto a SiO_2 molecule are absorbed and due to the graze angle at which the X-rays are incident on the grating, the molecule creates a shadow.

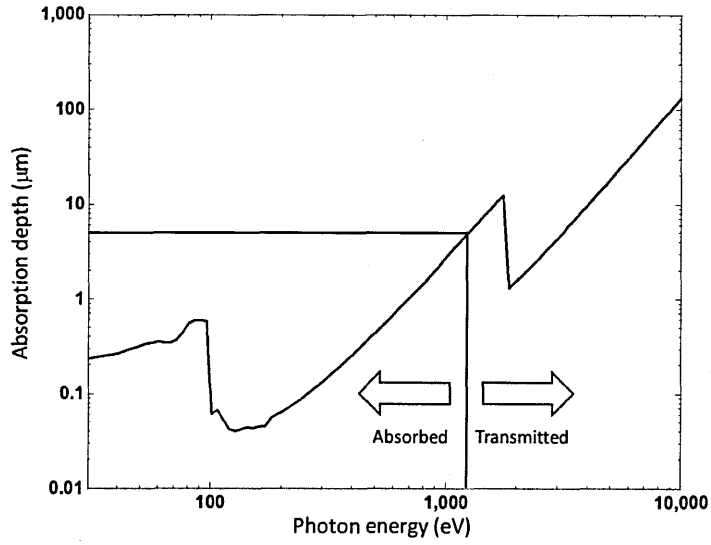

Figure 8.36: Absorption length for X-rays in SiO_2 [Henke, 1993].

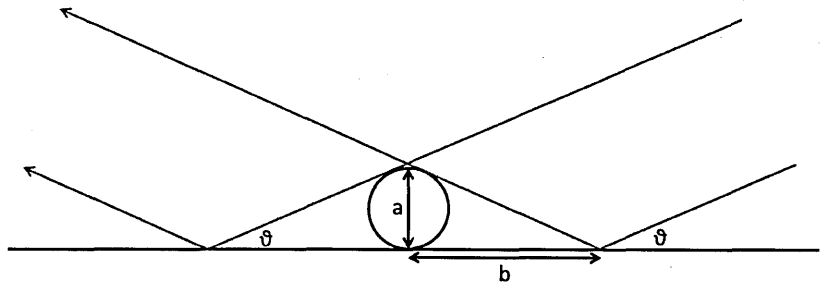

Figure 8.37: The effect of particle contamination creating a shadow on the grating and reducing throughput.

The size of this shadow is dependent on the size of the SiO_2 molecule, a, and the graze angle of the incident X-rays on the grating, θ (Figure 8.37). If the diameter of the molecule is taken to be 5 nm and the graze angle is 2.7°, then the shadow of the molecule is 106 nm (b). The shadow occurs before and after the molecule and so the total shadow created on the grating surface by a SiO_2 molecule is 212 nm. For simplicity the molecule in assumed to have a rectangular shadow as though the molecule is cubic. The shadow is also 5 nm wide in the direction perpendicular to the direction of incident X-rays due to the diameter of the SiO_2 molecule (Figure 8.38).

A single grating module is 100 cm x 100 cm and the area of shadow from a single SiO_2 molecule is 212 nm x 5 nm. Therefore, the amount by which the throughput falls due to a molecule can be calculated and, if the particle fallout rate is known, the time that it takes to build up particles and the relative throughput drop can be found.

According to the ESA specification, the fallout for different classes of cleanroom are given by Table 5.2 [ESA, 2008].

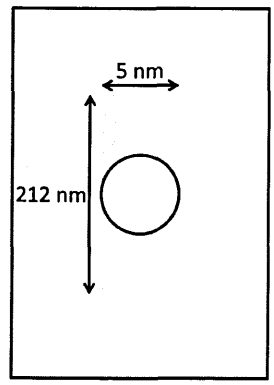

Figure 8.38: The shadow of an individual SiO_2 molecule on a grating assuming that the particle is a cube for ease and as a worst case scenario.

Table 8.2: Shows the extent of the shadow of an individual SiO_2 molecule [ESA, 2008].

ISO class (M)	PFO ($mm^2/m^2/24$ h)
5	2.0
6	10
7	52
8	275

The result is based on several measurements performed in different cleanrooms and is approximated by:

$$PFO = 0.069 \times 10^{(0.72M-2.16)} \quad (8.3)$$

Equation 8.3 allows predictions about particle build-up rate and drop in throughput to be made. It is assumed that the particles are evenly spaced ensuring that their shadows do not overlap.

Figure 8.39 shows that even in a class 5 cleanroom, the grating throughput would have a 1% drop in throughput after 0.2 years (2 ½ months). Particulate contamination is clearly a concern and so steps would have to be taken to make sure that its effect is minimised.

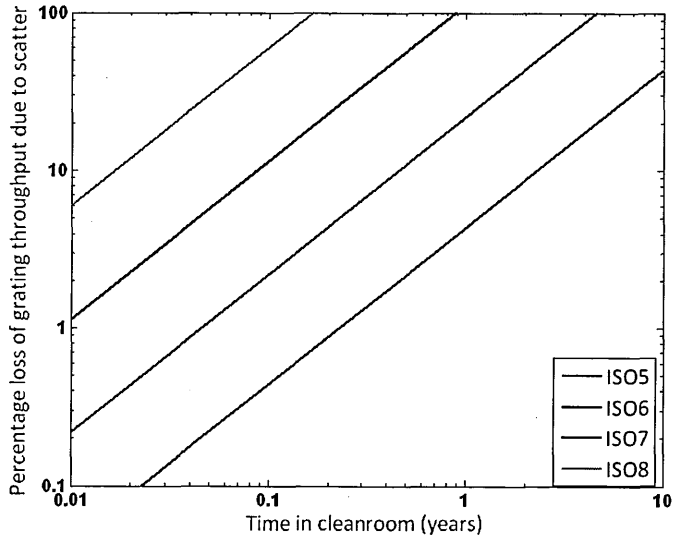

Figure 8.39: Drop in grating throughput due to an increase in particulate contamination after time in different cleanrooms.

Figure 8.39 is a worst case scenario with all of the gratings lying with their reflective surfaces up and separate from each other. In reality, the gratings would be stacked into modules with their edges facing up greatly reducing the amount of contamination that will be gathered by the reflective surface. It is assumed to be a reduction of $1/10^{th}$ over the worst case scenario (Figure 8.40) [ESA, 2008]. The figure shows that a 1% drop in throughput in an ISO 5 cleanroom would now take over a year of exposure; however, the contamination would still have an effect on the throughput of the gratings and so effective area of the instrument making careful handling necessary to minimise the effect.

It is assumed that the gratings will be manufactured and assembled in clean environments and that the majority of build-up will occur during instrument testing and spacecraft assembly. Through the use of cases and red-tag items, this can also be minimised. The red-tag items are designated as items that are removed just before launch to maximise the cleanliness of the instruments they protect.

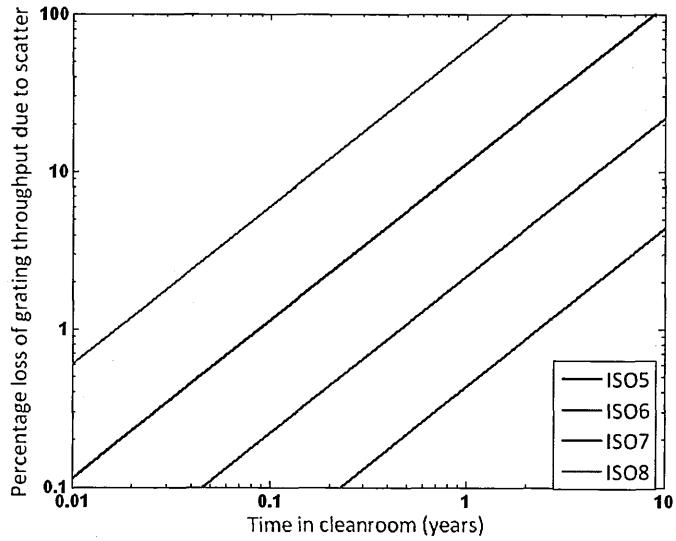

Figure 8.40: Drop in grating throughput due to an increase in particulate contamination after time in different cleanrooms with a further 10% reduction due to grating stacking and orientation.

It was assumed that the build-up of particulate contamination in space is negligible and so can be ignored.

It has been shown that a SiO_2 particle can stop X-rays incident onto it and so particulate contamination on the CCDs is also important to consider. If it is assumed that the particles fall uniformly over the CCD area, that the SiO_2 is completely opaque and that they have a diameter of 5 nm, the ISO particle fallout rates can be used to predict the rate at which the particles will build up on the device and so the drop in CCD active area can be calculated (Figure 8.41). In a class 5 cleanroom, a 1% loss of CCD active area will take over 10 years.

The major concern when it comes to particles contaminating the instrument occur on the ground and, due to the grazing incidence nature of their operation, the gratings are more susceptible. Particles in space however, will have a velocity relative to the spacecraft and so can cause impact damage with the spacecraft. There is nothing that can be done to mitigate for this problem, but it can have a major impact on the instrument and spacecraft. The RGS on XMM-Newton had damage caused by "micro-meteorites" that caused one of the CCDs to stop working, so the effect of particulates in space is important.

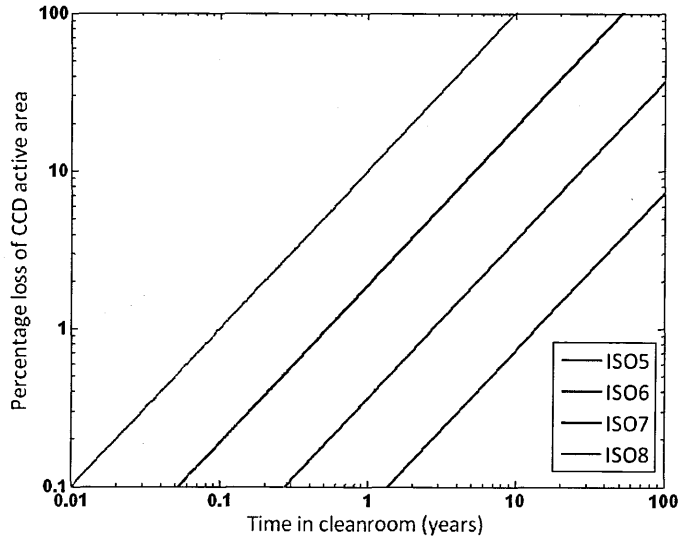

Figure 8.41: Drop in CCD active area due to an increase in particulate contamination after time in different cleanrooms.

8.6.7 Dispersion analysis

Taking the expected resolution performance of the instrument and the predicted bow-tie configuration it was possible to analyse the instrument's resolution. The study was completed by the author using simple thresholding analysis on the ray-trace data produced by the University of Colorado. Figure 8.42 allows analysis based on the number of photons that are included in the dataset and the threshold of how far away from the centre photons are counted as part of the event to be made.

Figure 8.42(b) shows the basis of the thresholding applied to the data to analyse the resolution achieved when some event recognition is applied. Figure 8.43 shows that if only central photons are used then event separation is very simple and the instrument has a very high resolution. When more events are included into the analysis, the resolution of the separate peaks deteriorates, falling to a resolution of 3000 with 100% of all of the counts included in the histogram. The result shows that event thresholding could be used to maximise the resolution of the image; however, the instrument is likely to be used in photon starved situations and so it may not be possible to reject photons.

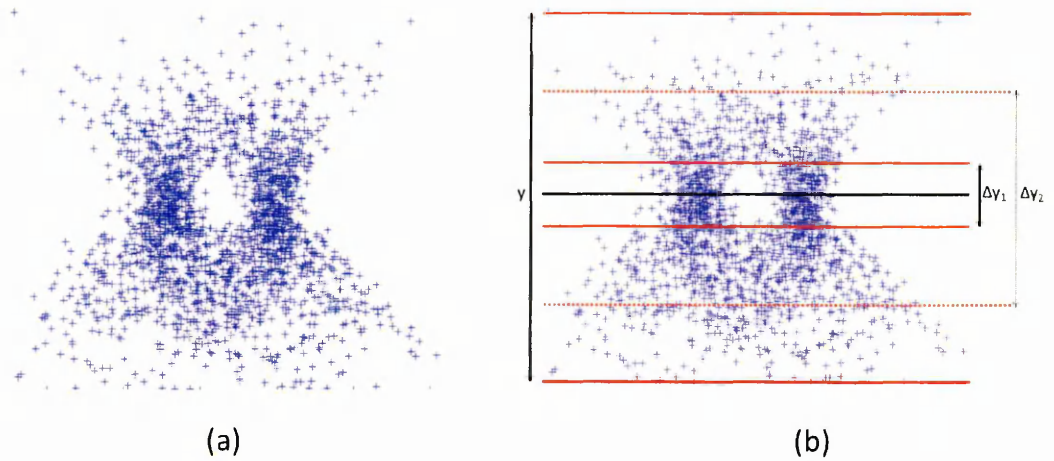

Figure 8.42: Overlapping bow-ties generated by ray-trace to test the instrument's ability to separate different events.

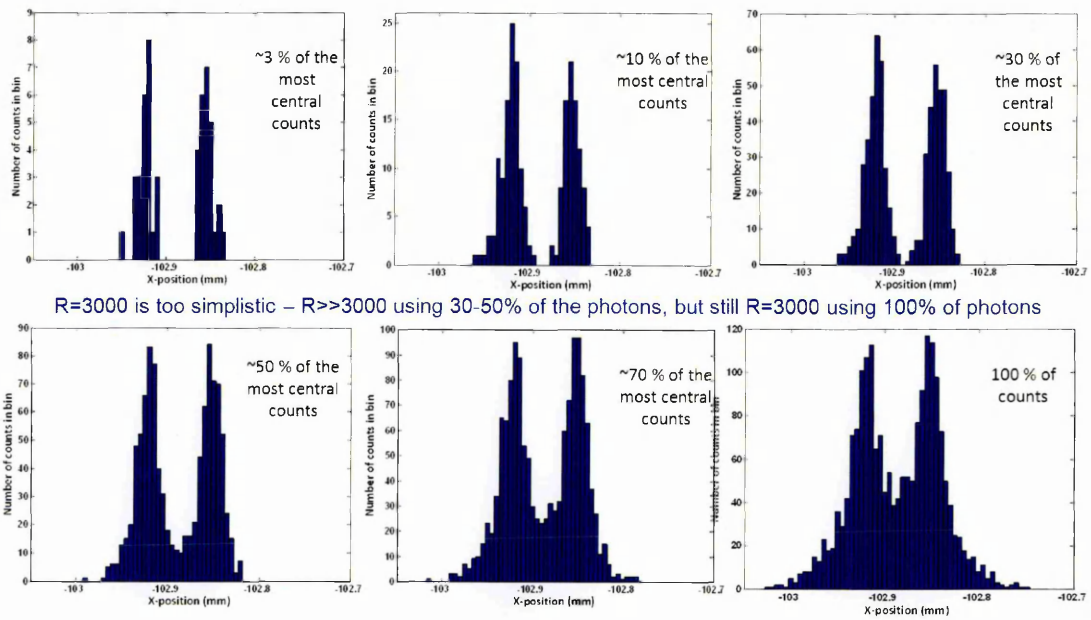

Figure 8.43: Histograms of the data for different levels of event thresholding based on y-position.

8.6.8 EM-CCDs on the OP-XGS camera array

A final consideration for the OP-XGS would be the use of EM-CCDs. The use of EM-CCDs for X-ray spectroscopy is a major theme in this thesis and the work completed is designed to be used on an X-ray spectrometer such as the OP-XGS. The OP-XGS works by using the position of a detected photon to determine the energy and the detectors inherent spectral resolution to determine the order. Therefore, if a low energy photon (lower than the current lower limit on the OP-XGS energy range) were to hit the CCD array it may not deposit all of its energy into the charge packet, but this smaller signal could still be collected. Through the use of multiplication gain this signal

could be amplified and detected by the instrument and so low energy photons could still be seen, increasing the potential and scope of the science possible with the OP-XGS.

EM-CCDs, as discussed in Section 7.7, are able to run faster without an increase in the readout noise as the internal gain acts to suppress this noise. The ability to readout the camera array faster will increases the tolerance of the instrument to stray light; hence thinner filters can be used. Thinner filters attenuate soft X-rays less and the QE of the detectors increases along with the instruments effective area. The possible increase in readout speed is a big advantage to using EM-CCDs on X-ray spectrometers.

EM-CCDs have not been used in space applications thus far and so have a low TRL. To use EM-CCDs in space applications, work needs to be completed to show they are a robust and reliable technology that offers benefits to future X-ray missions. The concern about using EM-CCDs on space missions is that their high field region that allows multiplication gain may be susceptible to radiation damage and not enough work has been completed to fully understand the ageing effect. As part of the study for the Gaia mission, EM-CCDs were tested against proton damage and found to behave no differently to conventional CCDs [Smith, 2006]. Through more extensive studies on the effect of ionising and non-ionisation radiation damage on the multiplication register and with the full characterisation of the gain ageing effect (Section 3.8.4) for the duration that the devices would be expected to run for in a space mission, the TRL of EM-CCDs can be increased. This would remove the remaining barriers to using EM-CCDs as the detectors for soft X-ray spectrometers.

8.7 Summary

The purpose of this study was the design of a high resolution spectrometer to be used on the International X-ray Observatory (IXO). IXO was proposed as the next generation large scale X-ray facility that would allow scientists to develop their understanding of the high energy Universe. With unprecedented effective area and angular resolution, the telescope's optics would allow a range of instruments to provide high resolution, effective area and field of view analysis of the

X-ray Universe to be performed. The highest resolution instrument planned for this facility was the X-ray Grating Spectrometer (XGS) and one possible design to meet the specification of this element, the OP-XGS, has been discussed in some detail.

Many challenges face such a large space mission and high resolution X-ray spectroscopy over the soft X-ray band requires a novel approach to grating spectrometers. To mitigate potential problems that the instrument would face, several aspects of its design were subjected to rigorous study, producing an instrument proposal that was of a high enough resolution to help IXO meet the proposed scientific goals for the instrument payload. The focus of this chapter was on studies involving the camera array, pointing stability, stray light tolerances, the system's effective area and instrument contamination.

The work carried out by the author was to understand various aspects of the instrument, which included:

- Looking into the basic instrument design. Knowledge of the parameters that the instrument would have to work within was essential in instrument design. A priority among these concerns was the pointing stability that would allow an accurate energy calibration of the camera array. By making calculations based on ray-tracing, the author was able to find that, for an energy calibration on the camera array that would allow the energy resolution requirement to be met, 4 photons per second had to be detected in the zero-order CCD using the tower instrument design and with a 2 Hz pointing knowledge.
- The camera array had to be laid out by the author in a manner than minimised dead-space, captured the necessary dispersed photons, monitored the zero-order positions and had in-built redundancy. This process went through many iterations as the grating design developed with the final array shown in Figure 8.19.
- The effective area of the instrument had to be estimated across the energy range. The throughput and effective area of the optic and gratings were calculated and then the author added in the effect of dead-space between the CCDs and their QE to get a final,

start of mission, effective area estimate. From this, more grating modules were added to the instrument design to create a larger margin.

- Based on the experience of the RGS on XMM-Newton, the effect of stray-light filters on the effective area was calculated using the author's QE model. It was found that if the CCDs were run at 10 frames per second, they could tolerate 10x more optical light than the CCD on the RGS with the thinnest filter. This allowed the author to suggest a filter of 30 nm Al, 13 nm MgF_2 that would be thick enough for the OP-XGS CCDs without incurring too high a background. More work is needed to test the viability of filters this thin.
- A contamination study was completed using the author's QE model and ESA cleanroom specifications to estimate the effect of contamination on the instrument. It was found that molecular contamination in space (C_8H_8) would cause a 10% drop in QE at the carbon edge with a contamination layer 27 nm thick, and a 50% drop by 180 nm. Water contamination would cause a 10% drop at the oxygen edge from a 65 nm layer and a 440 nm layer would cause a 50% drop. Particulate contamination was also considered and the author suggested that particles on the grating would cause the biggest loss in effective area although micro-meteorites in space could also be damaging to the whole spacecraft.
- The author also looked at how thresholding the number of events that are considered could be used to increase the resolution of the instrument; however, as most X-ray sources that IXO would be interested in are faint, the likelihood of thresholding being used is low.
- A final suggestion of using EM-CCDs on the focal plane array of IXO was considered by the author. The possibility of increasing the readout speed of the OP-XGS with very little cost to readout noise and with the increase in stray-light tolerance that it would bring make EM-CCDs a very tempting detector to use on the OP-XGS. More work is needed to increase these devices' TRL but, should they prove to be reliable detectors in space then the author would recommend their use.

Chapter 9: Conclusions and Further work

The research goal of this thesis was to characterise CCD and EM-CCD technology for high resolution X-ray spectroscopy. An instrument that can provide high resolution soft X-ray detection was designed using an off-plane grating and the detector developments that would improve this instrument's performance were investigated.

9.1 Back-illuminated CCD

A SIMS was used to analyse the back-surface of a CCD97 to better refine the author's QE model and to provide more information about e2v's back-surface passivation process.

- The result showed that a dead-layer of ~45 nm is formed.

The result was able to directly feed into effective area measurements for the OP-XGS and so provide a more accurate CCD QE performance.

Further work in this area would be to complete a UV, EUV and soft X-ray QE study of devices made by e2v using their standard and enhanced back-surface process. The results would allow an understanding of the benefits of having a thinner dead-layer over soft X-ray energies to be found, helping instrument design in the future. A comparison with a delta-doped CCD would further improve our understanding.

9.2 Conventional CCDs spectral resolution

Both the Hamamatsu and e2v CCD30-11 variants showed deviation from the theoretical spectral resolution based on Equation 3.19.

- The result showed evidence of an asymmetric peak effect that was caused due to a proportional of the detected photons interacting in the dead-layer. Some of the degradation was also caused by split events. The Hamamatsu device had larger spectral resolution deterioration than the e2v variants.
- The partial event fraction for the Hamamatsu device also degraded faster than was seen in the CCD30-11 variants.

The second result suggest that the Hamamatsu device has a thicker dead-layer than the e2v CCD30-11s and so more charge is lost at lower energies. The thicker dead-layer was also able to explain the faster degradation in spectral resolution as the asymmetric peak effect became more prominent at higher energies in the Hamamatsu device.

- The thicker dead-layer in the Hamamatsu device was confirmed through the QE study and was found to be ~75 nm compare with ~45 nm (the result from the SIMS of the CCD97), supporting the suggestion that a thicker dead-layer was the cause of the increased spectral resolution degradation.

The Hamamatsu device is also thought to be thicker than the CCD30-11s and so there is more likelihood of their being split events adding to the degradation effect.

To better understand the differences between the devices, more information is required. A QE study of all three devices across the UV to soft X-ray energy range will allow a better estimate of dead-layer thickness to be made. Also, higher energy X-ray tests will lead to a better prediction of relative device thickness.

A further study using an EM-CCD will allow the peak asymmetry effect to be studied. The gain in an EM-CCD allows the readout noise to be suppressed and so the improvement that is expected when more than half of the incident photons are detected in the dead-layer could be observed (Section 6.2.2.2).

9.3 The Modified Fano Factor

The Modified Fano Factor allows the theoretical spectral resolution performance of an EM-CCD to be predicted and is essential for their possible use on high resolution X-ray spectrometers and was verified across a range of X-ray energies. This work is vital to the use of EM-CCDs for direct X-ray detection and is the major work in this thesis.

9.4 The International X-ray Observatory

The author's contribution to the OP-XGS on IXO was as follows:

- Looking into the basic instrument design in order to ensure that the pointing knowledge of the telescope would be sufficient for effective energy calibration of the CCD array. The author found that for the tower accommodation of the grating, 4 photons per second were required in the telescope's zero-order monitors.
- The author designed camera arrangements that allowed the whole of the dispersed spectrum to be collected while minimising the dead-space between the CCDs and incorporating redundancy into the design.
- The author's QE model was used to make estimations of the total effective area of the instrument across the energy range. This would form the basis of the filter and contamination studies.
- Using experience from the RGS on XMM-Newton the author found that if the CCDs were run at 10 frames per second a filter of 30 nm Al and 13 nm MgF_2 would be thick enough to reduce the optical background to minimal levels. It is not yet known if this thickness of filter is technologically viable.
- A contamination study was completed using the author's QE model and ESA cleanroom specifications to estimate the effect of contamination on the instrument. It was decided that molecular contamination was a concern in space where the CCD was cold and particulates were a problem in cleanrooms. However, micro-meteorites could also cause damage to the instrument.
- A thresholding study by the author showed how a higher resolution could be achieved by the instrument, but as many applications of OP-XGS would be photon starved, the thresholding is unlikely to be used.
- EM-CCDs were also considered by the author as the focal plane array detectors and the findings are summarised in Section 9.5.

9.5 EM-CCDs as the detectors on high resolution X-ray spectrometers

EM-CCDs offer high detectability and readout noise suppression through the use of multiplication gain, which offers the opportunity to extend the energy range of a high resolution X-ray spectrometer.

- Readout noise suppression allows the device to be read out faster without a large increase in noise. The increase in readout speed increases the stray-light tolerance of the detector; therefore, thinner filters can be used. Thinner filters will attenuate less of the low energy X-rays that are incident onto the focal plane camera array, the detectors QE will be higher and the instrument will have a higher science yield.

However, EM-CCDs do have some disadvantages:

- EM-CCDs have been shown to have a degraded spectral resolution when multiplication gain is used. The degradation has been explained by the Modified Fano Factor. If the instrument can be designed to account for this degradation by increasing the dispersion from the gratings (increased groove density or throw (Section 2.3.7)) then EM-CCDs can still be used as the focal plane detector.
- EM-CCDs have a low TRL and so are seen as a risky technology. Through further studies on the effect of protons, electrons, neutrons and heavy ions on the multiplication register, the TRL of the devices can be improved.
- An ageing effect is seen in the multiplication register of an EM-CCD that is well known. The effect could be seen as a problem for space missions as the amount of gain achieved for a given voltage would fall off over time and time consuming recalibration would be necessary. The effect is well document and e2v typically "burn-in" their devices so that the ageing is slower (Section 3.8.4). With a greater level of understanding of this effect, ways to mitigate the ageing can be found.

If the TRL of EM-CCDs can be raised by testing them in space like situations then the author would recommend the use of EM-CCDs on high resolution soft X-ray spectrometers.

The work in this thesis could be used on future space missions. A proposal made to NASA in collaboration with the University of Iowa for a sounding rocket includes the use of a dispersive grating instrument similar to the one designed for the OP-XGS, with EM-CCDs at the optic focus. The experiment would help provide heritage to EM-CCD technology, improve its TRL and make its inclusion in future X-ray space missions more likely. Several mission proposals exist with ESA and NASA for X-ray observatories (WHIMEx, ATHENA) and, if chosen, any of these satellites could carry a high resolution X-ray spectrometer similar to the OP-XGS, using EM-CCDs at the optic focus.

References

1. AD829 datasheet, "High-Speed, Low-Noise Video Op Amp AD829", Analogue devices datasheet, Revision 1, http://www.analog.com/static/imported-files/data_sheets/AD829.pdf, 2011.
2. Amelio, G. F. et al., "Charge-Coupled Imaging Devices: Design Considerations", IEEE Transactions on Electron Devices, Vol. Ed-18, No. 11, (1971), p.p. 986-992.
3. Arnaud, M. et al., "The Evolution of Galaxy Clusters Across Comic Time", A Science Working Paper for the 2010 Decadal Survey, ASTRO 2010, (2010).
4. Audi, G., "The NUBASE Evaluation of Nuclear and Decay Properties", Nuclear Physics A (Atomic Mass Data Centre), Vol. 729, (2003), p.p. 3-128.
5. Ball, D. W., "Field Guide to X-ray Spectroscopy", SPIE Press, 2006.
6. Barret, D., et al., "X-ray Evolving-Universe Spectroscopy: The XEUS Instruments", ESA document SP-1273, (2003).
7. Basden, A. G., Haniff, C. A. and Mackay, C. D, "Photon counting strategies with low-light-level CCDs", Monthly Notices of the Royal Astronomical Society, Vol. 345, (2003), p.p. 985-991.
8. Barcons, X., et al., "IXO: The International X-ray Observatory", ESA Yellow book, Draft 0.4, (2010).
9. Bavdaz, M. et al., "The X-ray Evolving Universe Spectroscopy Mission (XEUS): The X-ray mirror design and technology", Proc. SPIE, Vol. 3766, (1999).
10. Bearden, J. A., "X-ray Wavelengths", Reviews of Modern Physics, Vol. 39, No. 1, (1967), p.p. 78-124.
11. BESSY, "PTB Laboratory at BESSY II", http://www.ptb.de/mls/aufgaben/bessylab.html, Last Updated 30-09-2011, Date Accessed 15-05-2012.
12. Beutier, G. et al., "Back-illuminated CCD for coherent soft X-ray imaging", European Physical Journal of Applied Physics, Vol. 42, (2008), p.p. 161-167.
13. Bogaart, E. W. et al., "Very Low Dark Current CCD Image Sensor", IEEE Transactions on Electron Devices, Vol. 56, No. 11, (2009), p.p. 2462-2467.
14. Bohr, N., "On the Constitution of Atoms and Molecules, Part 1", Philosophical Magazine, Vol. 26, (1913), p.p. 1-24.
15. Bootsma, T. M. V., et al., "Synchrotron calibration and response modelling of back-illuminated XMM-RGS CCDs", Nuclear Instruments and Methods, Vol. 439, (2000), p.p. 575-581.
16. Borson, E. N, Peterson, R. V., Rachal, L. H., "Evaluation of the ground contamination environment for STS payloads", Shuttle Environment Workshop, Space Division Air Force Systems Command, (1982).

17. Boyle, W. S. and Smith G. E., "Charge Coupled Semiconductor devices", Bell Systems Technical Journal, Vol. 49, (1970), p.p. 587-593.

18. Bregman, J. N. et al., "The Cosmic Web of Baryons", White Paper submitted to Galaxies across Cosmic Time (GCT) and The Cosmology and Fundamental Physics (CFP) Science Frontiers Panels, ASTRO 2010, (2010).

19. Bregman, J. N., "The Missing Baryons in the Milky Way and Local Group", White Paper submitted to the Galactic Neighborhood Scientific Frontiers Pannel, ASTRO 2010, (2010).

20. Brenneman, L. et al., "Spin and Relativistic Phenomena around Black Holes", White Paper submitted to Galaxies across Cosmic Time (GCT) and The Cosmology and Fundamental Physics (CFP) Science Frontiers Panels, ASTRO 2010, (2010).

21. Brinkman, A. et al., "The Reflection Grating Spectrometer on board XMM", Proc. SPIE, Vol. 2808, 463, (1996).

22. Brown, J. G., "X-rays and their applications", Plenum, 1975.

23. Brunn, S. D., Cutter S. L. & Harrington J. W. Jr., "Geography and Technology", Springer, 2004.

24. Burke, B. E., et al., "CCD Soft X-ray Imaging Spectrometer for the ASCA Satellite", IEEE Transactions on Nuclear Science, Vol. 41, No. 1, (1994), p.p. 375-385.

25. Burt, D., Private communication, 2012.

26. Burt, D., Private Communication, 2011.

27. Burt, D. J., "Basic Operation of the Charge-Coupled Device", International Conference on Technology and Applications of CCDs, University of Edinburgh, (1974), p.p. 1.

28. Cash, W. Private Communication, 2010.

29. Cash, W. C. Jr., "X-ray optics. 2: A techniques for high resolution spectroscopy", Applied Optics, Vol. 30, No. 13, (1991), p.p. 1749-1759.

30. Cash, W. et al, "X-ray Optics for WHIMEx, The Warm Hot Intergalactic Medium Explorer", Proc. SPIE, 8147, (2011).

31. Chandra X-ray Centre, "The Chandra Proposers' Observatory Guide", Chandra Project Science, MSFC, Version 14.0, (2011).

32. Chang, C. et al., "High fidelity blazed grating replication using nanoimprint lithography", Journal of Vacuum Science and Technology, Vol. B 22(6), (2004), p.p. 3260-3264.

33. Chauvet, G. and Baptist, R., "Inverse photoemission spectrometer in the range 20-100 eV", Journal of Electron Spectroscopy and Related Phenomena, Vol. 24, Issue 2, (1981), p.p. 255-265.

34. Clarke, R., "CCD X-ray detectors: opportunities and challenges", Nuclear Instrument and Methods, Vol. 347, (1994), p.p. 529-533.

35. Crowell, C. R. & Sze, S. M., "Temperature dependence of Avalanche Multiplication in Semiconductors", Applied Physics Letters, Vol. 9, No. 6, (1966), p.p. 242-244.

36. Danforth, C. W. et al., "The Low-Z Integalactic Medium, III. H_I and Metal Absorbers at Z < 0.4", The Astrophysical Journal, Vol. 679, (2008), p.p. 194-219.

37. Davis, R. D., Wong, F. S. L., "X-ray microtomography of bones and teeth", Physiological Measures, Vol. 17, (1996), p.p. 121-146.

38. de Korte, P. A. J. et al., "Cyrogenic imaging spectrometers for X-ray astronomy", Nuclear Instruments and Methods, Vol. A444, (2000), p.p. 163-169.

39. de Korte, P. A. J. et al., "The XEUS focal plane instruments", Proc. SPIE, Vol. 7011, (2008).

40. den Herder, J. W. et al., "The Reflection Grating Spectrometer on board XMM-Newton", Astronomy & Astrophysics, Vol. 365, (2001).

41. Denvir, D. J. & Conroy, E., "Electron Multiplying CCD: The new ICCD", Proc. SPIE, Vol. 4796, (2003), p.p. 164-174.

42. e2v technologies (UK) limited datasheet "CCD30-11 Back Illuminated high Performance CCD Sensor", A1A-100005 Issue 7, (2006).

43. e2v technologies (UK) limited datasheet, "CCD97-00 Back Illuminated 2-phase IMO Series Electron Multiplying CCD Sensor", A1A-CCD97BI_2P_IMO Issue 3, (2004).

44. e2v technologies (UK) limited datasheet, "CCD220 Back Illuminated Electron Multiplying Adaptive Optics CCD Sensor", Provisional Issue B, (2007).

45. Ebeling, H., et al., "The ROSAT Brightness Cluster Sample (BCS): The Cluster X-ray Luminosity Function within z = 0.3", Astrophysical Journal Letters, Vol. 479, (1997), p.p. L101-104.

46. Einstein, A., "Über einen die Erzeugung und Verwandlung des Lichtes betreffenden heuristischen Gesichtspunkt", Abbalen det Physik, Vol. 17, (1905), p.p. 132-148.

47. Endicott, J., Private Communication, 2010.

48. ESA (2008) ECSS Secretariat, "Space Produce Assurance. Microbial examination of flight hardware and cleanrooms", European Cooperation for Space Standardization (ECSS), ECSS-Q-ST-70-55C.

49. Esam, M. A. Hussein, "Handbook on radiation probing, gauging, imaging and analysis", Springer, 2003.

50. Evagora, A. M. et al., "Novel method for identifying the cause of inherent ageing in Electron Multiplying Charge Coupled Device", Proc. 9th International Conference on Position Sensitive Detectors (PSD), Journal of Instrumentation, (2012).

51. Fabian, A. C. et al., "Cosmic Feedback from Supermassive Black Holes", White Paper submitted to Galaxies across Cosmic Time (GCT) and The Cosmology and Fundamental Physics (CFP) Science Frontiers Panels, ASTRO 2010, (2010).

52. Fano, U., "Ionization Yield of Radiations. II. The Fluctuations of the Number of Ions", Physical Review, Vol. 72, No. 1, (1947).

53. Flora, L. & Arokia, N., "CCD Image Sensors in Deep-Ultraviolet: Degradation, Behaviour and Damage Mechanisms", Springer, 2005.

54. Follath, R. & Senf, F., "First undulator beamlines in operation at BESSY", Synchrotron Radiation News, Vol. 12, No. 3, (1999), p.p. 34-35.

55. Geist, J. and Zalewski, E. F., "The quantum yield of silicon in the visible", Applied Physics Letters, Vol. 35, (1979), p.p. 503-505.

56. Geist, J. et al., "New calculations of the quantum yield of silicon in the near ultraviolet", Physical Review, rev. B, Vol. 27, (1983), p.p. 4841-4847.

57. Giacconi, R., et al., "The Einstein/HEAO 2/ X-ray Observatory", Astrophysical Journal, Vol. 230, Part 1, (1979), p.p. 540-550.

58. Gondoin, P. et al., "Overview of ESA study activities on XEUS", Proc. SPIE, Vol. 7011, (2008).

59. Gorenstein, P. & Zombeck, M., "High resolution X-ray spectroscopy of cosmic plasmas", Proc. IAU Colloquium 115, 1990.

60. Hamamatsu Photonics K.K., Solid State Division, "CCD area image sensor S7170-0909, S7171-0909", Cat. No. KMPD1028E06, (2006).

61. Heilmann, R. K., "Diffraction efficiency of 200-nm-period critical-angle transmission gratings in the soft x-ray and extreme ultraviolet wavelength bands", Applied Optics, Vol. 50, Issue 10, (2011), p.p. 1364-1373.

62. Helliwell, J. R., "Synchrotron radiation facilities", Nature Structural & Molecular Biology, Vol. 5, (1998), p.p. 614-617.

63. Henke, B. L., Gullikson E. M. & Davis J. C., "X-ray interactions: photoabsorption, scattering, transmission and reflection at E=50-30000 eV, Z=1-92", Atomic and Nuclear Data Tables, Vol. 54, No. 2, (1993), p.p. 181-342.

64. Hoenk, E. et al., "Growth of a delta-doped silicon layer by molecular beam epitaxy on a charge-coupled device for reflection-limited ultraviolet quantum efficiency", Applied Physics Letters, Vol. 61, (1992), p.p. 1084-1086.

65. Hornschemeier, M., et al., "Con-X and JWST: NASA's Next Generation X-ray and Infrared Great Observatories", Astrophysics in the Next Decade: JWST and Concurrent Facilities, Tucson, AZ, USA, (2007).

66. Holland, A. D. et al., "MOS CCDs for the Wide Field Imager on the XEUS spacecraft", Proc. SPIE, Vol. 5898, (2005).

67. Holland, K., XCAM CCD Controller System CCD USB2REM Manual, Rev. 1.0, (2008).

68. Holst, G. C. & Lomheim, T. S., "CMOS/CCD Sensors and camera Systems", SPIE Press, Second Edition, 2011

69. Hook, J.R. & Hall, H.E., "Solid State Physics", Second edition, John Wiley & Sons Ltd., 1974.

70. Hopkinson, G. R., "Charge diffusion effects in CCD X-ray detectors – 1. Theory", Nuclear Instruments and Methods, Vol. 216, (1983), p.p. 423-429.

71. Horowitz, P. & Hill, W., "The Art of Electronics", Cambridge University Press, Second Edition, 1989.

72. Howes, M. J. & Morgan D. V., "Charge-Coupled Devices and systems", John Wiley & Sons, Inc., 1979.

73. Hynecek, J., "Impactron – A New Solid State Image Intensifier", IEEE Transactions on Electron Devices, Vol. 44, (2001), p.p. 2238-2241.

74. JAXA, "ASCA ASTRO-D", http://www.isas.ac.jp/e/enterp/missions/asca/index.shtml, Copyright 2008 Japan Aerospace Exploration Agency, Date Accessed 12-06-2012.

75. Janesick, J. R., et al., "Potential of CCDs for UV and X-ray plasma diagnostics (invited)", Review Scientific Instruments, Vol. 56 (5), (1985), p.p. 796-801.

76. Janesick, J. R. et al., "Charge-coupled device advances for X-ray scientific applications in 1986", Optical engineering, Vol. 26, No. 2, (1987), p.p. 156-166.

77. Janesick, J. et al., "Fano-noise-limited CCDs", Proc. SPIE, A89-40276, (1988), p.p. 17-35.

78. Janesick, J. R., "Scientific Charge-Coupled Devices", SPIE press, 2001.

79. Janesick, J. R., "Photon Transfer", SPIE press, 2007.

80. Jerram, P. Private Communication, 2011.

81. Jerram, P. et al, "The LLLCCD: Low Light Imaging without the need for an intensifier", Proc. SPIE, Vol. 4306, (2001), p.p. 178-186.

82. Johnson, J. B., "Thermal Agitation of Electricity in Conductors", Physical Review, Vol. 32, (1928), p.p. 97-109.

83. Kahn, S. M., et al., "High energy spectroscopic astrophysics", Springer, 2005.

84. Kane, E. O., "Theory of photoelectric emission from semiconductors", Physics Review, Vol. 127, (1962), p.p. 131-141.

85. Keay, A., "An investigation of fine structure effects in CCDs developed for JET-X", Doctoral Thesis, University of Leicester, (1997).

86. Kent, W. H., "Charge Distribution in Buried-Channel Charge-Coupled Devices", Bell Systems Technical Journal, Vol. 52, (1973), p.p. 1009.

87. Kittel, C., "Introduction to Solids State Physics", John Wiley & Sons, Inc., Eighth Edition, 2005.

88. Klein, R., Bahrdt, J., Herzog D. & Ulm g., "The PTB electromagnetic undulator for BESSY II", Journal of Synchrotron Radiation, Vol. 5, (1997) , p.p. 451-452.

89. Knoll, G. F., "Radiation detection and measurement", John Wiley & Sons, Inc., 3rd Edition, 2000.

90. Kozlowski, L. J., Luo, J., Tomasini, A., "Performance Limits in Visible and Infrared Imager Sensors", Electron Devices Meeting, IEDM Technical Digest International, (1999), p.p. 36.1.1-36.1.4.

91. Krause, M. O., "Atomic radiative and radiationless yields for K and L shells", Physical and Chemical Reference Data, Vol. 8, (1979), p.p. 307-327.

92. Laboratorie AIM, "Comsic Vision 2015-2025", Date Accessed 12-06-2012 http://irfu.cea.fr/Sap/Phocea/Vie_des_labos/Ast/ast.php?t=actu&id_ast=1791.

93. Lillie, C. F. et al., "The Warm-Hot Intergalactic Medium Explorer (WHIMEx) Mission", Proc. SPIE, Vol. 8145 (2011).

94. Lumb, D. H. and Hopkinson, G. R., "Charge diffusion effect in CCD X-ray detectors II. Experimental results", Nuclear Instrument and Methods, Vol. 216, (1983), p.p. 431-438.

95. Lumb, D. H., "Applications of Charge-Coupled Devices to X-ray Astrophysics Missions", Nuclear Instruments and Methods, Vol. A228, (1990), p.p. 219-226.

96. Lumb, D. H., et al., "ATHENA: The extremes of the Universe from black hole to large-scale structure", ESA Yellow book, (2011).

97. Lutz, G., "Semiconductor Radiation Detectors", Springer, First Edition, 1999.

98. Magorrian, B. G. & Allinson, N. M., "Soft X-ray damage in CCD detectors", Nuclear Instruments and Methods, Vol. A273, (1988), p.p. 599-604.

99. McEntaffer, R. L. et al., "An X-ray Test Facility for Diffraction Gratings", Proc. SPIE, Vol. 5168, (2004), p.p. 499-507.

100. McEntaffer, R. L. et al., "Off-Plane X-ray Grating Spectrometer for the International X-ray Observatory", Proc. SPIE, Vol. 7360, (2009), p.p. 73600H-1.

101. Meidinger, N., et al., "Soft X-ray damage in CCD detectors", Nuclear Instrument and Methods, Vol. 439, (2000), p.p. 319-336.

102. Miller, J. et al., "Fundamental Accretion and Ejection Astrophysics", White Paper submitted to Galaxies across Cosmic Time (GCT) and The Cosmology and Fundamental Physics (CFP) Science Frontiers Panels, ASTRO 2010, (2010a).

103. Miller, J. et al., "Stellar-Mass Black Holes and Their Progenitors", White Paper submitted to Galaxies across Cosmic Time (GCT) and The Cosmology and Fundamental Physics (CFP) Science Frontiers Panels, ASTRO 2010, (2010b).

104. Mitsuda, K. et al., "The X-ray observatory Suzaku", Astronomical Society of Japan, Vol. 59, (2007), p.p. S1-S7.

105. Morita, M., et al., "Growth of native oxide on a silicon surface", Journal of Applied Physics, Vol. 68 (3), (1990), p.p. 1272-1281.

106. Moseley, S. H., Mather, J. C. & McCammon, "Thermal detectors as X-ray spectrometers", Journal of Applied Physics, Vol. 56, (1984), p.p. 1257-1262.

107. Murray, N. J., "Improvements to MOS CCD technology for Future X-ray Astronomy Missions", Doctoral thesis, Brunel University, 2008.

108. Murray, N. J., et al., "Off-Plane Grating Spectrometer Camera for IXO", Proc. SPIE, Vol. 7742, (2010), p.p. 77420X-1.

109. Nandra, K. et al., "The Growth of Supermassive Black Holes across Cosmic Time", White Paper submitted to Galaxies across Cosmic Time (GCT) and The Cosmology and Fundamental Physics (CFP) Science Frontiers Panels, ASTRO 2010, (2010).

110. NASA, "Suzaku", http://www.nasa.gov/mission_pages/astro-e2/main/index.html, Last Updated 24-03-11, Date Accessed 12-06-12.

111. Ness, J. U., et al., "XMM-Newton Users Handbook", ESA document number XMM-PS-GM-14, Issue 2.7, (2009).

112. Nicastro, F., Mathur, S., Martin, E., "Missing Baryons and the Warm-Hot Intergalactic Medium", White Paper submitted to Galaxies across Cosmic Time (GCT) and The Cosmology and Fundamental Physics (CFP) Science Frontiers Panels, (2010).

113. Nikzad, S. et al., "Delta-doped CCDs: High QE with long-term stability at UV and visible wavelengths", Proc. SPIE, Vol. 2198, (1994).

114. Nyquist, H., "Thermal Agitation of Electric Charge in Conductors", Physical Review, Vol. 32, (1928), p.p. 110-113.

115. Optocorp b, "Chandra Science Instruments", Copyright 2008 Oceanside Photo and Telescope, http://www.optcorp.com/edu/articleDetailEDU.aspx?aid=2295, Date Accessed 12-06-2012.

116. Optocorp a, "The Reflection Grating Spectrometer (RGS) Onboard XMM-Newton", http://www.optcorp.com/edu/articleDetailEDU.aspx?aid=2295, Copyright 2008 Oceanside Photo and Telescope, Date Accessed 12-06-2012.

117. Owens, A. et al., "The X-ray energy response of silicon (B): Measurements", Nuclear Instruments and Methods in Physics Research A, Vol. 382, (1996), p.p. 503-510.

118. Paerels, F. et al., "The Behaviour of Matter under Extreme Conditions", White Paper submitted to the ASTRO2010 Decadal Survey of Astronomy and Astrophysics, ASTRO 2010, (2010).

119. Perotti, F. et al., "Observed energy dependence of Fano factor in silicon at hard X-ray energies" Nuclear Instruments and Methods in Physics Research A, Vol. 423, (1999), p.p. 356-363.

120. Pollock, A. M. T., "Status of the RGS Calibration", XMM-RGS ESA document, XMM_SOC_CAL_TN-0030, Issue 5, (2008).

121. Pollock, A. M. T., "Calibration status of the XMM-Newton RGS", XMM-Users Group, European Space Astronomy Centre, Villanueva de la Canada, Madrid, Spain, (2009).

122. Rayleigh, Philosophical Magazine (5), Vol. 8, (1879), p.p. 261.

123. Reich, R. et al., "Integrated Electronic Shutter for Back-illuminated Charge-Coupled Devices", IEEE Transactions on Electron Devices, Vol. 40, No. 7, (1993), p.p. 1231-1237.

124. Richter, R. H. et al., "Design and technology of DEPFET pixel sensors for linear collider applications", Nuclear Instruments and Methods, Vol. 511, Issues 1-2, (2003), p.p. 250-256.

125. Robbins, M. S. & Hadwen, B. J., "The noise Performance of Electron Multiplying Charge-Coupled Devices", IEEE Transactions on Electron Devices, Vol. 50, No. 5, (2003), p.p. 1227-1232.

126. Samson, J. A. & Ederer D. L., "Vacuum Ultraviolet Spectroscopy", Academic Press, New edition, 2000.

127. Scholze, F. et al., "High-Accuracy EUV Metrology of PTB Using Synchrotron Radiation", Proc. SPIE, Vol. 4344, (2001).

128. Struder, L. et al., "The European Photon Imaging Camera on XMM-Newton: The pn-CCD Camera", Astronomy and Astrophysics, 365, (2001), p.p. L18.

129. Sawhney, K. J. S. et al., "A novel undulator-based PGM beamline for circularly polarised synchrotron radiation at BESSY II", Nuclear Instruments and Methods in Physics Research, Vol. 390, (1997), p.p. 395-402.

130. Smith, D. R. et al., "Proton Irradiation of EMCCDs", IEEE Transactions on Electron Devices, Vol. 53, No. 2, (2006), p.p. 205-210.

131. Sze, S. M., "Physics of Semiconductor Devices", John Wiley & Sons, Inc., Second Edition, 1981.

132. Takahashi, T. et al., "Astro-E mission and the X-ray survey", Astronomische Nachrichten, Vol. 319, (1998), p.p. 159-162.

133. Tanaka, Y. and Inoue, H., "The X-ray Astronomy Satellite ASCA", Astronomical Society of Japan, Vol. 46, (1994), p.p. L37-L41.

134. Tananbaum, H.D. et al., "Constellation X-ray mission implementation concept and science overview", Proc. SPIE, Vol. 3765, (1999), p.p. 62-72.

135. Thornagel, R., Klein, R. & Ulm, G., "The electron storage ring BESSY II as a primary source standard from the visible to the X-ray range", Metrologia, Vol. 38, (2001), p.p. 385-389.

136. Tirinio, T. et al., "Temperature dependence of the impact ionization coefficients in GaAs, cubic SiC and zinc-blende GaN", Journal of Applied Physics, Vol. 94, No. 423, (2003), p.p. 423-430.

137. Tompsett, M. E., "Charge Transfer Devices", Journal of Vacuum Science and Technology, Vol. 9, Issue 4, (1972), p.p. 1166.

138. Townsley, L. K. et al., "Simulating CCDs for the Chandra Advanced CCD Imaging Spectrometer", Nuclear Instruments and Methods, Vol. 486, Issue 3, (2002), p.p. 716-750.

139. Truemper, J., "The ROSAT mission", COSPAR and International Astronomical Union, Symposium on Advanced Space Instrumentation in Astronomy, 1982.

140. Tsunemi, H., "Development of the X-ray CCD in Japan", Nuclear Instruments and Methods, Vol. 541, (2005), p.p. 295-303.

141. Tsusaka, Y. et al., "Characterization of the Advanced Satellite for Cosmology and Astrophysics x-ray telescope: pre-flight calibration and ray tracing", Applied Optics, Vol. 34, No. 22, (1995).

142. Tufnol Grade 10G/40, "Epoxy glass fabric laminate Product Information", Information Sheet No. PR 39, (1994).

143. Turner, M. J. L. et al., "The European Photon Imaging Camera on XMM-Newton: The MOS Cameras", Astronomy and Astrophysics, Vol. 365, (2000), p.p. L27.

144. Turner M. J. L. and Thomas, H. D., "The Large Area Counter on Ginga", Publications of the Astronomical Society of Japan, Vol. 41, (1989), p.p. 345-372.

145. Tutt, J. H., et al., "The Noise Performance of Electron Multiplying Charge-Coupled Devices at soft X-ray energies", IEEE Trans. Electrons Devices, (accepted May 2012).

146. Tutt, J. H., et al., "The Noise Performance of Electron Multiplying Charge-Coupled Devices at X-ray energies", IEEE Trans. Electrons Devices, Vol. 59, Issue 1, (2011), p.p. 167-175.

147. Tutt, J. H., et al., "A study of electron-multiplying CCDs for use on the International X-ray Observatory off-plane x-ray grating spectrometer", Proc. SPIE, Vol. 7742, (2010).

148. Van de Hulst, H. C., "Light scattering by small particles", Dover Publications Inc., 1981.

149. Van de Steeg, M. J. H. et al., "A Frame-Transfer CCD Color Imager with Vertical Antiblooming", IEEE Transactions on Electron Devices, Vol. ED-32, No. 8, (1985).

150. Van den Berg, M. L. et al., "Back-illuminated CCDs made by gas immersion laser doping", Nuclear Instruments and Methods in Physics Research, Vol. 377, (1996), p.p. 312-319.

151. Vikhlinin, A. et al., "Cosmological Studies with a Large-Area X-ray Telescope", White Paper submitted to Galaxies across Cosmic Time (GCT) and The Cosmology and Fundamental Physics (CFP) Science Frontiers Panels, ASTRO 2010, (2010).

152. Walden, R. H. et al., "The Buried Channel Charge-Coupled Device", Bell Systems Technical Journal, Vol. 51, (1972), p.p. 1635.

153. Weisskopf, M. C. et al., "An Overview of the Performance and Scientific Results from the Chandra X-ray Observatory", The American Astronomical Society, Vol. 114, (2002), p.p. 1-24.

154. Weitkamp, T., et al., "X-ray phase imaging with a grating interferometer", Optics Express, Vol. 13, No. 16, (2005).

155. Westhoff, R. C. et al., "Low dark current, back-illuminated charge-coupled devices", Proc. SPIE, Vol. 7249, (2009), p.p. 72490J-1.

156. White, M. H., Lampe, D. R., Blaha F. C., Mack I. A., "Characterisation of Surface Channel CCD Image Arrays at Low Light Levels", IEEE J. Solid-State Circuits, Vol. sc-9, No. 1, (1974).

157. Wiza, J. L., "Microchannel Plate Detectors", Nuclear Instruments and Methods, Vol. 162, (1979), p.p. 587-601.

158. Young, H. D. & Freedman, R. A., "University Physics with modern Physics", Addison Wesley Longman, Inc. 10th Edition, 2000.

159. Young, H. D. & Freedman, R. A., "University Physics", Addison Wesley, 9th Edition, 1996.